TRANSIENT LIQUID PHASE BONDING OF A THIRD GENERATION

GAMMA-TITANIUM ALUMINUM ALLOY – GAMMA MET PX

Except where reference is made to the work of others, the work described in this dissertation is my own or was done in collaboration with my advisory committee. This dissertation does not include proprietary, restricted or classified information.


Daniel A. Butts


Certificate of Approval:


Jeffery W. Fergus
Associate Professor
Mechanical Engineering

William F. Gale, Chair
Professor
Mechanical Engineering

Ruel A. Overfelt
Professor
Mechanical Engineering

Lewis N. Payton
Assistant Research Professor
Industrial and Systems Engineering

Stephen L. McFarland
Dean
Graduate School

TRANSIENT LIQUID PHASE BONDING OF A THIRD GENERATION

GAMMA-TITANIUM ALUMINUM ALLOY – GAMMA MET PX

Daniel A. Butts

A Dissertation

Submitted to

the Graduate Faculty of

Auburn University

in Partial Fulfillment of the

Requirements for the

Degree of

Doctor of Philosophy

Auburn, Alabama

August 8, 2005

VITA

Daniel Alan Butts, son of Eric and Mavis Butts of Greenville, Alabama, was born February 8, 1978, in Montgomery, Alabama. He graduated from Greenville High School in 1996 and then entered Auburn University later that year. He graduated Magna Cum Laude from Auburn University in June of 2000 with a Bachelor degree in Textile Engineering, and immediately entered the Doctoral program in Materials Engineering at Auburn University. He married Rebecca Laurel Blanton, daughter of Garilyn Blanton of Frisco City, Alabama and the late Charles D. Blanton, on May 19, 2001.

DISSERTATION ABSTRACT

TRANSIENT LIQUID PHASE BONDING OF A THIRD GENERATION

GAMMA-TITANIUM ALUMINUM ALLOY – GAMMA MET PX

Daniel A. Butts

Doctor of Philosophy, August 8, 2005
(B.S. Auburn University, 2000)

Directed by William F. Gale

The research work presented here discusses transient liquid phase (TLP) bonding of a current (i.e. third) generation γ-TiAl alloy known as Gamma Met PX (GMPX). Effective implementation of GMPX in service is likely to require fabrication of complicated geometries for which a high performance metallurgical joining technique must be developed. Although a number of joining processes have been investigated, all have significant disadvantages that limit their ability to achieve sound joints.

TLP bonding has proved to be a successful method of producing joints with microstructures and compositions similar to that of the bulk substrates. Hence, bonds with parent-like mechanical and oxidation properties are possible.

The interlayer and bonding conditions employed for joining of GMPX were based on successful wide-gap TLP joining trials of an earlier generation cast γ-TiAl alloy

with a composition of Ti − 48Al − 2Cr − 2Nb in atomic percent (abbreviated here to 48−2−2). A composite interlayer consisting of a 6:1 weight ratio (7 vol.% copper) of gas atomized 48−2−2 powders (−270 mesh) and pure copper powders (−325 mesh) was employed. When applied to GMPX, these interlayer ratio and bonding conditions produced undesirable microstructures and poor mechanical performance in as-bonded joints. Thus, modifications to the joining technique were required. Initially these modifications were based purely on empirical and phenomenological studies, however, detailed mechanistic studies of the underlying joining mechanisms were conducted to aid in selecting these modifications. Mechanisms such as diffusion, solubility and wettability of copper in/on GMPX and 48−2−2 bulk substrates were investigated and compared. A difference in solubility of copper in GMPX and 48−2−2 bulk substrates was attributed to (at least in part) to the observed differences in GMPX and 48−2−2 bonds. The copper solubility, at the bonding temperature, in the 48−2−2 and GMPX alloys was determined to be ~2 at.% and ~1 at.% respectively. To compensate for the lower copper solubility in GMPX, the copper content of the composite interlayer employed in GMPX bonds was reduced was reduced from an initial ratio of 6:1 to 50:1. GMPX TLP bonds employing a 50:1 weight ratio (1 vol.% copper) of Gamma Met plus copper powders produced joints with a microstructure and room temperature mechanical properties somewhat comparable to the bulk material after bonding. A subsequent post-bond heat treatment produced a bond-line with a microstructure and room temperature mechanical properties similar to those of the bulk material subjected to the same thermal cycle.

# ACKNOWLEDGMENTS

The author would like to thank Dr. William F. Gale for his guidance during the course of this investigation and for his genuine concern for the well-being and success of his students. The author is also grateful to Sue Draper of NASA Glenn Research Center, Cleveland, Ohio, for serving as project monitor.

The author would like to express sincere thanks to his beloved wife, Laurel, for her unconditional love, devotion and patience for the past four years. The author would also like to recognize and extend thanks to family members Eric, Mavis, Jessica, Eric, Walter, Garilyn, Chuck, Wade, Ann, Danny, Hazel, Charles, Joyce, Eddie Mae, Mike and the Stallings for their constant support and encouragement.

Thanks are also due to the following, not only for their assistance in this work, but for their friendship as well: Jon Sofyan, Venu Krishnardula, Rajeev Aluru, Subhadra Chitti, Robert Love, Ben Beyer, Chad Callender, Courtney Guasti, Dave Lindahl and Tony Overfelt.

Style manual or journal used Metallurgical Transactions A

Computer software used Microsoft Word 2003

TABLE OF CONTENTS

LIST OF TABLES ........................................................................................X

LIST OF FIGURES ...................................................................................... XI

1. INTRODUCTION ........................................................................................ 1

2. LITERATURE REVIEW ................................................................................ 3

2.1 Crystal Structures ........................................................................................3
2.2 Microstructures and Phase Transformations ......................................................4
2.3 Mechanical Properties.....................................................................................9
2.3.1 Influence of Microstructure .........................................................................12
2.3.2 Effects of Alloy Composition .......................................................................13
2.3.3 Temperature Influence ...............................................................................17
2.4 Processing ...................................................................................................17
2.5 Advantages and Applications of Current Generation γ-TiAl Alloys ..........................19
2.6 Shortcomings of γ-TiAl Alloys ........................................................................20
2.7 Joining Technologies of Gamma TiAl Alloys .......................................................21
2.7.1 The Need for Joining of γ-TiAl Alloys .............................................................21
2.7.2 Brazing ..................................................................................................22
2.7.3 Conventional Fusion Welding .......................................................................23
2.7.4 Diffusion Bonding ......................................................................................24
2.7.5 Transient Liquid Phase Bonding ....................................................................25

3. RESEARCH OBJECTIVES ............................................................................. 36

4. MATERIALS AND EXPERIMENTAL PROCEDURES ............................................ 41

4.1 Materials ......................................................................................................41
4.2 Joining Procedure ..........................................................................................45
4.3 Post-Bond Heat Treatment Procedure.................................................................46
4.4 Metallographic Preparation ...............................................................................46
4.5 Specimen Characterization ...............................................................................47
4.6 Hotstage Light Microscopy ...............................................................................47
4.7 Mechanical Testing .........................................................................................48
4.7.1 Bend Testing ..............................................................................................49
4.7.2 Tensile Testing ...........................................................................................49
4.7.3 Hardness Testing .........................................................................................50

5. RESULTS AND DISCUSSION ........................................................................ 52

5.1 Characterization of As-bonded Wide-gap TLP joints.............................................52
5.1.1 Characterization of Composite Interlayer Powders..............................................74
5.1.2 Automated Technique for Depositing Composite Powder Interlayer.......................80
5.2 Characterization of Bonds Employing a Ti-Cu-Ni Braze Foil ...................................88
5.3 Structure-Property Relationship for As-bonded TLP Joints.....................................93

5.3.1 Four-Point Bend Testing ........................................ 93
5.3.2 Tensile Testing ........................................ 106
5.4 Characterization of Post-Bond Heat Treated Wide-gap TLP joints ........................................ 110
5.4.1 Duplex Microstructure ........................................ 110
5.4.2 Fully Lamellar Microstructures ........................................ 116
5.5 Structure-Property Relationship for TLP Joints Following a PBHT ........................................ 124
5.5.1 Four-Point Bend and Tensile Testing ........................................ 124
5.6 Comparison of 48–2–2 and GMPX Materials and TLP Bonds ........................................ 128
5.6.1 Substrate Materials ........................................ 128
5.6.2 Interlayer Materials ........................................ 133
5.6.3 Wide-Gap TLP Bonds ........................................ 135
5.7 Mechanistic Studies ........................................ 141
5.7.1 Diffusion of Copper ........................................ 142
5.7.2 Copper Solubility ........................................ 147
5.7.3 Wettability (Spreading) of Liquid Copper ........................................ 153
5.7.4 Dissolution ........................................ 162
5.7.5 Contribution of Other Observations ........................................ 164
5.7.6 Summary of Mechanistic Studies ........................................ 165
5.8 Modeling of Wide-gap TLP Bonding for 48–2–2 and GMPX Alloys ........................................ 168
5.8.1 Modeling on Wide-Gap TLP Bonding of 48–2–2 ........................................ 169
5.8.2 Modeling on Wide-Gap TLP Bonding of GMPX ........................................ 189
6. CONCLUSIONS ........................................ 198
7. FUTURE WORK ........................................ 201
8. BIBLIOGRAPHY ........................................ 205

LIST OF TABLES

Table 1−Properties of γ-TiAl alloys in comparison with commercial superalloys.[2,41] ... 10

Table 2−Summary of SEM based EDS analysis of GMPX bonds employing various interlayers. Analysis of 48−2−2 bonds are provided as a comparison and will be discussed at length in section 5.6.3. ‡ Values are for localized regions only. ... 60

Table 3−Optimum parameters for successful automated deposition of 48−2−2 plus copper composite interlayer.[27,29] ... 86

Table 4−GMPX and 48−2−2 intensity ratio calculations for the $\alpha_2(Ti_3Al)$ peaks observed using the intensity of the γ(111) peak as a reference. Here, $I_{Int.}$ and $I_{Ref.}$ represent intensity for peak of interest and intensity for reference peak respectively. ... 132

Table 5−The distribution of copper in 48−2−2 bonds during various stages of the TLP bonding process. ... 184

Table 6−The distribution of copper in GMPX bonds during various stages of the TLP bonding process. ... 195

LIST OF FIGURES

Figure 1–Ti-Al binary phase diagram.[31] .......... 6

Figure 2–The crystal lattice structures of (a) TiAl and (b) $Ti_3Al$.[31] .......... 7

Figure 3–Mid-section of binary Ti-Al phase diagram and corresponding microstructures.[39,40] .......... 8

Figure 4–Variation of the specific tensile strength with temperature for recently developed GKSS γ-TiAl alloys. For comparison, data for various commercially available high temperature alloys and a forged conventional γ-TiAl alloy with a composition of Ti – 48.5 at.% Al – 0.2 at.% Si is also shown (Figure courtesy of GKSS, Germany – used with permission). .......... 11

Figure 5–Nominal stages in a TLP bonding process employing a substrate with composition A ($C_A$) and an interlayer with eutectic composition ($C_E$). (a) Initial condition; (b) Dissolution; (c) Isothermal solidification; (d) Completion of isothermal solidification; (e) Solid state homogenization; (f) Final condition; $C_L$ = liquidus composition; $C_S$ = solidus composition; $T_B$ = bonding temperature. Figure based on reference 141, but with omission of some additional steps such as initial melting. .......... 28

Figure 6–Flow chart of project objectives showing application TLP joining technique developed originally for 48–2–2 to that of GMPX. .......... 39

Figure 7–SEM (scanning electron microscopy) micrograph, in SEI (secondary electron imaging) mode, of as-received GMPX in the (a) transverse and (b) longitudinal directions. Arrows indicate elongated $TiB_2$ particles. .......... 43

Figure 8–LM micrograph of as-received 48–2–2 substrate. .......... 44

Figure 9–Schematic of (a) four-point bend testing set-up and (b) tensile test sample with nominal dimensions. Arrows indicate approximate location of bond-line. Typical bond-line width = 100 μm. .......... 51

Figure 10–LM micrograph of an as-bonded GMPX joint using 6:1 Gamma Met to copper interlayer ratio. Copper lean phases (a) with a copper concentration of 5 – 6 at.% were found surrounding the original Gamma Met powder particles. Large copper containing intermetallics (b) with average copper content of 32 at.% resulted in scatter of bond-line hardness (see Figure 11). .......... 56

Figure 11–Vickers microhardness across bond-line of an as-bonded GMPX joint employing a 6:1 Gamma Met to copper interlayer ratio (joint width ~80 μm). Note the copper rich intermetallics observed in the bond-line resulted in significant scatter of bond-line hardness. In addition, the large epitaxial grown grains at the bond-line/substrate interface resulted in hardness less than that of the substrates. 57

Figure 12–Composition profile, obtained using SEM-based EDS analysis, across bond-line of an as-bonded GMPX joint employing a 6:1 Gamma Met to copper interlayer ratio (joint width ~80 μm). Right side of graph refers to composition of copper across bond-line, whereas the left side of the graph refers to the composition of aluminum, titanium, chromium and niobium detected by EDS analysis. Since composition of GMPX is proprietary to GKSS Research Center, only the relative compositions for the latter elements are shown. 58

Figure 13–LM micrograph showing the interface of the (a) substrate and (c) bond-line of an as-bonded GMPX joint employing a 6:1 Gamma Met to copper interlayer ratio. (b) Indicates region of epitaxially grown grains. 59

Figure 14–LM micrograph of an as-bonded GMPX bond-line employing a 20:1 Gamma Met to copper interlayer ratio. No copper-rich intermetallics were observed, however numerous regions of completely dissolved Gamma Met powders (indicated by arrows) were apparent. 62

Figure 15–Vickers microhardness across bond-line of an as-bonded GMPX joint employing a 20:1 Gamma Met to copper interlayer ratio (joint width ~200 μm). 63

Figure 16–Composition profile across bond-line of an as-bonded GMPX joint employing a 20:1 Gamma Met to copper composite interlayer ratio (joint width ~200 μm). Right side of graph refers to composition of copper across bond-line, whereas the left side of the graph refers to the composition of aluminum, titanium, chromium and niobium detected by EDS analysis. 64

Figure 17–LM micrograph of an as-bonded GMPX joint employing a 50:1 Gamma Met to copper interlayer ratio. No copper-rich intermetallics were observed. A few random regions of (a) completely dissolved Gamma Met powders, with a lamellar-like microstructure, and (b) porous regions were observed (refer to Figure 37 for a detailed micrograph of these porous regions). 68

Figure 18–LM micrograph showing the interface of the (a) substrate and (c) bond-line of an as-bonded GMX joint employing a 6:1 Gamma Met to copper interlayer ratio. (c) indicates region of epitaxially grown grains. 69

Figure 19–Vickers microhardness across bond-line of an as-bonded GMPX joint employing a 50:1 Gamma Met to copper interlayer ratio (joint width ~100 μm). 70

Figure 20–Composition profile across bond-line of an as-bonded GMPX joint employing a 50:1 Gamma Met to copper interlayer ratio (joint width ~100 µm). Right side of graph refers to composition of copper across bond-line, whereas the left side of the graph refers to the composition of aluminum, titanium, chromium and niobium detected by EDS analysis. ....................................... 71

Figure 21– SEM micrographs, in SEI mode, of an as-bonded GMPX joint employing a 100:1 Gamma Met to copper interlayer ratio. (a) Localized region of bond-line containing 1 – 2 at.% copper. (b) Typical microstructure of bond-line containing only sintered Gamma Met powders. ............................................ 73

Figure 22– SEM micrograph, in SEI mode, of 6:1 weight ratio mixture of -200 mesh Gamma Met plus -325 mesh copper powders showing (a) spherical gas-atomized Gamma Met and (b) irregular shaped copper powders. .................. 75

Figure 23–SEM micrograph, in SEI mode, of cross-section of as-received gas-atomized Gamma Met powders showing fine cellular microstructure, which is typical of gas-atomized powders. ........................................................................ 76

Figure 24–XRD pattern of as-received Gamma Met powders. The predominant phase present was determined to be the α(Ti)-Al solid solution phase. Note: Unlabeled peak at approximately 40° could not be identified. ...................... 77

Figure 25–SEM micrographs, in SEI mode, showing the (a) surface and (b) cross-section of the gas atomized Gamma Met powders after a bond cycle of $T_B$ for X hr. 78

Figure 26–XRD pattern of Gamma Met powders after a thermal cycle of $T_B$ for X hr. The predominant phase present was determined to be the γ(TiAl) phase with a small volume fraction of the $\alpha_2(Ti_3Al)$ phase ................................................ 79

Figure 27–Schematic representation of the automated deposition system.[27] ................. 84

Figure 28–Anticipated relation between sedimentation velocity and particle size for 48–2–2 and copper powder particles.[29] ........................................................ 85

Figure 29–Variation in the composition of as-deposited 48–2–2 plus copper interlayer during a deposition run as a function of position, where 0 is defined as the location where deposition commenced. Each point was determined by EDS analysis and represented an average composition at the location shown, using a scan covering an area of ~1 $mm^2$.[29] ........................................................ 87

Figure 30–LM micrograph of as-bonded GMPX joint employing a 50 µm TiCuNi-70 braze foil for X hr at $T_B$ showing one large apparent brittle intermetallic in the bond-line. ......................................................................................... 90

Figure 31–Composition profile across the bond-line of an as-bonded GMPX joint employing a 50 µm TiCuNi-70 braze foil. Right side of graph refers to composition of copper and nickel across bond-line, and left side of the graph refers to the composition of aluminum, titanium and niobium detected by EDS analysis. ........................................................................................ 91

Figure 32–Vickers microhardness across the bond-line of an as-bonded GMPX joint employing a 50 µm TiCuNi-70 braze foil (joint width ~115 µm). Note high microhardness of entire bond-line. 92

Figure 33–Results of four-point bend testing for as-bonded wide-gap TLP joints employing various Gamma Met to copper interlayer ratios. Bend strengths of the bulk material in the as-received and bond cycled condition are included for comparison. The mean bend strength and standard deviation data are as follows: 97

Figure 34–SEM micrograph, in SEI mode, showing fracture surface of as-received GMPX bulk material. The fracture path of the nearly lamellar microstructure was macroscopically flat and dominated by transgranular cleavage fracture. 98

Figure 35–SEM micrograph, in SEI mode, showing fracture surface of GMPX bulk material after a bond cycle. The fracture path dominated by transgranular cleavage fracture. 99

Figure 36–SEM micrograph, in SEI mode, showing fracture surface of GMPX bond employing a 50:1 Gamma Met to copper interlayer ratio. (a) fracture path through Gamma Met bond-line powder dominated by transgranular cleavage fracture, whereas (b) fracture through copper containing phases surrounding the Gamma Met powders appeared very planar (possibly delamination of the lamellar-like microstructure observed in the areas of dissolved Gamma Met powder particles). 100

Figure 37–SEM micrograph, in SEI mode, of fracture surface of GMPX bond employing a 50:1 Gamma Met to copper interlayer ratio. This particular region of the fracture surface shows a porous region consisting only of Gamma Met particles which had sintered during the bonding process. 101

Figure 38–SEM micrograph, in SEI mode, showing fracture surface of GMPX bond employing a 6:1 Gamma Met to copper interlayer ratio. The majority of the fracture path dominated by transgranular cleavage. However, there were several regions where failure appeared significantly different than the majority of the fracture surface. It is not clear whether these regions are due to porosity or failure by interfacial fracture between large copper-rich intermetallics and the matrix of the bond-line. 102

Figure 39–SEM micrograph, in SEI mode, showing cross sectional view of fracture surface of a GMPX bond employing a 6:1 Gamma Met to copper interlayer ratio. Failure occurred at the interface of the bond-line and one of the substrates. 103

Figure 40–SEM micrographs, in SEI mode, showing cross sectional view of fracture surface of a GMPX bond employing a 50:1 Gamma Met to copper interlayer ratio. Failure occurred at the interface of the bond-line and one of the substrates. 104

Figure 41–SEM micrograph, in SEI mode, showing cross sectional view of fracture surface of a GMPX bond employing a 65:1 Gamma Met to copper interlayer ratio. Fracture seemingly propagated at random within the bond-line, except at localized copper-rich regions where a fair amount of Gamma Met powder particles had been dissolved. At these regions, fracture tended to occur at the perimeter of these copper containing regions where there was significant epitaxial growth of Gamma Met powder particles. One such region is indicated by an arrow. ........ 105

Figure 42–Results of tensile testing for as-bonded wide-gap TLP joints employing 6:1 and 50:1 Gamma Met to copper interlayer ratios. Tensile strengths of the bulk material in the as-received and bond cycled condition are included for comparison. The mean tensile strength and standard deviation data are as follows:........ 107

Figure 43–Schematic of a narrow-gap (i.e. bond-line width < 250 μm) as-bonded sample subjected to a uniaxial stress state. According to Schimd's Law,[167] the maximum resolved shear stress ($\tau_{max}$) occurs on planes, such as *AA*, which are oriented 45° (value of $\theta$) to the tensile axis. It is obvious from the schematic that a minimal amount of the bond-line is oriented on this plane. Hence, it can be argued that tensile testing of narrow-gap bonds does not effectively test the bond-line........ 108

Figure 44–SEM micrograph, in SEI mode, showing fracture surface of GMPX bond employing a 50:1 Gamma Met to copper interlayer ratio. The fracture path was dominated by transgranular cleavage fracture and compared well to the fracture surface of the bond cycled bulk shown in Figure 35........ 109

Figure 45–LM micrograph of a GMPX joint employing a 50:1 Gamma Met to copper interlayer ratio after a PBHT at 1290°C for (a) 6X hr (b) 12X hr. Arrows indicate original bond-line. Residual copper in (a) was not effected by the etchant used to prepare this sample, thus the bond-line appears very light.. 112

Figure 46–Composition profile across bond-line as-bonded GMPX joint employing a 50:1 Gamma Met to copper interlayer ratio after a PBHT at 1290°C for 24X hr. Right side of graph refers to composition of copper across bond-line, and left side of the graph refers to the composition of aluminum, titanium, chromium and niobium detected by EDS analysis. ........ 114

Figure 47–Vickers microhardness across bond-line of an as-bonded GMPX joint employing a 50:1 Gamma Met to copper interlayer after a PBHT at 1290°C for 24X hr........ 115

Figure 48–SEM micrograph, in SEI mode, of an as-bonded GMPX joint employing a 50:1 interlayer ratio after a PBHT of 1350°C for 1 hr. Copper containing phases (as indicated by an arrow) prohibited epitaxial growth of lamellar grains across the bond-line........ 118

Figure 49–LM micrograph of GMPX substrate after heat treatment of 1350°C for 1 hr, which resulted in excessive grain growth. ........ 119

Figure 50–LM micrograph of GMPX substrate after heat treatment of 3X hr at 1340°C, which resulted in a relatively fine grain fully lamellar microstructure......... 120

Figure 51–LM micrograph of a GMPX joint employing a 50:1 Gamma Met to copper interlayer ratio after a PBHT of 24X hr at 1290°C plus 3X hr at 1340°C. A fine grain fully lamellar microstructure was formed across the original bond-line (indicated by arrows). Although no copper was detectable by EDS analysis, the lighter contrast of the bond region is attributed to residual copper below the EDS detection limit, which influences the response to the etchant used to prepare this sample. ...................................................................... 121

Figure 52–Composition profile across GMPX joint employing a 50:1 Gamma Met to copper interlayer ratio after a PBHT of 24X hr at 1290°C plus 3X hr at 1340°C. Right side of graph refers to composition of copper across bond-line, and left side of the graph refers to the composition of aluminum, titanium, chromium and niobium detected by EDS analysis. .................................... 122

Figure 53–Vickers microhardness across bond-line of an as-bonded GMPX joint employing a 50:1 Gamma Met to copper interlayer ratio after a PBHT of 24X hr at 1290°C plus 3X hr at 1340°C. .......................................................... 123

Figure 54–Results of bend and tensile testing for as-bonded wide-gap TLP joints employing a 50:1 Gamma Met to copper interlayer ratio after a PBHT of 24X hr at 1290°C plus 3X hr at 1340°C. Bend and tensile strengths of the bulk material after the PBHT thermal cycle are included for comparison. The mean bend and tensile strength and standard deviation data are as follows: 125

Figure 55: SEM micrograph, in SEI mode, showing fracture surface of GMPX bond employing a 50:1 Gamma Met to copper interlayer ratio after a PBHT of 24X hr at 1290°C plus 3X hr at 1340°C. The fracture path dominated by translamellar fracture with extensive crack deflection by the lamellae........ 126

Figure 56–SEM micrograph, in SEI mode, showing fracture surface of a GMPX bulk material subjected to a bond cycle and a PBHT of 24X hr at 1290°C plus 3X hr at 1340°C. The fracture path dominated by translamellar fracture with extensive crack deflection by the lamellae. ................................................ 127

Figure 57–XRD pattern of as-received GMPX. The predominant phase was determined to be the $\gamma$(TiAl) phase with a small volume fraction of the $\alpha_2$($Ti_3Al$) phase. ........................................................................................................... 130

Figure 58–XRD pattern of as-received 48–2–2. The predominant phase was determined to be the $\gamma$(TiAl) phase with a small volume fraction of the $\alpha_2$($Ti_3Al$) phase. ........................................................................................................... 131

Figure 59–Gamma Met and 48–2–2 powder particle size distribution. ........................ 134

Figure 60–LM micrograph of an as-bonded 48–2–2 joint employing a 6:1 48–2–2 to copper composite interlayer. (a) indicates copper-rich intermetallic (~20 at.% copper) occasionally observed in bond-line of 48–2–2 joints. .................... 137

Figure 61–Composition profile across bond-line of an as-bonded 48–2–2 joint employing a 6:1 48–2–2 to copper interlayer ratio (joint width ~150 μm). Right side of graph refers to composition of copper across bond-line, and left side of the graph refers to the composition of aluminum, titanium, chromium and niobium detected by EDS analysis. .......... 138

Figure 62–LM micrograph showing the bond-line/substrate interface of an as-bonded 48–2–2 joint employing a 6:1 48–2–2 to copper composite interlayer. Note (a) minimal epitaxial growth of substrates into bond-line (relative to GMPX bonds) and (b) dissolution of grain boundaries were observed. .......... 139

Figure 63–LM micrograph showing typical fillet produced in (a) 48–2–2 and (b) GMPX TLP bonds when employing a 6:1 TiAl alloy plus copper composite interlayer ratio. The copper concentration in the 48–2–2 fillets was determined to be ~11 at.% copper, whereas GMPX fillets had a copper concentration of ~15 at.% copper. Note the difference in cross-sectional area. .......... 140

Figure 64–Arrhenius plot for diffusion of copper in GMPX and 48–2–2 as-received substrates and corresponding values for Q and $D_0$. .......... 146

Figure 65–LM micrographs of (a) as-received GMPX after melting without copper addition and (b) GMPX with 0.5 at.% copper. .......... 150

Figure 66–Ternary Ti-Al-Cu phase diagram at 800°C.[150] .......... 152

Figure 67–HSLM images of sessile copper droplets on 48–2–2 (left column) and GMPX (right column) substrates (at a nominal temperature of $T_B$). Initial spreading rate of droplet on both substrates appear similar. At approximately 30 sec after melting, spreading of the droplet on GMPX ceases due to isothermal solidification of the spreading front. The droplet on 48–2–2 continues to spread until isothermal solidification occurs at approximately 120 sec after melting. Note the spreading front of the droplet on the 48–2–2 substrate has traveled out of the microscope's field of view. .......... 156

Figure 68–Spreading data for liquid copper on GMPX and 48–2–2 (two runs for each substrate material), with a nominal set point of $T_B$ and zero time defined as melting of copper foil. The decrease in diameter of the droplet a few seconds after melting is due to an initial dewetting stage before the onset of spreading. The undulations apparent in the data (see Figure 68b for greater detail) are associated with the flow of the liquid over a "dam" of solid produced by the onset of isothermal solidification at the spreading front. .......... 157

Figure 69–Terminal spreading distance of sessile droplets on 48–2–2 and GMPX substrates given by $A_f \setminus A_i$, where $A_f$ = final area of droplets and $A_i$ = initial area of droplet. .......... 159

Figure 70–Composition of HSLM sessile droplets on 48–2–2 and GMPX substrates. . 160

Figure 71–Cu-Cr binary phase diagram.[182] .......... 161

Figure 72–Flow chart summarizing the results of the mechanistic studies and how these mechanisms might contribute to the observed microstructural and mechanical property differences observed in 48–2–2 and GMPX bonds. ...................... 167

Figure 73–Schematic for the diffusion in sphere.[29,180]................................................ 175

Figure 74–Concentration distributions at various times in a sphere with surface concentration $C_0$. Numbers on curves are values of $Dt/a^2$.[185] ................ 176

Figure 75–The relation between the size of 48–2–2 particles and the saturation time for Cu during the isothermal solidification process.......................................... 177

Figure 76–Percentage (by weight) of copper lost to fillets as a function of bond surface area, assuming no change in cross-sectional area of fillets.......................... 183

Figure 77–Schematic of (a) post-bond condition when employing a composite interlayer; (b) pre-PBHT condition employing an equivalent copper foil interlayer; and (c) concentration profile across bond-line at t = 0 (i.e. prior to homogenization process). .......................................................................................... 185

Figure 78–Schematic of copper concentration profile across one half of bond-line during the homogenization stage. The concentration of copper in the foil interlayer is given as $C_F$ and the solubility of copper in the TiAl substrate material is given as $C_{TiAl}$. The net flux of copper atoms that must be moved to advance the interface a distance $dx$ during a given time is given as $J_{Cu}$. The homogenization stage is complete when the interlayer-substrate interface reaches the joint centerline (i.e. x = 0)....................................................... 186

Figure 79– Schematic of copper concentration profile across one half of bond-line during the homogenization stage. According to the law of conservation of solute: $A_1 = A_2$.......................................................................................... 187

Figure 80–Prediction of PBHT (homogenization) times for 48–2–2 bonds as a function of equivalent copper interlayer thickness and PBHT temperature. ............. 188

Figure 81–Plot of equivalent copper foil thickness as a function of Gamma Met to copper interlayer weight ratios.................................................................... 196

Figure 82–Prediction of PBHT (homogenization) times for GMPX bonds as a function of equivalent copper interlayer thickness and PBHT temperatures. ................ 197

# 1. INTRODUCTION

The increasing demand to conserve energy and improve efficiency in the aerospace and automotive industries has led to interest in using γ-TiAl alloys to replace various relatively dense high-temperature alloys. Alloys based on γ-TiAl offer a low density, hence high specific strengths, and moderate high temperature properties. A current generation γ-TiAl alloy, known as Gamma Met PX[1] (abbreviated here to GMPX), with a nominal composition of Ti − 45 at.% Al − X at.% (Nb, B, C) has been studied. Alloys based on this composition are known to offer improved high temperature strengths, creep resistance and oxidation resistance when compared with early generation γ-TiAl alloys.[1-3] These current generation γ-TiAl alloys are being considered for high temperature space, military and commercial applications, where weight reduction is critical to increasing efficiency.[4-6] However, a key technology that must be developed prior to effective implementation of γ-TiAl alloys, such as GMPX, is a suitable joining technique that is compatible with the temperatures, stresses and atmospheres that the alloys will see in operation. A number of joining processes, such as vacuum or induction brazing,[7-12] conventional fusion welding[13-16] and diffusion bonding[7,17-20] have been investigated, but all have limitations when used in joining γ-TiAl alloys. Transient liquid phase (TLP) bonding has proven to be a successful method of producing joints with microstructural characteristics and hence mechanical, oxidation and corrosion properties

[1] Gamma Met PX is a trademark of PLANSEE AG, Austria. Alloy composition is based on TNB alloys developed by GKSS Research Center, Germany. The full composition of this family of alloys is proprietrary to GKSS.

similar to those of the substrate material.[21-24] Thus, the TLP bonding process is well suited to the joining of current generation γ-TiAl alloys, such as GMPX, which depend on carefully tailored microstructures to produce desired properties.

Previous microstructural development studies of an earlier generation cast γ-TiAl alloy with a composition Ti – 48 at.% Al – 2 at.% Cr – 2 at.% Nb (abbreviated here to 48–2–2) suggested that a suitable TLP bonding plus solid-state homogenization process provided a bond-line with microstructural and hence mechanical properties similar to the substrate material.[25-29] Recent studies, by the present author, have attempted to apply the TLP bonding technique developed originally for 48–2–2 to GMPX. However, due to different observed behaviors in the 48–2–2 and GMPX bonds and post bond heat treated samples, modifications to the joining process were necessary. Initially these modifications were based purely on empirical and phenomenological studies; however, more detailed mechanistic studies of the underlying joining mechanisms were conducted to aid in selecting these modifications. Gamma-TiAl alloy compositions and microstructures are not yet fixed and will probably continue to evolve as intended application requirements and the capability of meeting these requirements are more clearly defined. Thus, the knowledge gained from the detailed mechanistic studies will aid in avoiding a large empirical joining test matrix with every change to the alloy.

# 2. LITERATURE REVIEW

## 2.1 Crystal Structures

Intermetallic compounds based on titanium and aluminum offer properties such as low densities (3800 – 4200 kg $m^{-3}$) and moderate high temperature properties (up to ~800° C). Due to these attractive properties, an extensive amount of research has been conducted on these compounds since their discovery in 1953.[30] Examination of the binary Ti-Al phase diagram,[31] shown in Figure 1, reveals three ordered intermetallic compounds, γ(TiAl), $\alpha_2(Ti_3Al)$ and $(TiAl_3)$. Among these, structural materials have emerged only from alloys based on the γ(TiAl) or $\alpha_2(Ti_3Al)$ phase. The brittleness of the $(TiAl_3)$ phase has prohibited its use as a structural material,[32] notwithstanding numerous attempts to ductilize $(TiAl_3)$[33,34] which were driven by a desire to exploit the low density and alumina-forming ability of the $(TiAl_3)$ phase. The presence of strong ordering decreases the plastic deformation capability of both the $\alpha_2(Ti_3Al)$ and γ(TiAl) phases. Thus, the ductility in these phases is quite low at room temperature (RT) and temperatures up to ~700 °C. As a result, alloys based on single phase γ(TiAl) or $\alpha_2(Ti_3Al)$ are not of great engineering importance.[35] Although it has been reported that single phase γ(TiAl) or $\alpha_2(Ti_3Al)$ alloys perform better than two-phase γ(TiAl) + $\alpha_2(Ti_3Al)$ alloys in hostile environments, two-phase TiAl alloys typically have improved RT ductility and fracture toughness, especially when alloyed with specific elements

(see section 2.3.2 for effects of alloying).[36,37] Consequently, most TiAl alloys for engineering applications contain a mixture of the $\gamma$(TiAl) and $\alpha_2$($Ti_3Al$) phases.

The $\gamma$(TiAl) phase has an ordered face-centered tetragonal $L1_0$ structure with a=400 pm and c=407 pm (Figure 2a). The slight tetragonal distortion in the $\gamma$(TiAl) phase is due to the different atomic radii of titanium and aluminum. The $\alpha_2$($Ti_3Al$) phase has an ordered hexagonal structure with a=578 pm and c=463 pm (Figure 2b).[38] The reader should be made aware that a TiAl alloy containing a mixture of the $\gamma$(TiAl) and $\alpha_2$($Ti_3Al$) phases, is confusingly called a "$\gamma$-TiAl alloy."

## 2.2 Microstructures and Phase Transformations

There are four main microstructures associated with $\gamma$-TiAl alloys: near gamma, duplex, nearly lamellar and fully lamellar.[39,40] Unlike cast $\gamma$(TiAl)-base alloys, which generally have a coarse-grained microstructure, wrought alloys tend to possess a fine-grained microstructure. The morphology of this fine-grained microstructure can be altered by appropriate thermal treatments (Figure 3). A near gamma microstructure can be obtained by annealing slightly above the eutectoid temperature (~1118°C) and into the $\alpha + \gamma$ region, followed by slow cooling to RT (see Ti-Al binary phase diagram in Figure 1). This microstructure consists of equiaxed $\gamma$ grains and usually a small volume fraction of $\alpha_2$ found surrounding the $\gamma$ grain boundaries.[39] Duplex microstructures are typically the finest microstructure and are formed after annealing to the middle of the $\alpha + \gamma$ region where the volume fraction of alpha and gamma phases are approximately equal. Competitive growth between the $\alpha$ and $\gamma$ phases results in a fine duplex microstructure, consisting of $\gamma$ grains and $\gamma/\alpha_2$ colonies, upon cooling to RT.[40] A small volume fraction

of $\alpha_2$ precipitates can be found in the $\gamma$ grains. The volume fraction of the lamellar colonies and the spacing of the lamellae are dependent upon the cooling rate to RT. Near lamellar microstructures are formed after heat treatments in the $\alpha + \gamma$ region of temperatures slightly below the $\alpha$-transus temperature. Fully lamellar microstructures are formed after annealing above the $\alpha$-transus temperature. The lamellar spacing in the colonies in both near lamellar and fully lamellar is strongly dependent upon the cooling rate to RT. It should be noted that excessive grain growth can occur, when annealing in the single $\alpha$-phase region, due to the absence of a second phase combined with the rapid kinetics at this relatively high temperature.[39]

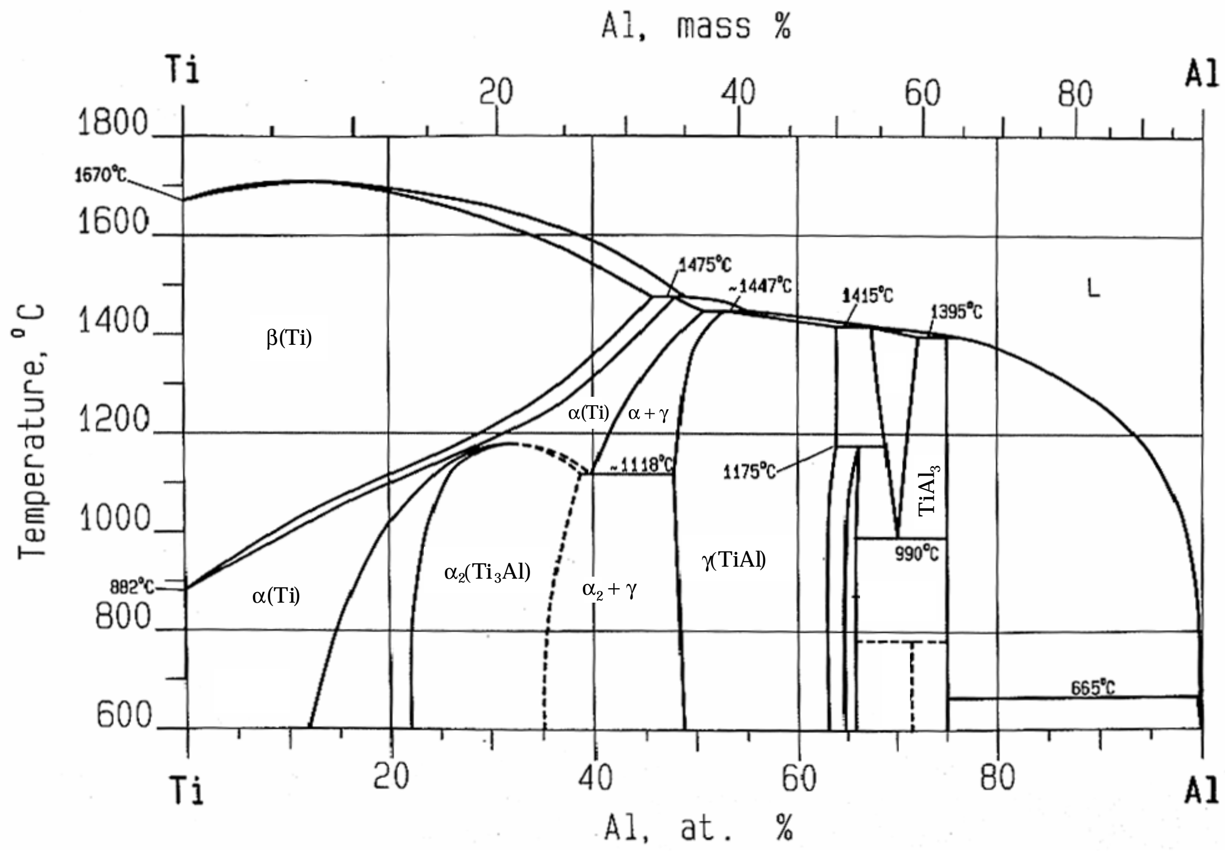


Figure 1−Ti- Al binary phase diagram.[31]

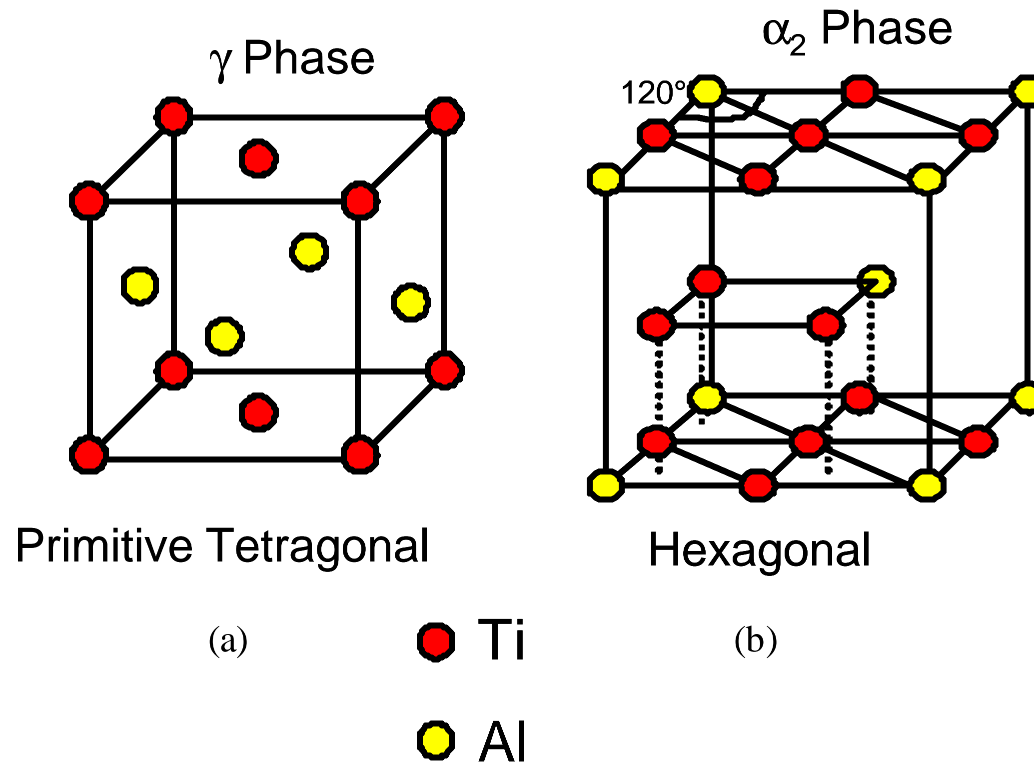


Figure 2–The crystal lattice structures of (a) TiAl and (b) $Ti_3Al$.[31]

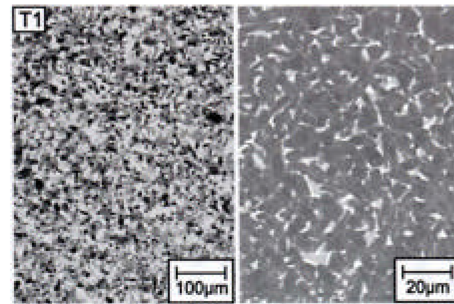


**Near Gamma**

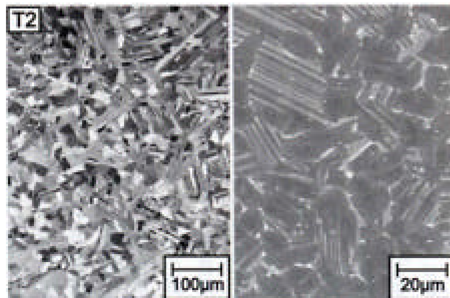


**Duplex**

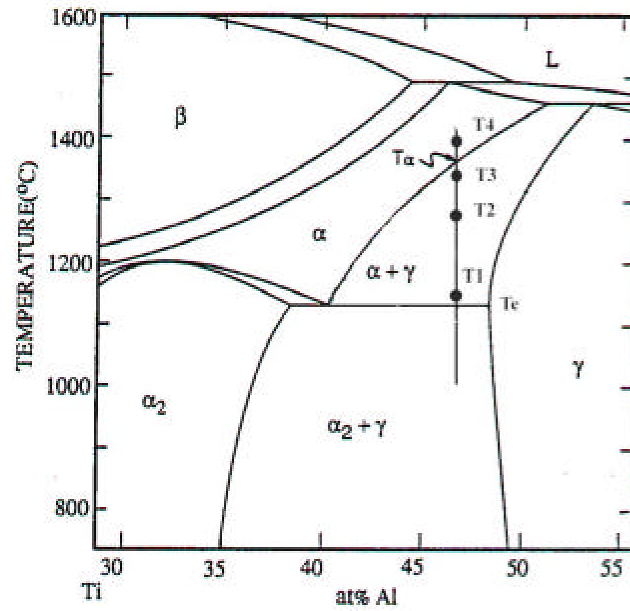


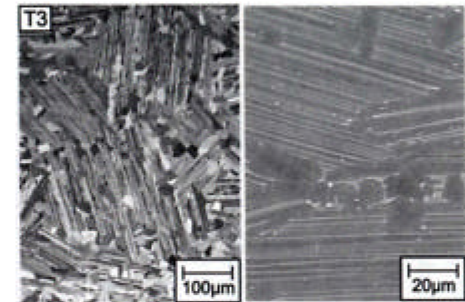


**Nearly Lamellar**

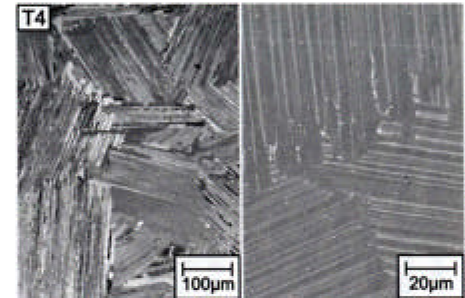


**Fully Lamellar**

Figure 3–Mid-section of binary Ti-Al phase diagram and corresponding microstructures.[39,40]

## 2.3 Mechanical Properties

Alloys based on γ-TiAl have shown RT tensile yield and tensile strength values of 350 to 1040 MPa and 400 to 1130 MPa, respectively. Corresponding RT tensile ductilities range from 0.4 to 4.0% elongation.[2,35,40-42] Mechanical properties of γ-TiAl alloys compared with commercial nickel-base superalloys are shown in Table 1. The reasonably high strength, combined with the low density associated with γ-TiAl alloys, offers the possibility of attaining high specific strengths. The variation of specific yield strength with temperature of γ-TiAl alloys in comparison with commercial nickel-base superalloys and titanium alloys is shown in Figure 4. The specific strength of alloys based on γ-TiAl are superior to titanium alloys, particularly in the temperature range of 600 and 800°C, and at least similar, if not higher, than heavier nickel-base superalloys.[39] Alloys based on γ-TiAl also offer attractive high temperature strengths, moderate oxidation and creep resistance up to a temperature of ~800°C.[1-3,43-46] However, the properties of γ-TiAl alloys are strongly dependent upon microstructure, which can significantly be affected by alloy composition and processing method.[40] This section discusses metallurgical and environmental factors that affect the mechanical properties of γ-TiAl alloys.

| Property | g-TiAl | Superalloys |
| --- | --- | --- |
| Density (kg m$^{-3}$) | 3700 – 4000 | 7900 – 8500 |
| Young's Modulus (GPa) | 160 – 180 | 198 – 230 |
| RT Ductility (%) | 0.4 – 4 | 3 – 25 |
| RT Tensile Strength (MPa) | 400 – 1130 | 1250 – 1450 |
| RT Yield Strength (MPa) | 350 – 1040 | 800 – 1200 |
| RT Fracture Toughness (MPa m$^{1/2}$) | 12 – 35 | 30 – 100 |
| Creep Limit (°C) | 750 – 950 | 800 – 1090 |
| Oxidation Limit (°C) | 800 – 950$^{\dagger}$ | 870 – 1090 |

$^{\dagger}$Coated / Actively cooled

Table 1–Properties of γ-TiAl alloys in comparison with commercial superalloys.[2,41]

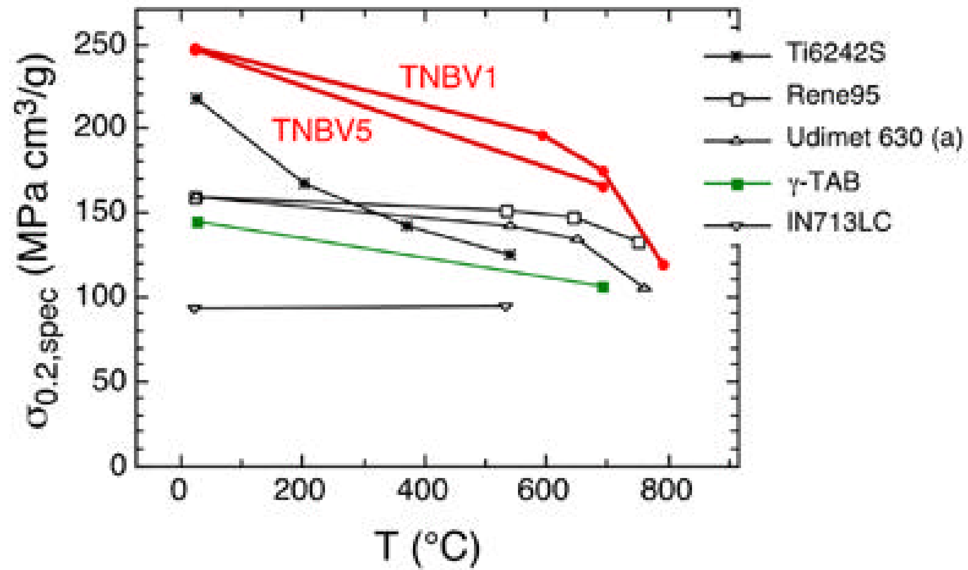


Figure 4–Variation of the specific tensile strength with temperature for recently developed GKSS γ-TiAl alloys. For comparison, data for various commercially available high temperature alloys and a forged conventional γ-TiAl alloy with a composition of Ti – 48.5 at.% Al – 0.2 at.% Si is also shown (Figure courtesy of GKSS, Germany – used with permission).

### 2.3.1 *Influence of Microstructure*

In general, the influence of microstructures on mechanical properties of alloys based on γ-TiAl can be summarized by the following statement. A fully lamellar microstructure comprised of lamellar $\gamma + \alpha_2$ colonies tend to exhibit good fracture toughness and good creep resistance, but poor tensile ductility and strength, particularly at RT. Conversely, near gamma and duplex microstructures that consist predominately of equiaxed γ grains, plus small amounts of lamellar colonies, tend to exhibit moderate tensile ductility and strength at room and elevated temperatures, but have poor fracture toughness and creep resistance.[39,47]

The RT tensile properties (both yield strength and elongation) of γ-TiAl alloys have been directly linked to grain size. The best tensile and ductility properties result from duplex microstructures, which have grain sizes that typically range from 10 – 40 μm for forged materials.[40,48] The poor ductility and RT strengths of fully lamellar microstructures have been attributed to their large grain size (some grains ≥500 μm),[48,49] the lack of slip/twinning activity,[48] the tendency for platelet interfacial separation,[50] and low cleavage stresses.[51] Efforts to reduce the fully lamellar grain size through innovative heat treatments and thermomechanical processing have been conducted.[40,52]

Alloys with fully lamellar microstructure and random colony orientations exhibit a RT fracture toughness of $K_Q = 25 - 30$ MPa $m^{1/2}$, while duplex microstructures exhibit RT fracture toughness values of $K_Q = 22 - 15$ MPa $m^{1/2}$.[53] The relatively high fracture toughness values for lamellar alloys is generally attributed to the ability of the alternating γ and $\alpha_2$ platelets to cause crack tip immobilization and crack deflection, which results in a tortuous crack path.[53,54] Failure in lamellar alloys ultimately results from decohesion

of lamellar boundaries and translamellar fracture.[38] In contrast, the equiaxed $\gamma$ grains in duplex microstructures result in a relatively planar crack path along grain boundaries (intergranular fracture) and cleavage planes.[50]

The creep resistance exhibited by fully lamellar microstructures has been shown to be significantly greater than that of duplex microstructures. This superior creep resistance has been attributed to many mechanisms. However, many aspects of creep are still a matter of debate. Some proposed mechanisms attribute the superior creep resistance of lamellar structures to their large grain size[40] and serrated grain boundary morphology.[55] The latter two characteristics are most likely effective at reducing vacancy diffusion during creep. Another proposed mechanism suggests that the $\alpha_2$ platelets provide a composite-like reinforcement strengthening.[56]

An optimum balance must be found between this inverse correlation of tensile properties and resistance to fracture (fracture toughness) and creep resistance. Ultimately this optimum balance is governed by the conditions that the alloys will see in operation, but in general, an optimum balance between fracture toughness and creep resistance, and RT tensile ductility and strength is observed in relatively fine-grained fully lamellar microstructures (50 to 400 $\mu$m) with narrow lamellar spacing.[41] This optimum microstructure can be controlled by proper thermomechanical processing and composition.[57]

### *2.3.2 Effects of Alloy Composition*

During the past decade, there has been an extensive amount of research which has proven that minute changes in alloy composition can have profound effects on the properties of $\gamma$-TiAl alloys. However, the role that various alloying elements play in

improving/degrading the performance of $\gamma$-TiAl alloys is not exactly clear. Nonetheless, certain rules have been established that may be used as guidelines when designing alloys to meet desired requirements.[58]

Considering aluminum is one of the major elements of $\gamma$-TiAl alloys, it is not surprising that minute changes in aluminum content have profound effects on microstructure and hence mechanical properties. In general, a reduction in aluminum content tends to increase ductility and strength levels.[38,57] The increase in ductility with decreasing aluminum content has been attributed to a reduction in the c/a ratio of the $\gamma$(TiAl) phase and decreased covalent bonding or increased metallic bonding.[57] However, other mechanisms involving the increased formation of twins have been proposed.[57] A decrease in aluminum content has also been said to suppress grain size,[57] which is known to increase strength levels.[49]

In addition to affecting mechanical properties, changes in aluminum content have also affected oxidation resistance.[38] TiAl alloys with high aluminum content are known to be very oxidation resistance due to preferential tendency to form the protective oxide layer, $Al_2O_3$, opposed to the non-protective oxide layer[2], TiO.[36] In contrast, the oxidation resistance is reduced with decreasing aluminum content primarily due to the formation of the titanium-rich $\alpha_2$($Ti_3Al$) phase, and the resulting preferential tendency to form TiO.[40]

---

[2] Thermodynamically speaking, the stability of $Al_2O_3$ and TiO are quite similar. However, the kinetics associated with these two oxides are significantly different. Unlike $Al_2O_3$, inherent vacancies in the TiO lattice allow significant mass transport through the oxide layer, and hence the oxide grows at a rapid rate (relative to $Al_2O_3$). Conversely, the lack of a large number of vacancies in the $Al_2O_3$ lattice reduces the amount of mass transport through the oxide layer, and hence the oxide growth is significantly retarded. Therefore, once formed, the slow growing $Al_2O_3$ oxide layer is very protective to further oxidation.[46]

Due to the inherent poor RT ductility of γ-TiAl, much work has been conducted to improve the ductility by alloying additions. It has been shown that alloying additions of chromium, vanadium and manganese, up to a level of 2 at.%, enhance the ductility of γ-TiAl, especially at low temperatures.[5,38,40,42,57] It is thought by Kim[57] that the addition of manganese stabilizes twins, resulting in more pronounce twinning opposed to ordinary dislocation slip. The effect of vanadium and chromium additions, as well as other elements, on ductility is not clearly understood.[57] However, four beneficial effects of alloying on ductility have been proposed. The first is to relax the restriction on unfavorable slip systems. The second is to retard the kinetics of ordering or to change the degree of long-range order. The third is introduce ductile second phases that can arrest the growth of microcracks. The fourth is to alter the phase transformations during thermal treatment and processing to allow microstructural refinement and stability.[42] It should be noted that further alloy development suggested that vanadium was harmful to elevated temperature oxidation and hot corrosion resistance, thus vanadium is no longer used as an alloying element.[5,40,42]

Boron additions of 0.5 to 2 at.% act as a grain refining constituent, especially in as-cast structures, and are also used for stabilizing the microstructure during high temperature service.[58-60] Due to the low solubility of boron in TiAl (~0.01 at.% in γ and <0.003 at.% in $\alpha_2$),[61] very small additions of boron lead to the formation of many types of borides, with $TiB_2$ being most prevalent. It is generally assumed that these borides precipitate first during solidification and subsequently act as nucleation sites for α and β phases in the melt,[62] however, other mechanisms have been proposed.[63] The small lamellar colonies produced by additions of boron enhance RT ductility, but as previously

stated, small grains are detrimental to creep resistance.[42] As a result, additions of tungsten, molybdenum,[58] silicon[60,64] and carbon[65] have been made to improve creep resistance. The addition of these elements increases the activation energy of dislocation and vacancy diffusion or form precipitates that increase in activation energy of dislocation and vacancy diffusion.

In an effort to improve the performance of γ-TiAl alloys, the current focus is on alloys with a niobium content in the range of 5 to 10 at.%. These third generation γ-TiAl alloys being developed by GKSS, Germany are referred to as TNB alloys.[39]

Recently, it has been shown that niobium additions significantly enhance RT strengths as well as high temperature properties, such as creep and oxidation resistance.[2,3,58,66-74] Despite the vast body of research confirming these results, there is some controversy surrounding the mechanism(s) responsible for these enhancements. Chen *et al.*[75] attributed the superior RT strength to the solid solution hardening effect of niobium additions. However, Woodward *et al.*[76] warned that the very small misfit of titanium and niobium atoms (0.2% maximum) would not likely contribute to a solid solution hardening effect of high niobium-containing alloys. Paul *et al.*[71] and Liu *et al.*[70] suggested that the high strength is a result of the decreased aluminum content in a Ti – 45 at.% Al – 10 at.% Nb alloy and that niobium plays no role in strengthening or work hardening. Concerning high temperature deformation and creep resistance, it has been suggested that niobium additions increase the activation energy of diffusion assisted deformation mechanisms.[77]

In addition to enhancing room and high temperature strengths, niobium additions are clearly beneficial to oxidation resistance of γ-TiAl alloys.[45,73,78] Although like the

improvements to room and high temperature strengths, the mechanism(s) responsible for this effect are not well understood. It is generally assumed that that addition of niobium stimulates the formation of $Al_2O_3$ at the metal/scale interface.[45,79-83] However, other mechanisms such as niobium doping of the $TiO_2$ oxide layer, which leads to a reduction in oxygen diffusion through the $TiO_2$ oxide layer, have been proposed.[84] In addition to improving isothermal oxidation resistance, niobium has also been shown to enhance cyclic oxidation.[85]

One such high niobium-containing γ-TiAl alloy, GMPX, is the alloy under investigation by the present author. This particular alloy has been shown to exhibit superior fatigue strengths and high temperature properties, such as oxidation and creep resistance, when compared with conventional γ-TiAl alloys.[1-3]

### *2.3.3 Temperature Influence*

The tensile properties of γ-TiAl alloys at elevated temperatures are related to the ductile-brittle transition temperature (DBTT), which varies from 550 – 750°C depending on alloy composition and microstructure. The yield strength gradually decreases up to the DBTT and then decreases at a more rapid rate at temperatures above the DBTT. The ductility is also related to the DBTT. Ductility levels increase slightly with temperature up to the DBTT, but increase rapidly above the DBTT.[40] The latter is a result of the increased activity of twinning and mobility of dislocations.[47]

## 2.4 Processing

The processing routes for γ-TiAl alloys generally resemble those of conventional nickel-base and titanium alloys, but with some inherent differences. In this section, the

processing routes of ingot metallurgy (IM), casting and powder metallurgy (PM) will be discussed briefly.

The most commonly used method of manufacturing ingots is by means of vacuum arc remelting (VAR). Meltstocks are typically double or triple melted in order to obtain good chemical homogeneity throughout the ingots. However, even after triple melting, segregation is commonly observed. This segregation is due to the unavoidable peritectic solidification of γ-TiAl alloys and is the most serious problem of ingot production. Prior to further processing, the ingots are usually hot isostatically pressed (HIP) in the $\alpha + \gamma$ phase field to reduce casting porosity. Further processing of ingots includes isothermal forging, conventional canned forging and extrusion. Other methods of producing ingots currently under development include plasma arc melting and induction skull melting.[38,86]

Casting has been considered the classical near-net-shape process. Unlike forging, casting can produce complex components without the need of expensive machining. Casting of γ-TiAl components, such as low-pressure turbine blades[87] and turbocharger wheels,[88] have been successful. Despite this progress, there are significant problems associated with casting of γ-TiAl. These problems include loss of strength and ductility, insufficient microstructural control and casting porosity. However, microstructural inhomogeneities and porosity can be eliminated by post-casting HIP treatments.[38,89]

Recent developments suggest that powder metallurgy has potential of being an alternative near-net-shape processing method.[90-93] Pre-alloyed γ-TiAl powders are produced by high-pressure argon gas atomization. The powders are generally spherical

and have cellular microstructures with cell sizes of a few μm. These fine, almost segregation-free powders are consolidated by HIPing into fully dense components. Typically, the mechanical properties of PM materials are superior to those of cast components and are comparable to those of forged components.[89] In addition to producing complex components, the PM route is ideal for the production of feedstock for sheet rolling of γ-TiAl.[92,94,95] Problems that plague PM of γ-TiAl alloys are microstructural irregularities, inclusions and microporosity.[96]

## 2.5 Advantages and Applications of Current Generation γ-TiAl Alloys

While some advantages of γ-TiAl alloys have already been mentioned, the advantages of current generation γ-TiAl alloys, such as GMPX, as outlined by Venskutonis,[97] are as follows:

- more than 50% lighter than superalloys;
- can replace superalloys currently used in propulsion systems, saving component mass by a factor of 20;
- specific stiffness is approximately twice that of superalloys (based on modulus normalized with respect to density);
- good high temperature properties (e.g. creep and oxidation resistance) should enable the substitution for some dense superalloy components in the temperature regime of 500 – 800°C;
- fabrication costs are potentially the same as for existing superalloys.

Due to these attractive properties, current generation γ-TiAl alloys are being considered for high temperature aerospace components for both propulsion systems and airframes. Proposed aerospace applications include low pressure turbine blades, compressor blades and exhaust nozzles for gas turbine engines. Other aerospace applications include airframe components, thermal protection systems and exhaust impinged surfaces for future hypersonic aircraft.[2,6,39,91,98,99] Current generation γ-TiAl alloys have also been considered for non-aerospace applications. Reciprocating and rotating automotive engine components, that continually operate in the temperature regime of 500 – 800°C, are ideal applications for current generation γ-TiAl alloys. The potential advantages of employing lightweight γ-TiAl alloys in automotive engines are improved fuel economy, noise reduction and higher engine revolution speeds.[100] Proposed automotive applications for current generation γ-TiAl alloys include turbocharger wheels, supercharger wheels and exhaust valves for automotive engines.[99,101-105] Current generation γ-TiAl alloys are also being considered for biomedical applications.[106]

## 2.6 Shortcomings of g-TiAl Alloys

Due to their attractive properties and considerable potential, an extensive amount of research has been conducted on γ-TiAl alloys since their discovery. Despite the latter, there are still some concerns that hinder the widespread application of these alloys. Some key concerns include:

- inverse relations between tensile properties and fracture/creep resistance, resulting in unbalanced properties;[41]

- low room temperature ductility;[41]
- effect of high temperature (800°C) air exposure on room temperature ductility;[2]
- detrimental effect of hydrogen on dynamic elastic modulus;[107]
- lack of a suitable joining technique.[108]

## 2.7 Joining Technologies of Gamma TiAl Alloys

### *2.7.1 The Need for Joining of γ-TiAl Alloys*

Dimiduk *et al.*[108] identified the lack of a suitable joining technique for structural intermetallic compounds, such as γ-TiAl alloys, as a major limiting factor to the application of these alloys in service. The need for joining of structural intermetallics, as outlined by Gale,[109] can be divided into three categories:

- Primary fabrication: The fabrication of components with complex geometries, such as honeycomb panels or large jet engine exhaust nozzles, in near-net-shape form is extremely difficult, if not impossible. Therefore, a joining technique, which bonds several small, simple parts, is often required for primary fabrication of large complex components.
- Joining of dissimilar materials: Due to the inherent poor low temperature ductility of most structural intermetallics, initial application of these materials will likely be confined to localized regions. Thus joining to dissimilar materials (e.g. nickel-base superalloys) will be required. Additionally, joining of structural intermetallics to dissimilar materials allows exploitation of the properties of both materials.

- Repair joining – pre- and post service: The application of structural intermetallics, such as γ-TiAl, will likely be expensive (at least initially). Furthermore, structural intermetallics are typically more damage sensitive compared to nickel-base superalloys. Thus, the ability to make pre- and post service repairs will likely have a profound impact on the economics of operation.

The compositions and microstructures of γ-TiAl alloys, especially current generation alloys, are carefully tailored to meet the demanding mechanical requirements of elevated temperature service. Similarly, the technique used to join these materials must be carefully tailored in order to be compatible with the temperatures, stresses and atmospheres that the alloys will see in operation. As mentioned in the introduction, a number of joining processes, such as vacuum or induction brazing,[7-12] conventional fusion welding[13-16] and diffusion bonding have been investigated,[7,17-20] but all have limitations when used in joining γ-TiAl alloys.

### *2.7.2 Brazing*

Although brazing techniques offer advantages such as low thermal exposures, low mechanical stresses and the ability to join complicated geometries, brazing does possess some significant limitations. Selection of a braze material that fulfills all the requirements of low braze temperature, low erosion of base material, good wettability of base material, high diffusivity and solubility in base material is extremely difficult.[39] The main problem associated with brazing is that the chemical composition, and hence re-melt temperature, of the bond-line is significantly different than that of the base material. Thus, the maximum temperature this braze joint can see in operation is severely

limited. This difference in chemical composition also leads to other undesirable effects. For example, when brazing γ-TiAl alloys using a Ti-Cu-Ni interlayer, a reduction in aluminum content in the bond region significantly reduces the oxidation resistance of the bond-line.[8] Additionally, brittle phase(s) formed at the bond-line, when employing a Ti-Cu-Ni interlayer in GMPX bonds, resulted in a joint with poor mechanical properties (see section 5.2).

### *2.7.3 Conventional Fusion Welding*

Conventional fusion welding processes, such as electron beam (EB) welding and gas tungsten arc (GTA) welding have been used to join γ-TiAl alloys. Patterson *et al.* employed EB welding to join Ti – 48 at.% Al – 6.5 vol.% $TiB_2$ substrates.[16] Although high quality welds were made, the welds were susceptible to solid-state cracking due to the low ductility of the material below the DBTT, combined with the high thermal residual stresses associated with fusion welding. This susceptibility to cracking was minimized by selecting suitable welding parameters that resulted in a very slow cooling rate of the heat affected zone (HAZ). However, even when employing optimum welding parameters, the microhardness of the fusion zone was determined to be at least 60% greater than that of the base metal. This increase in hardness suggests a decrease in ductility, which could lead to brittle failure in the fusion zone.

Arenas *et al.*[14] employed GTA welding to produce crack-free welds in 48–2–2 without the use of preheating. However, microhardness measurements of the fusion zone and tensile testing indicated that the mechanical properties of the weld significantly decreased relative to the base metal. In a later study, Arenas *et al.* suggested than a post-

weld heat treatment (PWHT) of 48 hr at 1000°C was effective at altering the microstructure and decreasing the hardness of the as-welded fusion zone.[110]

Other problems associated with conventional fusion welding are as follows:

- Due to the melting and resolidification employed during fusion welding, significant changes can occur in composition and microstructure of the fusion zone relative to the base metal. This can be a significant limitation for materials, such as current generation γ-TiAl alloys, that have carefully tailored compositions and microstructures in order to obtain optimum mechanical properties.

- Conventional fusion welding is predominately a line-of-site process. Thus conventional fusion welding is not a practical joining technique for corrugated or honeycomb panel structures, an envisaged application of γ-TiAl alloys,[4,91] which have predominately joints not accessible by a line-of-site process.

### *2.7.4 Diffusion Bonding*

Diffusion bonding is an isothermal, solid-state bonding process, which sidesteps the problems associated with rapid heating and cooling rates employed during conventional fusion welding. However, this bonding process still relies on relatively high temperatures (e.g. 0.75 $T_M$, where $T_M$ is the absolute melting temperature) in order to achieve rapid kinetics. Even at these temperatures (e.g. 1000 – 1200°C), diffusion bonding of γ-TiAl alloys can be extremely long in order to achieve high quality bonds. When diffusion bonding a γ-TiAl alloy based on Ti – 47 at.% Al – 4.5 at.% (Cr, Mn, Nb,

Si, B), Cam *et al.*[18] concluded that sound bonds could be achieved in primary annealed gamma sheets at 1000°C for 8 hr and at a pressure of 5 MPa. Cam *et al.* also concluded that the bonding time could be reduced to 5 hr if a bonding pressure of 10 – 20 MPa was employed. Nonetheless, a post bond heat treatment (PBHT) at 1430°C for 30 min was required to enhance the bond quality for both cases.

Besides protracted bonding times at elevated temperatures, another issue that limits the applicability of diffusion bonding is related to geometry of the bonding surfaces. Since no liquid is produced in this process, the mating surfaces must be brought into intimate, atomic scale contact.[111] Failure to do so could result in the presence of porosity at the bond-line. In addition, the presence of continuous oxide layers on faying surface can have detrimental effects on diffusion bonds.

#### *2.7.5 Transient Liquid Phase Bonding*

Transient liquid phase bonding, a derivative of high-temperature fluxless vacuum brazing, is widely used in aerospace, land-based power generation and other industries for primary fabrication, pre-service and post-service repairs.[22,24,112-118] In common with brazing,[119] TLP bonding depends upon the use of a thin liquid-forming interlayer (typically less than 50 µm), with a melting-point (initially) below that of the substrate material. However, unlike brazing, interdiffusion between the interlayer and the substrates results in a joint that has a re-melt temperature and composition similar to that of the bulk material, after completion of the TLP bonding process. Thus, in contrast to brazing, TLP bonding is suitable for the joining of components intended for elevated temperature service.

TLP bonding has been used to join a wide range of materials, such as nickel-base superalloys,[22,24,112-115] oxide dispersion strengthened alloys,[120-122] metal matrix composites[123-125] and structural intermetallics[27,126,127] that are difficult to join by other processes. TLP bonding also offers the advantage of allowing joining of dissimilar materials,[128,129] including bonding of metals to ceramics via derivatives of conventional TLP bonding.[123,130,131]

TLP bonding is usually conducted in a vacuum (*e.g.* 1 – 100 mPa) or inert atmosphere in an effort to avoid the formation of oxide layers on the interlayer and faying surfaces of the substrates. A wide variety of heating methods have been used for TLP bonding. Some examples include radiant heating in a standard vacuum furnace,[132] resistance heating,[27] induction heating[24] and infra-red heating.[124] Interlayers can be deposited in the form of foils (crystalline or amorphous[3] [136,137]), powders (with or without a fugitive tape),[27,138] paste,[139] or sputter coatings.[140]

### *2.7.5.1 Stages in the TLP Bonding Process*

Conventional models of TLP bonding assumes three distinctly different stages that occur in a sequential fashion – dissolution, isothermal solidification, and homogenization (Figure 5).[141] Once the bonding temperature (which must be greater than the melting point of the interlayer material but below that of the substrates) is attained, the interlayer melts and immediately begins to dissolve the substrate material. This dissolution process dilutes and widens the liquid interlayer and continues until local equilibrium is established at the solid-liquid interface. Upon establishing local

[3] Brittle intermetallics (e.g. $Ni_3B$) involved in many eutectic forming interlayer systems limit the production of thin rolled foils in the crystalline form. Fortunately, for some systems, the formation of a deep eutectic allows an amorphous foil [133] to be produced, usually by melt-spinning.[134,135] The production of an amorphous (and hence second-phase free) foil allows placement of a thin, ductile interlayer into the joint cavity.

equilibrium, the composition of the liquid and the adjacent solid remain fixed so long as the temperature remains constant and the liquid remains stationary. The dissolution stage is typically rapid (seconds to minutes) since the process does not rely on long range diffusion in the solid phase. During the second stage of bonding, isothermal solidification, the original interlayer constituents begin to diffuse along a concentration gradient from the liquid to the solid substrates (or vice-versa). Provided the composition of the liquid remains constant, the width of the liquid interlayer will decrease until the joint fully isothermally solidifies. Unlike the dissolution stage, isothermal solidification is governed by solid-state diffusion. Thus depending on the system employed, isothermal solidification times can range from minutes to days. In the final stage of bonding, any remaining inhomogeneity remaining in the bond-line can be removed. Like isothermal solidification, the homogenization stage depends on solid-state diffusion, and thus could also be very protracted. It should be noted that the homogenization stage is not required to immediately follow the isothermal solidification stage, but can be in the form of a separate PBHT process. For a recent review of TLP bonding see reference 142.

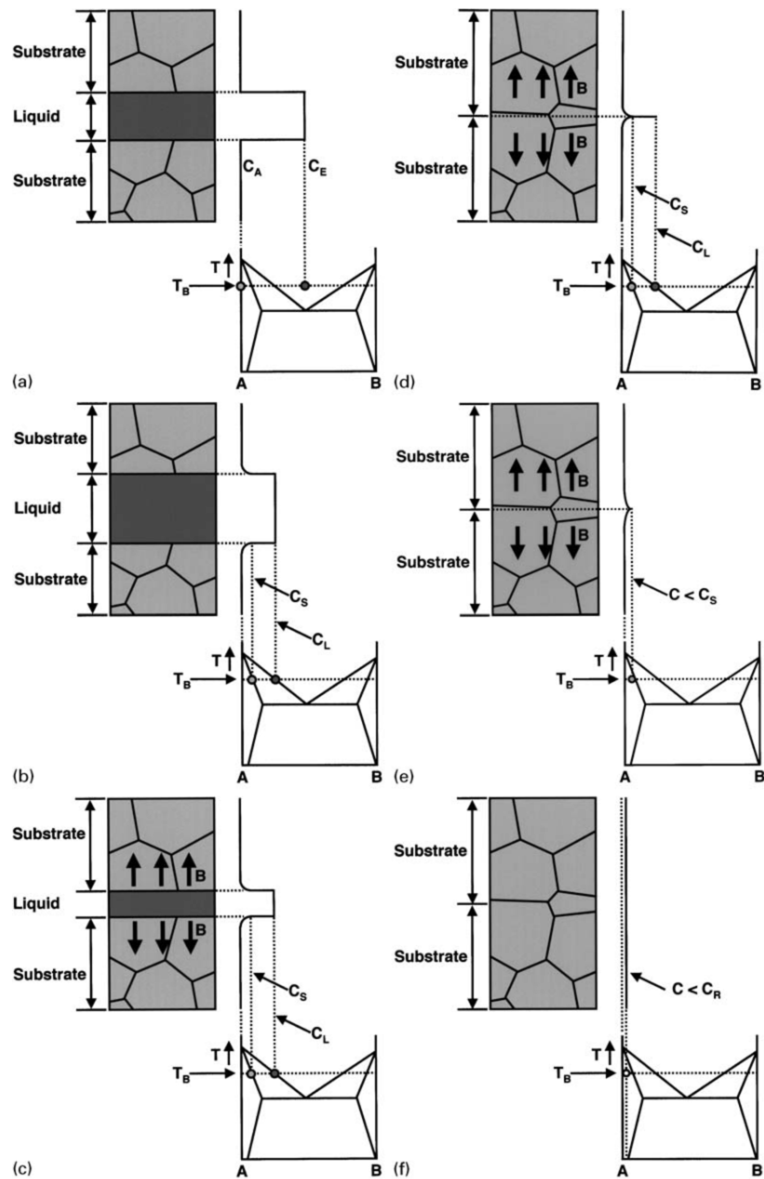


Figure 5–Nominal stages in a TLP bonding process employing a substrate with composition A ($C_A$) and an interlayer with eutectic composition ($C_E$). (a) Initial condition; (b) Dissolution; (c) Isothermal solidification; (d) Completion of isothermal solidification; (e) Solid state homogenization; (f) Final condition; $C_L$ = liquidus composition; $C_S$ = solidus composition; $T_B$ = bonding temperature. Figure based on reference 141, but with omission of some additional steps such as initial melting.

#### *2.7.5.2 Advantages and Disadvantages of TLP Bonding*

TLP bonding offers several advantages over other joining processes, some of which have already been mentioned. Additional advantages and the disadvantages associated with TLP bonding are summarized below.

*Advantages:*

- Large and complicated geometries with non-line of site joints, such as honeycomb panels, can be joined.
- In contrast to brazing, the formation of undesired brittle intermetallics in the bond-line can be avoided, thus the microstructure, and hence mechanical properties, of the joint can be similar to those of the bulk material.
- Unlike fusion welding, TLP bonding is an isothermal process, thus is ideal for joining of materials susceptible to hot cracking or PWHT.[143]
- In contrast to diffusion bonding, TLP bonding is tolerant of stable oxide layers on faying surfaces and requires minimal fixturing pressure and surface preparation.[126]

*Disadvantages:*

- Rapid heating may be required to avoid significant diffusion of interlayer and/or substrate constituents during heat-up.
- The entire joint must be elevated to high temperatures (except induction heated joints), which could cause microstructural changes in the bulk materials and implies a very large (vacuum) furnace in some cases.

- A lengthy PBHT process is often needed to achieve complete chemical and microstructural homogenization of the bond-line.

#### *2.7.5.3 Wide-gap TLP bonding*

One aspect of TLP bonding, the width of the joint gap, warrants further discussion. As mentioned above, isothermal solidification and subsequent solid-state homogenization requires a lengthy bonding time for most systems. This is particularly true when thick interlayers are used to fill a wide joint gap. Thus conventional TLP bonds rarely employ a joint gap greater than 50 μm (in some cases an order of magnitude less than 50 μm).[142] However, wide joint gaps are often required to enable industrial feasibility.[144] For TLP bonds that must use a wide joint gap, composite interlayers, consisting of a liquid forming constituent and a non-melting constituent, can be employed. The liquid forming constituent is typically selected to have a melting temperature slightly below the bonding temperature, while the non-melting constituent is selected to have a composition, and hence a solidus temperature, similar to the substrate material. The incorporation of the non-melting constituent in powder form serves the following two functions:[25,142,145]

- Reduces the amount of liquid necessary to fill the joint, thereby reducing the amount of solute that must be diffused to produce isothermal solidification and solid-state homogenization.
- Increases the interfacial area between the liquid and solid phases, thereby creating a more efficient path for diffusion of the solute from the liquid into the solid.

The choice of an appropriate ratio of liquid former to non-melting phase is a key variable in the wide gap process. If insufficient liquid former is employed, the liquid will

begin to isothermally solidify and hence cease to spread, before it has been able to penetrate throughout the joint. This would result in a joint with excessive porosity. In contrast, if too much liquid is formed, then the amount of the solid-phase that must be dissolved to produce local equilibrium at the solid-liquid interface will be very high and the joint will resemble a very wide conventional TLP bond. Thus, the benefits of using the composite interlayer would be lost. The use of an excessive liquid former can also lead to the precipitation of undesired second phases in the bond region.[146]

#### 2.7.5.3.1 *Wide-gap TLP Bonding of γ-TiAl Alloys*

When TLP bonding TiAl alloys, selecting a suitable interlayer and appropriate bonding conditions are a persistent challenge. Interlayers such as Ag–Cu, Au–Ni, Ni–Cr–B, Ti–Cu–Ni and Ti–Zr–Cu–Ni[8,22,147,148] have been proposed for use in TLP bonding of TiAl alloys. However, most contain constituents with low solubilities and/or diffusivities in γ-TiAl. Thus unless narrow gaps are employed, bonding times tend to be very long. However, as mentioned above, industrial feasibility often prohibits the use of narrow joint gaps. Thus "wide-gap" TLP bonding using a composite interlayer for TLP bonding γ-TiAl alloys seems a reasonable solution.

Wide-gap TLP bonding (gap width ~500 μm) of a cast 48–2–2 alloy has previously been researched by Zhou.[25-29] A composite interlayer consisting of a 6:1 weight ratio (7 vol.% Cu) of gas atomized 48–2–2 powders (–270 mesh) and pure copper powders (–325 mesh) was employed. Copper was chosen as the liquid forming phase since copper has some solubility in γ-TiAl[149,150] and offers good wettability of the 48–2–2 substrate surface (even in the presence of an oxide layer).[151-153] Average as-bonded four-point bend strength was determined to be ~68% of that of the bulk material

subjected to same thermal treatment. A subsequent PBHT efficiently allowed for complete chemical homogenization of the joint and simultaneously resulted in the formation of a fully lamellar microstructure in the bulk and at the original bond-line. The resulting average as-PBHT bend strength was determined to be ~90% of bulk material subjected to same thermal treatment. Room and high temperature (700°C) tensile strengths were determined to be comparable to the bulk material subjected to the same thermal conditions. Thus, this bonding plus solid-state homogenization process was determined to be a successful joining technique for the 48–2–2 alloy. The application of this wide-gap process to a current generation γ-TiAl alloy, GMPX, is the scope of the work presented here.

#### *2.7.5.4 Modeling of TLP Bonding*

As previously mentioned, TLP bonding has proved to be a successful method of producing joints with microstructural characteristics and hence mechanical properties similar to those of the substrate material. However, since the bonding process is governed by solid-state diffusion, bonding times for some systems can be very protracted (hours to days). Therefore, a quantitative prediction of the time required for completion of the bonding process is highly desirable. Additionally, prediction of the optimum bonding conditions (e.g. bonding temperature and filler metal composition) necessary to provide a sound joint is also highly desired.

Several TLP process models have been developed to address the latter issues.[154-157] These process models can be divided into three basic categories: analytical models, numerical models, and hybrid models based on an analytical approach, with numerical solutions for specific terms. Analytical models offer great simplicity, while numerical

models offer flexibility, at the expense of complexity. Hybrid models offer a compromise between these two extremes. This section discusses some examples of analytical models for the TLP bonding process.

Most analytical models assume four sequentially occurring stages in the bonding process: heating stage, dissolution stage, isothermal solidification stage and homogenization stage. Although interdiffusion between the interlayer and base metal can occur during heating to the bonding temperature, some models ignore the heating stage provided a rapid heating rate is employed. However, Niemann and Garret[158] reported that the heating stage is particularly important when employing a very thin interlayer, since the interlayer can be completely consumed by the base metal during heating to the bonding temperature.

For the dissolution stage of bonding, Nakao *et al.*[159] proposed a model that employed the Nernst-Brunner theory to develop a dissolution parameter ($P$). This dissolution parameter described the width of substrate material ($w_t$) dissolved by the liquid interlayer in a specific time ($t$), such that:

$$P = Kt = h_i \ln\left[\frac{w_0\left(w_t + \mathbf{r}h_i\right)}{\mathbf{r}h_i\left(w_0 - w_t\right)}\right] \qquad [1]$$

where: $K$ = constant;

$\mathbf{r}$ = ratio of the densities of the liquid and solid phases;

$h_i$ = half of the liquid width prior to dissolution;

$w_0$ = liquid width at which local equilibrium is established at the solid-liquid interface (i.e. the liquid composition becomes that of the liquidus and there is no further driving force for dissolution).

However, Nakagawa *et al.*[160] argued that some of the assumptions of the Nernst-Brunner theory are not applicable in TLP bonding. For example, the Nernst-Brunner theory assumes a thin boundary layer and semi-infinite liquid, which are unreasonable in a TLP bond. In addition, the above equation neglects diffusion of the liquid interlayer constituents into the base metal and suggests that the time necessary for completion of dissolution (for $w_t$ to equal $w_0$) will be infinite. Nakagawa *et al.* developed a more physically plausible numerical model that assumed a moving solid-liquid interface where the dissolution process is controlled by solute diffusion into the base material and not by any interface reaction.

Analytical solutions for the isothermal solidification stage in TLP bonding proposed by Nakao,[159] Tuah-Poku[141] and Zhou[161] follow the same general form. These solutions depend on a few assumptions in order to maintain simplicity. First, solute build-up in the solid (base metal) is small, and thus is generally ignored. Secondly, the solute distribution in the liquid is considered to be homogeneous during the isothermal solidification stage. Finally, the base metal is assumed to be semi-infinite with a surface on which the solute concentration is maintained at $C_S$. Based on these assumptions, the following error function, which describes the concentration profile of the solute in the base metal as a function of time, can be produced:[141]

$$C(x,t) = C_S\left[1 - erf\left(\frac{x}{2\sqrt{Dt}}\right)\right] \quad [2]$$

where: $C(x,t)$ = concentration of the solute in the base metal as a function of distance ($x$) and time ($t$);

$D$ = solute diffusivity in the base metal.

Continuing from Equation 2, Tuah-Poku *et al.* developed the following equation, based on the conservation of mass, to predict the total time required for isothermal solidification:

$$t = \frac{\pi}{16D}\left(\frac{C_F W_0}{C_S}\right)^2 \qquad [3]$$

where: $W_0$ = initial width of the filler metal;

$C_F$ = original solute concentration in the filler metal.

This solution is based on the assumption that the solid-liquid interface is in equilibrium and stationary with respect to the base metal. As presented by Zhou *et al.*,[162] a more accurate approach (theoretically), is to treat the solid-liquid interface as a moving boundary.

Models for the final homogenization stage are similar in form to the models for isothermal solidification. However, considering this is a single-phase process, the need to preserve local equilibrium at the phase boundaries is not required.

# 3. RESEARCH OBJECTIVES

As mentioned above, a successful TLP bonding technique for an earlier generation γ-TiAl alloy, 48−2−2, has been researched and developed. However, a highly successful bonding process for newly emerged γ-TiAl alloys, such as GMPX, has not been developed. Recent studies, by the present author, have attempted to apply the TLP bonding technique developed originally for 48−2−2 to that of GMPX. However, these two somewhat compositionally similar systems produced bonds with obvious microstructural and mechanical property (relative to the bulk) differences. Thus, modifications to the GMPX joining process were required. These modifications included selection of a composite interlayer ratio that was compatible with the GMPX substrates and selection of an appropriate PBHT. Therefore, the main technical objective of this project is to develop a suitable TLP bonding technique for GMPX by modifying the TLP bonding process developed originally for joining of 48−2−2. It should be noted that the as-cast 48−2−2 alloy required a thermal treatment prior to service.[29] Thus, a suitable PBHT was employed to transform the bulk substrate to a desired microstructure as well as fully homogenize (i.e. both chemically and microstructurally) the bond-line. However, depending on the intended application, the as-extruded microstructure of the bulk GMPX substrate may be suitable for service without further thermal processing (see section 5.4 for further discussion). Therefore, unlike the requirements of the 48−2−2 alloy, the strength of as-bonded GMPX joints should be a significant fraction of the bulk material

subjected to the same thermal treatment. Some GMPX applications may require a microstructure other than that of the as-extruded condition (see section 5.4 for further discussion). Therefore, like the requirements of the 48–2–2 alloy, the strength of as-PBHT joints should be a significant fraction of the bulk material subjected to the same thermal treatment, if a PBHT is required. In summary, a suitable TLP joining technique for GMPX can be defined as one that has the following characteristics:

- A bond-line that contains no brittle intermetallics following the bonding process and suitable PBHT (if required).
- A bond-line that has a microstructure and hence mechanical properties comparable to the bulk material (subjected to the same thermal conditions) following the bonding process and suitable PBHT (if required).

The development of a suitable TLP joining technique will involve empirical and phenomenological studies as well as mechanistic studies. The empirical and phenomenological studies will mainly be a trial and error method of determining a suitable TLP joining technique by employing various interlayer mixture ratios and post-bond heat treatments. Although empirical and phenomenological studies alone could produce the above characteristics, mechanistic studies are needed to understand the influence of the joining mechanisms involved in TLP bonding of GMPX and 48–2–2. Gamma-TiAl alloy compositions and microstructures are not yet fixed and will probably continue to evolve as the intended application requirements and the capability of meeting these requirements are more clearly defined. Thus, understanding the influence of the involved joining mechanisms will allow a non-empirical approach to be used in the TLP bonding of future $\gamma$-TiAl alloys. The outcomes of the empirical and mechanistic studies

will provide feedback which should ultimately lead to the determination of a TLP joining technique that has the characteristics listed above. A flowchart to aid in the understanding of the goals of this project is shown in Figure 6.

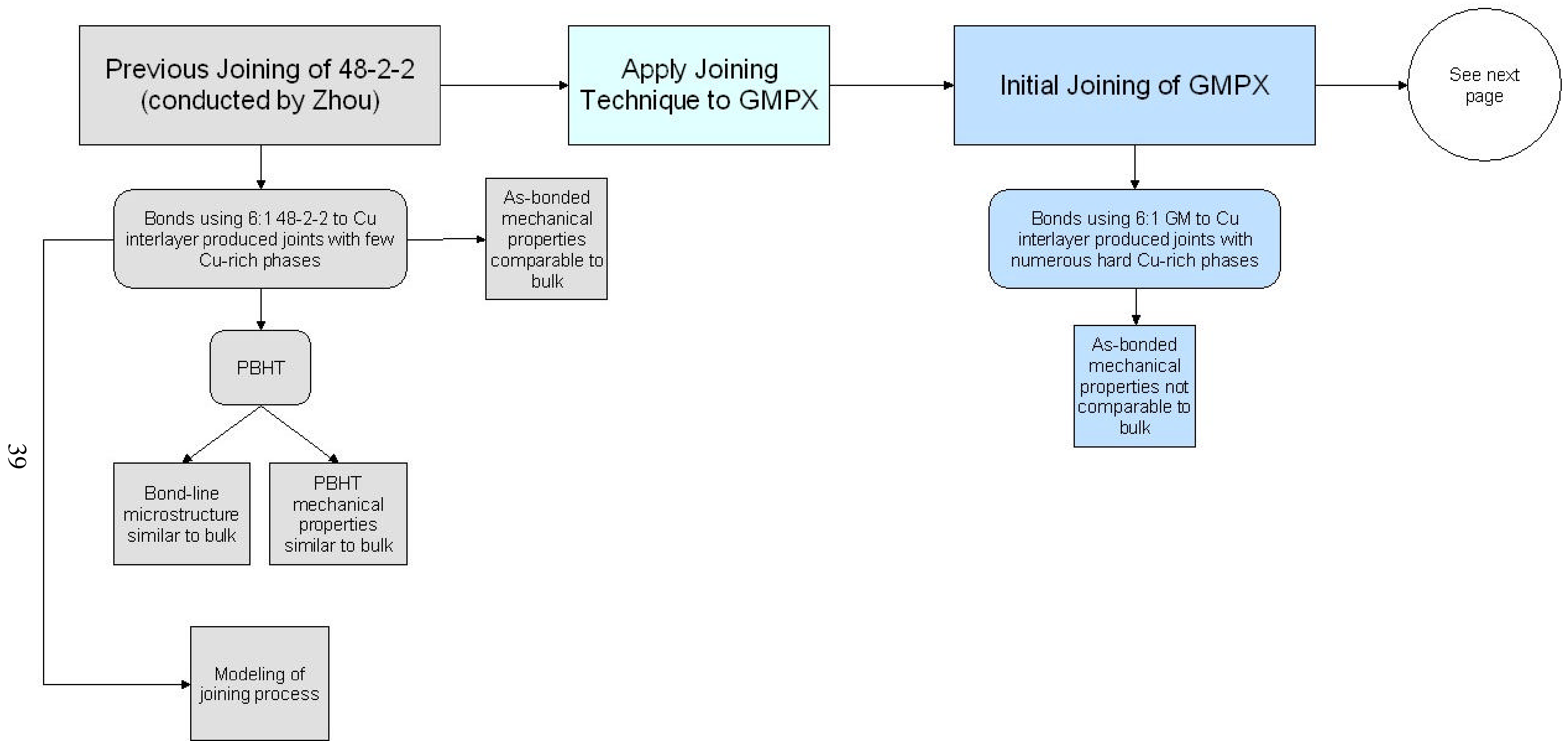


**Legend:**
48-2-2 - Ti-48Al-2Cr-2Nb (in at.%)
GMPX - Gamma Met PX
GM - Gamma Met
PBHT - Post bond heat treatment

Figure 6–Flow chart of project objectives showing application TLP joining techniq ue developed originally for 48–2–2 to that of GMPX.

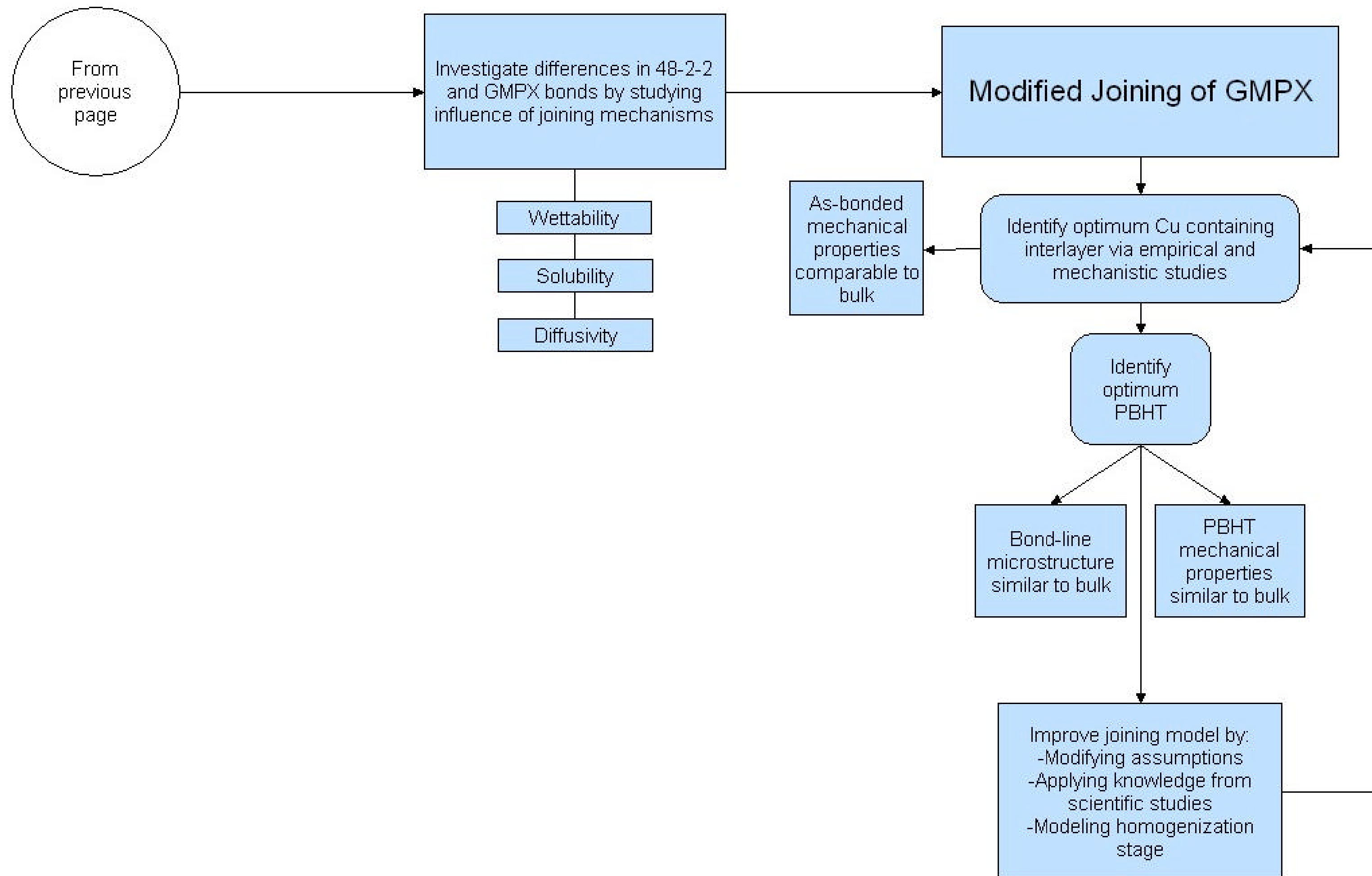


Figure 6 (continued)–Flow chart of project objectives showing empirical and scientific objectives and how these will aid in developing a suitable TLP joining technique for GMPX.

# 4. MATERIALS AND EXPERIMENTAL PROCEDURES

## 4.1 Materials

The primary materials used in this project were GMPX, Gamma Met and copper. The substrate material, GMPX, was produced by extruding triple vacuum arc remelted Ti – 45 at.% Al – X at.% (Nb, B, C) γ-TiAl ingots at a nominal temperature of 1280°C to a final extrusion ratio of 100:1.[4] The as-extruded cylindrical bars were 12.7 mm in diameter and 152 mm in length. The microstructure of the as-extruded bars was duplex with a high volume fraction of lamellar grains and a grain size of approximately 20 μm (Figure 7). This microstructure is referred to as "nearly lamellar." Detailed microstructural studies performed by Draper *et al.*[2] revealed very fine recrystallized gamma grains (~4 μm in diameter) in between the lamellar colonies and at the periphery of the extruded bars. The extrusion process resulted in flow lines in the longitudinal direction and were observed to be nearly symmetrical across the diameter of the extruded bar. The extrusion process also resulted in highly strained lamellar grains which were evident by the distorted γ and $\alpha_2$ lamellae. Elongated particles of $TiB_2$ in the extrusion direction were also observed by Draper *et al.* (Figure 7b).

[4] Extrusion performed by PLANSEE AG, Austria. Bars were received in the as-extruded condition. Although received bars were from different heat lots, no significant microstructural or hardness variation was observed from lot to lot.

Cylindrical specimens with a diameter of 12.7 mm and a thickness of 5 mm were sectioned from the bars using electric discharge machining[5] (EDM) and ground to a 1200 FEPA (Federation of European Producers of Abrasives) grit finish prior to bonding.

The composite interlayer used in this work was comprised of commercially pure (99.8 wt.%) copper powder of −325 mesh (particle diameter ≤45 μm) and gas atomized Gamma Met powder[6] of −200 mesh (particle diameter ≤75 μm). The Gamma Met powder had a nominal composition of Ti – 46.5 at.% Al – 2.5 at.% Cr – 1 at.% Nb – 0.5 at.% Ta – 0.1 at.% B. Gamma Met and copper powders were mixed using a dry jar milling process for 2 hrs.

GMPX substrates and Gamma Met powders were manufactured by PLANSEE AG and the copper powders were obtained from Alfa Aesar.

Some comparisons were made with 48–2–2 wide-gap TLP bonds. These 48–2–2 wide-gap TLP bonds were made by the present author and exactly replicated the work done by Zhou.[25-29] The microstructure of the as-received 48–2–2 substrates consisted predominately of fully lamellar grains with an average grain size of 170 ±50 μm (Figure 8). The composite interlayer used in 48–2–2 TLP bonds was comprised of commercially pure (99.8 wt.%) copper powder of −325 mesh (particle diameter ≤45 μm) and gas atomized 48–2–2 powders of −270 mesh (particle diameter ≤53 μm).

---

[5] Qin *et al.*[163] has conducted work which suggests electric discharge machining induces hydrides and microcracks in TiAl alloys, but these were not observed in the present work.

[6] The TiAl interlayer powder chosen for GMPX bonds was based on the substrate composition. Since atomized Gamma Met PX powder was not available and pulverizing GMPX material was unsuccessful, atomized Gamma Met powder was chosen.

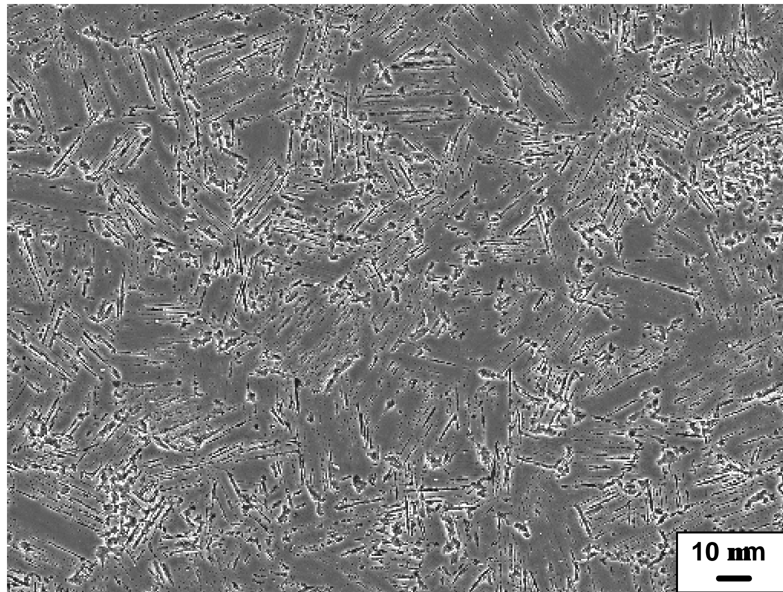


(a)

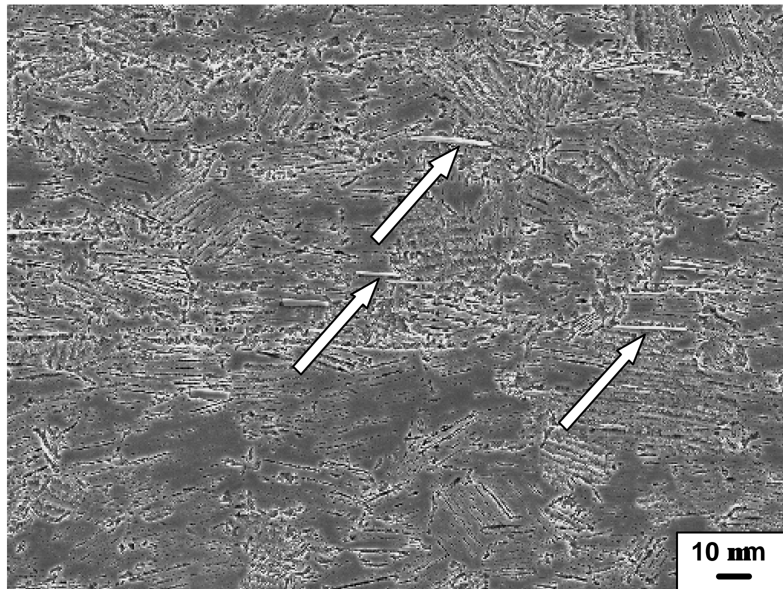


(b)

Figure 7−SEM (scanning electron microscopy) micrograph, in SEI (secondary electron imaging) mode, of as-received GMPX in the (a) transverse and (b) longitudinal directions. Arrows indicate elongated $TiB_2$ particles.

Figure 8−LM micrograph of as-received 48−2−2 substrate.

### 4.2 Joining Procedure

The Gamma Met plus copper powder mixture was manually placed directly onto one of two substrates. A few drops of ethanol were then placed atop the interlayer, as this was found to enhance the evenness of the interlayer (as-placed interlayer thickness typically ranged from 350 to 500 μm).[7] After the interlayer was appropriately deposited, the other substrate was placed on top of the interlayer. Bonding of the assembly was conducted in a Gleeble (Duffers Scientific, Inc., Model 1500), which provided a sufficient vacuum, rapid thermomechanical cycling, a bonding force using a compressed air loading system, and heating via direct resistance. Bonding was conducted at a temperature above the melting temperature of copper (abbreviated here to $T_B$) for X hr.[8] Heating and cooling rates were approximately 5 and 15°C $s^{-1}$ respectively in a, at worst, 1.3 mPa ($10^{-6}$ torr) vacuum atmosphere. A rapid heating rate was used to prevent interdiffusion between the copper powders and non-melting constituents. If the composition of the copper powder was changed by interdiffusion with the Gamma Met powders or GMPX substrates, the wettability of copper could be negatively affected due to the premature onset of isothermal solidification at the spreading front. A slight change in composition of the copper powders could also increase the melting temperature, thus the copper powders may not melt at the bonding temperature. Conversely, if the copper diffused into the Gamma Met powders or GMPX substrates during heating, a minimal amount of liquid would be formed upon reaching the bonding temperature. The bonding temperature was monitored using a K-type thermocouple, which was spot-welded no

---

[7] Considering the time required to manually place the composite powder interlayer and the variability of the as-placed interlayer thickness, an automated interlayer deposition process was investigated (see Section 5.1.2).

[8] Parameters such as exact temperature, time and compressive force used in TLP bonding of GMPX are controlled by ITAR (International Traffic in Arms Regulation). X refers to a numerical factor.

more than 2 mm from the bond-line. All bonding was done in the extruded direction (i.e. transverse surface of the extruded bar to another transverse surface).

All GMPX bonds discussed here relied on manually deposited interlayers. Although successful for small size coupon samples, this interlayer deposition method is not suitable for large scale industrial applications. Successful TLP bonding of 48–2–2 substrates using an automated interlayer deposition method has been conducted in part by the present author.[27] The details of this automated interlayer deposition method are discussed in section 5.1.2.

### 4.3 Post-Bond Heat Treatment Procedure

Following the bonding process, some samples were subjected to a PBHT. Post-bond heat treatments were conducted using a Linberg single zone tube furnace with, at worst, a 1.3 mPa vacuum atmosphere. Heating and cooling rates employed were approximately 5 and 3°C $min^{-1}$ (furnace cooled) respectively. Other PBHT conditions, such as time and temperature, are discussed in section 5.4.

### 4.4 Metallographic Preparation

The samples, both as-bonded and PBHT, were sectioned using a Struers Accutom-5 high speed wafering saw employing a cubic boron nitride (CBN) blade. Once sectioned, the samples were mounted using a Struers Labopress-3. Samples were ground to a 1200 FEPA (Federation of European Producers of Abrasives) grit finish and then polished using a 6 µm diamond spray followed by a 0.04 µm alumina suspension solution. The metallographic samples were etched for a few seconds at room temperature in a solution consisting of 97 vol.% distilled water, 1 vol.% hydrofluoric acid, 1 vol.% hydrochloric acid and 1 vol.% nitric acid.

## 4.5 Specimen Characterization

Both as-bonded and PBHT bonds were characterized using light microscopy (LM) and scanning electron microscopy (SEM), supplemented with SEM and transmission electron microscopy (TEM) based energy dispersive X-ray spectroscopy (EDS). SEM investigations employed a JEOL JSM840 instrument operated at an accelerating voltage of 20 kV. All SEM micrographs were collected using secondary electron imaging (SEI). Edge-on (i.e. cross-sectional) samples for TEM were prepared using a dual gun argon ion milling machine (Gatan 600 Duo-Mill) with nitrogen cooled stages. Milling was conducted at an accelerating voltage of 5 kV and a gun current of 500 μA per gun. TEM investigations, performed by William Gale, employed a JEOL JEM2010 microscope at an accelerating voltage of 200 kV. The SEM and TEM based EDS analysis employed ultra-thin window detectors and Oxford Instruments ISIS analyzers. EDS analysis was used to determine the composition of phases observed in the bond-line and compositional profiles across the joint.

X-ray diffraction (XRD) was also used to characterize the phases present in both the substrate and powder materials employed in this work. X-ray diffraction was conducted using a Rigaku D/MAX-B diffractometer employing a Cu-K$\alpha$ radiation ($\lambda \sim 1.5418$ Å).

## 4.6 Hotstage Light Microscopy

Testing to measure the ability of liquid copper to wet and spread along the surface of GMPX and 48–2–2 substrates was conducted via the sessile drop method. GMPX and 48–2–2 substrates were prepared with a diameter of 5 mm and a thickness of 1 mm and ground to a 1200 FEPA grit finish. Disks with a diameter of 1 mm were mechanically

punched from a 50 μm thick commercially pure copper foil. Both the foil and substrates were ultrasonically cleaned in acetone prior to testing. Sessile drop tests were dynamically observed using a Leitz 1750 heating stage mounted on a Leitz DMR metallurgical light microscope. A nominal temperature of $T_B$ was used for the sessile drop tests. The experiments were conducted in a 1.3 mPa vacuum atmosphere. The sessile drop tests were video recorded, so that measurements of displacement of the solid-liquid interface could be made as a function of holding time.[9]

Sessile drop tests to measure the terminal spreading distance of liquid copper on GMPX and 48–2–2 substrates were conducted. These experiments were performed in a Linberg single zone tube furnace for 2 hr at $T_B$ with a 1.3 mPa vacuum atmosphere and a heating rate of approximately 5°C $s^{-1}$ followed by furnace cooling (~3°C $s^{-1}$). For ease of handling and measurement, copper disks with a diameter of 3 mm were used rather than disks of 1 mm.

### 4.7 Mechanical Testing

Mechanical property studies of the bonds were performed via bend and tensile testing. All specimens for bend and tensile testing were extracted using an EDM and electropolished prior to testing. Considering the inherent low RT ductility of GMPX, the presence of any surface defects could have a profound effect on mechanical testing. Thus, electropolishing was performed in an attempt to minimize the influence of surface defects that may have been created during sample preparation. Electropolishing was conducted in a solution of 97 vol.% distilled water, 1 vol.% hydrofluoric acid, 1 vol.% hydrochloric acid and 1 vol.% nitric acid (same solution used for etching) at 0°C at a

[9] Hot Stage Light Microscopy (HSLM) work was conducted by Subhadra Chitti and displacement measurements were performed by Robert Love.

voltage of ~3 V. Mechanical testing was supplemented by fractographic investigations using SEM and EDS analysis.

The details of the mechanical testing procedures employed are discussed below. However, it should be noted that shear testing of the bonds, as developed by Yan and Wallach,[19] was intentionally not conducted. When TLP bonding 48−2−2, Zhou[29] observed that large fillets (relative to the small bond area of the shear specimens) produced during bonding led to initiation sites for brittle fracture during shear testing. Thus bend testing, which employs a specimen extracted from within the bond, hence the absence of fillets, was conducted as an alternative means of testing the strength of the bond.

### *4.7.1 Bend Testing*

Four-point bend specimens employed a specimen geometry with nominal dimensions of 2.8 mm thick, 3.5 mm wide and 40 mm long. The upper and lower roller spacing was 12 mm and 30 mm respectively. Schematic of testing set-up is shown in Figure 9a. A MTS Q-Test 1000 screw-driven machine was employed to conduct these tests. Testing was performed at a speed of 2 mm/min.

### *4.7.2 Tensile Testing*

Tensile testing at room temperature was employed to supplement four-point bend testing. The specimen geometry, shown in Figure 9b, had a nominal cross section dimension of 1.5 mm by 2.5 mm and a nominal gage length of 8 mm. These tests were also conducted on a MTS Q-Test 1000 screw-driven machine at a grip separation rate of 2 mm/min.

### *4.7.3 Hardness Testing*

Vickers microhardness testing was also employed to determine the hardness of intermetallics present in the bond region and the hardness profile across the bond-line. Microhardness testing was conducted using a 300 g load for a duration of 10 sec.

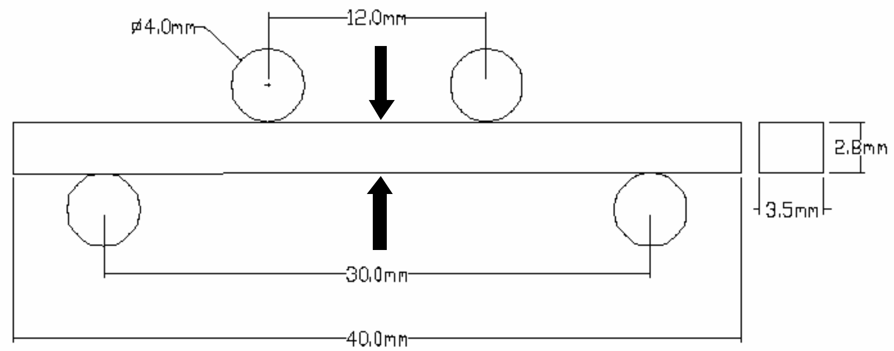


(a)

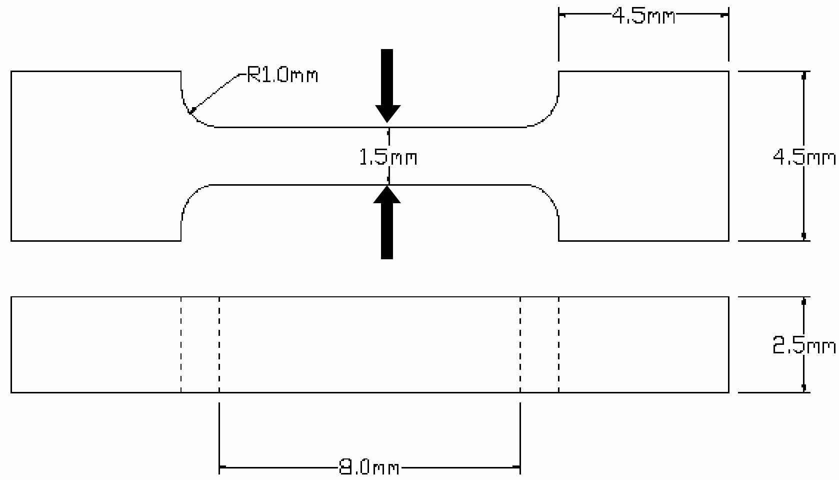


(b)

Figure 9–Schematic of (a) four-point bend testing set-up and (b) tensile test sample with nominal dimensions. Arrows indicate approximate location of bond-line. Typical bond-line width = 100 μm.

# 5. RESULTS AND DISCUSSION

## 5.1 Characterization of As-bonded Wide-gap TLP joints

As mentioned in section 2.7.5.3.1, studies of 48–2–2 wide-gap TLP bonds suggested that bonds employing a 6:1 weight ratio of 48–2–2 plus copper powders, produced joints with strengths that were a significant fraction of the bulk strength. Thus, initial wide-gap TLP bonding of GMPX began by employing a 6:1 (all ratios are given by weight) ratio Gamma Met plus copper powders and using bonding conditions similar to those employed in 48–2–2 bonds.

Isothermal solidification of the bond-line occurred predominately by epitaxial growth of the GMPX substrates and some epitaxial growth of the Gamma Met powder particles. Reactions within the Gamma Met plus copper interlayer were characterized dynamically using hot stage light microscopy (HSLM). It was observed that melting of the copper was immediately followed by partial dissolution of the Gamma Met powder particles into the liquid. Subsequently, isothermal solidification occurred rapidly at the holding temperature of $T_B$. The time required to complete isothermal solidification varied from region to region, but was in the range of 1 – 2 min. This rapid isothermal solidification time seems surprising at first, but diffusivity data discussed in section 5.7.1 suggests that this isothermal solidification time is plausible.

Figure 10 shows an SEM micrograph of a GMPX bond employing a 6:1 Gamma Met to copper interlayer ratio. Following the bonding process, a significant number of

regions contained large copper-rich intermetallics. These copper-rich intermetallics had a nominal composition of 27 at.% Al, 38 at.% Ti, 32 at.% Cu, 2 at.% Cr and 1 at.% Nb, as determined by SEM-based EDS analysis, and were primarily observed in regions of the bond-line where the Gamma Met powder particles were completely dissolved (Figure 10b). Considering the composition, these intermetallics are likely TiCuAl, however, TEM analysis is needed to be definitive. Nonetheless, these copper-rich intermetallics resulted in a fair amount of scatter in GMPX bond-line hardness, as shown in Figure 11.

Copper containing regions were also observed in between the copper saturated Gamma Met powders. These regions had a nominal composition of 34 at.% Al, 57 at.% Ti, 6 at.% Cu, 1 at.% Cr and 2 at.% Nb, as determined by EDS analysis, and a hardness similar to or less than that of the bulk substrates. It is interesting to note that these regions in between the Gamma Met powder particles were lower in aluminum and slightly richer in titanium than the original Gamma Met powder particles. This result would seem to indicate the preferential leaching of titanium from the Gamma Met powders rather than uniform dissolution of the powder particles.

The composition across the bond-line is shown in Figure 12. Since the composition of GMPX is proprietary to GKSS Research Center, only relative compositions are shown. From this figure, it can be seen that the concentration of copper in the bond-line peaks at about 9 at.% and decreases to approximately 3 at.% at the interface of the bond-line and substrate. The concentration of titanium is fairly constant across the bond-line, except at the interface of the bond-line and substrate where there is a slight decrease in concentration. There is also a slight peak in concentration of aluminum at the interface. This interface consists of epitaxial growth of the GMPX

substrate into the bond-line as can be seen in Figure 13. These epitaxially grown grains do not appear to have a fully lamellar $\gamma$(TiAl) plus $\alpha_2$($Ti_3Al$) microstructure and the composition (richer in aluminum than titanium) does not reflect that of the single $\gamma$(TiAl) or $\alpha_2$($Ti_3Al$) phase. The reason for a slight decrease in the concentration of titanium and increase in aluminum at this interface is not well understood.

Concerning the composition in the bond-line, a significant deficiency in aluminum was observed in the joint compared to that of the substrate. Considering the as-received GMPX substrate and Gamma Met powders contain approximately the same concentration of aluminum, this large deficiency is not well understood. The increase in chromium and decrease in niobium concentration across the bond-line is a result of the different concentrations of chromium and niobium in the GMPX substrates and Gamma Met powders.

As mentioned in the literature review, a key variable in the wide gap process is the selection of the ratio of liquid former to non-melting phase that is suitable for the substrates employed. If insufficient liquid former is employed, the liquid will begin to isothermally solidify and hence cease to spread, before it has been able to penetrate throughout the joint. This would result in a joint with excessive porosity. In contrast, if too much liquid is formed, then the amount of the solid-phase that must be dissolved to produce local equilibrium at the solid-liquid interface will be very high and the joint will resemble a (very wide) conventional TLP bond. Thus the benefits of using the composite interlayer would be lost. The large regions of completely dissolved Gamma Met powders and numerous copper-rich intermetallics observed when using a 6:1 Gamma Met to copper interlayer suggests the employment of an excessive amount of liquid former. In

addition, the latter would likely be detrimental to as-bonded mechanical performance. Thus, an empirical study was conducted employing a range of composite interlayers with lower concentrations of copper. The results of this study are discussed below and summarized in Table 2.

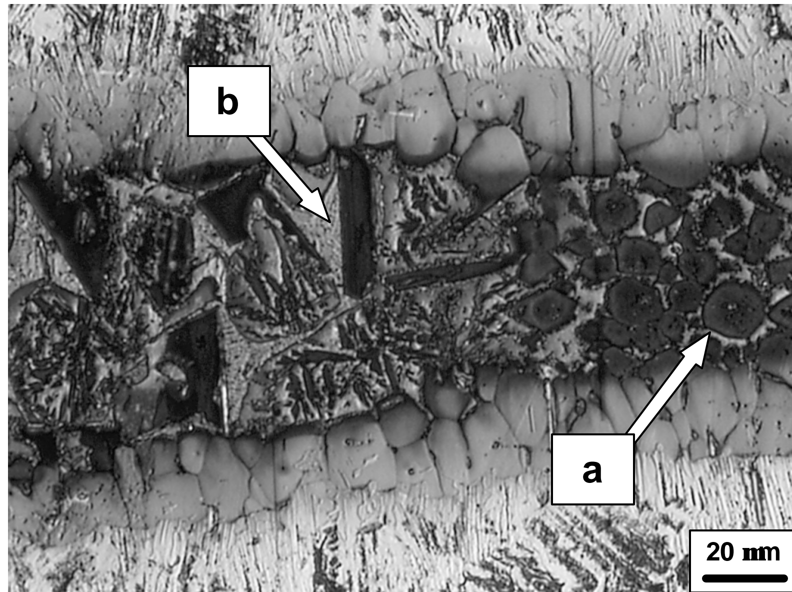


Figure 10–LM micrograph of an as-bonded GMPX joint using 6:1 Gamma Met to copper interlayer ratio. Copper lean phases (a) with a copper concentration of 5 – 6 at.% were found surrounding the original Gamma Met powder particles. Large copper containing intermetallics (b) with average copper content of 32 at.% resulted in scatter of bond-line hardness (see Figure 11).

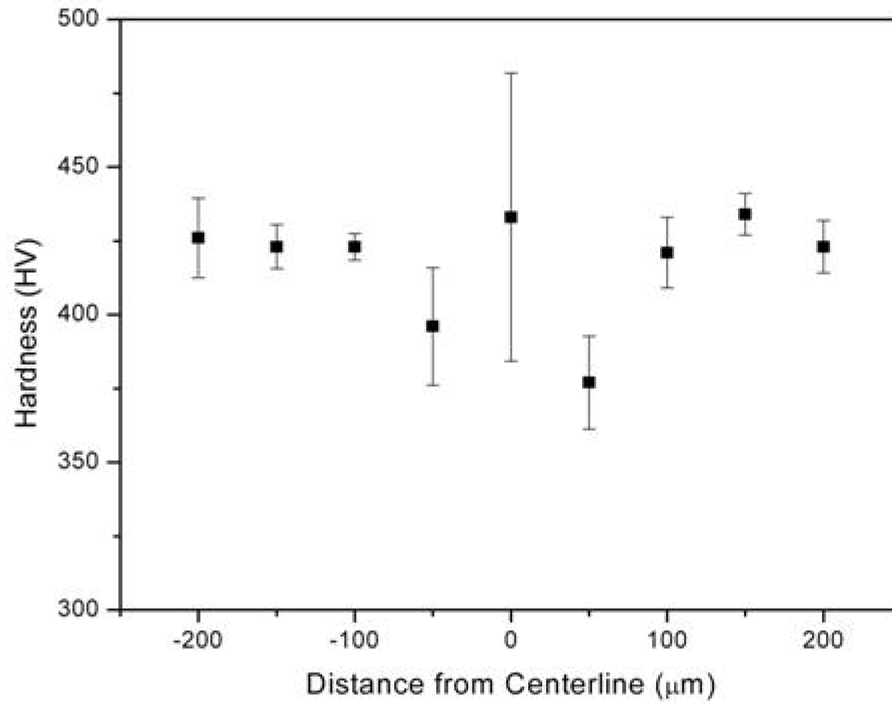


Figure 11–Vickers microhardness across bond-line of an as-bonded GMPX joint employing a 6:1 Gamma Met to copper interlayer ratio (joint width ~80 μm). Note the copper rich intermetallics observed in the bond-line resulted in significant scatter of bond-line hardness. In addition, the large epitaxial grown grains at the bond-line/substrate interface resulted in hardness less than that of the substrates.

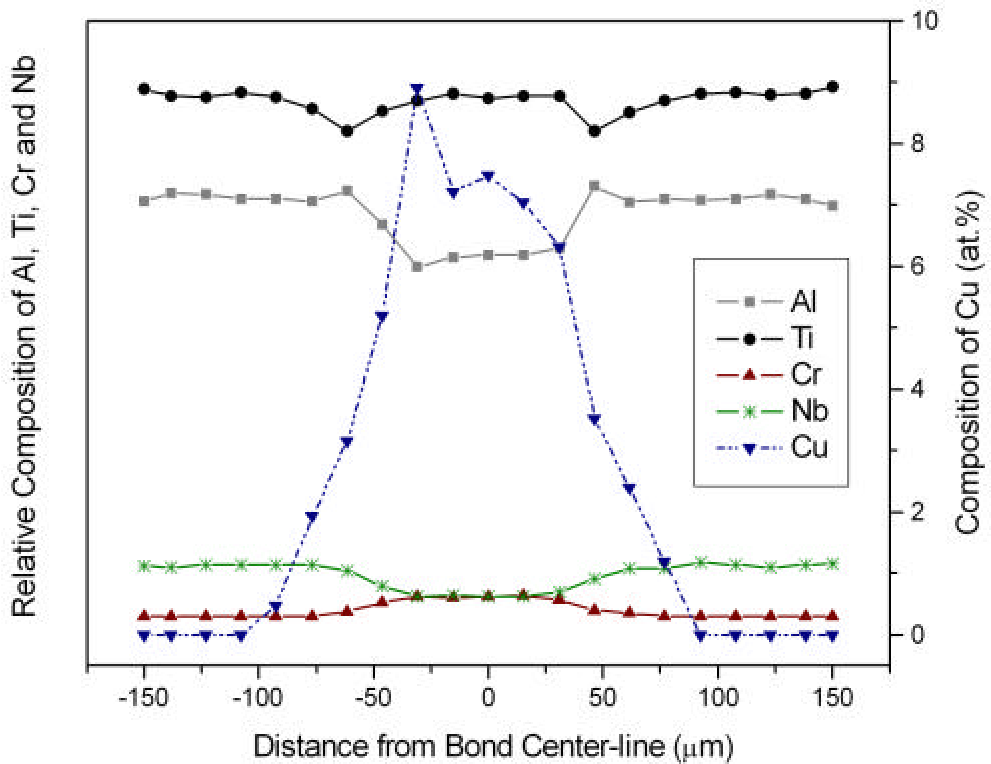


Figure 12–Composition profile, obtained using SEM-based EDS analysis, across bond-line of an as-bonded GMPX joint employing a 6:1 Gamma Met to copper interlayer ratio (joint width ~80 μm). Right side of graph refers to composition of copper across bond-line, whereas the left side of the graph refers to the composition of aluminum, titanium, chromium and niobium detected by EDS analysis. Since composition of GMPX is proprietary to GKSS Research Center, only the relative compositions for the latter elements are shown.

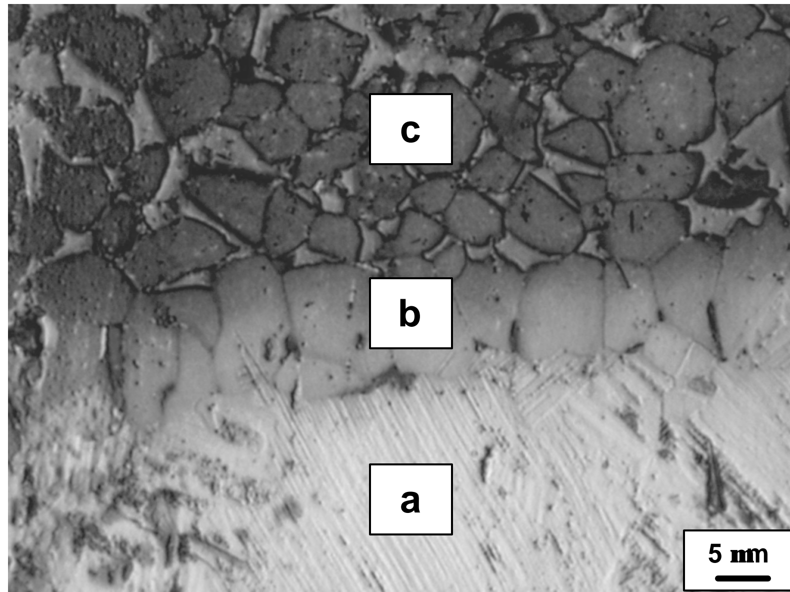


Figure 13–LM micrograph showing the interface of the (a) substrate and (c) bond-line of an as-bonded GMPX joint employing a 6:1 Gamma Met to copper interlayer ratio. (b) Indicates region of epitaxially grown grains.

| GMPX TLP Bonds | | | | | |
|---|---|---|---|---|---|
| **Interlayer Weight Ratio (Gamma Met: Cu)** | **Volume Percent of Copper in As-placed Interlayer (Assuming Fully Dense)** | **Copper Content of Overall Bond-line (at.% Cu)** | **Copper Content in Gamma Met Powder Particles (at.% Cu)** | **Copper Content of Phases Surrounding Gamma Met Powder Particles (at.% Cu)** | **Copper Rich Phases (at.% Cu)** |
| 6:1 | 7 | 6-7 | 3 | 5-6 | 30 |
| 20:1 | 2 | 2-3 | 2 | 4-5 | None Observed |
| 50:1 | 1 | 1-2 | 1 | 2-3 | None Observed |
| 65:1 | 0.75 | $1^{\ddagger}$ | $1^{\ddagger}$ | $2^{\ddagger}$ | None Observed |
| 100:1 | 0.5 | $< 1^{\ddagger}$ | $0\text{-}1^{\ddagger}$ | $1^{\ddagger}$ | None Observed |
| 150:1 | 0.3 | 0 | 0 | 0 | None Observed |
| **48-2-2 TLP Bonds** | | | | | |
| **Interlayer Weight Ratio (48-2-2: Cu)** | **Volume Percent of Copper in As-placed Interlayer (Assuming Fully Dense)** | **Copper Content of Overall Bond-line (at.%Cu)** | **Copper Content in Gamma Met Powder Particles (at. % Cu)** | **Content of Copper Lean Phases Surrounding Gamma Met Powder Particles (at.% Cu)** | **Copper Rich Phases (at.% Cu)** |
| 6:1 | 7 | 4-5 | 3 | 3-4 | 20 |

Table 2–Summary of SEM based EDS analysis of GMPX bonds employing various interlayers. Analysis of 48–2–2 bonds are provided as a comparison and will be discussed at length in section 5.6.3. ‡ Values are for localized regions only.

Figure 14 shows a GMPX bond using a 20:1 Gamma Met to copper interlayer powder ratio. Although numerous regions of completely dissolved Gamma Met powders were observed, no large copper-rich intermetallics were apparent. Bond-line hardness measurements supported this observation (Figure 15). However, the average hardness of the entire bond-line was found to be considerably less than that of the substrates. The latter is attributed to the regions of completely dissolved Gamma Met powders in the bond-line following the bonding process.

Composition across the bond-line is shown in Figure 16. From this figure, it can be seen that the concentration of copper in the bond-line peaks at about 4 at.% and decreases to less than 1 at.% at the interface of the bond-line and substrate. Like the bonds employing a 6:1 interlayer ratio (recall Figure 12), there is a slight decrease in titanium and increase in aluminum at this interface. Unlike the bonds employing a 6:1 interlayer ratio, the concentration of aluminum in the bond-line is fairly consistent with that of the bulk, with a maximum difference of 2 at.% aluminum.

In an attempt to eliminate the large regions of completely dissolved Gamma Met powders, the copper content of the composite interlayer was further reduced. The microstructure of bonds employing a 30:1 interlayer ratio closely resembled those of bonds employing a 20:1 interlayer ratio. The only discernable microstructural difference was the regions of completely dissolved Gamma Met powders were observed less frequently in bonds employing a 30:1 interlayer ratio.

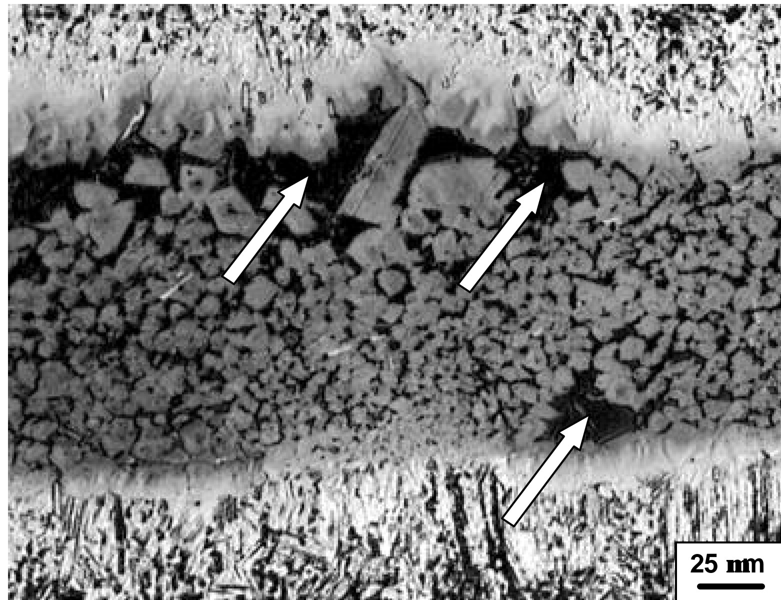


Figure 14–LM micrograph of an as-bonded GMPX bond-line employing a 20:1 Gamma Met to copper interlayer ratio. No copper-rich intermetallics were observed, however numerous regions of completely dissolved Gamma Met powders (indicated by arrows) were apparent.

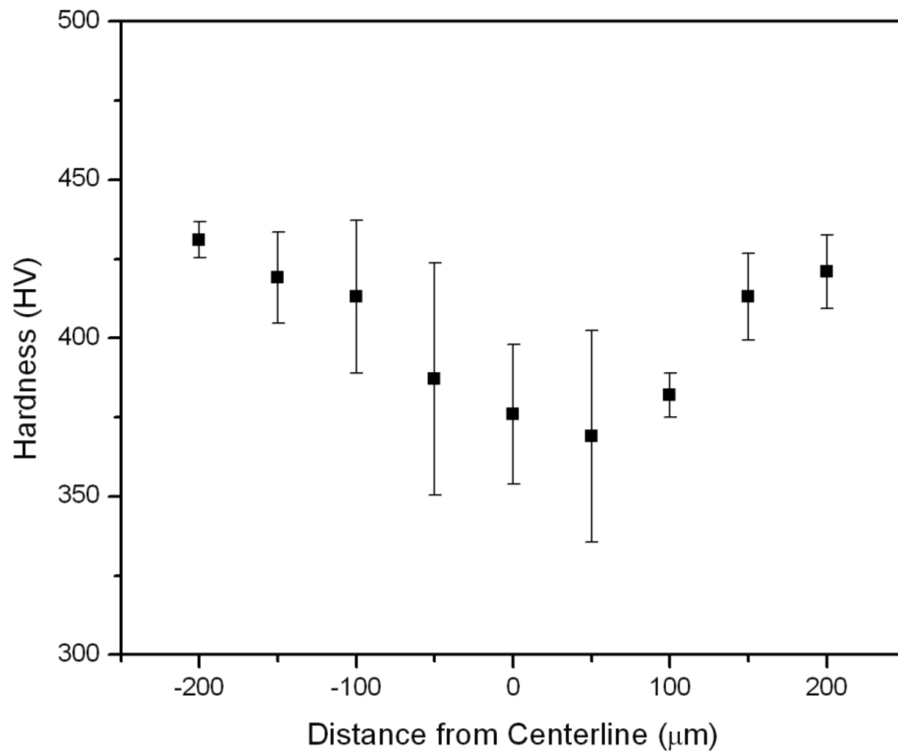


Figure 15−Vickers microhardness across bond-line of an as-bonded GMPX joint employing a 20:1 Gamma Met to copper interlayer ratio (joint width ~200 μm).

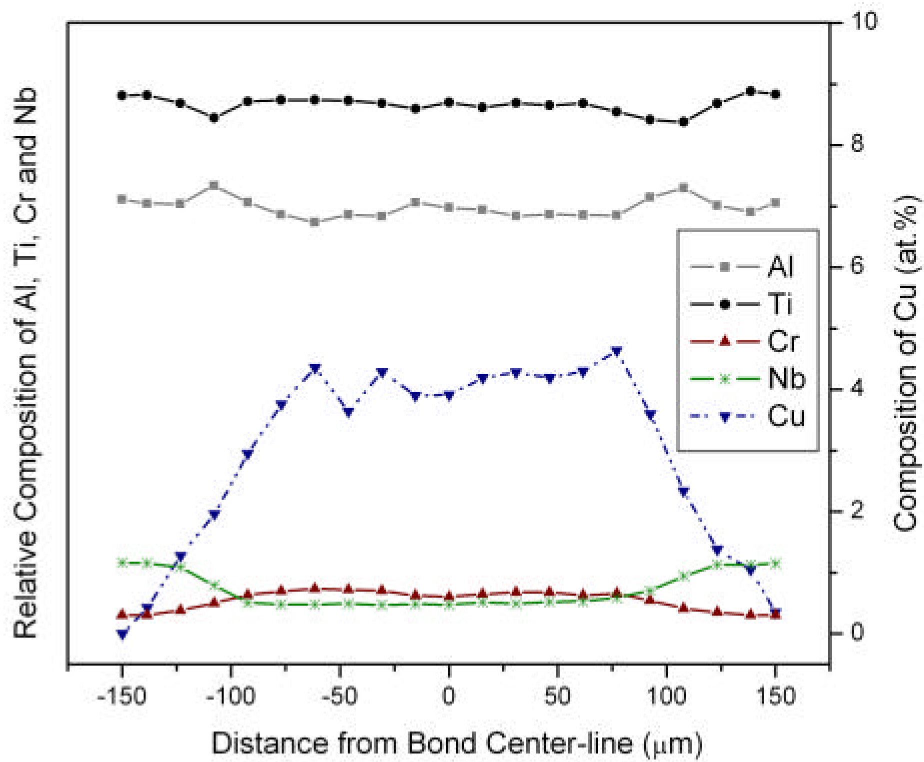


Figure 16–Composition profile across bond-line of an as-bonded GMPX joint employing a 20:1 Gamma Met to copper composite interlayer ratio (joint width ~200 μm). Right side of graph refers to composition of copper across bond-line, whereas the left side of the graph refers to the composition of aluminum, titanium, chromium and niobium detected by EDS analysis.

A GMPX bond employing a 50:1 Gamma Met to copper interlayer powder ratio is shown in Figure 17. The majority of the bond-line contained copper saturated Gamma Met powders surrounded by unknown phase(s) with a copper concentration of 2 – 3 at.%. However, a few random regions of completely dissolved Gamma Met powders were observed in the bond-line. These regions of completely dissolved Gamma Met powders appeared to have a lamellar-like microstructure. A few porous regions were also observed in the bond-line. Refer to Figure 37 for a detailed micrograph of these porous regions. These regions consisted entirely of Gamma Met powders which had partially sintered together during the bonding process. The presence of these porous regions could be attributed to the employment of insufficient liquid former and hence the inability of the liquid to spread throughout the joint cavity. However, as will be discussed, the presence of a few porous regions did not seem to have a significant detrimental effect on mechanical properties of as-bonded joints employing a 50:1 Gamma Met to copper interlayer powder ratio.

Some TEM analysis of GMPX bonds employing a 50:1 interlayer was conducted. Of the samples extracted from the bond-line, no copper, and hence no copper-rich intermetallics, was detected by TEM-based EDS analysis. Also, according to selected area diffraction (SAD) patterns, the predominant phase observed in the bond center-line was cubic with a lattice parameter of ~400 pm. The lattice parameters of Gamma Met powders subjected to a thermal cycle of $T_B$ for X hr were calculated using Cohen's method [164] with the (001), (110), (111), (002), (200), and (202) peaks for the $\gamma$(TiAl) phase and the (002), (200), (201), and (220) peaks for the $\alpha_2$($Ti_3Al$) phase (see Figure 26 for representative XRD pattern). The calculated lattice parameters were a = 400 pm and

c = 400 pm for the $\gamma$(TiAl) phase and a = 570 pm and c = 470 pm for the $\alpha_2(Ti_3Al)$ phase. According to the latter results, the predominant phase observed in the SAD patterns is likely $\gamma$(TiAl).

Further SEM and LM studies revealed less epitaxial growth of the Gamma Met powder particles, and especially the GMPX substrates (Figure 18), in the bonds employing a 50:1 interlayer, as compared with bonds using interlayers with a higher concentration of copper. The latter observation is not surprising considering the lower starting concentration of copper in the composite interlayer and hence a more rapid isothermal solidification time. These smaller epitaxially grown grains had a hardness similar to that of the substrate and only the centerline of the bond using a 50:1 interlayer ratio had a hardness considerably less than that of the substrates (Figure 19).

The composition across the bond-line is shown in Figure 20. In this figure, it can be seen that the concentration of copper in the bond-line peaks at about 2 at.% and decreases to less than 1 at.% at the interface of the bond-line and substrate. Unlike the bonds employing an interlayer with a higher concentration of copper, the concentrations of titanium and aluminum were found to be constant across the bond-line. Like the bonds employing a 6:1 interlayer ratio, the increase in chromium and decrease in niobium concentration across the bond-line is attributed to the different concentrations of chromium and niobium in the GMPX substrates and Gamma Met powders.

Reactions within the Gamma Met plus copper interlayer were characterized dynamically using HSLM. It was observed that melting of the copper was immediately followed by minimal dissolution of the Gamma Met powder particles into the liquid. Subsequent isothermal solidification occurred very rapidly at the nominal holding

temperature of $T_B$. The time required to complete isothermal solidification varied from region to region, but was generally less than one minute. Considering this very short time required for isothermal solidification to occur, there is potential for producing quality bonds using a very rapid bonding time at $T_B$. However, in an effort to prevent a very large test matrix, all bonds were conducted at $T_B$ for X hr.

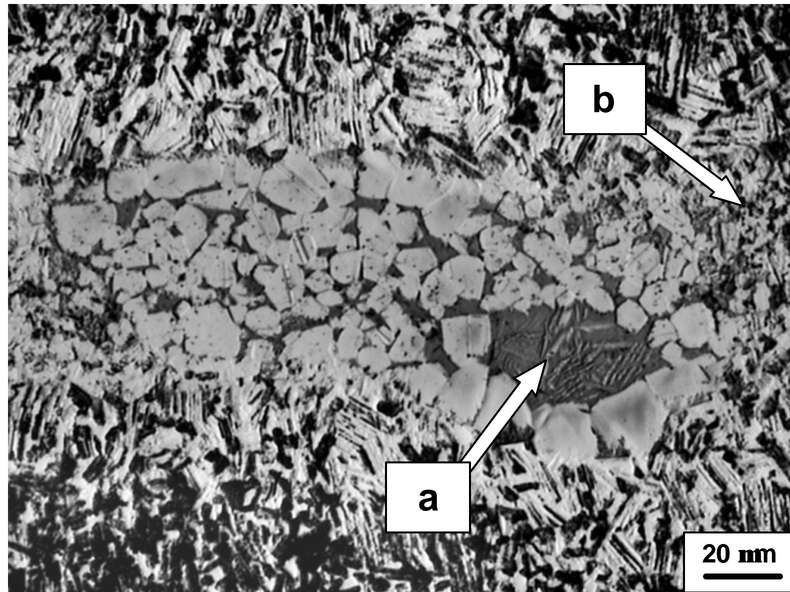


Figure 17–LM micrograph of an as-bonded GMPX joint employing a 50:1 Gamma Met to copper interlayer ratio. No copper-rich intermetallics were observed. A few random regions of (a) completely dissolved Gamma Met powders, with a lamellar-like microstructure, and (b) porous regions were observed (refer to Figure 37 for a detailed micrograph of these porous regions).

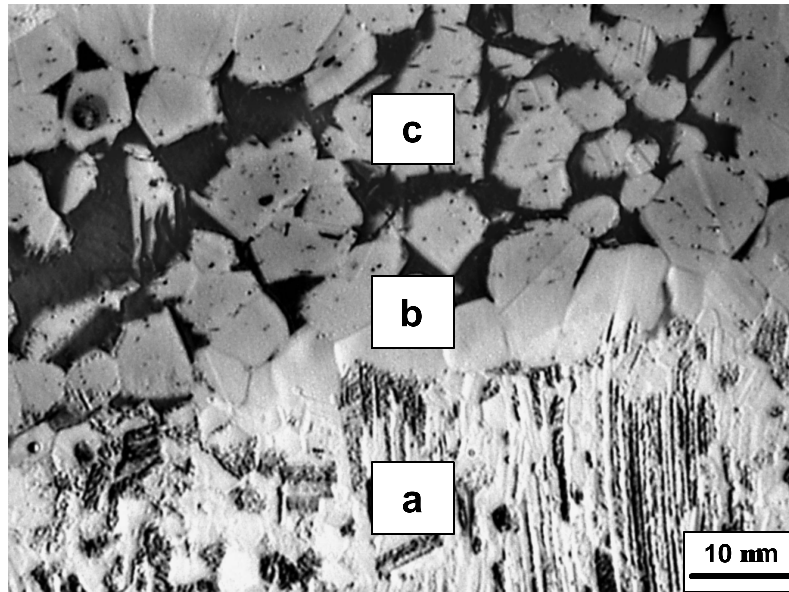


Figure 18–LM micrograph showing the interface of the (a) substrate and (c) bond-line of an as-bonded GMX joint employing a 6:1 Gamma Met to copper interlayer ratio. (c) indicates region of epitaxially grown grains.

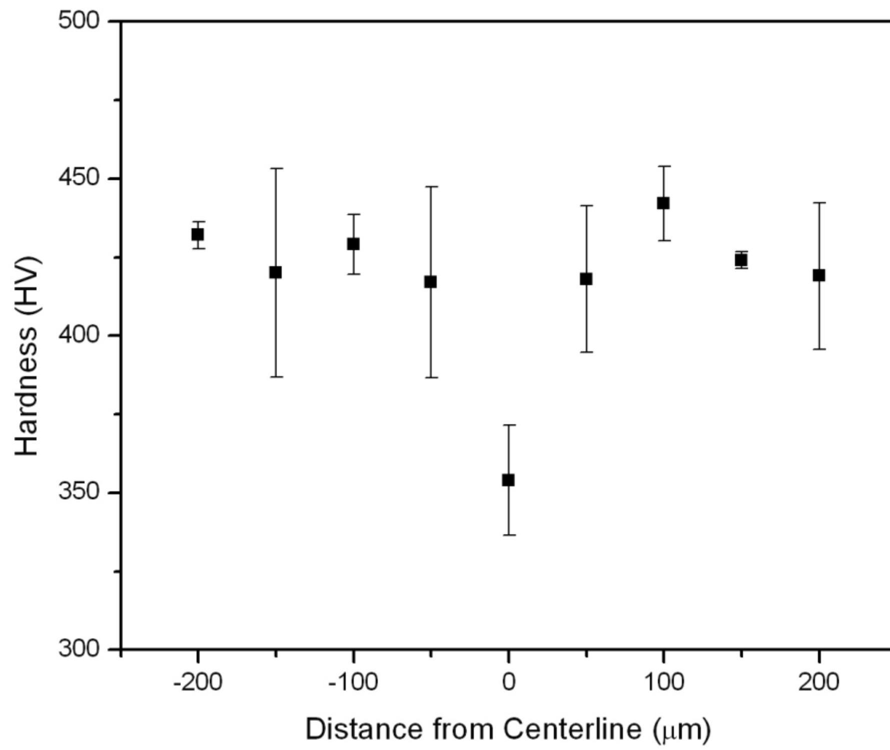


Figure 19–Vickers microhardness across bond-line of an as-bonded GMPX joint employing a 50:1 Gamma Met to copper interlayer ratio (joint width ~100 μm).

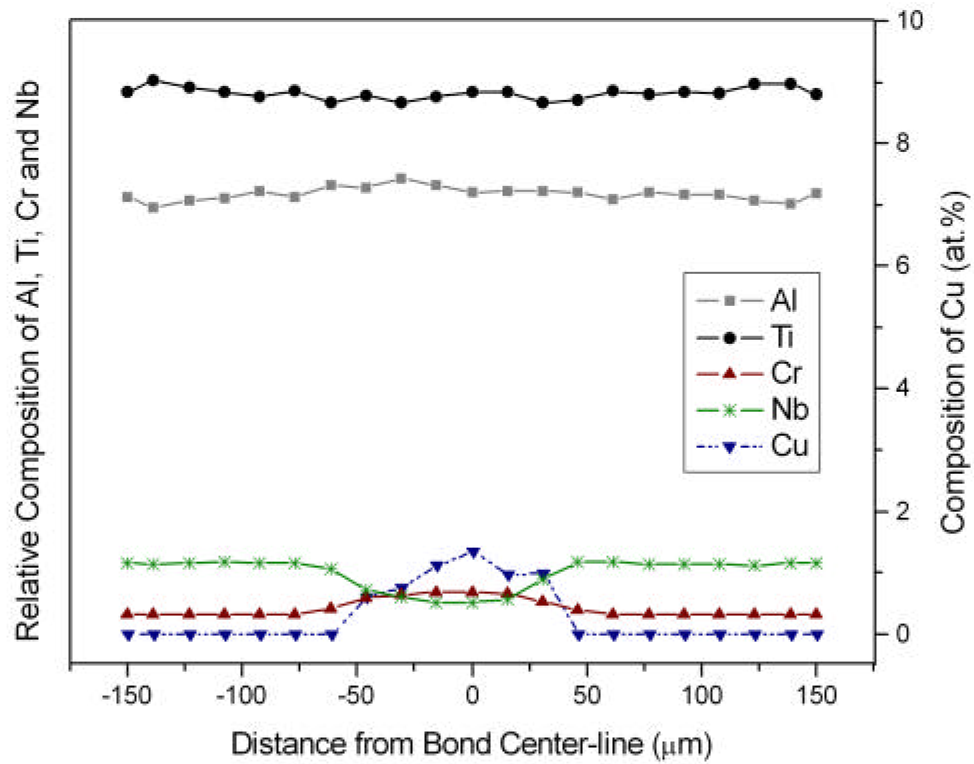


Figure 20–Composition profile across bond-line of an as-bonded GMPX joint employing a 50:1 Gamma Met to copper interlayer ratio (joint width ~100 μm). Right side of graph refers to composition of copper across bond-line, whereas the left side of the graph refers to the composition of aluminum, titanium, chromium and niobium detected by EDS analysis.

As a matter of interest, the study of reducing the copper content of the composite interlayer continued. GMPX bonds employing composite interlayers of 65:1 by weight (or less) contained a few localized regions of copper (1 – 2 at.% copper) and only sintered Gamma Met powders were apparent in the remainder of the bond-line (Figure 21). This observation suggests the employment of insufficient liquid former. It should be noted that bonds using interlayers containing even less copper, such as 150:1 by weight, resembled that of a diffusion bond employing a soft interlayer (i.e. an interlayer that conforms to any irregularities of the faying surfaces), as opposed to TLP bonding. Microstructural studies revealed only sintered Gamma Met powders. These microstructural studies and mechanical testing (see section 5.3.1) suggested that bonds of good, but non-optimum, quality could be produced when employing the latter interlayers.

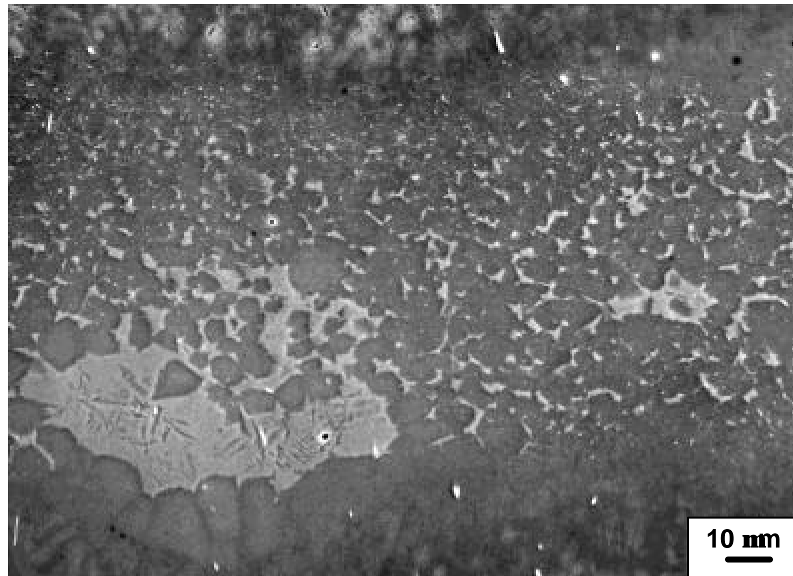


(a)

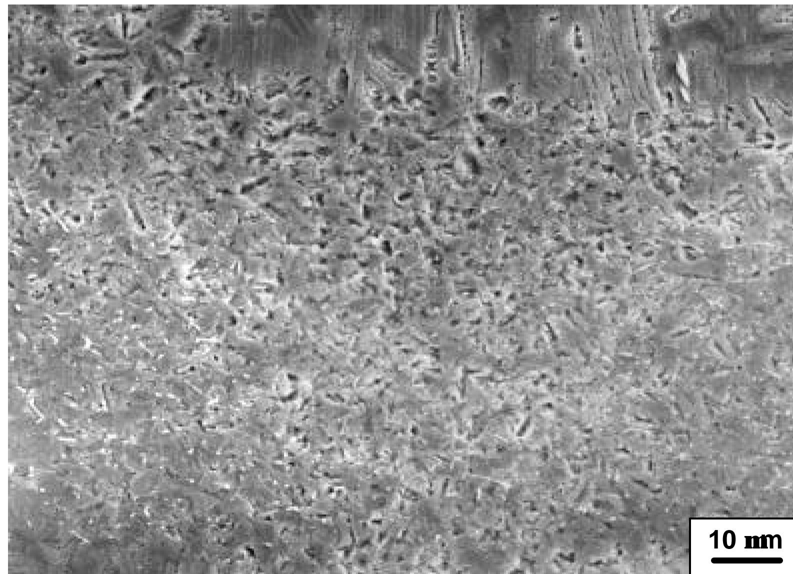


(b)

Figure 21− SEM micrographs, in SEI mode, of an as-bonded GMPX joint employing a 100:1 Gamma Met to copper interlayer ratio. (a) Localized region of bond-line containing 1 − 2 at.% copper. (b) Typical microstructure of bond-line containing only sintered Gamma Met powders.

### *5.1.1 Characterization of Composite Interlayer Powders*

Considering the microstructure and phases present in the Gamma Met powder particles would directly affect the microstructure and kinetics at the bond-line, some studies of the powders before and after a bond cycle were conducted.

Figure 22 shows a 6:1 weight ratio mixture of −200 mesh gas atomized Gamma Met plus −325 mesh copper powders. The Gamma Met powder particles were mostly spherical and had a very fine cellular microstructure (seen more clearly in Figure 23), which is typical of rapidly solidified gas-atomized powders.[93] The copper powders on the other hand, had a non-uniform geometry.

XRD analysis of the as-received Gamma Met powders determined the powders to be predominantly the $\alpha$(Ti)-Al solid solution phase (Figure 24). Considering the rapid solidification of the as-atomized powders, this is not surprising. After a bonding cycle of $T_B$ for X hr, the Gamma Met powders appeared to have a near gamma microstructure as shown in Figure 25. XRD analysis of the Gamma Met powders after at thermal cycle of $T_B$ for X hr revealed the powders to be predominately the $\gamma$(TiAl) phase with a small volume fraction of the $\alpha_2$($Ti_3Al$) phase (Figure 26). XRD analysis of a 6:1 weight ratio mixture of Gamma Met plus copper powders, after at thermal cycle of $T_B$ for X hr, produced a similar XRD pattern.

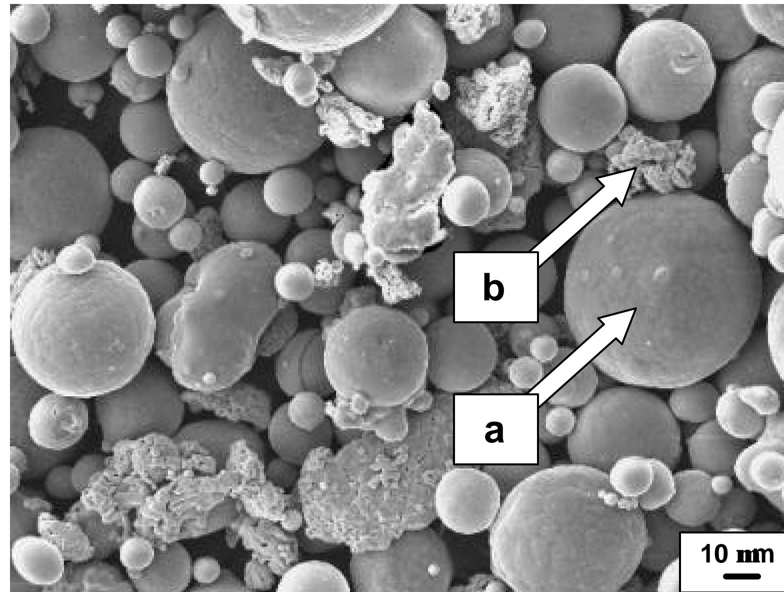


Figure 22– SEM micrograph, in SEI mode, of 6:1 weight ratio mixture of -200 mesh Gamma Met plus -325 mesh copper powders showing (a) spherical gas-atomized Gamma Met and (b) irregular shaped copper powders.

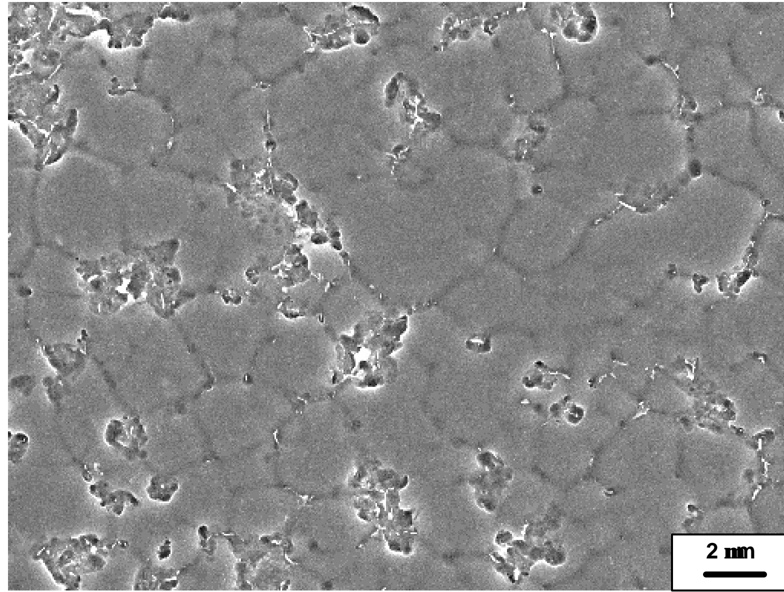


Figure 23–SEM micrograph, in SEI mode, of cross-section of as-received gas-atomized Gamma Met powders showing fine cellular microstructure, which is typical of gas-atomized powders.

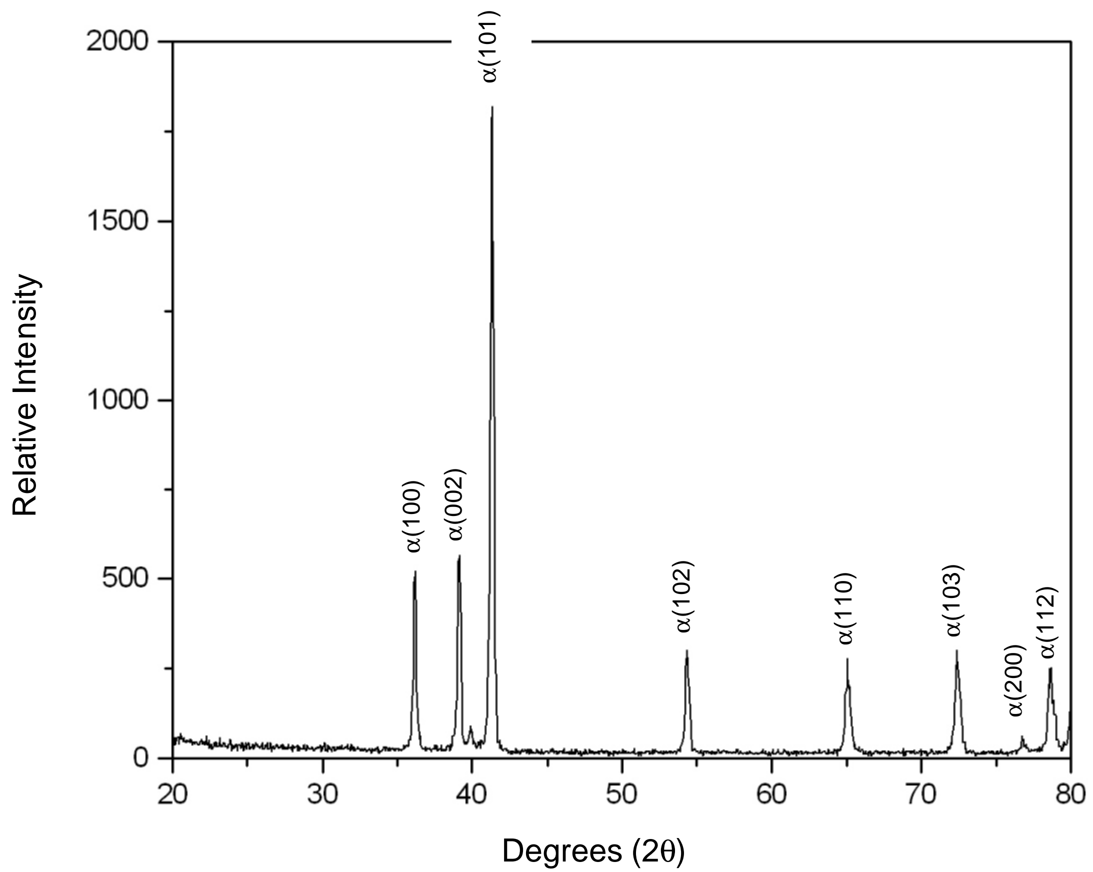


Figure 24−XRD pattern of as-received Gamma Met powders. The predominant phase present was determined to be the α(Ti)-Al solid solution phase. Note: Unlabeled peak at approximately 40° could not be identified.

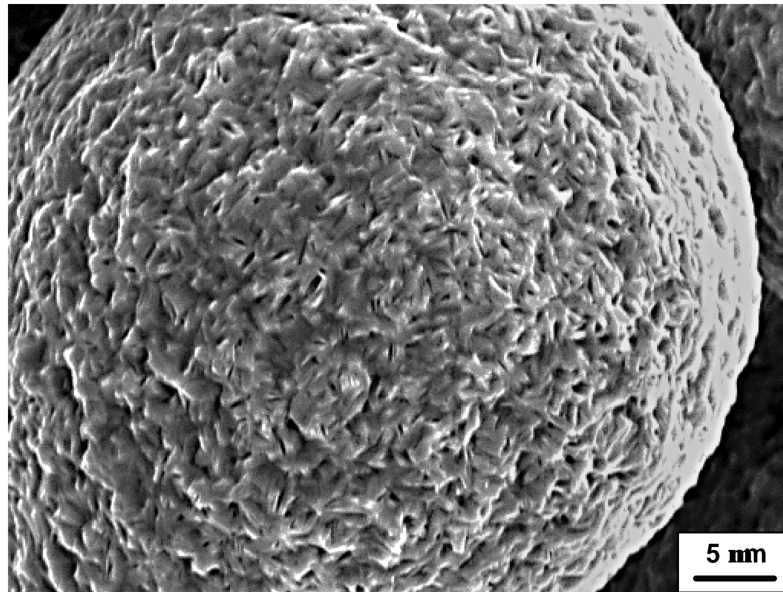


(a)

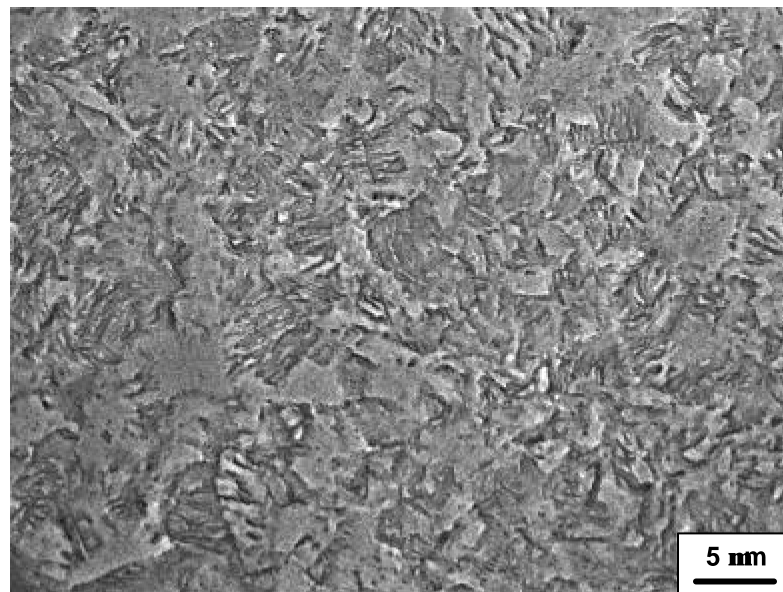


(b)

Figure 25–SEM micrographs, in SEI mode, showing the (a) surface and (b) cross-section of the gas atomized Gamma Met powders after a bond cycle of $T_B$ for X hr.

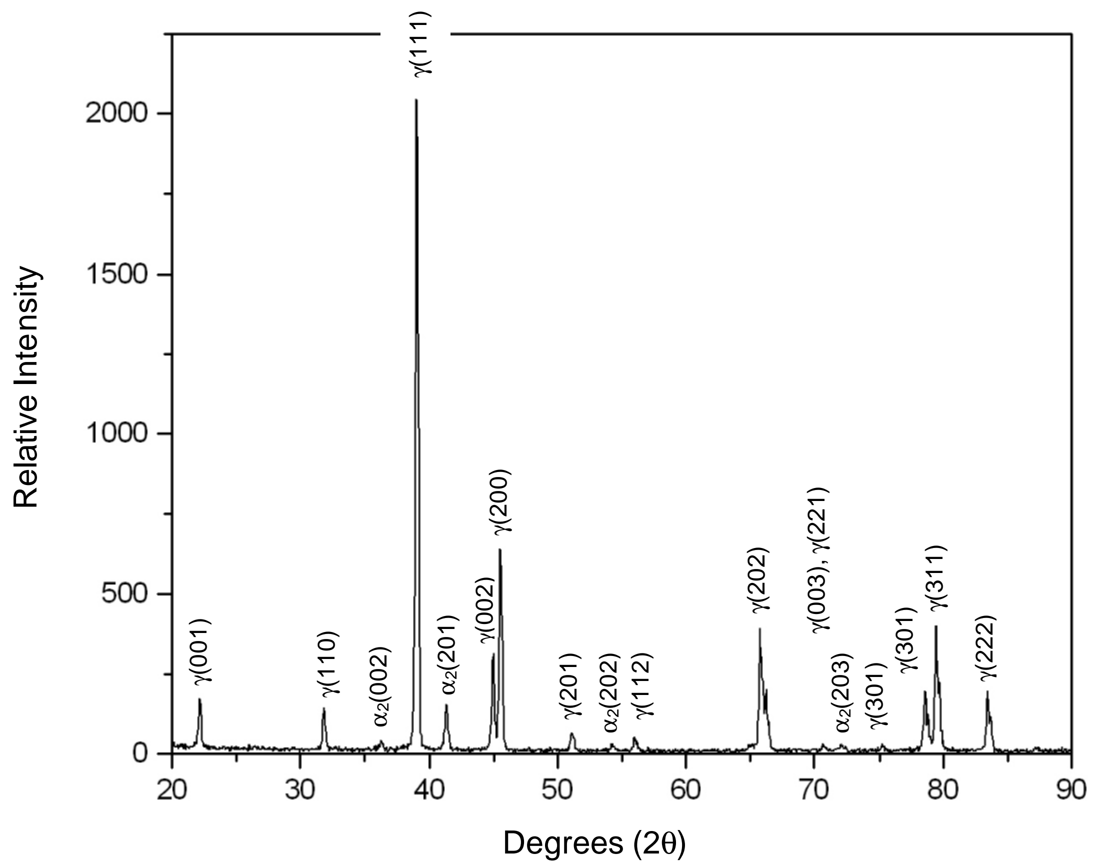


Figure 26–XRD pattern of Gamma Met powders after a thermal cycle of $T_B$ for X hr. The predominant phase present was determined to be the γ(TiAl) phase with a small volume fraction of the $\alpha_2$($Ti_3Al$) phase.

### *5.1.2 Automated Technique for Depositing Composite Powder Interlayer*

Transient liquid phase bonding of 48−2−2 has successfully been conducted using pre-sintered[25,29] and loose 48−2−2 plus copper composite powder interlayers.[26,27,29] The pre-sintered method involved cold pressing and sintering of the 48−2−2 plus copper powder mixture. The sintered powders were then sectioned into 100 − 200 μm thick slices and then placed between the two substrates to be joined. The loose powder method involved deposition of the 48−2−2 plus copper powder mixture without sintering. In this method, as discussed in section 4.2, the powder mixture was manually deposited onto the faying surface of one of the two substrates to be joined. Although successful wide-gap TLP bonding techniques, these interlayer deposition methods are not suitable for industrial applications. Both methods are tedious, time consuming and difficult to precisely control. Successful TLP bonding of 48−2−2 using an automated interlayer deposition method has been conducted.[27,29] Furthermore, this deposition method has potential of being extended to joining of other materials requiring a powder based interlayer.

Mike Di Ruscio performed the design work and initial construction of the automatic deposition system for pure copper powder. The present author made improvements to the deposition system and was successful at depositing uniform 48−2−2 plus Cu powder interlayers. Zhou analyzed the distribution of 48−2−2 and Cu particles to confirm the production of a homogeneously deposited interlayer and conducted all bonding employing automatically deposited interlayers. A schematic of the automated deposition system is shown in Figure 27.

Considering the differences in the density of TiAl (3900 kg m$^{-3}$) and copper (8940 kg m$^{-3}$), the main concern about this deposition technology was the unequal sedimentation of TiAl and copper powder in ethanol, which has a density of 789 kg m$^{-3}$. If copper or 48–2–2 powder particle is dropped into the ethanol solution, the particle will accelerate in that liquid until a constant velocity (V) is obtained (assuming the powder particle is a smooth, rigid sphere). Zhou[29] estimated the sedimentation velocity of copper and 48–2–2 powder particles in ethanol using Stokes' law, which can be described as:

$$V = \frac{2(gr^2)(d_1 - d_2)}{9\mu} \qquad [4]$$

where $V$ is the velocity of fall (m/sec), $g$ is the acceleration due to gravity (9.8 m sec$^{-2}$), $r$ is the radius of particle, $d_1$ is particle density (8940 kg m$^{-3}$ for copper and 3900 kg m$^{-3}$ for 48–2–2 alloy), $d_2$ is the density of the liquid (789 kg m$^{-3}$ for ethanol) and $\mu$ is the liquid viscosity ($1.2 \times 10^{-3}$ Pa·sec for ethanol at room temperature).

The maximum radius of −325 mesh copper powder particles is approximately 23 µm. However, the copper particles tended to form clumps with irregular shapes and cross-sectional areas up to 2800 µm$^2$. Clumping of copper powers occurred during powder mixing process, but did not have an obvious impact on bond quality. In order to have a radius value for the Stokes' equation, the copper clumps were assumed to be spherical with a maximum radius of 30 µm. The maximum radius of −270 mesh 48–2–2 alloy particles was approximately 26 µm. A minimum radius of approximately 5 µm was observed for both copper and 48–2–2 powder particles.

Figure 28 shows the relation between the sedimentation velocity and the particle size for copper and 48−2−2 particles. From this figure, it can be observed that the expected sedimentation velocity for copper and 48−2−2 particles of the same size is significantly different, especially for large size particles. During the deposition process, the reservoir containing the interlayer powder and ethanol solution was aggressively stirred. As a result, sedimentation in the reservoir was not an issue. However, sedimentation of interlayer powders, especially the copper powders, in the lines carrying the solution from the reservoir to the delivery nozzle was observed. In order to achieve a good quality auto-deposited interlayer, a low flow rate was required (see Table 3 for optimum deposition parameters). This low flow rate exacerbated the sedimentation problem even further. The use of passive in-line mixers reduced sedimentation of powders, but did not completely eliminate this problem. As a result, the as-deposited interlayer contained approximately half the copper of that of the original powder mixture. Thus, a starting powder mixture with a ratio of 6:1 48−2−2 plus copper powders resulted in an auto-deposited interlayer with a ratio of approximately 12:1.

A second observation by Zhou was that the auto-deposited powders contained a relatively smaller number of large particles (both large 48−2−2 and large copper particles). According to Figure 28, a particle with a large radius has a significantly faster sedimentation velocity than a particle with a small radius. Therefore is it likely that the larger particles fell out of solution during the transportation process and were not present in the auto-deposited interlayers. Despite the greater tendency for sedimentation of copper particles and the tendency for sedimentation of large powder particles, the average interlayer composition (as determined by SEM based EDS analysis using area scans at

regularly spaced intervals along the deposited interlayer) remained constant from the start to the end of deposition (Figure 29).

Despite the above observations, Zhou[29] was able to make high quality bonds using an auto-deposited interlayer. In fact, the bonds employing the auto-deposited interlayer resulted in a higher four-point bend strengths than those bonds employing a manually deposited interlayer. The present author attributes this increase to strength solely to the decrease in copper concentration of the auto-deposited interlayer and not the smaller size 48−2−2 powder particles. In studies conducted by Zhou, no distinct microstructural difference was observed in bonds employing a manually deposited interlayer with varying 48−2−2 powder particle sizes. However, Zhou did not conduct microstructural and subsequent mechanical testing studies of 48−2−2 bonds employing manually deposited interlayers with less copper (i.e. 48−2−2 to copper ratios of 12:1, 24:1, etc.), thus it is difficult to be definitive whether reducing the copper content of the as-placed interlayer contributed to higher strengths.

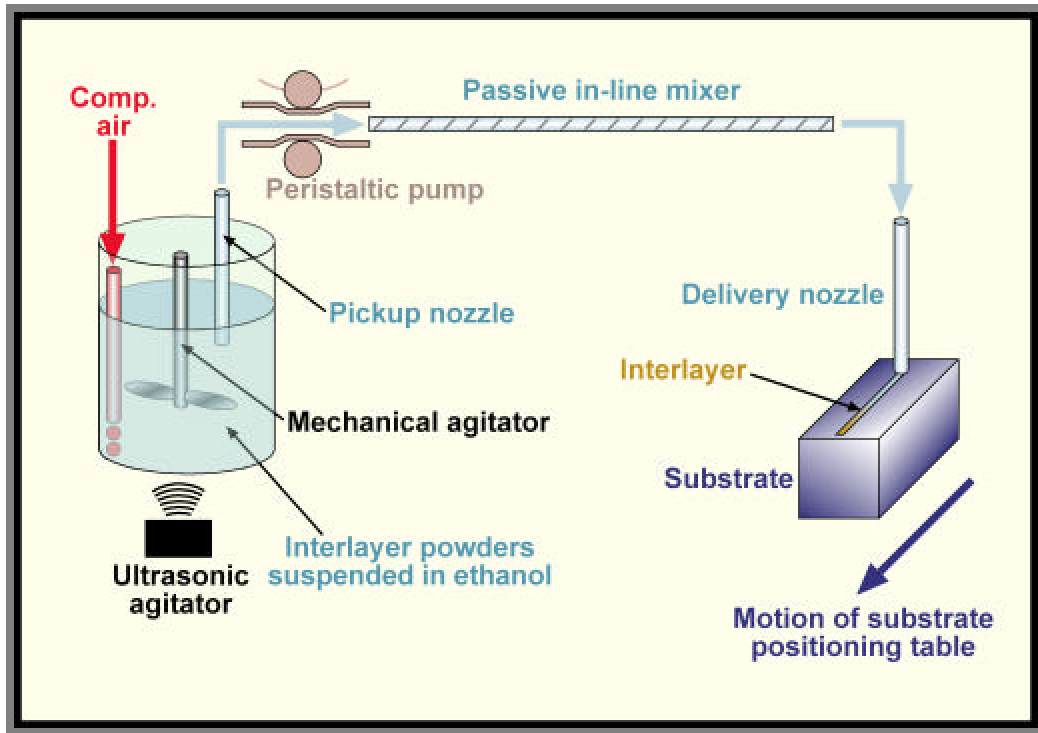


Figure 27–Schematic representation of the automated deposition system.[27]

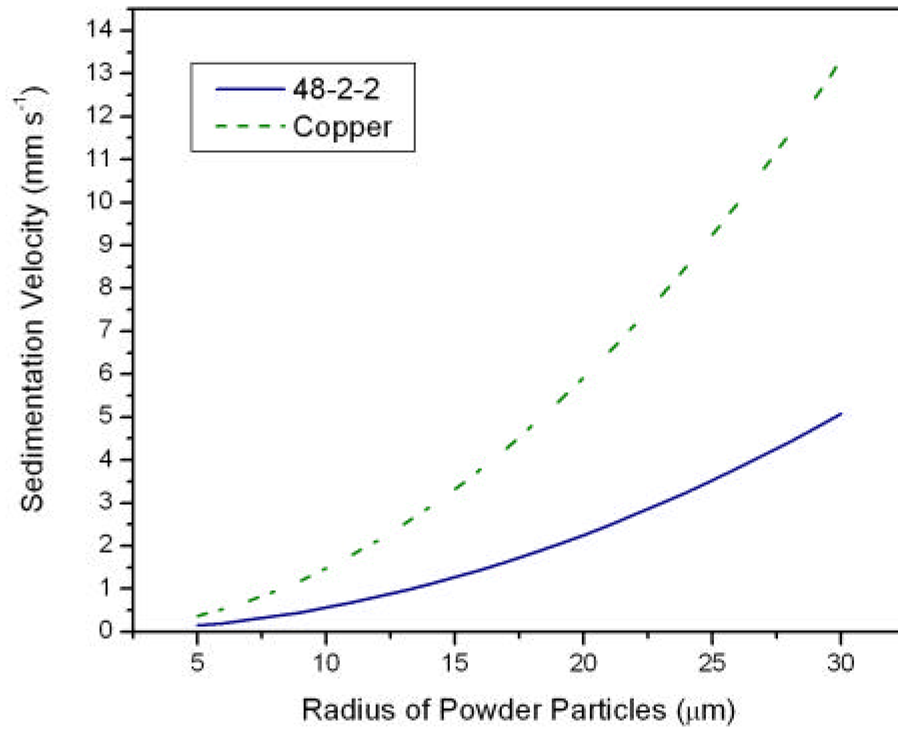


Figure 28−Anticipated relation between sedimentation velocity and particle size for 48−2−2 and copper powder particles.[29]

| Variable | Typical Value For Successful Deposition |
|---|---|
| Dry interlayer powder mixture | 6:1 weight ratio of 48−2−2 to copper |
| Concentration of interlayer powder mixture in ethanol (in feed reservoir) | 133 g $l^{-1}$ |
| Total volume (interlayer + ethanol) of feed reservoir at start of deposition | 154 ml |
| Delivery nozzle diameter | 3 mm |
| Carrier flow rate (measured in absence of interlayer powder) | 2 ml $s^{-1}$ |
| Total flow rate (powder plus carrier) | 2 ml $s^{-1}$ |
| Substrate velocity | 1.6 mm $s^{-1}$ |
| Thickness of interlayer deposited per pass (after air drying) | ~500 μm |
| Width of interlayer deposited per pass (after air drying) | ~8 mm |

Table 3−Optimum parameters for successful automated deposition of 48−2−2 plus copper composite interlayer.[27,29]

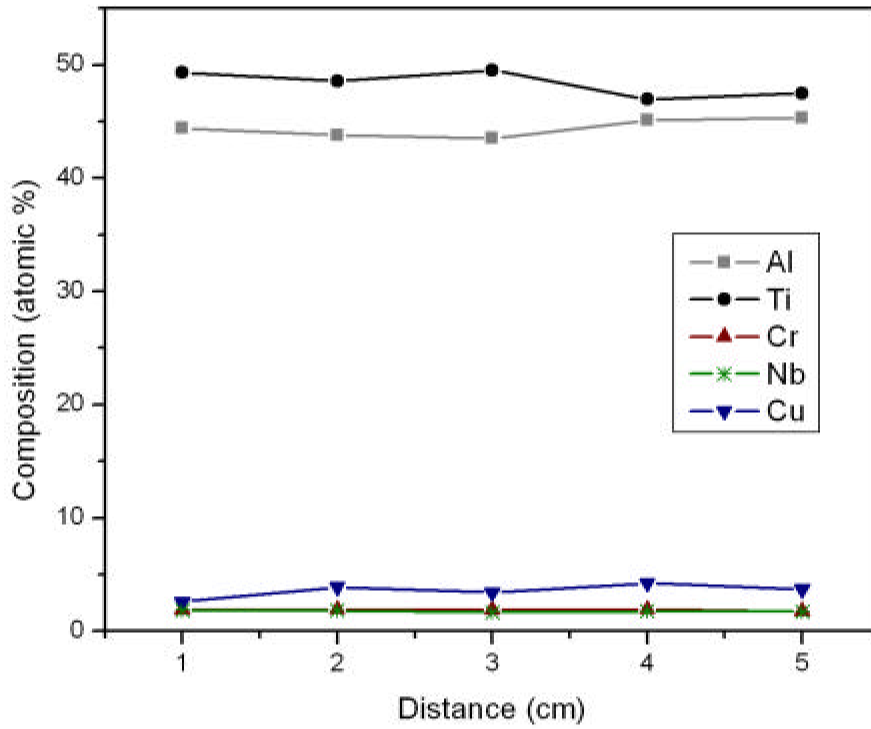


Figure 29−Variation in the composition of as-deposited 48−2−2 plus copper interlayer during a deposition run as a function of position, where 0 is defined as the location where deposition commenced. Each point was determined by EDS analysis and represented an average composition at the location shown, using a scan covering an area of ~1 $mm^2$.[29]

### 5.2 Characterization of Bonds Employing a Ti-Cu-Ni Braze Foil

High-temperature Ti-Cu-Ni-based filler metal has been used to braze titanium alloys (e.g. Ti–6 wt.% Al–4 wt. % V).[148,165] Recent studies have suggested that this braze material can be successfully employed in joining of γ-TiAl alloys.[7-11,166] Although a fair amount of microstructural characterization has been performed, very few mechanical testing results of γ-TiAl joints employing a Ti-Cu-Ni braze foil have been reported. This section discusses GMPX bonds employing the latter braze foil. These bonding experiments, microstructural characterization and mechanical property determination studies were conducted only as a matter of interest and were not intended to be part of the scope of the work presented here. Thus, only a few bonds were produced and minimal characterization and mechanical testing was performed.

GMPX bonds using a 50 μm TiCuNi-70 braze foil (foil courtesy of Engineered Materials Solutions, Attleboro, MA) were conducted at the same conditions employed in wide-gap TLP bonds. The nominal composition of the foil was Ti – 15 wt.% Cu – 15 wt.% Ni, which relates to Ti – 12 at.% Cu – 13 at.% Ni. Figure 30 shows a bond after X hr at $T_B$. The width of the bond-line after bonding was ~115 μm. This suggests a fairly large amount of substrate dissolution considering the original foil thickness of 50 μm.

The composition across the bond-line is shown in Figure 31. The concentration of titanium and aluminum across the bond-line was constant at about 57 at.% and 35 at.% respectively. The concentration of niobium in the bond-line was found to be similar to that of the substrate material. Nickel and copper were only detected in the bond region and remained constant at a concentration of about 2 at.%. This low concentration of

nickel and copper seemed surprising considering the content of nickel and copper in the original interlayer, combined with the observation that these constituents were not observed in the bulk substrates. It is assumed that the high amount of aluminum and niobium detected in the bond region diluted the concentration of nickel and copper.

Considering the high microhardness across the entire bond-line (Figure 32), the phase present in the joint could likely be one large intermetallic (recall Figure 30). This brittle phase present in the bond-line is likely the reason for the poor four-point bend strengths, which averaged 730 ±30 MPa compared to 1510 ±80 MPa for bulk substrates subjected to the same thermal cycle.

The results of these experiments suggest that bonds of poor quality (in terms of composition, hardness and four-point bend strengths) are produced when employing a TiCuNi-70 braze foil and using the bonding conditions detailed in section 4.2.

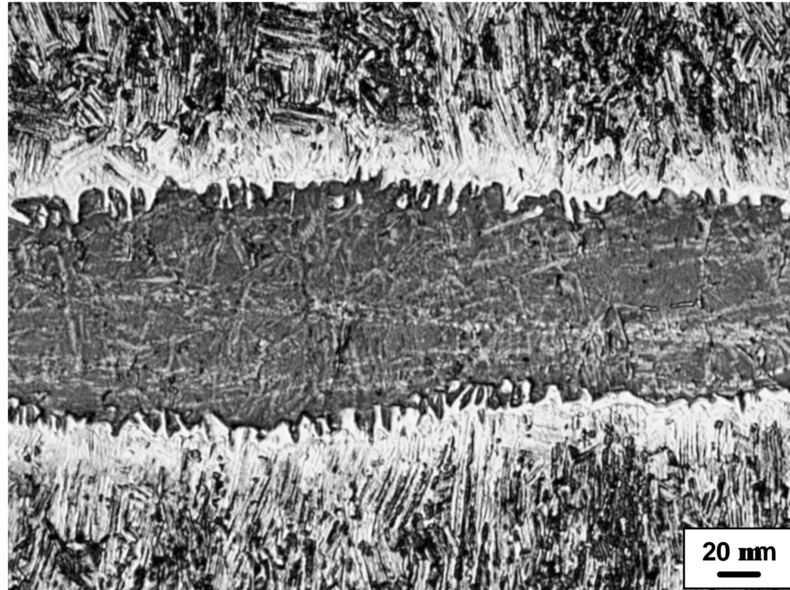


Figure 30–LM micrograph of as-bonded GMPX joint employing a 50 µm TiCuNi-70 braze foil for X hr at $T_B$ showing one large apparent brittle intermetallic in the bond-line.

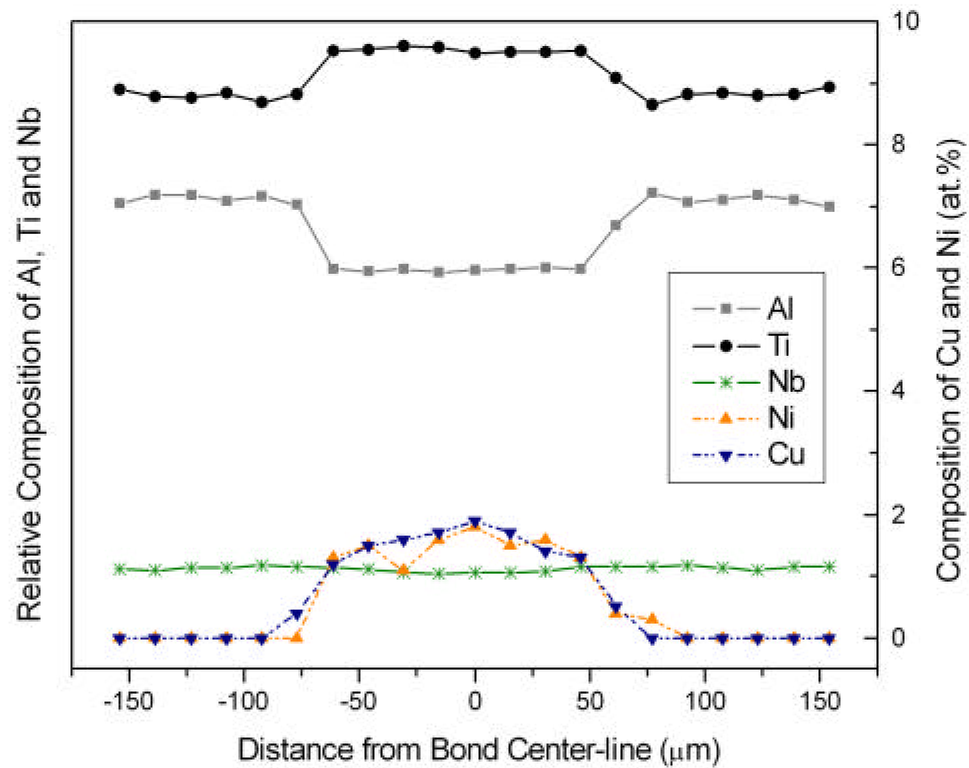


Figure 31−Composition profile across the bond-line of an as-bonded GMPX joint employing a 50 μm TiCuNi-70 braze foil. Right side of graph refers to composition of copper and nickel across bond-line, and left side of the graph refers to the composition of aluminum, titanium and niobium detected by EDS analysis.

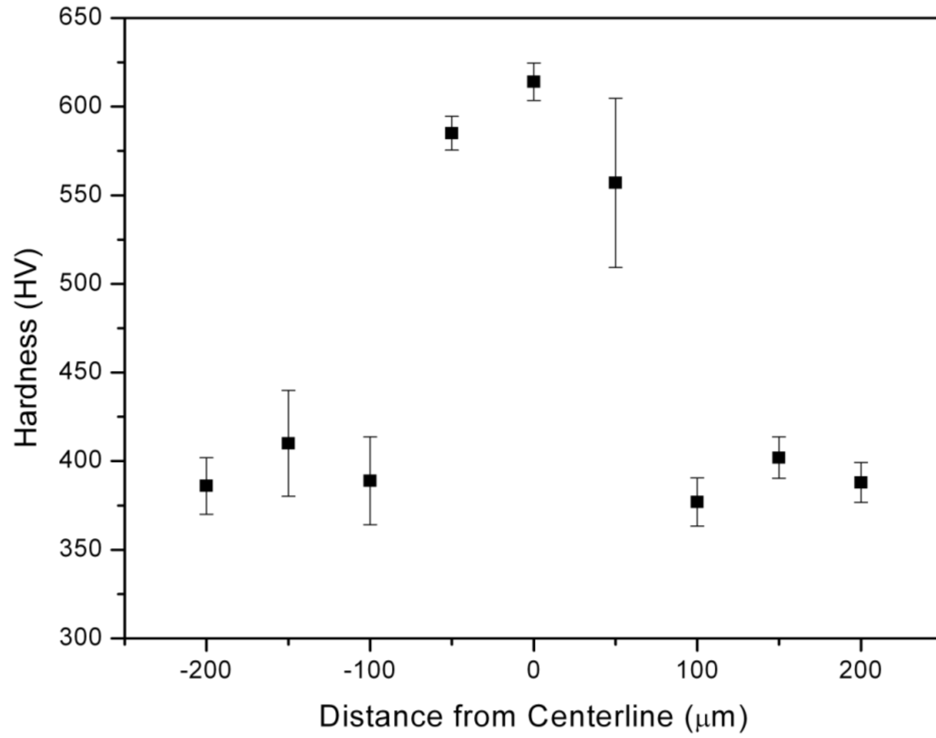


Figure 32–Vickers microhardness across the bond-line of an as-bonded GMPX joint employing a 50 μm TiCuNi-70 braze foil (joint width ~115 μm). Note high microhardness of entire bond-line.

## 5.3 Structure-Property Relationship for As-bonded TLP Joints

### *5.3.1 Four-Point Bend Testing*

Before discussing the bend strength of bonds employing a composite interlayer, the effect of the bond cycle on the bulk material should be discussed. The mean four-point bend strength of the bond cycled samples were 270 MPa lower than the samples in the as-received condition (Figure 33). This reduction in strength was also evident in Vickers microhardness measurements, taken in the extruded direction, which averaged 430 ±10 and 410 ±20 HV for samples in the as-received condition and bond cycled condition respectively. This reduction in strength is attributed to small degree of grain coarsening during the bonding cycle, however, no significant increase in grain size was observed in microstructural analysis. Figure 34 shows a fractographic image of the bulk alloy in the as-received condition. The fracture path of the nearly lamellar microstructure was macroscopically flat and dominated by transgranular cleavage fracture. Figure 35 shows a fractographic image of the bulk alloy after bond cycling. This fracture surface appears very similar to the as-received condition.

Four-point bend testing of bonded specimens correlated well with the microstructural studies. Four-point bend testing also suggested that TLP bonding of GMPX can produce as-bonded joints with mechanical properties somewhat comparable to that of the bulk material, when employing a suitable Gamma Met plus copper interlayer ratio. Bonds employing a 50:1 Gamma Met to copper interlayer ratio resulted in an average bend strength of 1100 ±160 MPa. This as-bonded bend strength value was more comparable to that of the bulk GMPX material subjected to the same thermal cycle,

which averaged 1510 ±80 MPa, than other interlayer ratios tested (Figure 33).[10] A fractographic image of a bend specimen employing a 50:1 interlayer ratio is shown in Figure 36. Two distinctly different microstructures were observed in this image. One region had a microstructure which was similar to that of the bond cycled sample. This region was determined to be where failure occurred through the Gamma Met powder particles. The second region of interest appeared to have a very planar fracture surface. Considering the appearance of the fracture surface, these regions could likely be delamination of the lamellar-like microstructure observed in the areas of dissolved Gamma Met powder particles.

As mentioned in section 5.1, porous regions were occasionally observed in the bond-line of joints employing a 50:1 Gamma Met to copper interlayer. These regions were evident in the fracture surface of the bond-line as shown in Figure 37. As mentioned in the microstructural development, the presence of these porous regions could suggest the employment of insufficient liquid former. Although relatively high bend strengths were obtained, there is inconclusive evidence that 50:1 Gamma Met plus copper is the optimum interlayer ratio. Further studies are needed to determine if GMPX bonds employing a composite powder interlayer with slightly more or less copper would produce bonds of greater bend strengths. Nonetheless, one obvious conclusion that can be drawn is the 6:1 interlayer ratio, which produced bonds with strengths somewhat comparable to the bulk in 48–2–2 studies, is not the optimum interlayer ratio for GMPX substrates when employing the interlayer and bonding conditions discussed here.

[10] The least square difference method (LSD) was used to determine if a significant difference exists between the mean bend strength of bonds employing a 50:1 interlayer ratio and bonds employing a 6:1, 20:1, 30:1, 65:1, 100:1 or 150:1. The differences between the mean bend strength of bonds employing a 50:1 interlayer ratio and those bonds employing a 6:1, 20:1, 100:1 and 150:1 were found to be significant at a 95% confidence level.

For comparison, a fractographic image of a bend specimen employing a 6:1 Gamma Met plus copper interlayer ratio is shown in Figure 38. The majority of the fracture path dominated by transgranular cleavage. However, there were several regions where failure appeared significantly different than the majority of the fracture surface. It is not clear whether these regions are due to porosity or failure by interfacial fracture between large copper-rich intermetallics and the matrix of the bond-line. Nonetheless, these regions likely contributed (at least in part) to the poor mechanical properties of as-bonded joints employing a 6:1 Gamma Met plus copper interlayer ratio.

Continued factographic investigations indicated that all GMPX bonds prepared with composite interlayers in the range of 6:1 to 50:1 failed at the interface between the bond-line and one of the substrates. Recall from section 5.1, this interface consisted of large grains resulting from epitaxial growth of the substrate into the bond region. Figure 39 and Figure 40 show the cross section of the fracture surface for GMPX bonds employing a 6:1 and 50:1 composite interlayer respectively. Although all failures initiated at this interface, crack propagation occasionally deviated from this interface into the bulk substrate material. However, no consistent difference in strength (or fracture mechanism, which was dominated by transgranular cleavage) was observed between specimens with crack propagation entirely at the interface or with crack propagation initially at the interface and then into the bulk. Considering failure occurred predominantly in the region of epitaxially grown grains, the higher bend strength of bonds employing a 50:1 interlayer ratio compared to those using a 6:1 interlayer ratio could be attributed to less epitaxial growth, and hence smaller grains at this interface.

Fractographic investigations of GMPX bonds prepared with a composite interlayer of 65:1 and 100:1 indicated that all failures occurred entirely within the bond-line (Figure 41). Crack propagation appeared to occur at random within the bond-line, except at localized copper containing regions. These regions consisted primarily of completely dissolved Gamma Met powder particles (recall Figure 21a). Crack propagation tended to occur at the perimeter of these regions where there was significant epitaxial growth of Gamma Met powder particles. The large amount of scatter in the four-point bend strengths for GMPX bonds employing an interlayer ratio of 65:1 and 100: are attributed to the non-uniform distribution of copper containing regions in the samples tested.

GMPX bonds employing a 150:1 interlayer did not contain localized copper containing regions. Considering the small amount of copper in these interlayers (0.32 vol.%), the copper most likely diffused into the Gamma Met powder particles or substrates during heat-up or in the early stages of bonding. This interlayer appears to be the equivalent of a pure Gamma Met powder interlayer. It is of interest to note the low amount of scatter in four-point bend tests employing this interlayer. This low scatter is attributed to the absence of the localized copper containing regions which were observed in bonds employing 65:1 and 100:1 Gamma Met to copper interlayer ratios.

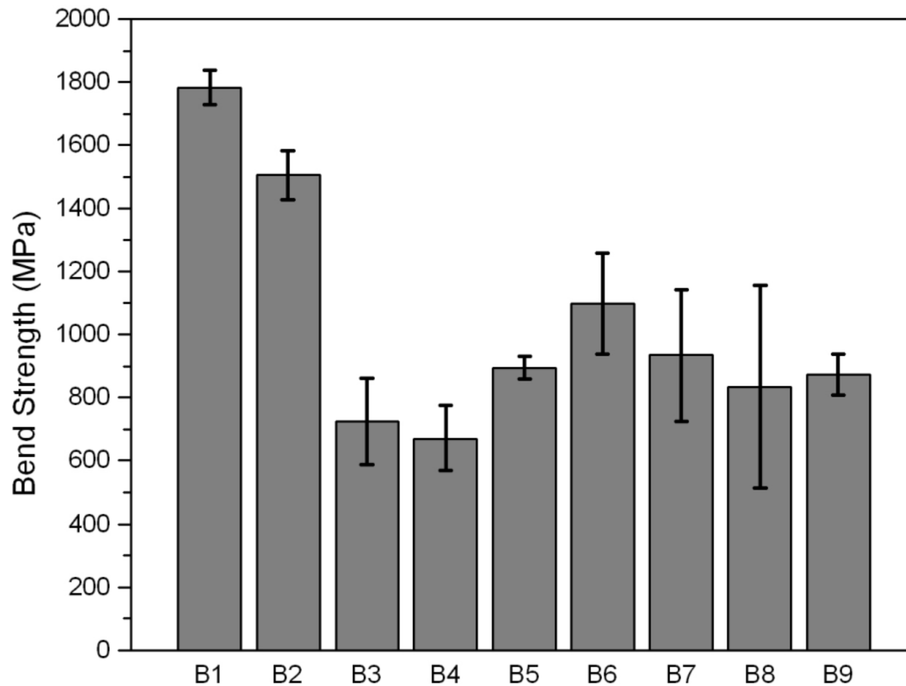


Figure 33–Results of four-point bend testing for as-bonded wide-gap TLP joints employing various Gamma Met to copper interlayer ratios. Bend strengths of the bulk material in the as-received and bond cycled condition are included for comparison. The mean bend strength and standard deviation data are as follows:

B1: As-received bulk material; 1780 ±50 MPa

B2: Bond cycled bulk material; 1510 ±80 MPa

B3: As-bonded joint employing 6:1 interlayer weight ratio; 730 ±140 MPa

B4: As-bonded joint employing 20:1 interlayer weight ratio; 670 ±100 MPa

B5: As-bonded joint employing 30:1 interlayer weight ratio; 900 ±40 MPa

B6: As-bonded joint employing 50:1 interlayer weight ratio; 1100 ±160 MPa

B7: As-bonded joint employing 65:1 interlayer weight ratio; 930 ±210 MPa

B8: As-bonded joint employing 100:1 interlayer weight ratio; 840 ±320 MPa

B9: As-bonded joint employing 150:1 interlayer weight ratio; 870 ±70 MPa

Note: At least two repeatable samples for each of the above conditions were prepared. At least two bend specimens were extracted from each of these samples for testing. The error bars and standard deviation values represent the standard deviation (±1 σ) for all specimens tested.

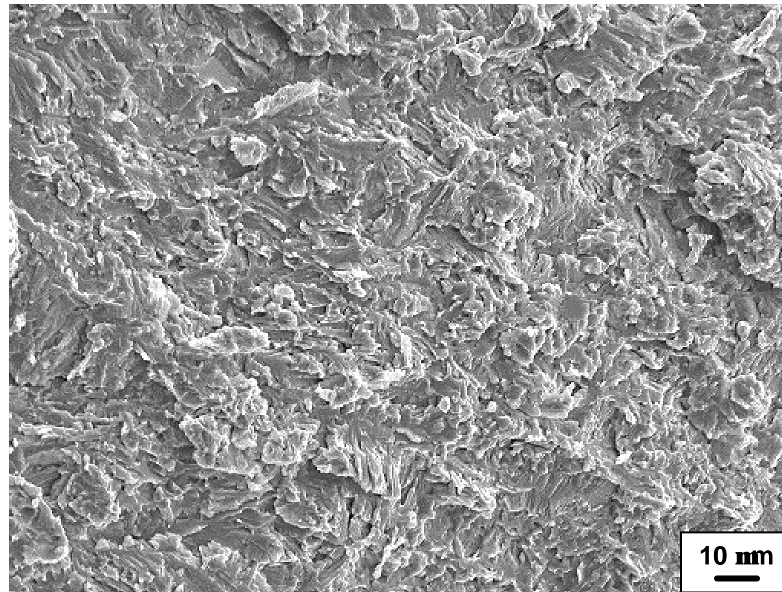


Figure 34−SEM micrograph, in SEI mode, showing fracture surface of as-received GMPX bulk material. The fracture path of the nearly lamellar microstructure was macroscopically flat and dominated by transgranular cleavage fracture.

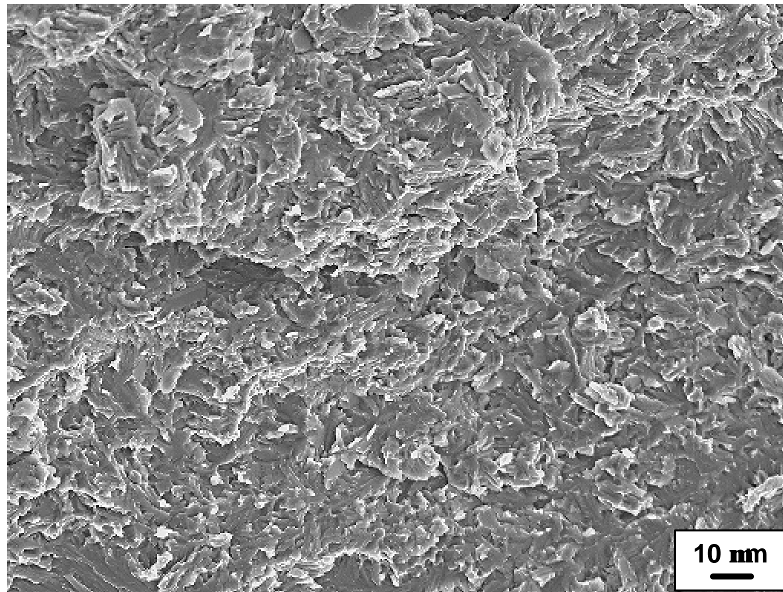


Figure 35−SEM micrograph, in SEI mode, showing fracture surface of GMPX bulk material after a bond cycle. The fracture path dominated by transgranular cleavage fracture.

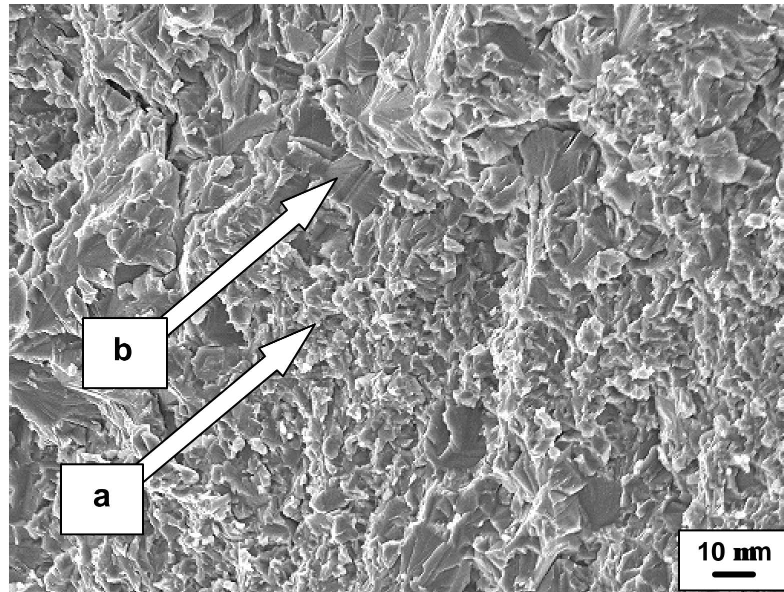


Figure 36–SEM micrograph, in SEI mode, showing fracture surface of GMPX bond employing a 50:1 Gamma Met to copper interlayer ratio. (a) fracture path through Gamma Met bond-line powder dominated by transgranular cleavage fracture, whereas (b) fracture through copper containing phases surrounding the Gamma Met powders appeared very planar (possibly delamination of the lamellar-like microstructure observed in the areas of dissolved Gamma Met powder particles).

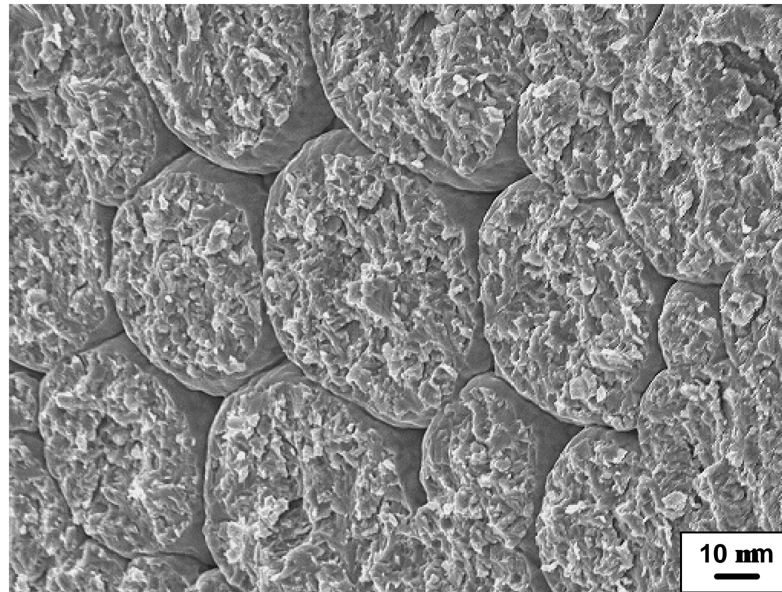


Figure 37–SEM micrograph, in SEI mode, of fracture surface of GMPX bond employing a 50:1 Gamma Met to copper interlayer ratio. This particular region of the fracture surface shows a porous region consisting only of Gamma Met particles which had sintered during the bonding process.

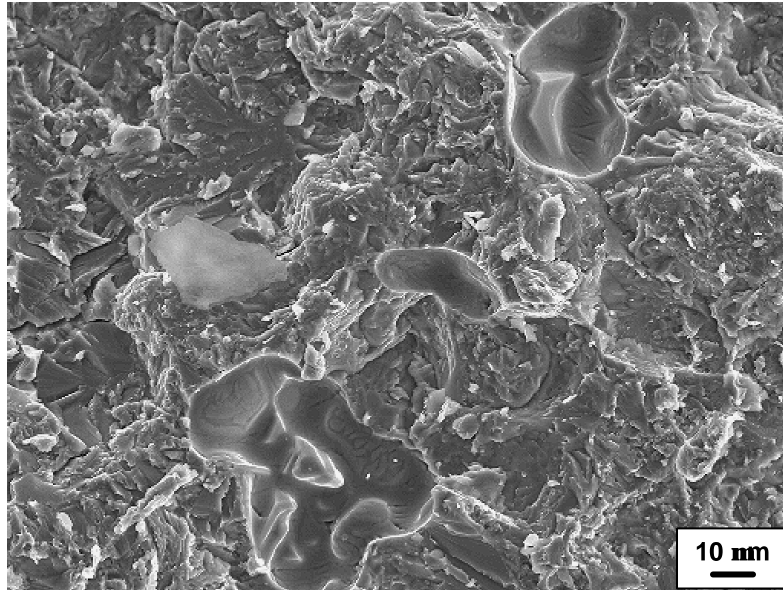


Figure 38–SEM micrograph, in SEI mode, showing fracture surface of GMPX bond employing a 6:1 Gamma Met to copper interlayer ratio. The majority of the fracture path dominated by transgranular cleavage. However, there were several regions where failure appeared significantly different than the majority of the fracture surface. It is not clear whether these regions are due to porosity or failure by interfacial fracture between large copper-rich intermetallics and the matrix of the bond-line.

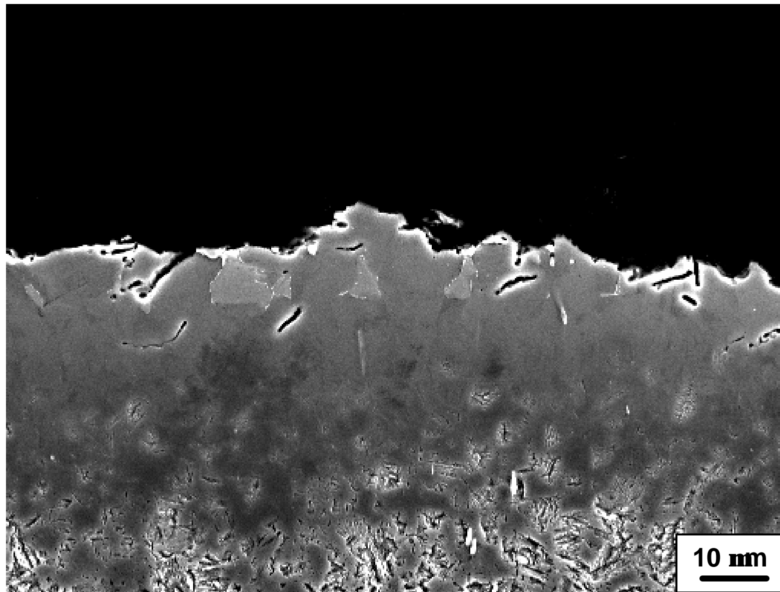


Figure 39–SEM micrograph, in SEI mode, showing cross sectional view of fracture surface of a GMPX bond employing a 6:1 Gamma Met to copper interlayer ratio. Failure occurred at the interface of the bond-line and one of the substrates.

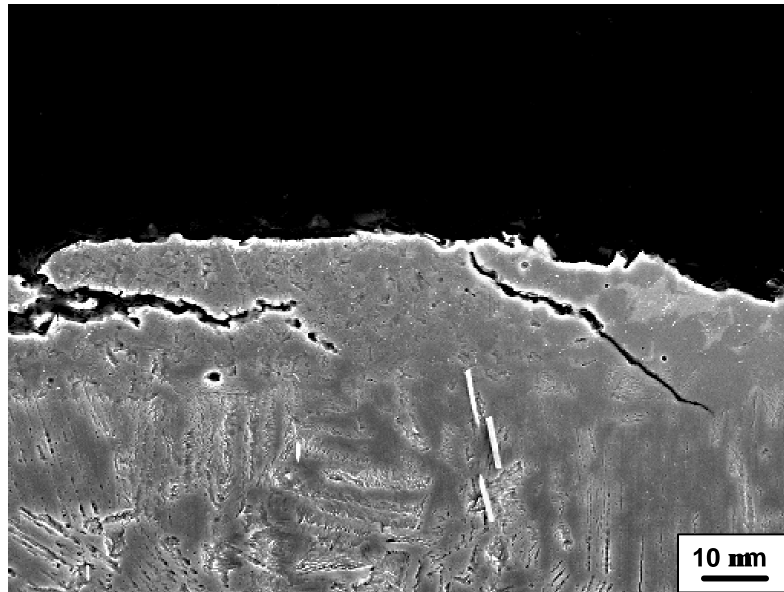


Figure 40–SEM micrographs, in SEI mode, showing cross sectional view of fracture surface of a GMPX bond employing a 50:1 Gamma Met to copper interlayer ratio. Failure occurred at the interface of the bond-line and one of the substrates.

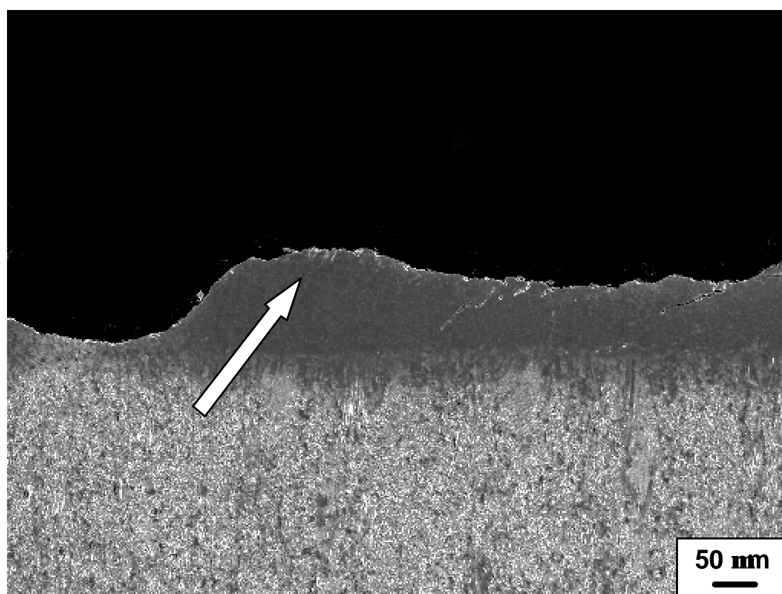


Figure 41–SEM micrograph, in SEI mode, showing cross sectional view of fracture surface of a GMPX bond employing a 65:1 Gamma Met to copper interlayer ratio. Fracture seemingly propagated at random within the bond-line, except at localized copper-rich regions where a fair amount of Gamma Met powder particles had been dissolved. At these regions, fracture tended to occur at the perimeter of these copper containing regions where there was significant epitaxial growth of Gamma Met powder particles. One such region is indicated by an arrow.

### *5.3.2 Tensile Testing*

Tensile testing was conducted to supplement four-point bend testing. Although a limited number of specimens were tested, the results seemed to correlate fairly well with the four-point bend testing (results are shown in Figure 42). Like four-point bend testing, bonds employing a 50:1 interlayer ratio produced higher strengths than bonds employing a 6:1 interlayer ratio. However, a difference of 370 MPa was observed for the mean bend strengths of bonds using a 6:1 and 50:1 interlayer ratio, while a difference of only 120 MPa was observed for the mean tensile strength of bonds using a 6:1 and 50:1 interlayer ratio. This dissimilarity in mean tensile strength difference could be attributed to potential problems associated with tensile testing narrow-gap bonds (i.e. bond-line width < 250 µm). Consider an as-bonded material subjected to a uniaxial stress state as shown in Figure 43. According to Schimd's Law,[167] the maximum resolved shear stress ( $t_{max}$ ) occurs on those planes, such as *AA*, that are oriented 45° (value of $q$ ) to the tensile axis. It is obvious from Figure 43 that a minimal amount of the bond-line is oriented on the plane experiencing the maximum resolved shear stress. Hence, it can be argued that tensile testing of narrow-gap bonds does not effectively test the bond-line.

An image showing the fracture surface of a GMPX bond employing a 50:1 interlayer ratio after tensile testing is shown in Figure 44. The fracture path dominated by transgranular cleavage fracture and compared well to the fracture surface of the bond cycled bulk shown in Figure 35.

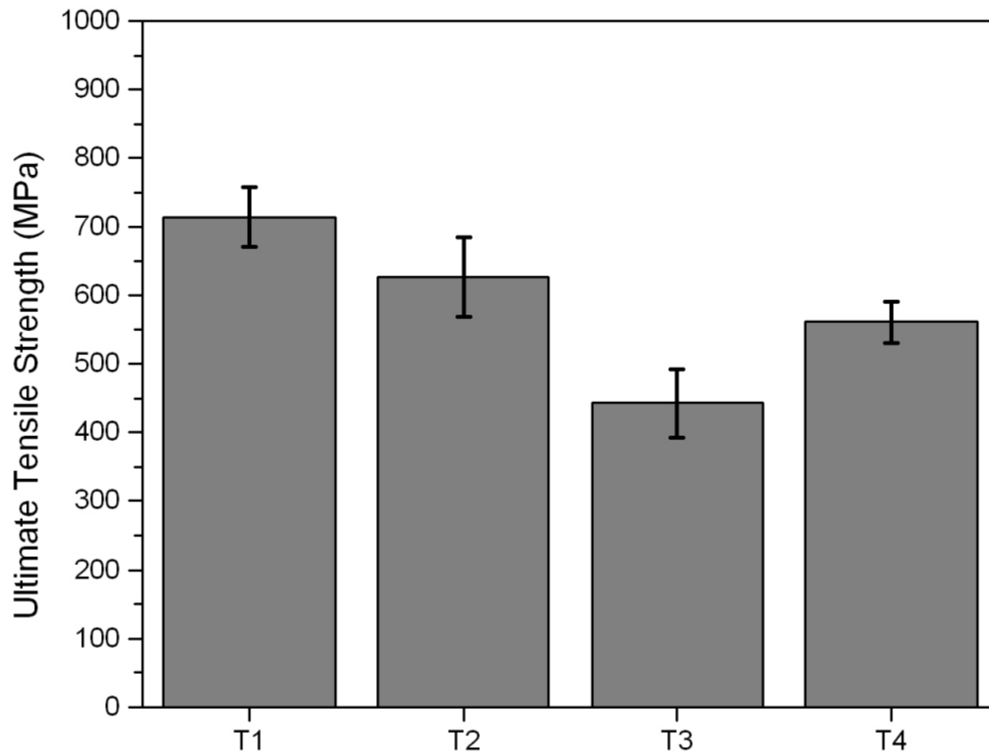


Figure 42–Results of tensile testing for as-bonded wide-gap TLP joints employing 6:1 and 50:1 Gamma Met to copper interlayer ratios. Tensile strengths of the bulk material in the as-received and bond cycled condition are included for comparison. The mean tensile strength and standard deviation data are as follows:

T1: As-received bulk material; 710 ±40 MPa

T2: Bond cycled bulk material; 630 ±60 MPa

T3: As-bonded joint employing 6:1 interlayer weight ratio; 440 ±50 MPa

T4: As-bonded joint employing 50:1 interlayer weight ratio; 560 ±30 MPa

Note: Only one bond sample for each of the above conditions was prepared. At least two tensile specimens were extracted from each of these samples for testing. The error bars and standard deviation values represent the standard deviation (±1 $\sigma$) for all specimens tested.

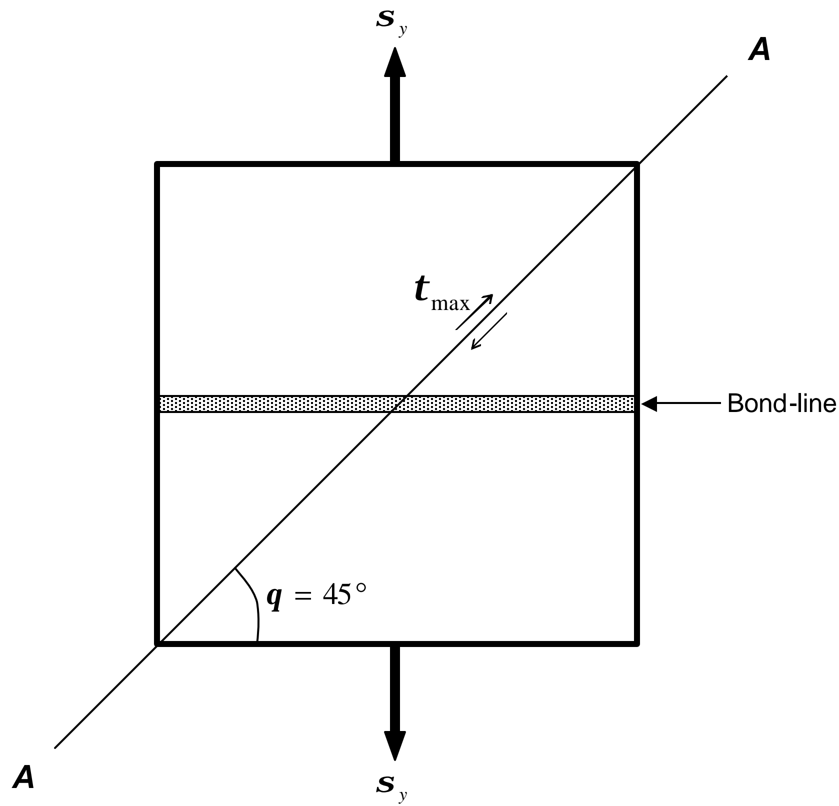


Figure 43–Schematic of a narrow-gap (i.e. bond-line width < 250 µm) as-bonded sample subjected to a uniaxial stress state. According to Schimd's Law,[167] the maximum resolved shear stress ($\tau_{max}$) occurs on planes, such as *AA*, which are oriented 45° (value of $\theta$) to the tensile axis. It is obvious from the schematic that a minimal amount of the bond-line is oriented on this plane. Hence, it can be argued that tensile testing of narrow-gap bonds does not effectively test the bond-line.

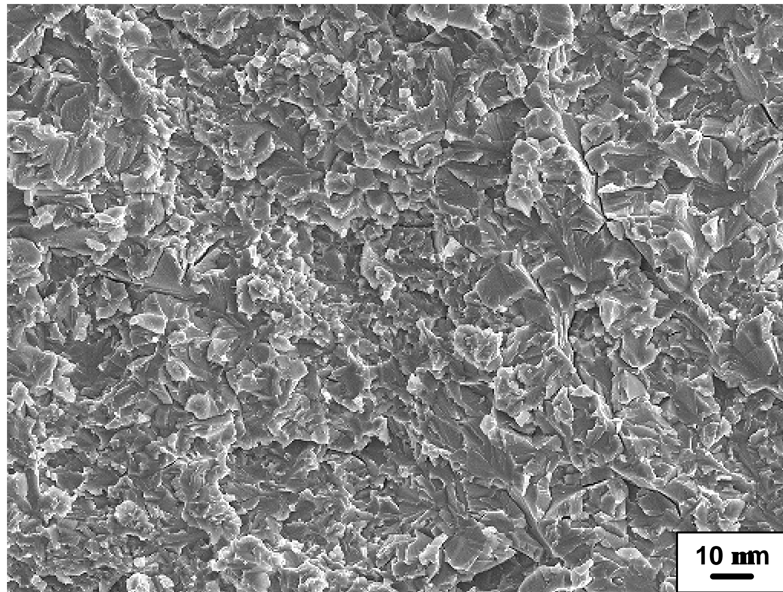


Figure 44−SEM micrograph, in SEI mode, showing fracture surface of GMPX bond employing a 50:1 Gamma Met to copper interlayer ratio. The fracture path was dominated by transgranular cleavage fracture and compared well to the fracture surface of the bond cycled bulk shown in Figure 35.

## 5.4 Characterization of Post-Bond Heat Treated Wide-gap TLP joints

Since some γ-TiAl applications will require a microstructure other than the fine grained, nearly lamellar microstructure of the as-extruded GMPX, post-bond heat treatment experiments that produced a fully lamellar and duplex microstructure were conducted. Both microstructures are of potential commercial importance considering the duplex microstructure exhibits good tensile ductility and strength, whereas a fully lamellar microstructure exhibits relatively good fracture toughness and moderate creep resistance.[168] Hence, a turbine blade or turbo/supercharger wheel are examples of components requiring a fully lamellar microstructure since creep is a major concern, due to the high rotational stresses combined with the high temperature experienced in service. Conversely, the skin structure of an aerospace vehicle is an example of an application likely requiring a duplex microstructure considering the requirements of good ductility and strength opposed to creep.

### *5.4.1 Duplex Microstructure*

Studies conducted by Das[169] determined heat treatments to produce a duplex microstructure in bulk substrates were 6X, 12X, 24X, 48X hr[11] at 1290°C. As the time at temperature increased, the volume percent of equiaxed gamma grains observed increased to 5.6%, 15.9%, 24.3% and 28.5% respectively.

Post-bond heat treatments to produce a duplex microstructure, performed by the present author, were conducted at 1290°C for 6X, 12X, 24X, 48X hr (Figure 45). Of the post bond heat treatments tested, a time of at least 24X hr was found to be sufficient to produce a bond-line with a microstructure and chemical composition similar to the bulk

[11] PBHT times are controlled by ITAR. As before, X refers to a numerical factor. For example, if X = 2, 6X hr = 12 hr.

material. After 6X hr at 1290°C, some copper containing phases with ~2 at.% copper were observed in the joint and apparently prohibited the formation of a duplex microstructure across the entire bond-line. After 12X hr at 1290°C, no copper containing phases were observed, however the microstructure of the bond-line did not closely resemble that of the bulk. A PBHT of 24X and 48X hr at 1290°C produced a duplex microstructure in the bulk and at the original bond-line. No copper was detected in the bond region by EDS analysis (and so the center-line copper content is assumed to be considerably less than 1 at.% copper). The composition across the bond-line of a sample after a PBHT of 24X hr at 1290°C is shown in Figure 46. Although similar, the composition in the region of the original bond-line did not exactly match that of the substrate. This variation is attributed to the slight difference in composition of the GMPX substrate and Gamma Met powder particles. The dissimilar composition in the bond region could account for the coarse microstructure which caused the joint to remain slightly discernable following the PBHT. Although the grains in the bond region were slightly larger than those in the bulk, the hardness of the bond-line, as shown in Figure 47, was found to be somewhat similar to the bulk material.

(a)

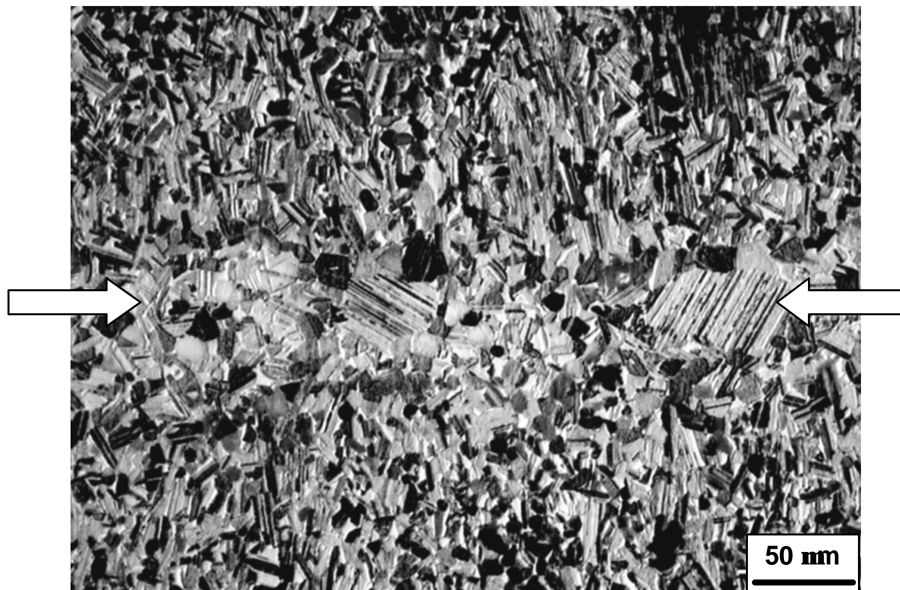


(b)

Figure 45–LM micrograph of a GMPX joint employing a 50:1 Gamma Met to copper interlayer ratio after a PBHT at 1290°C for (a) 6X hr (b) 12X hr. Arrows indicate original bond-line. Residual copper in (a) was not effected by the etchant used to prepare this sample, thus the bond-line appears very light.

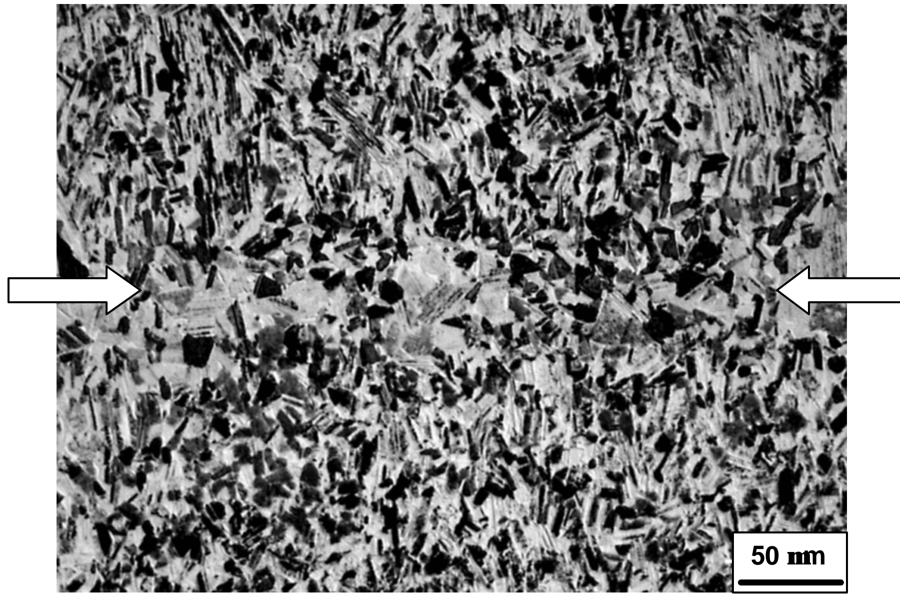


(c)

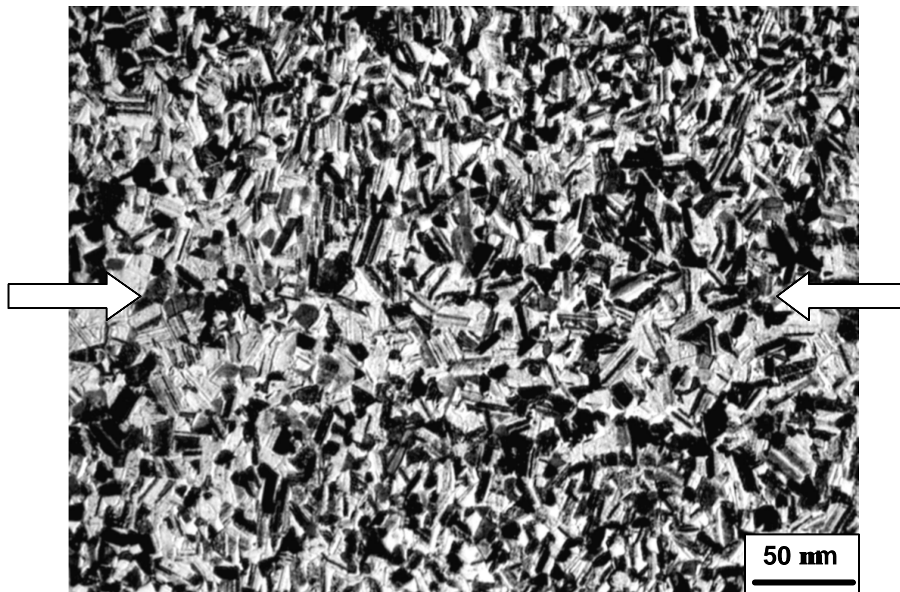


(d)

Figure 45 (continued)−LM micrograph of an as-bonded GMPX joint employing a 50:1 Gamma Met to copper interlayer ratio after a PBHT at 1290°C for (c) 24X hr (d) 48X hr. Arrows indicate original bond-line.

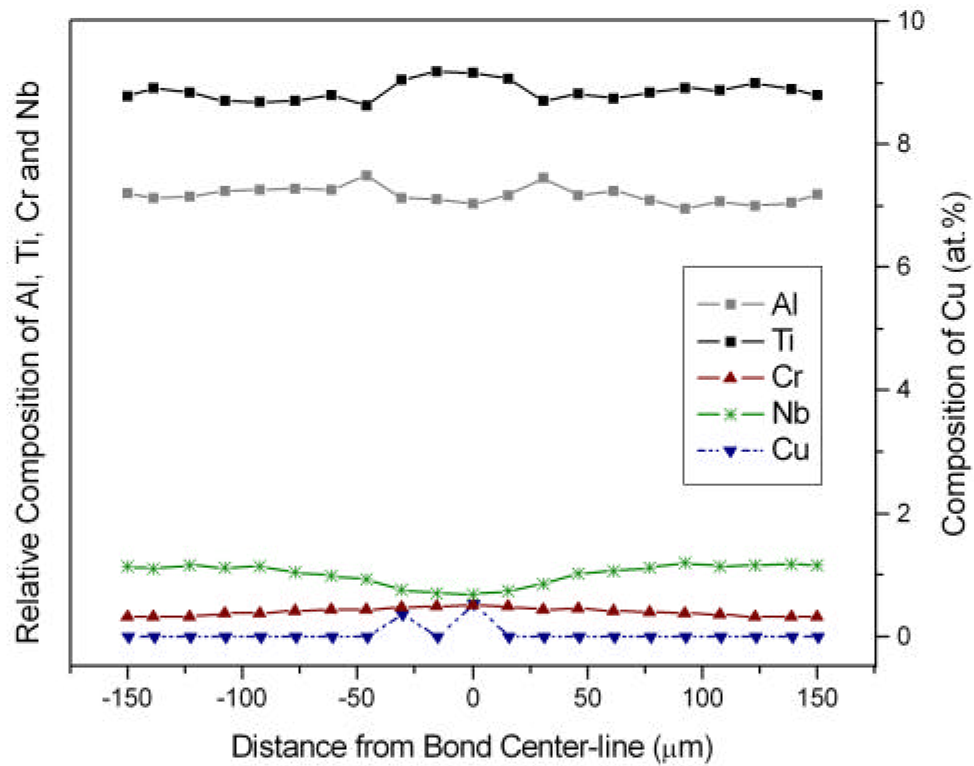


Figure 46–Composition profile across bond-line as-bonded GMPX joint employing a 50:1 Gamma Met to copper interlayer ratio after a PBHT at 1290°C for 24X hr. Right side of graph refers to composition of copper across bond-line, and left side of the graph refers to the composition of aluminum, titanium, chromium and niobium detected by EDS analysis.

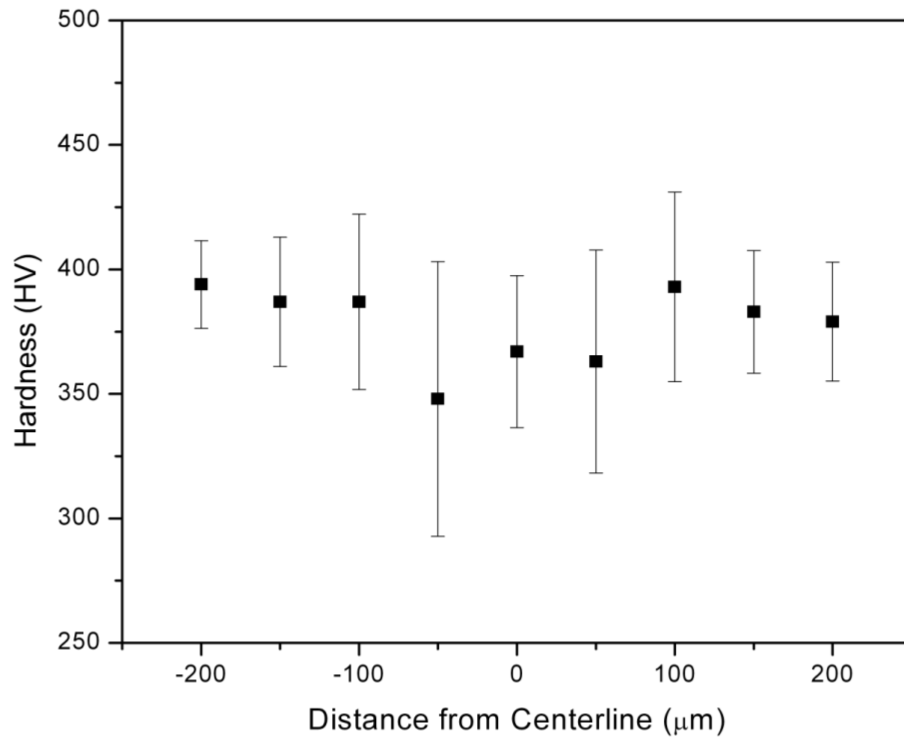


Figure 47−Vickers microhardness across bond-line of an as-bonded GMPX joint employing a 50:1 Gamma Met to copper interlayer after a PBHT at 1290°C for 24X hr.

### *5.4.2 Fully Lamellar Microstructures*

Microstructural development studies of 48–2–2 TLP bonds suggested that 1350°C for 1 hr represented the PBHT necessary for copper diffusion into the substrates and to produce a fully lamellar microstructure in the substrates and at the original bond-line.[27,29] The resulting average as-PBHT bend strengths were determined to be ~90% of bulk material subjected to same thermal treatment.[27] Thus, initial PBHT experiments on GMPX bonds were conducted using these same conditions. However, even with bonds employing a 50:1 interlayer ratio, this PBHT did not produce a fully lamellar $\gamma$(TiAl) + $\alpha_2$($Ti_3Al$) microstructure across the entire bond-line. Copper containing phases were observed in the bond center-line (Figure 48) and apparently prohibited the growth of fully lamellar grains across the bond-line. Possible reasons for the latter observation are discussed in section 5.7. In addition, this PBHT resulted in excessive grain growth (some grain diameters >500 μm) in the GMPX bulk material (Figure 49). The latter observation is attributed to a lower alpha transus temperature for GMPX than 48–2–2. High additions of niobium have proven to decrease the alpha transus temperature up to about 30°C.[67]

Studies conducted by Das[169] suggested that a suitable thermal cycle to produce a fully lamellar microstructure in the bulk substrates was 3X hr at 1340°C.[11] Heat treatment experiments, by the present author, on the bulk GMPX material confirmed Das's observations that 3X hr at 1340°C produced a relatively fine grained fully lamellar microstructure with equiaxed lamellar colonies averaging 230 ±70 μm in diameter. Although a fine grained fully lamellar microstructure was produced in the bulk material (Figure 50), this PBHT did not allow sufficient copper diffusion into the substrates. Like

the specimens subjected to a PBHT at 1350°C for 1 hr, copper containing phases in the bond-line prohibited the formation of a fully lamellar $\gamma$(TiAl) + $\alpha_2$($Ti_3Al$) microstructure across the entire bond-line. Thus, a dual heat treatment process was studied. A PBHT of 24X hr at 1290°C plus 3X hr at 1340°C provided sufficient time for copper diffusion into the bulk substrates and produced a relatively fine grained fully lamellar microstructure (equiaxed lamellar colonies averaged 250 ±90 μm in diameter) in the bulk and the original bond-line. Figure 51 shows an image of a GMPX TLP bond using 50:1 Gamma Met to copper powder ratio followed by a PBHT of 24X hr at 1290°C plus 3X hr at 1340°C followed by furnace cooling. A fine grain fully lamellar microstructure was formed in the bulk and at the original bond-line and, as seen in Figure 52, no copper was detected in the bond region by EDS analysis (and so the center-line copper content is assumed to be considerably less than 1 at.% copper). Furthermore, the hardness of the bond-line, as shown in Figure 53, was similar to that of the substrate.

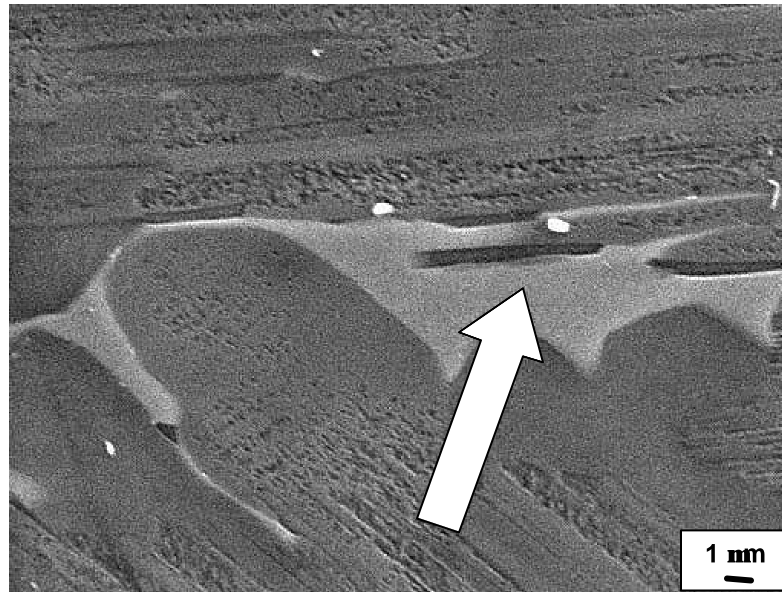


Figure 48−SEM micrograph, in SEI mode, of an as-bonded GMPX joint employing a 50:1 interlayer ratio after a PBHT of 1350°C for 1 hr. Copper containing phases (as indicated by an arrow) prohibited epitaxial growth of lamellar grains across the bond-line.

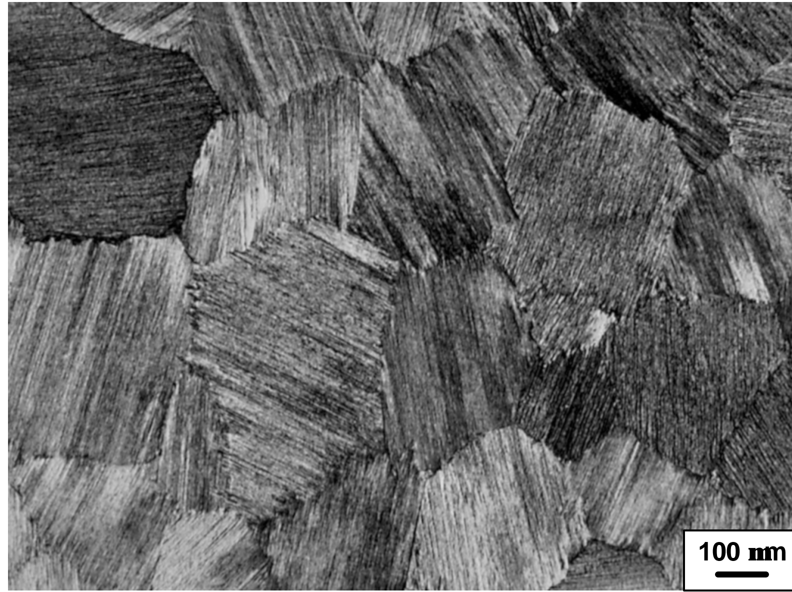


Figure 49−LM micrograph of GMPX substrate after heat treatment of 1350°C for 1 hr, which resulted in excessive grain growth.

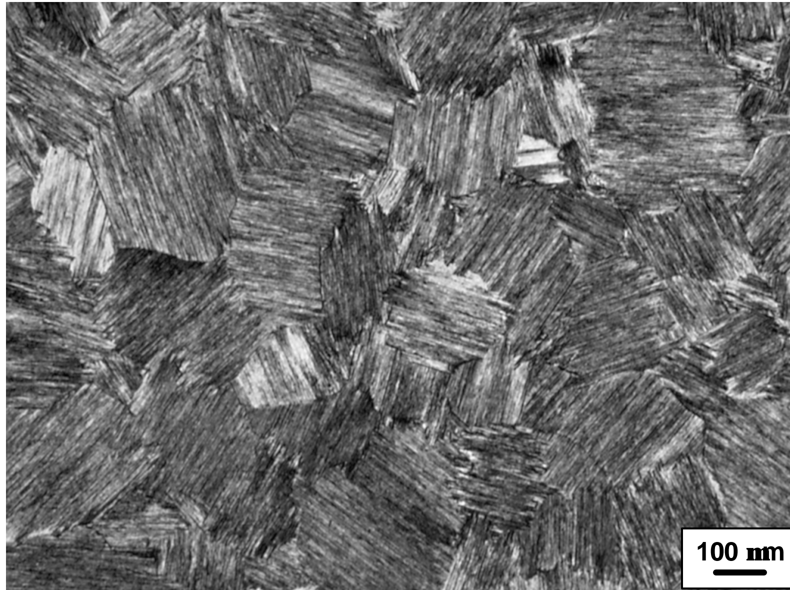


Figure 50−LM micrograph of GMPX substrate after heat treatment of 3X hr at 1340°C, which resulted in a relatively fine grain fully lamellar microstructure.

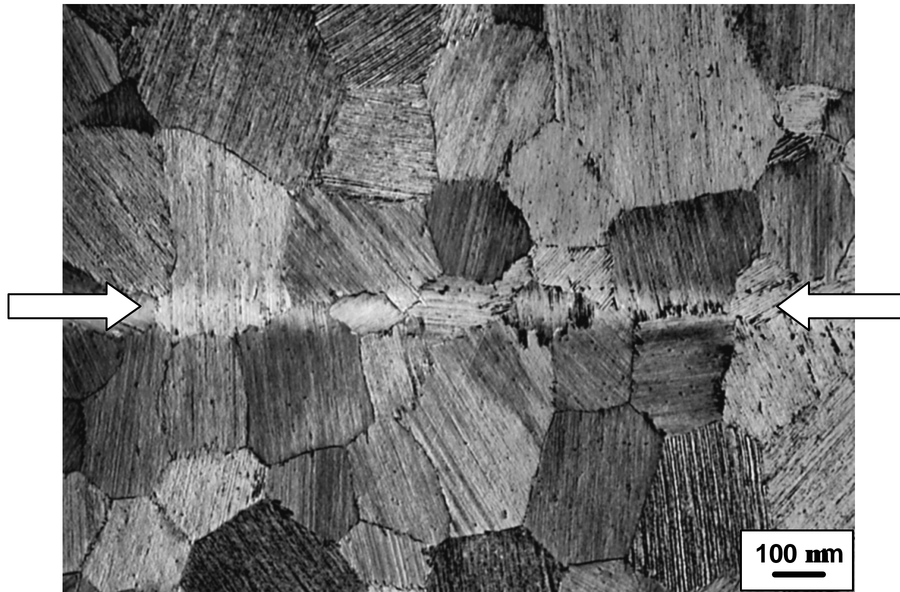


Figure 51–LM micrograph of a GMPX joint employing a 50:1 Gamma Met to copper interlayer ratio after a PBHT of 24X hr at 1290°C plus 3X hr at 1340°C. A fine grain fully lamellar microstructure was formed across the original bond-line (indicated by arrows). Although no copper was detectable by EDS analysis, the lighter contrast of the bond region is attributed to residual copper below the EDS detection limit, which influences the response to the etchant used to prepare this sample.

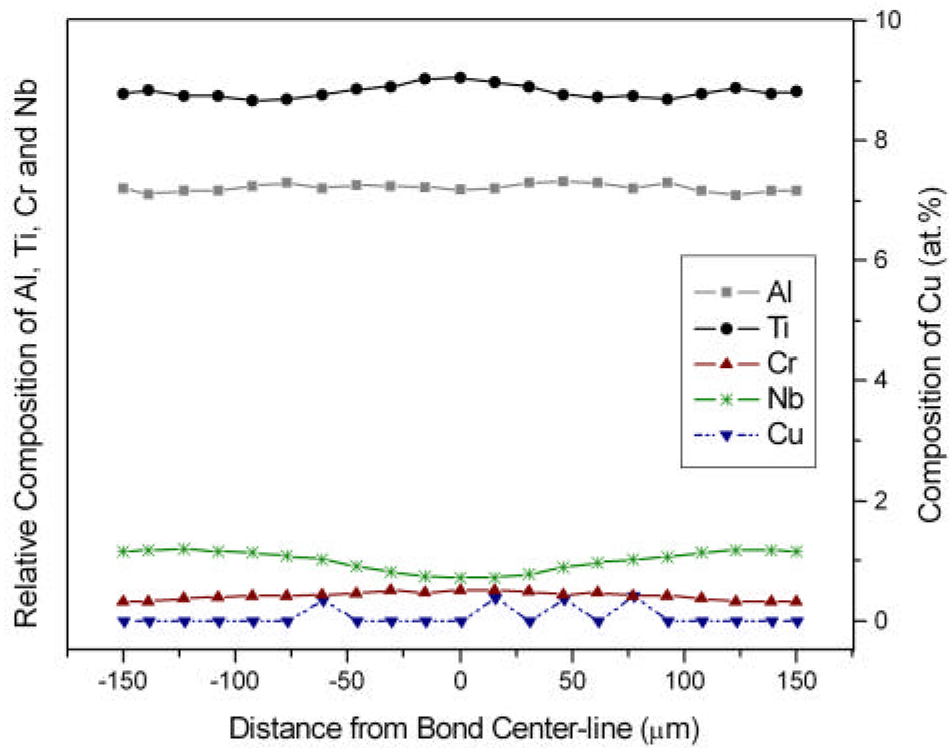


Figure 52−Composition profile across GMPX joint employing a 50:1 Gamma Met to copper interlayer ratio after a PBHT of 24X hr at 1290°C plus 3X hr at 1340°C. Right side of graph refers to composition of copper across bond-line, and left side of the graph refers to the composition of aluminum, titanium, chromium and niobium detected by EDS analysis.

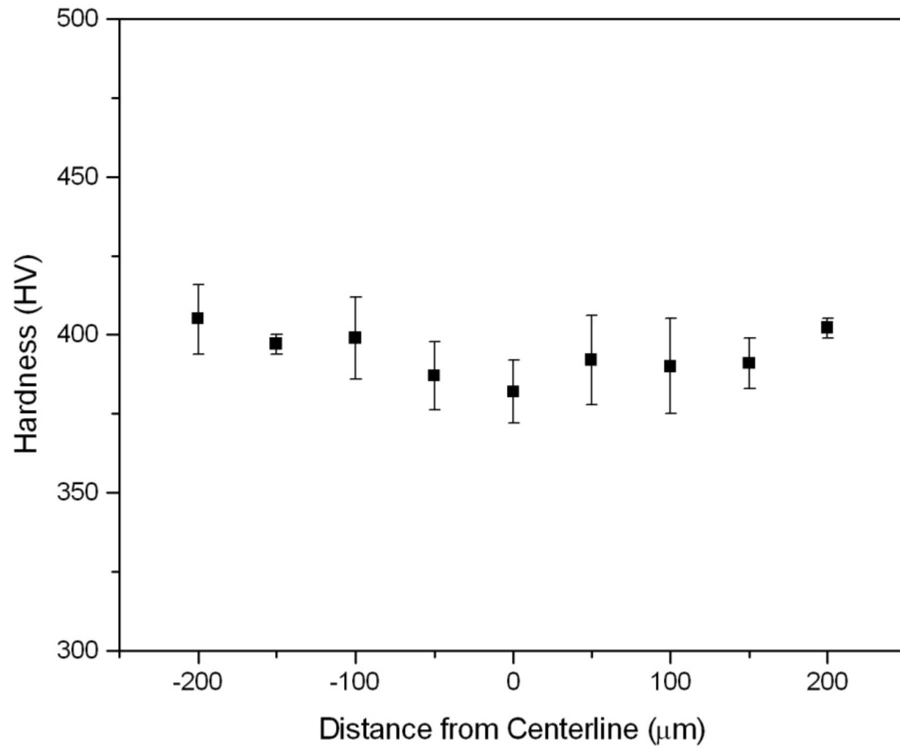


Figure 53–Vickers microhardness across bond-line of an as-bonded GMPX joint employing a 50:1 Gamma Met to copper interlayer ratio after a PBHT of 24X hr at 1290°C plus 3X hr at 1340°C.

## 5.5 Structure-Property Relationship for TLP Joints Following a PBHT

### *5.5.1 Four-Point Bend and Tensile Testing*

At the time of this work, GMPX was being considered for applications requiring good creep resistance,[2] therefore, mechanical testing focused on bonds and substrates that consisted of a fully lamellar microstructure following a PBHT. Also, considering the 50:1 interlayer ratio was determined to be the most optimum interlayer ratio of those tested, mechanical testing focused on bonds employing this interlayer ratio. Four-point bend and tensile strengths are shown in Figure 54. Both four-point bend and tensile strengths, of bonds employing a 50:1 interlayer ratio followed by a PBHT of 24X hr at 1290°C plus 3X hr at 1340°C, compared very well to the bulk material after a similar thermal cycle.

Fractographic investigations correlated well with mechanical testing. These investigations determined that the fracture surface of a bonded sample after PBHT (Figure 55) closely resembled the fracture surface of the bulk material subjected to the same thermal conditions (Figure 56). Fracture in both samples dominated by translamellar fracture with extensive crack deflection due to the alternating $\gamma$(TiAl) + $\alpha_2$($Ti_3Al$) lamellae.

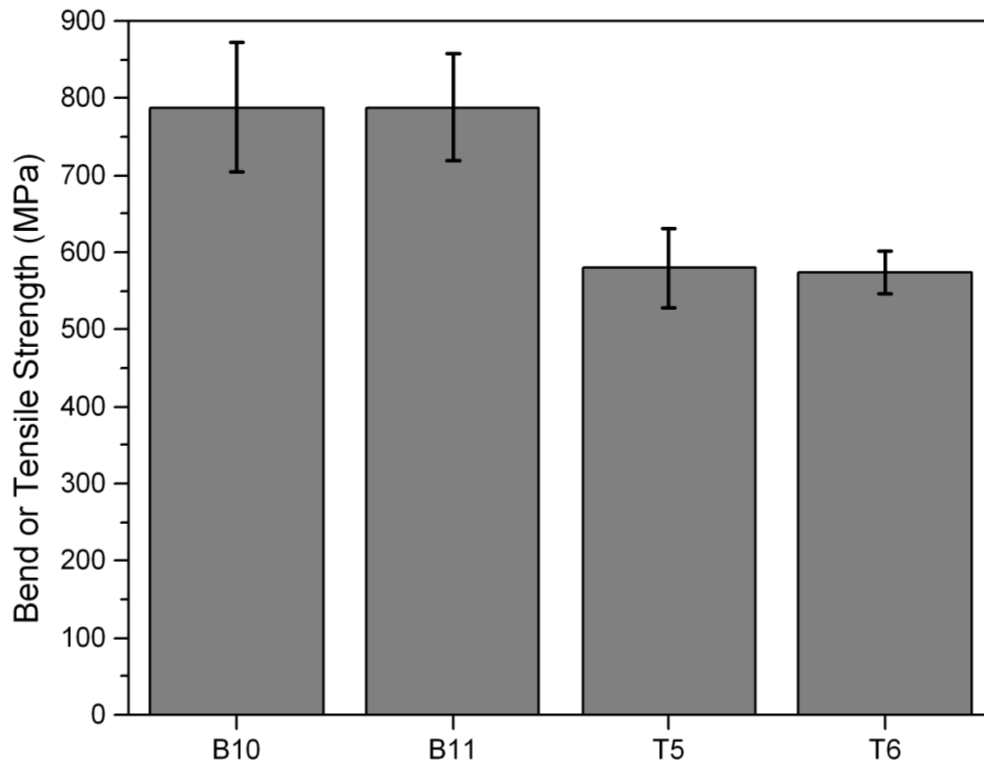


Figure 54–Results of bend and tensile testing for as-bonded wide-gap TLP joints employing a 50:1 Gamma Met to copper interlayer ratio after a PBHT of 24X hr at 1290°C plus 3X hr at 1340°C. Bend and tensile strengths of the bulk material after the PBHT thermal cycle are included for comparison. The mean bend and tensile strength and standard deviation data are as follows:

B10: Bend strength of bulk material after PBHT; 790 ±80 MPa

B11: Bend strength of bond employing a 50:1 interlayer ratio after PBHT; 790 ±70 MPa

T5: Tensile strength of bulk material after PBHT; 580 ±50 MPa

T6: Tensile strength of bond employing a 50:1 interlayer ratio after PBHT; 570 ±30 MPa

Note: Only one bonded sample for each of the above conditions was prepared. At least two tensile specimens were extracted from each of these samples for testing. The error bars and standard deviation values represent the standard deviation (±1 σ) for all specimens tested.

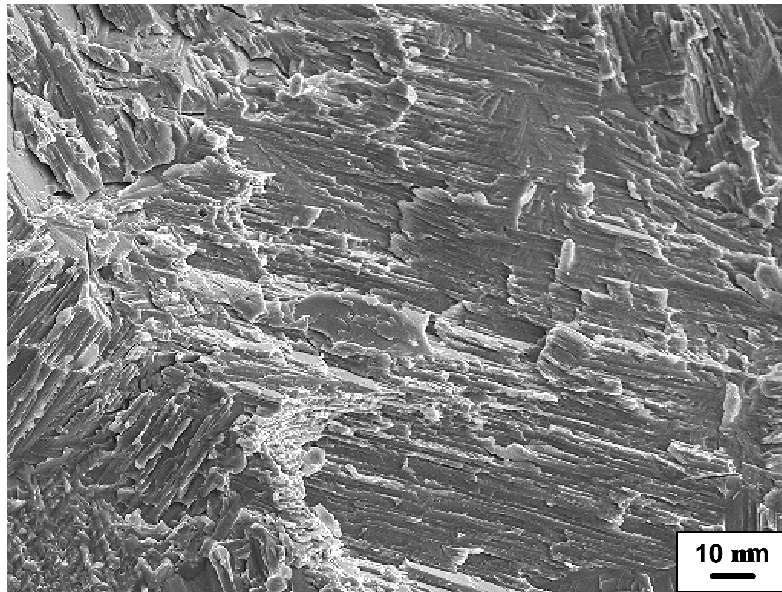


Figure 55: SEM micrograph, in SEI mode, showing fracture surface of GMPX bond employing a 50:1 Gamma Met to copper interlayer ratio after a PBHT of 24X hr at 1290°C plus 3X hr at 1340°C. The fracture path dominated by translamellar fracture with extensive crack deflection by the lamellae.

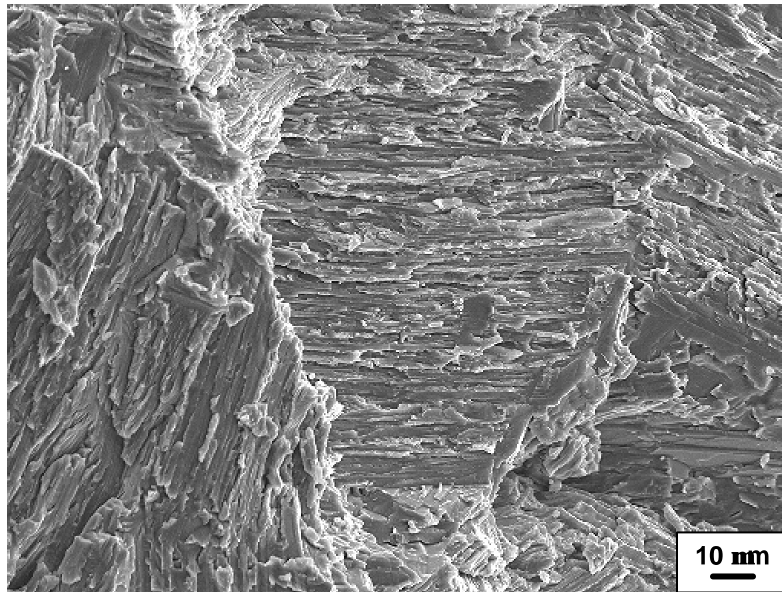


Figure 56–SEM micrograph, in SEI mode, showing fracture surface of a GMPX bulk material subjected to a bond cycle and a PBHT of 24X hr at 1290°C plus 3X hr at 1340°C. The fracture path dominated by translamellar fracture with extensive crack deflection by the lamellae.

## 5.6 Comparison of 48- 2- 2 and GMPX Materials and TLP Bonds

As stated earlier, the bonding and solid-state homogenization processes for GMPX were initially the same as those employed in previous work on 48–2–2 substrates. These initial studies suggested the bonding and solid-state homogenization processes employed for 48–2–2 substrates did not produce the same results when used with GMPX materials. Thus modifications to the GMPX joining process were necessary. Before discussing the observed differences in 48–2–2 and GMPX wide-gap TLP bonds, the differences in substrate and interlayer materials employed are discussed.

### *5.6.1 Substrate Materials*

The most obvious difference in the 48–2–2 and GMPX materials was a difference in composition and as-received microstructure. As discussed, the 48–2–2 materials had a composition of Ti – 48 at.% Al – 2 at.% Cr – 2 at.% Nb. Since the composition of GMPX is proprietary to GKSS Research Center, it can only be stated here that GMPX has the composition of Ti – 45 at.% Al – X at.% (Nb, B, C). One obvious difference in composition is the higher concentration of aluminum and presence of chromium in 48–2–2. Secondly, as discussed in the literature review, current generation γ-TiAl alloys, such as GMPX, contain a higher concentration of niobium than earlier generation γ-TiAl alloys such as 48–2–2.

Concerning as-received microstructures, the as-cast 48–2–2 materials, as shown in Figure 8, consisted of a nearly lamellar microstructure with an average grain size of 170 μm. The as-extruded GMPX materials also consisted of nearly lamellar microstructure, but with an average grain size of 20 μm, as shown in Figure 7. This

difference in grain size is attributed to the different processing routes of the 48−2−2 and GMPX bulk materials. XRD analysis revealed that the GMPX and 48−2−2 materials consisted predominately of the γ(TiAl) phase, with a small volume fraction of the $\alpha_2(Ti_3Al)$ phase (Figure 57 and Figure 58). However, according to the XRD results, GMPX appeared to contain a higher volume fraction of the $\alpha_2(Ti_3Al)$ phase. Quantitative data for the $\alpha_2(Ti_3Al)$ volume fraction in 48−2−2 and GMPX was not found in the literature and quantification via optical microscopy was difficult due to the thin γ(TiAl) and $\alpha_2(Ti_3Al)$ lamellae. Thus, an intensity ratio calculation was done for the $\alpha_2(Ti_3Al)$ peaks observed using the intensity of the γ(111) peak as a reference. The results of this intensity ratio calculation are shown in Table 4. Ideally the intensity ratio values should be the same for a given substrate. However, considering the samples were polycrystalline aggregates, rather than powders, it is likely that some preferred orientation may exist. Also, the accuracy of this method is probably low in view of the use of maximum intensities rather than integrated intensities. Nonetheless, all of the intensity ratios for GMPX were greater than those of 48−2−2. The apparent difference in volume fraction of the $\alpha_2(Ti_3Al)$ phase is attributed to the different processing routes and/or differences in composition. The temperature, time and cooling rates associated with the processing route can significantly affect the volume fraction of phases present in the alloy. The composition of the alloy can also control the volume fraction of phases present. For example, according to the binary Ti-Al phase diagram (Figure 1), a reduction in aluminum tends to increase the volume fraction of the $\alpha_2(Ti_3Al)$ phase. GMPX, in fact, has a slightly lower concentration of aluminum than that of 48−2−2.

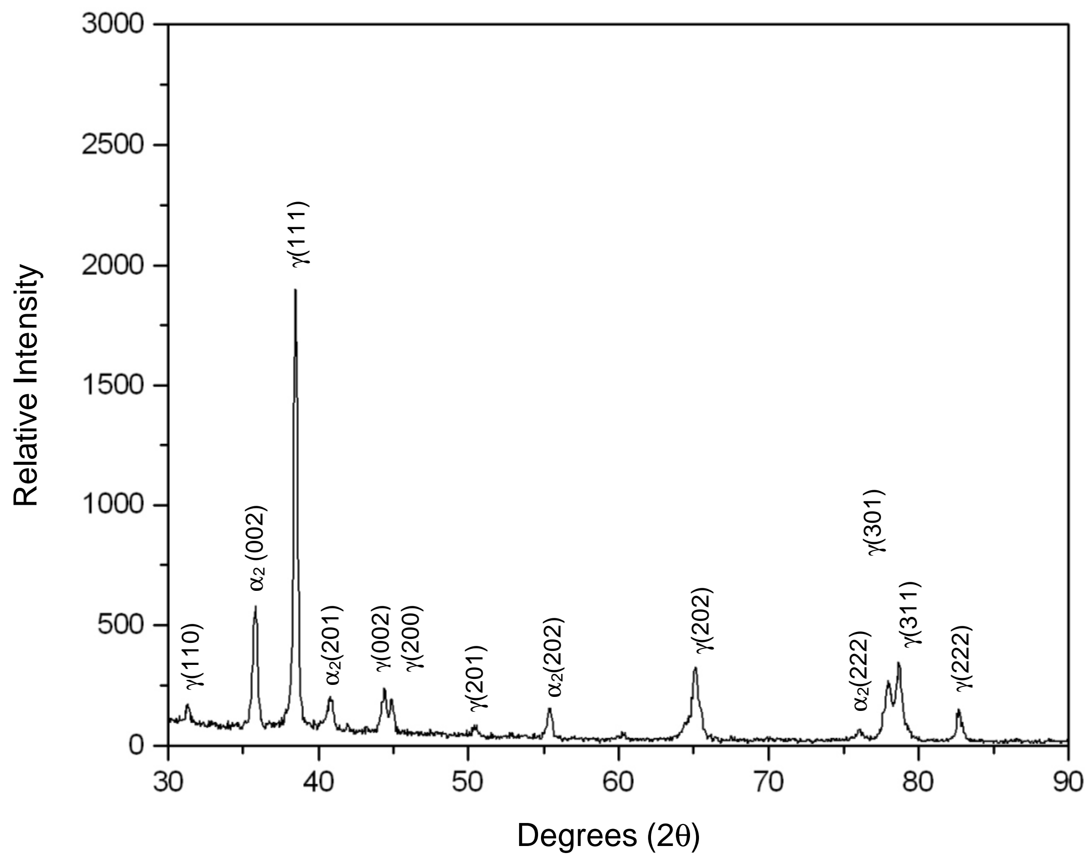


Figure 57−XRD pattern of as-received GMPX. The predominant phase was determined to be the γ(TiAl) phase with a small volume fraction of the $\alpha_2(Ti_3Al)$ phase.

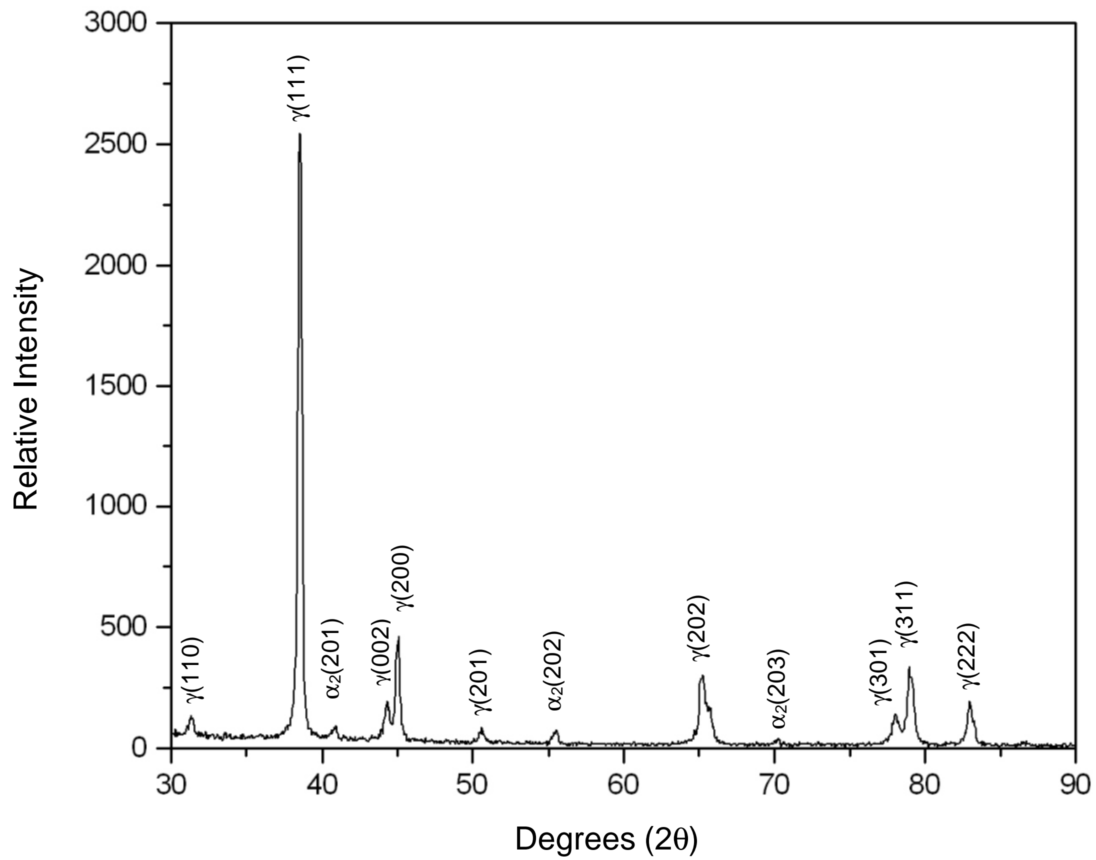


Figure 58−XRD pattern of as-received 48−2−2. The predominant phase was determined to be the γ(TiAl) phase with a small volume fraction of the $\alpha_2$($Ti_3Al$) phase.

| $I_{Int.} / I_{Ref.}$ | GMPX | 48−2−2 | $[I_{Ref.}/ I_{Int.}]_{GMPX} / [I_{Ref.}/ I_{Int.}]_{48-2-2}$ |
|---|---|---|---|
| $\alpha_2$(002) / $\gamma$(111) | 0.31 | 0.02 | 13.7 |
| $\alpha_2$(201) / $\gamma$(111) | 0.10 | 0.04 | 2.8 |
| $\alpha_2$(202) / $\gamma$(111) | 0.07 | 0.03 | 2.2 |
| $\alpha_2$(203) / $\gamma$(111) | 0.02 | 0.02 | 1.2 |
| $\alpha_2$(222) / $\gamma$(111) | 0.03 | 0.01 | 3.1 |

Table 4−GMPX and 48−2−2 intensity ratio calculations for the $\alpha_2(Ti_3Al)$ peaks observed using the intensity of the $\gamma$(111) peak as a reference. Here, $I_{Int.}$ and $I_{Ref.}$ represent intensity for peak of interest and intensity for reference peak respectively.

### *5.6.2 Interlayer Materials*

The primary difference in the composite interlayer materials used in 48–2–2 and GMPX wide-gap TLP bonds was the TiAl alloy powders. The 48–2–2 materials employed TiAl alloy powders with a composition identical to the substrate materials. However, as mentioned in section 4.1, this was not possible with GMPX wide-gap TLP bonds. Instead, Gamma Met powders with a composition of Ti – 46.5 at.% Al – 2.5 at.% Cr – 1 at.% Nb – 0.5 at.% Ta – 0.1 at.% B were employed. The studies conducted on the Gamma Met powders, as discussed in section 5.1.1, were also conducted on 48–2–2 powders. Of the studies conducted, no differences in microstructure, grain size and XRD were observed in the as-received Gamma Met and 48–2–2 powders.

Besides composition, the only significant difference in the Gamma Met and 48–2–2 powders was the particle size used in bonding. GMPX bonds employed −200 mesh Gamma Met particles, while 48–2–2 bonds employed −270 mesh 48–2–2 particles. Both bonds employed −325 mesh commercially pure copper powders. Although different size particles were used, the as-received particle size distribution for both Gamma Met and 48–2–2 powders was determined to be somewhat similar, with the majority of powders ranging from 6 to 65 μm in diameter (Figure 59).

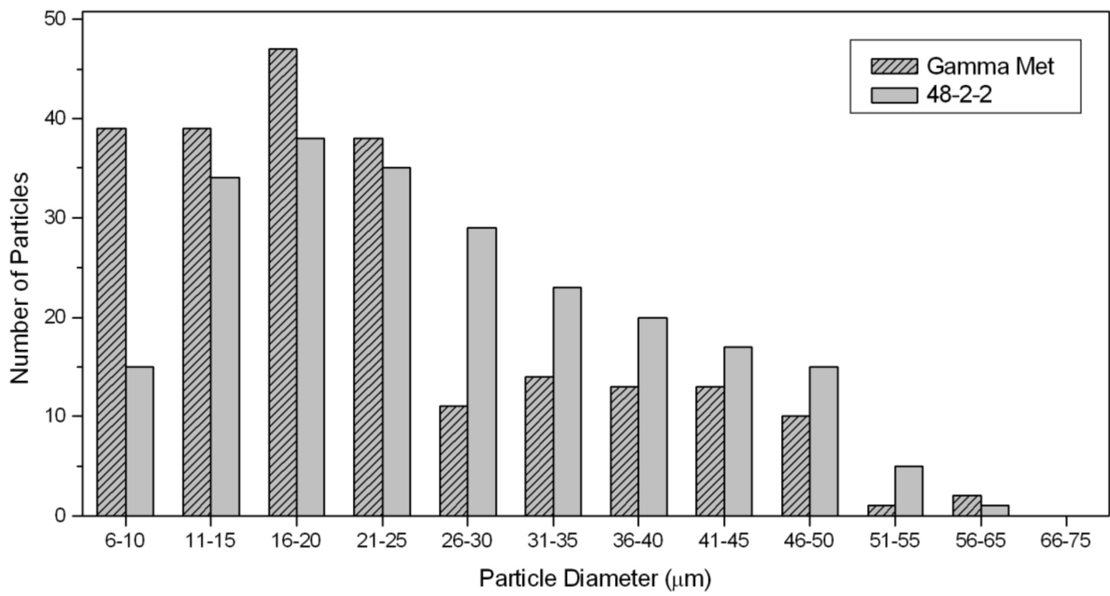


Figure 59−Gamma Met and 48−2−2 powder particle size distribution.

### *5.6.3 Wide-Gap TLP Bonds*

During microstructural and mechanical property studies, some obvious differences in GMPX and 48–2–2 wide-gap TLP bonds were observed, when employing a 6:1 TiAl alloy to copper composite interlayer ratio and using similar bonding conditions. These differences are summarized below:

- Although copper-rich intermetallics were observed in 48–2–2 bonds (Figure 60), they were observed less frequently and had a lower concentration of copper (i.e. ~20 at.% compared to ~30 at.% copper) than those observed in GMPX bonds (recall Figure 10).
- EDS analysis determined the copper concentration of copper containing phases in GMPX bonds to be 5 – 6 at.% copper, whereas the copper concentration of copper containing phases in 48–2–2 bonds to be 3 – 4 at.% copper.
- The overall copper content in the bond-line of GMPX joints was determined to be 6 – 7 at.% copper, whereas the overall copper content in the bond-line of 48–2–2 joints was 4 – 5 at.% copper. Figure 61 shows the composition profile across bond-line of 48–2–2 joint.
- GMPX bonds tended to have more epitaxial growth of the substrate into the bond-line (recall Figure 13) than 48–2–2 bonds (Figure 62).
- Significant dissolution of some grain boundaries was observed in 48–2–2 bonds, but not in GMPX bonds (Figure 62).

- Fillets of 48–2–2 bonds tended to be larger than those of GMPX bonds (Figure 63). Average cross-sectional area of fillets observed in 48–2–2 and GMPX bonds was 0.25 ±0.06 $mm^2$ and 0.18 ±0.11 $mm^2$ respectively.
- Mechanical testing revealed a significant difference in as-bonded GMPX and 48–2–2 four-point bend strengths (relative to the bulk) employing a 6:1 interlayer ratio. Average as-bonded GMPX bend strength was determined to be ~48 % of bulk GMPX material subjected to the same thermal cycle, whereas Zhou[27,29] determined average as-bonded 48–2–2 bend strength to be ~68% of the 48–2–2 substrate subjected to the same thermal cycle.
- Concerning PBHT specimens, there was an obvious difference in the time necessary to complete the solid-state homogenization process. In 48–2–2 bonds employing a 6:1 48–2–2 plus copper interlayer ratio, 1 hr at 1350°C was sufficient time and temperature to allow for complete homogenization of the bond-line. In contrast, GMPX bonds employing an interlayer with a much lower concentration of copper (e.g. 50:1), a PBHT of 1 hr at 1350°C was still insufficient to allow for complete homogenization of the bond-line.

In an effort to understand these observed differences between GMPX and 48–2–2 bonds, detailed mechanistic studies of the underlying joining mechanisms associated with TLP bonding were conducted. The results of these studies are discussed in the next section.

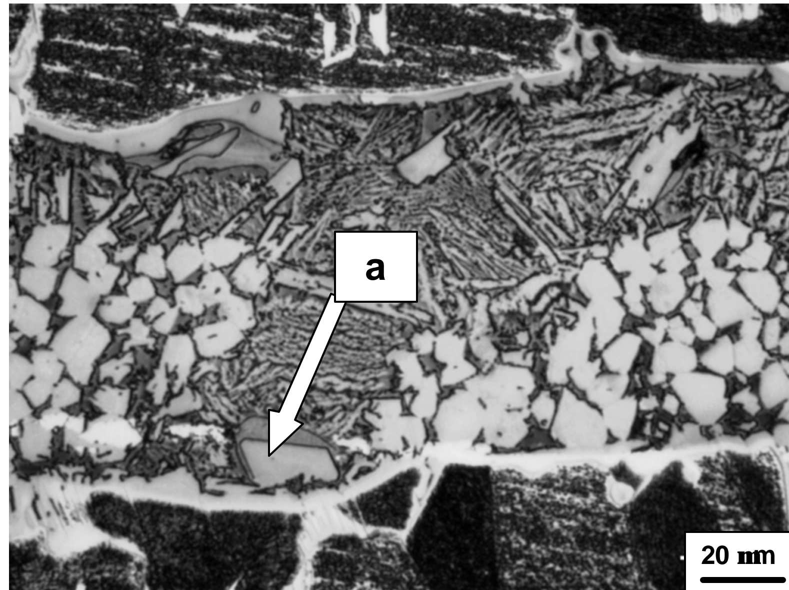


Figure 60–LM micrograph of an as-bonded 48–2–2 joint employing a 6:1 48–2–2 to copper composite interlayer. (a) indicates copper-rich intermetallic (~20 at.% copper) occasionally observed in bond-line of 48–2–2 joints.

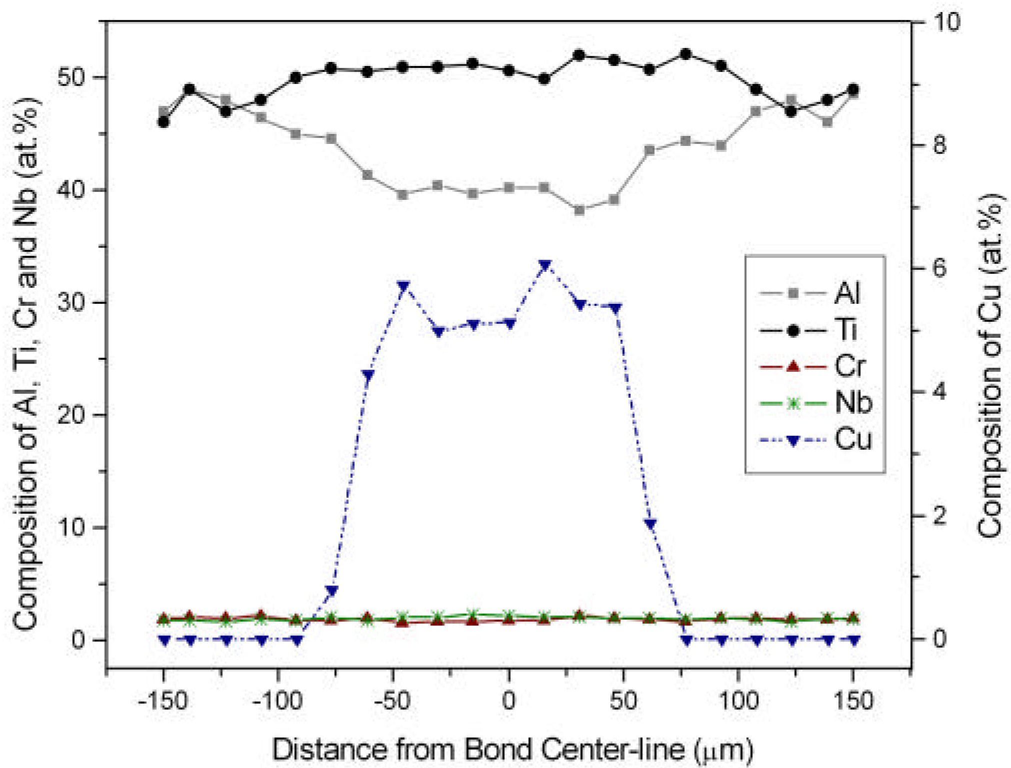


Figure 61−Composition profile across bond-line of an as-bonded 48−2−2 joint employing a 6:1 48−2−2 to copper interlayer ratio (joint width ~150 μm). Right side of graph refers to composition of copper across bond-line, and left side of the graph refers to the composition of aluminum, titanium, chromium and niobium detected by EDS analysis.

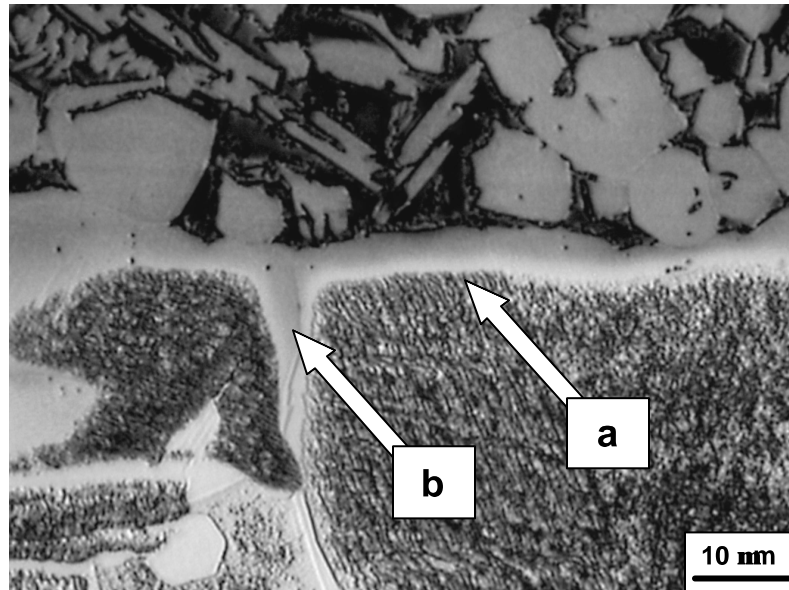


Figure 62−LM micrograph showing the bond-line/substrate interface of an as-bonded 48−2−2 joint employing a 6:1 48−2−2 to copper composite interlayer. Note (a) minimal epitaxial growth of substrates into bond-line (relative to GMPX bonds) and (b) dissolution of grain boundaries were observed.

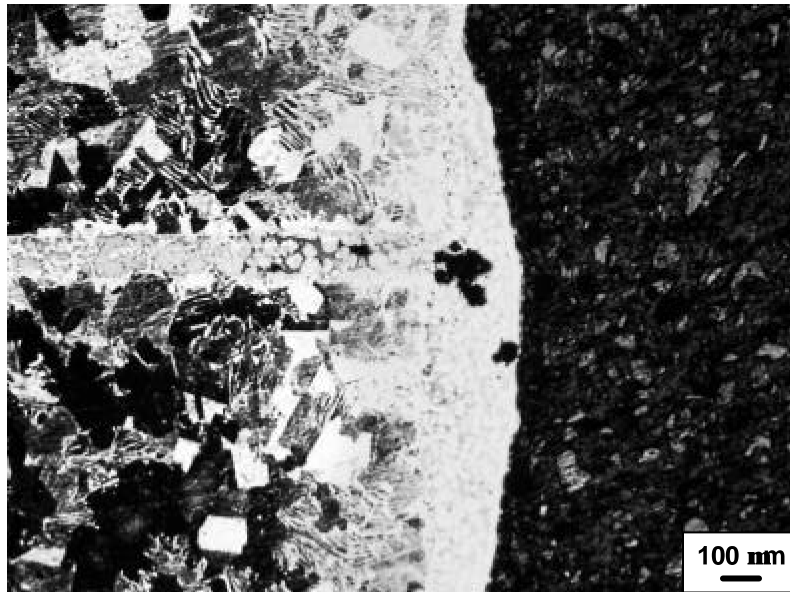


(a)

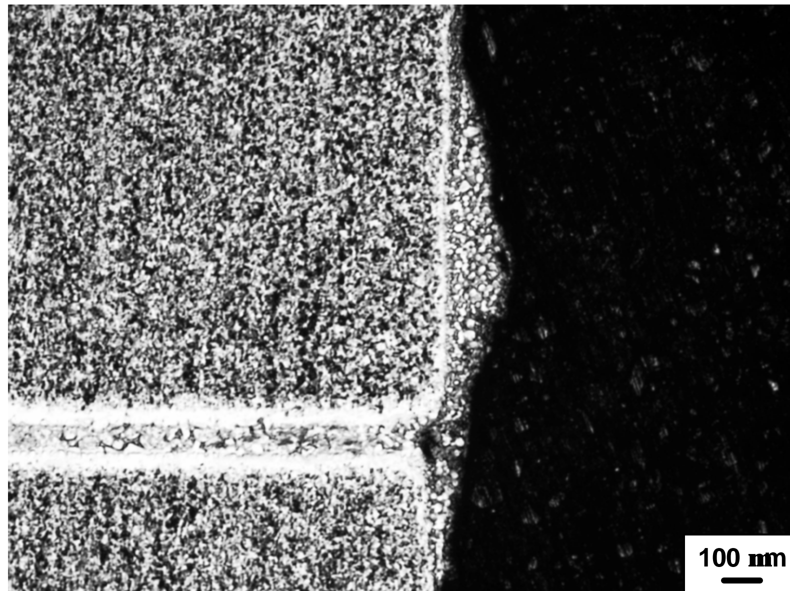


(b)

Figure 63−LM micrograph showing typical fillet produced in (a) 48−2−2 and (b) GMPX TLP bonds when employing a 6:1 TiAl alloy plus copper composite interlayer ratio. The copper concentration in the 48−2−2 fillets was determined to be ~11 at.% copper, whereas GMPX fillets had a copper concentration of ~15 at.% copper. Note the difference in cross-sectional area.

## 5.7 Mechanistic Studies

Conducting the empirical and phenomenological studies discussed in section 5.1 would determine the most suitable composite interlayer ratio and PBHT time for a given γ-TiAl alloy. However, γ-TiAl alloy compositions and microstructures are not yet fixed and will probably continue to evolve as intended application requirements and the capability of meeting these requirements are more clearly defined. Thus, understanding the influence of the joining mechanisms involved in TLP bonding could aid in reducing the test matrix for wide-gap TLP bonding of future γ-TiAl alloys. The basis on which the studied joining mechanisms were selected is discussed below.

As with any capillary joining process, success depends on the ability of the liquid metal or alloy to wet the component being joined so that the liquid readily spreads over the surfaces to be joined. Previous work has shown that copper offers good wettability of the 48–2–2 substrate surface (even in the presence of an oxide layer).[151-153] However, considering the differences in the GMPX and 48–2–2 bulk materials, as discussed in section 5.6.1, comparison studies of the wettability of copper on these substrates were conducted.

As discussed in section 2.7.5.1, the isothermal solidification and subsequent homogenization stages of TLP bonding rely on solid-state diffusion. Hence, the process times for these stages are governed by the diffusion rate of the constituents of the liquid former into the base metal. Knowledge of the copper diffusivity in GMPX and 48–2–2 at the bonding temperature and PBHT temperatures would provide an interesting comparison study. In addition, these data would aid in estimating the time necessary to complete the isothermal solidification and subsequent homogenization stages.

Although rapid kinetics may exist, diffusion could be limited by the solubility of the diffusing constituent in the base material. Although limited, there is some data on the solubility of copper in TiAl alloys.[149,150] However, existing data is not sufficient to provide an accurate comparison of copper solubility in the present systems. Thus, values for the copper solubility in GMPX and 48–2–2 at the bonding temperature were also determined experimentally.

The results of these detailed mechanistic studies and how these mechanisms might contribute to the observed microstructural and mechanical property differences in wide-gap TLP bonding of GMPX and 48–2–2 are discussed below.

### *5.7.1 Diffusion of Copper*

A considerable body of work has been conducted on the self-diffusion and impurity diffusion in the Ti-Al system,[170-178] however, no work was found on the diffusion of copper in the Ti-Al system. Thus, these data were determined experimentally. Diffusion coefficients of copper in GMPX and 48–2–2 (in the temperature regime of 850°C and 1450°C) were experimentally determined using a rough order of magnitude estimate, which can be expressed as:

$$x \sim \sqrt{Dt} \qquad [5]$$

where $x$ is the diffusing distance, $D$ the diffusion coefficient and $t$ is the diffusion time. A commercially pure 5 μm copper foil was placed between two substrates and heat treated at various temperatures for 2 hr in a tube furnace. The specimens were then analyzed by EDS to determine the diffusion distance of copper. Knowing the diffusion distance and time, the diffusivity at different temperatures was then estimated. In Figure

64, it can be seen that the temperature-dependent diffusion coefficients follow an Arrhenius relationship, which can be expressed as:

$$D = D_0 \exp\left(-\frac{Q}{RT}\right) \quad [6]$$

where $D_0$ is the pre-exponential diffusion coefficient, $Q$ is the activation energy, $R$ the universal gas constant and $T$ is the temperature in Kelvin. The activation energy of copper diffusion in 48–2–2 and GMPX was determined to be 185 and 179 kJ $mol^{-1}$ respectively. Considering these results, the diffusion coefficient of copper would not appear to account for the observed differences in 48–2–2 and GMPX TLP bonds.

It should be noted that the apparent activation energy of copper diffusion seems low if copper diffuses in TiAl as a substitutional element (typical values for substitutional or self diffusion range from 200 to 300 kJ $mol^{-1}$ [179]). However, Mishin and Herzig[178] discussed somewhat similar activation energy values for some transition elements, such as iron, cobalt and nickel in γ(TiAl), and suggested that this rapid diffusion could be explained by a combination of substitutional and interstitial mediated diffusion. Thus, the results obtained here for the copper diffusion coefficients in 48–2–2 and GMPX seem plausible. It should be noted that, given the non-planar interfaces observed between the bonds and substrates, accurately defining the starting position (i.e. $x = 0$) for copper diffusion was somewhat difficult and could have led to errors.

An Arrhenius plot was not produced for diffusion of copper in microstructures other than that present in the as-received condition. However, the diffusion coefficients of copper in the as-received, duplex and fully lamellar microstructures at the bonding

temperature were determined to be within the same order of magnitude – $10^{-13}$ $m^2$ $s^{-1}$. These data were determined using a method similar to the above, except the substrates were heat treated to produce the desired microstructure prior to bonding.

In addition to the diffusion of copper in the bulk materials, the diffusion of copper in the TiAl alloy bond-line powders should also be considered. Unlike the substrates, the TiAl alloy powder particles are not semi-infinite and will become saturated with copper at some finite time. Once saturated, they can play no further role in the bonding process. Knowledge of the time require for saturation could aid in determining an appropriate bonding time. As discussed above, the as-received Gamma Met and 48–2–2 powders consisted predominately of the $\alpha$(Ti)-Al solid solution phase, while the GMPX and 48–2–2 bulk materials consisted predominately of the $\gamma$(TiAl) with a small volume fraction of $\alpha_2$($Ti_3Al$). Considering the difference in phases present, there could be a difference in the diffusivity of copper in the substrates and powders (at least before the powder transforms to the $\gamma$(TiAl) + $\alpha_2$($Ti_3Al$) phases during the bonding cycle).

According to radiotracer measurements conducted by Mishin and Herzig,[178] the diffusion coefficients of some transition elements, such as iron, cobalt and nickel, in pure $\alpha$(Ti) at 860°C are approximately $10^{-12}$ $m^2$ $s^{-1}$. No data was found for copper diffusion in the $\alpha$(Ti)-Al solid solution within the temperature of interest, however, interdiffusion measurements by Kainuma and Inden,[177] suggest that the impurity diffusion coefficients show a tendency to increase at higher temperatures and with increasing aluminum content.

Detailed experiments to determine the diffusivity of copper in the Gamma Met and 48–2–2 powders at the bonding temperature were not conducted. However, copper was detected, by EDS analysis, at the center of particles with a radius of ~10 μm after approximately 2 minutes at $T_B$. Thus, using a rough order of magnitude estimate, as done in Equation 5, it was determined that the copper diffusivity could be between $10^{-12}$ to $10^{-13}$ $m^2$ $s^{-1}$.

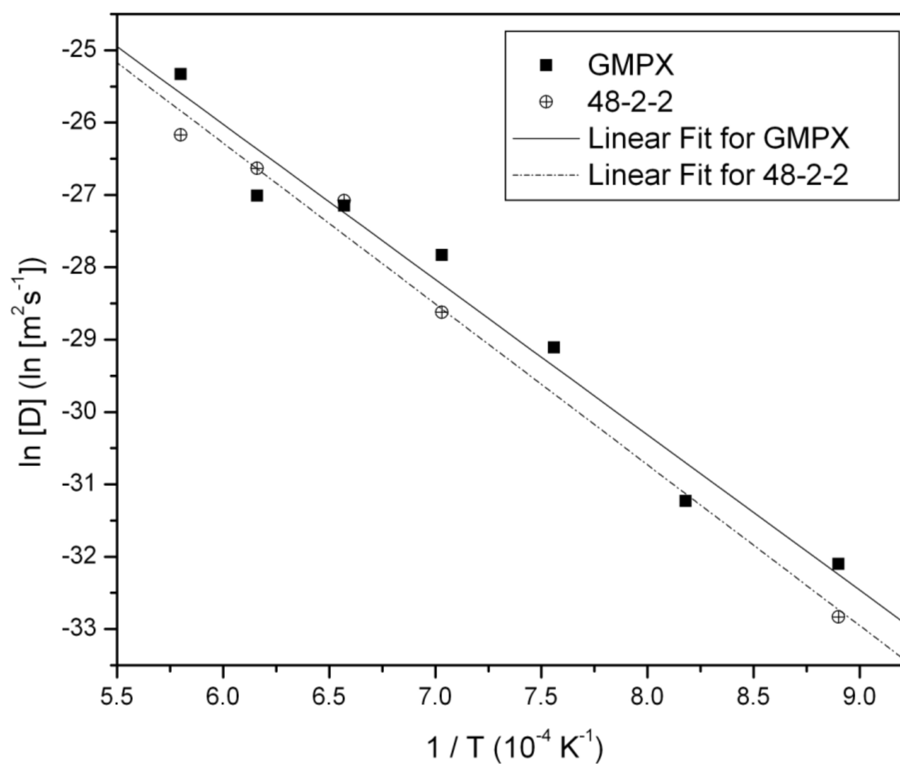


| | **GMPX** | **48-2-2** |
|---|---|---|
| **Q (kJ mol$^{-1}$)** | 179 | 185 |
| **$D_0$ (m$^2$ s$^{-1}$)** | 2.0 x10$^{-6}$ | 2.4 x10$^{-6}$ |

Figure 64−Arrhenius plot for diffusion of copper in GMPX and 48−2−2 as-received substrates and corresponding values for Q and $D_0$.

### *5.7.2 Copper Solubility*

In modeling of wide-gap TLP bonding of 48–2–2 materials, Zhou and Gale[180] suggested that the 48–2–2 powder particles were rapidly saturated with copper. Thus, most (~94%) of the copper originally placed in the joint must diffuse into the substrates during the remainder of the isothermal solidification and subsequent homogenization stages. Assuming this model is valid with Gamma Met in GMPX bonds, one possible explanation of the observed differences in 48–2–2 and GMPX TLP bonds is that the copper solubility in the GMPX substrates is much lower than in 48–2–2. Hence copper not absorbed by the bond-line powder particles or the substrate material, could result in the formation of copper-rich bond-line intermetallics. Thus, experiments to approximate the copper solubility in GMPX were conducted. These experiments were similar to Dang's[149] copper solubility in 48–2–2 studies.

Alloys containing 0.5, 1.0, 1.5 and 2.0 at.% copper were prepared in a vacuum arc melter with a copper crucible, which was backfilled will argon to a pressure of 500 torr. The samples were then homogenized in a 1.3 mPa vacuum atmosphere for 100 hr at $T_B$ followed by water quenching. Because melting caused microstructural and possible compositional changes, a GMPX sample with no copper addition was processed in the same manner as the alloys containing copper. EDS analysis of the melted and homogenized samples compared quite well to the intended compositions.

The alloy with 0 at.% copper consisted of a duplex microstructure of $\gamma$(TiAl) grains and lamellar colonies of alternating $\gamma$(TiAl) and $\alpha_2$($Ti_3Al$) platelets after remelting (Figure 65a). The sample with 0.5 at.% copper after remelting also has a duplex microstructure (Figure 65b). However, the sample containing 1.0 at.% copper has a

significantly different morphology and large copper-rich precipitates begin to appear (Figure 65c). Likewise, the samples with 1.5 at.% copper, shown in Figure 65d, and 2.0 at.% copper also have significantly different morphologies and the number of copper-rich precipitates observed increases with copper content. This suggests that the copper solubility in GMPX at the bonding temperature is less than 1 at.% copper, whereas the findings of Dang suggested the copper solubility in 48−2−2 at the bonding temperature was slightly less than 2 at.% copper.[149] The solubility tests were repeated for 48−2−2, by the present author, and the results were found to correlate well with Dang's findings.

The exact reason for this determined difference in solubility of copper in the GMPX and 48−2−2 materials is not well understood, but could be attributed to a difference in phases present in the bulk substrates. As discussed above, XRD analysis suggested the as-received GMPX had a higher volume fraction of $\alpha_2(Ti_3Al)$ than the as-received 48−2−2 materials. The Ti-Al-Cu ternary phase diagram[150] shown in Figure 66 suggests that copper has a lower solubility in $\alpha_2(Ti_3Al)$ than $\gamma(TiAl)$ at 800°C (an isotherm at the bonding temperature could not be found in the literature). Thus, the greater presence of the $\alpha_2(Ti_3Al)$ phase in the as-received GMPX substrates could account for the lower copper solubility. It should be noted however, that the system is not ternary, thus solubilities could be affected by other alloying elements.

The lower solubility of copper in the GMPX substrates could account for some of the differences observed in GMPX as-bonded and as-PBHT specimens. These differences include numerous copper-rich intermetallics, higher copper content in bond-line, and the need for protracted post-bond heat-treatments for GMPX when compared with 48−2−2.

Like the diffusivity studies, the solubility of copper in the TiAl alloy bond-line powder is of equal importance. Considering the difference in phases present in the TiAl substrates and powders, the copper solubility in these materials are not necessarily the same. In fact, EDS analysis of the copper saturated GMPX and 48–2–2 powders in TLP bonds detected a copper concentration of ~3 at.% copper at the bonding temperature for both alloys. Thus, for the modeling work discussed in section 5.8, it is assumed that the solubility of copper in the 48–2–2 and Gamma Met powders is 3 at.% copper.

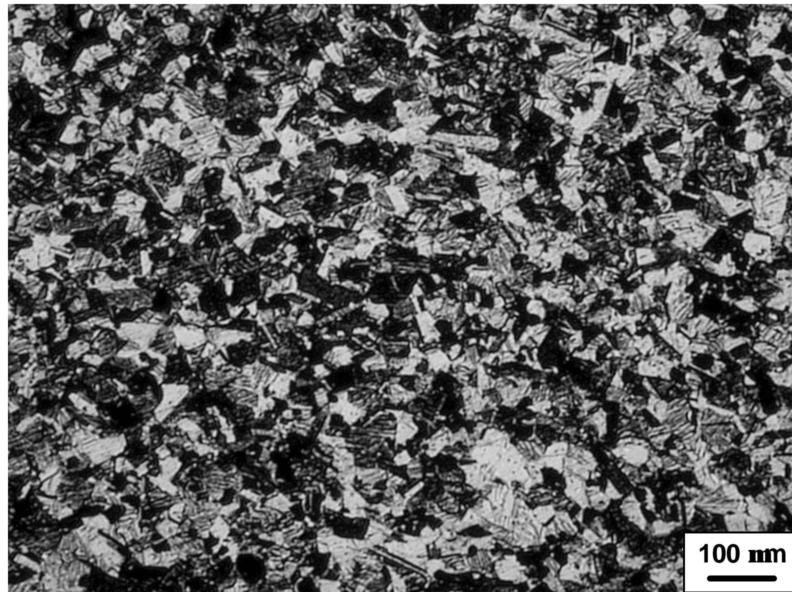


(a)

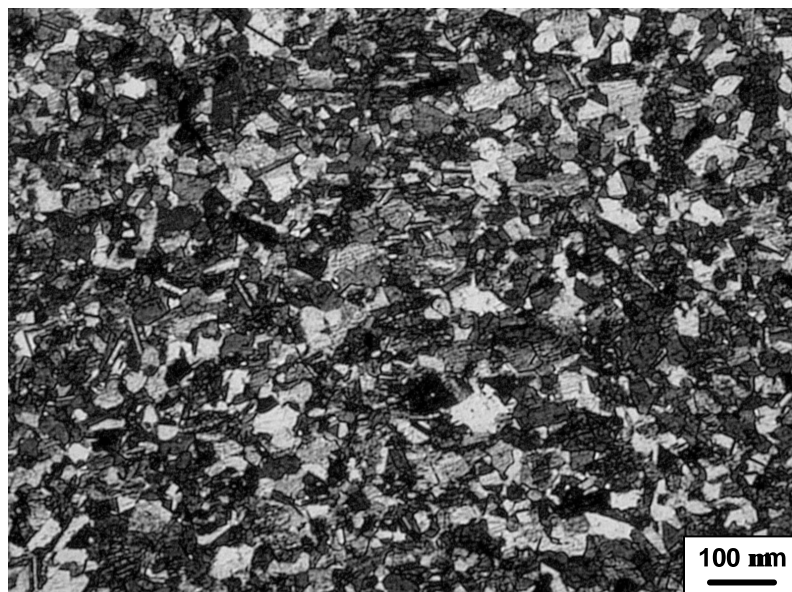


(b)

Figure 65−LM micrographs of (a) as-received GMPX after melting without copper addition and (b) GMPX with 0.5 at.% copper.

(c)

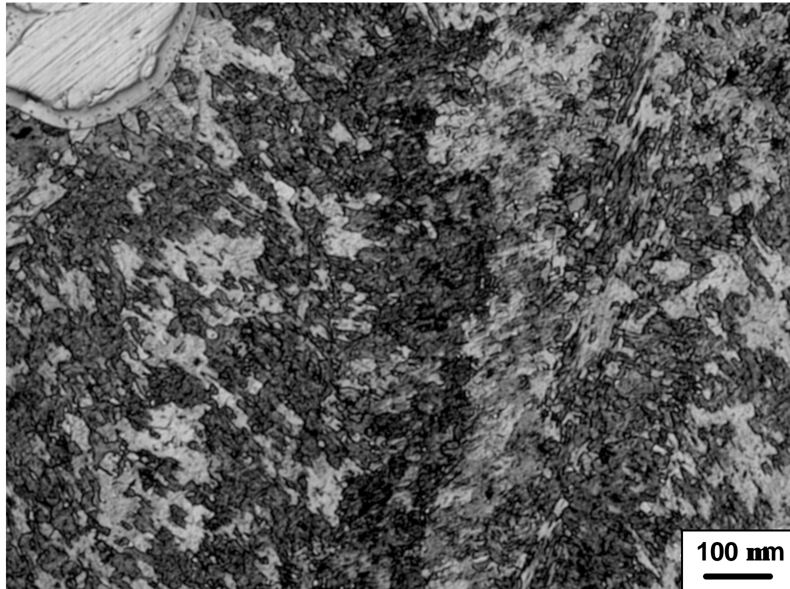


(d)

Figure 65 (continued)–LM micrographs of (c) GMPX with 1.0 at.% copper and (d) GMPX with 1.5 at.% copper.

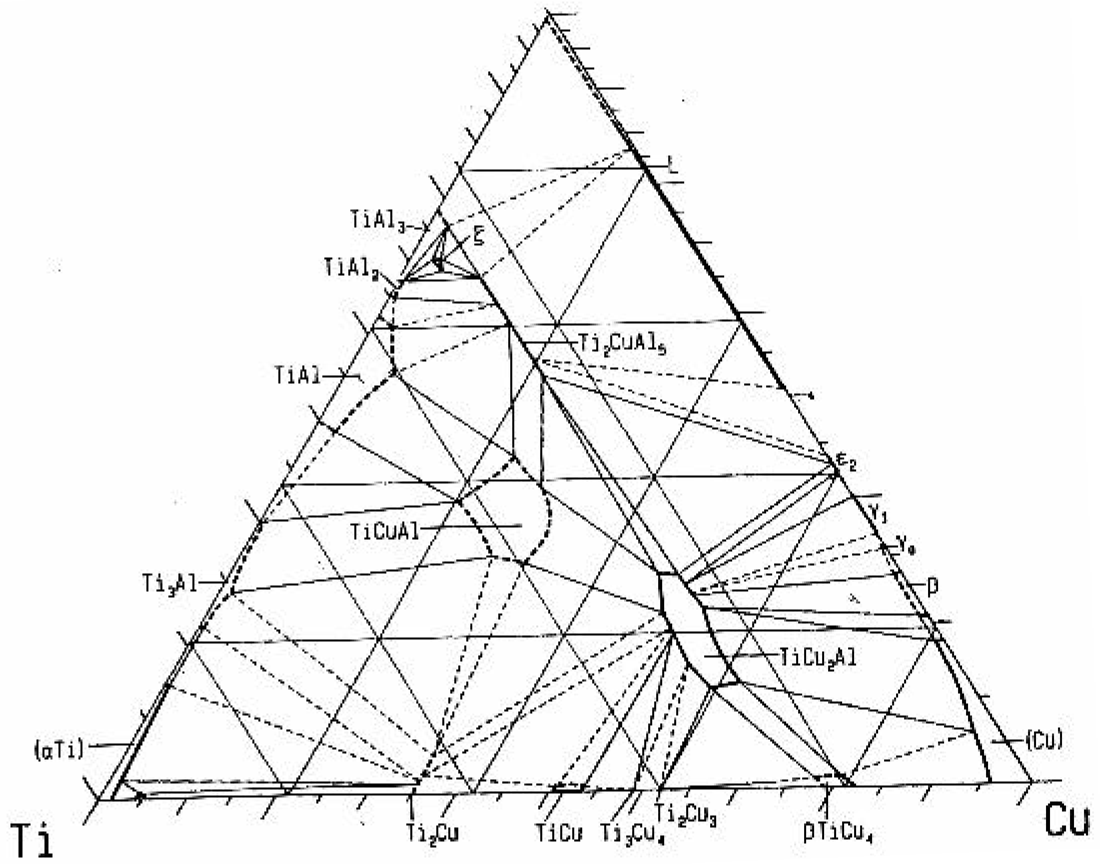


Figure 66–Ternary Ti-Al-Cu phase diagram at 800°C.[150]

### 5.7.3 *Wettability (Spreading) of Liquid Copper*[12]

Wettability testing of GMPX and 48−2−2 by liquid copper was conducted via the sessile drop method. These wettability studies were conducted in a fashion similar to those previously performed by Gale *et al.*[151] on 48−2−2 materials. Micrographs of the liquid droplet on 48−2−2 and GMPX substrates at various time intervals are shown in Figure 67. The displacement of the solid-liquid interface as a function of holding time can be seen in Figure 68. Although the initial spreading rates of liquid copper on 48−2−2 and GMPX were quite similar, the terminal spreading distance of the liquid on the two substrates appeared significantly different. Isothermal solidification of the spreading front on GMPX occurred very quickly while the spreading on 48−2−2 continued out of the field of view of the Leitz microscope. Therefore, sessile drop tests to measure the terminal spreading distance of the liquid on GMPX and 48−2−2 were conducted (Figure 69). These experiments were performed in a Linberg single zone tube furnace for 2 hr at $T_B$. The resulting average terminal spreading diameter of copper droplets on GMPX and 48−2−2 substrates was approximately 4.0 mm and 4.9 mm respectively.

EDS analysis of the sessile droplets from the HSLM are shown in Figure 70. The copper concentration in the droplets on 48−2−2 and GMPX substrates were approximately equal (~58 at.% copper). The concentration of the remaining elements reflected the composition of the substrates. For example, the droplets on 48−2−2 substrates contained a higher concentration of chromium and a lower concentration of

[12] It should be noted that "wettability" and "spreading" are used synonymously and are treated in the present work as a measure of the liquid's ability to spread.

niobium compared to the GMPX droplets. In fact, the composition of 48−2−2 contains more chromium and less niobium than GMPX.

Determining the exact reason for the observed difference in terminal spreading distance could prove to be problematic. However, the difference could be attributed to alloying between the liquid and the substrates. The relationship between alloying and spreading can be divided into 1) promotion of spreading due to alloying and 2) termination of spreading due to alloying.

Klein-Wassink[181] determined that a relation exists between increased mutual solubility of alloying elements in the base metal and enhanced wetting properties. Thus wetting can be improved by adding a relatively small amount of a suitable element to the base metal. Chromium is the only major alloying element present in 48−2−2 that is not present in GMPX. The binary Cr-Cu phase diagram[182], shown in Figure 71, shows that ~3 at.% chromium is soluble in liquid copper at $T_B$.

In contrast, Ambrose *et al.*[183] observed termination of spreading due to alloying. Compositional changes in the liquid copper droplet could increase the melting point of the droplet such that spreading is terminated by premature solidification during isothermal holding. The greater concentration of the high melting point material, niobium, in the GMPX sessile droplets could account for the smaller spreading distance than 48−2−2 sessile droplets. It should be noted that these possible explanations are very speculative and can only be verified by detailed studies.

Initially it was thought that the difference in fillet size for 48−2−2 and GMPX bonds was directly related to the difference in spreading results discussed above.

However, results of experiments to determine the liquidus composition in 48−2−2 and GMPX bonds, see section 5.7.4, suggested that liquid copper could dissolve more 48−2−2 material than GMPX/Gamma Met. Dissolution of a greater amount of the solid phase would produce more liquid, and could result in a larger terminal spreading distance and larger fillets. Thus, the difference in fillet size could be indirectly related to the difference in terminal spreading distance.

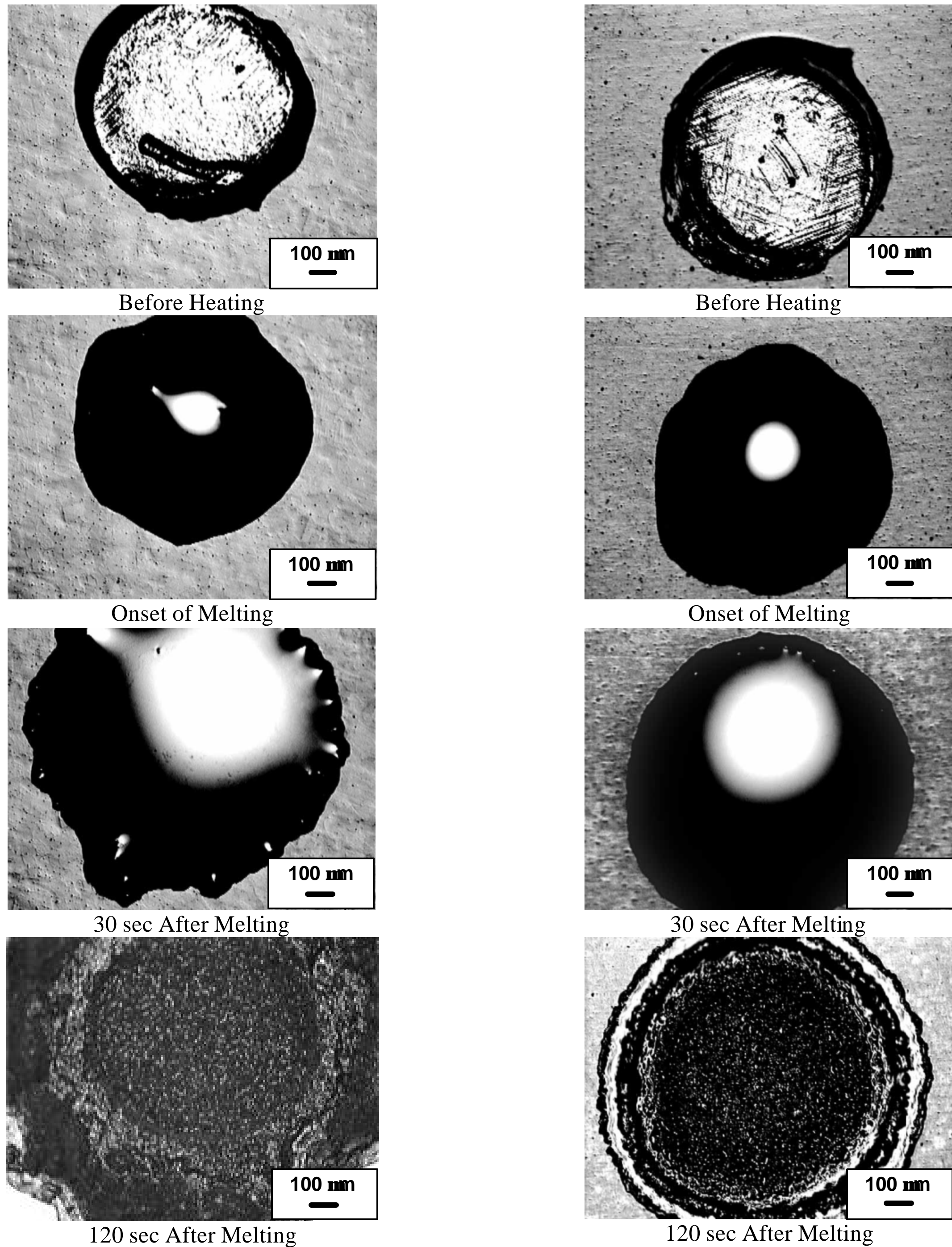


Figure 67−HSLM images of sessile copper droplets on 48−2−2 (left column) and GMPX (right column) substrates (at a nominal temperature of $T_B$). Initial spreading rate of droplet on both substrates appear similar. At approximately 30 sec after melting, spreading of the droplet on GMPX ceases due to isothermal solidification of the spreading front. The droplet on 48−2−2 continues to spread until isothermal solidification occurs at approximately 120 sec after melting. Note the spreading front of the droplet on the 48−2−2 substrate has traveled out of the microscope's field of view.

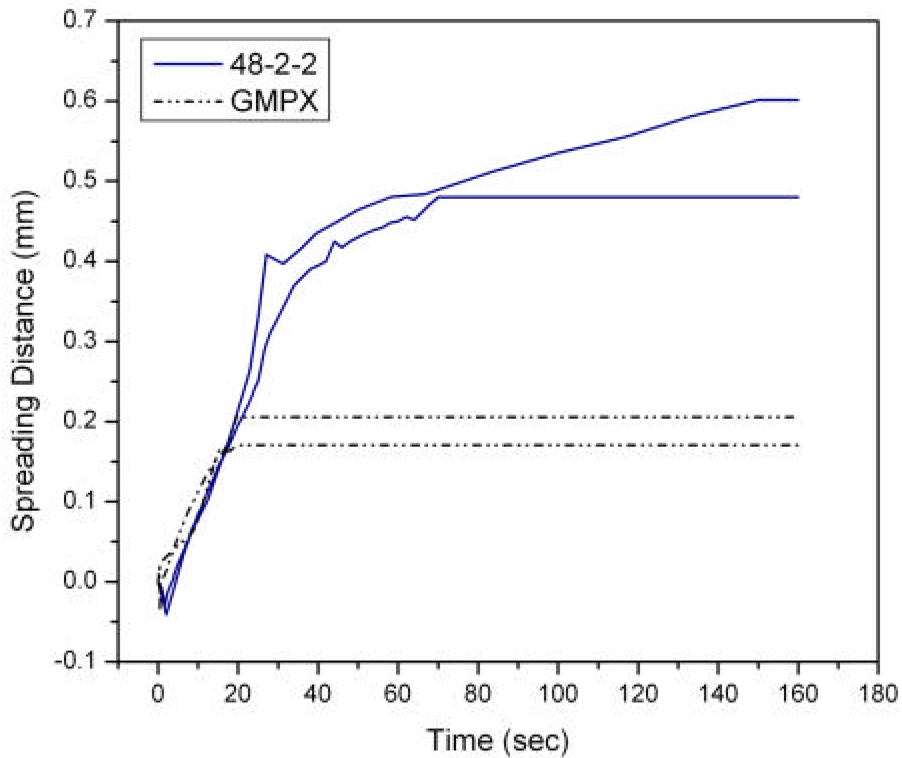


(a)

Figure 68−Spreading data for liquid copper on GMPX and 48−2−2 (two runs for each substrate material), with a nominal set point of $T_B$ and zero time defined as melting of copper foil. The decrease in diameter of the droplet a few seconds after melting is due to an initial dewetting stage before the onset of spreading. The undulations apparent in the data (see Figure 68b for greater detail) are associated with the flow of the liquid over a "dam" of solid produced by the onset of isothermal solidification at the spreading front.

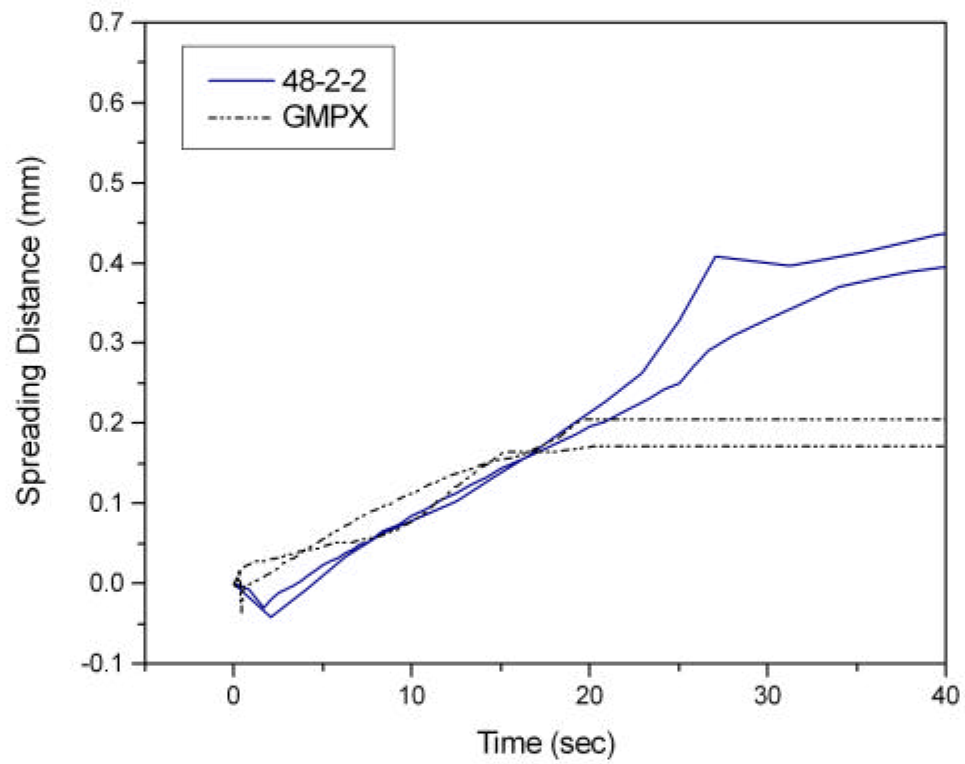


(b)

Figure 68 (continued)–Spreading data for liquid copper on GMPX and 48–2–2 substrates for the first 40 sec of spreading.

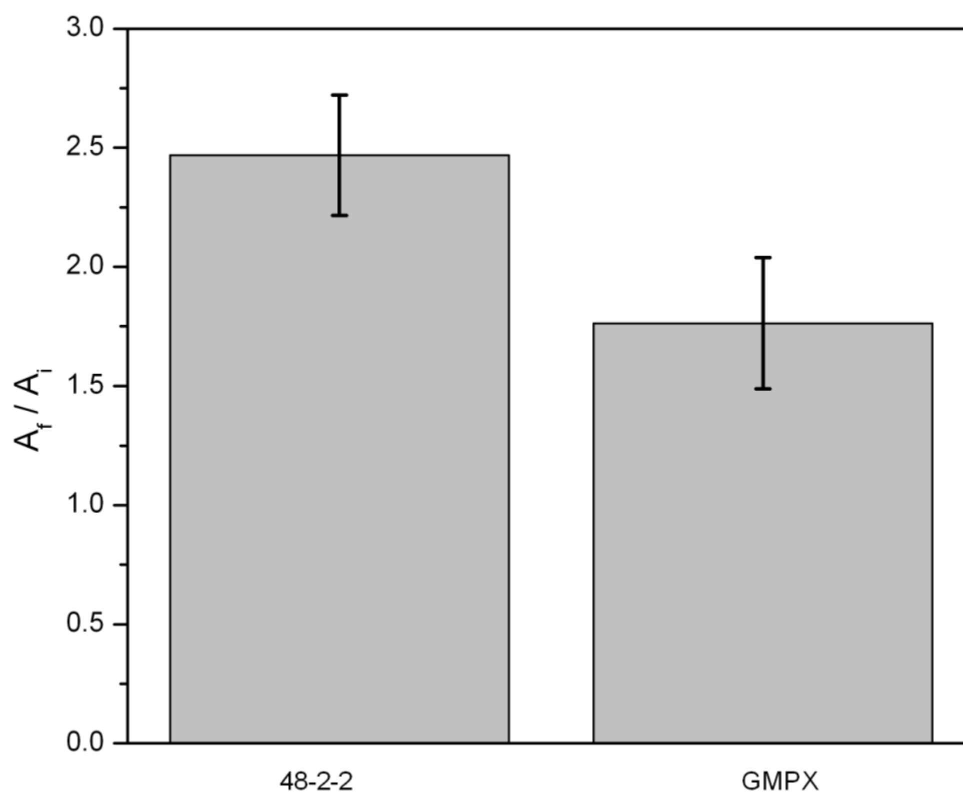


Figure 69−Terminal spreading distance of sessile droplets on 48−2−2 and GMPX substrates given by $A_f \setminus A_i$, where $A_f$ = final area of droplets and $A_i$ = initial area of droplet.

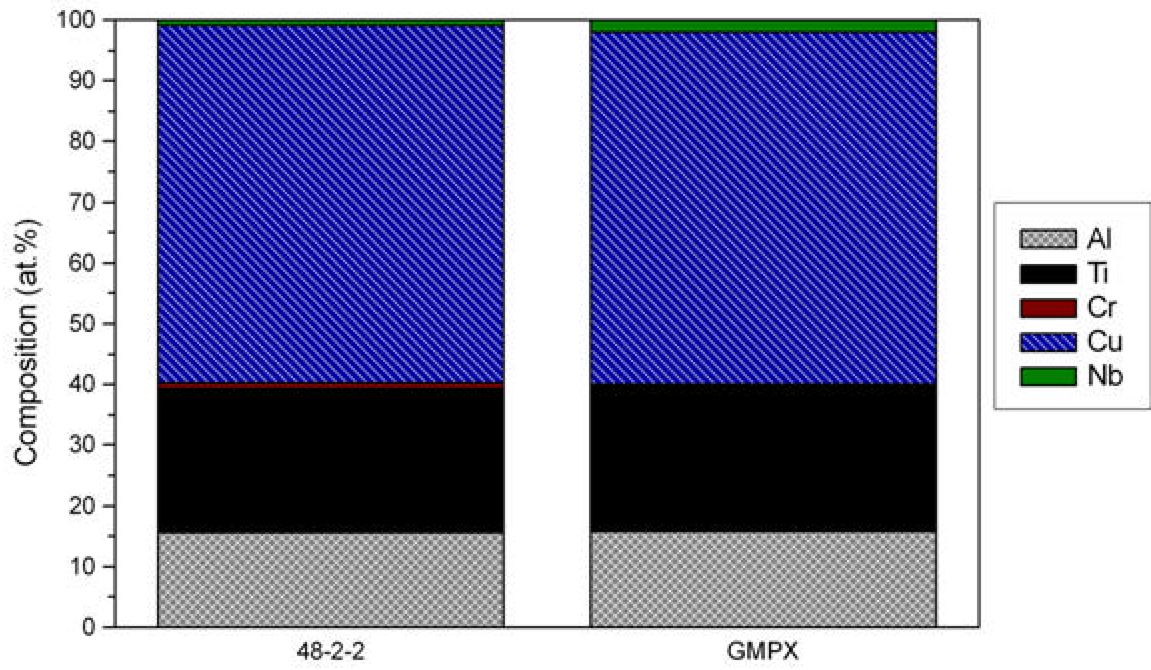


Figure 70–Composition of HSLM sessile droplets on 48–2–2 and GMPX substrates.

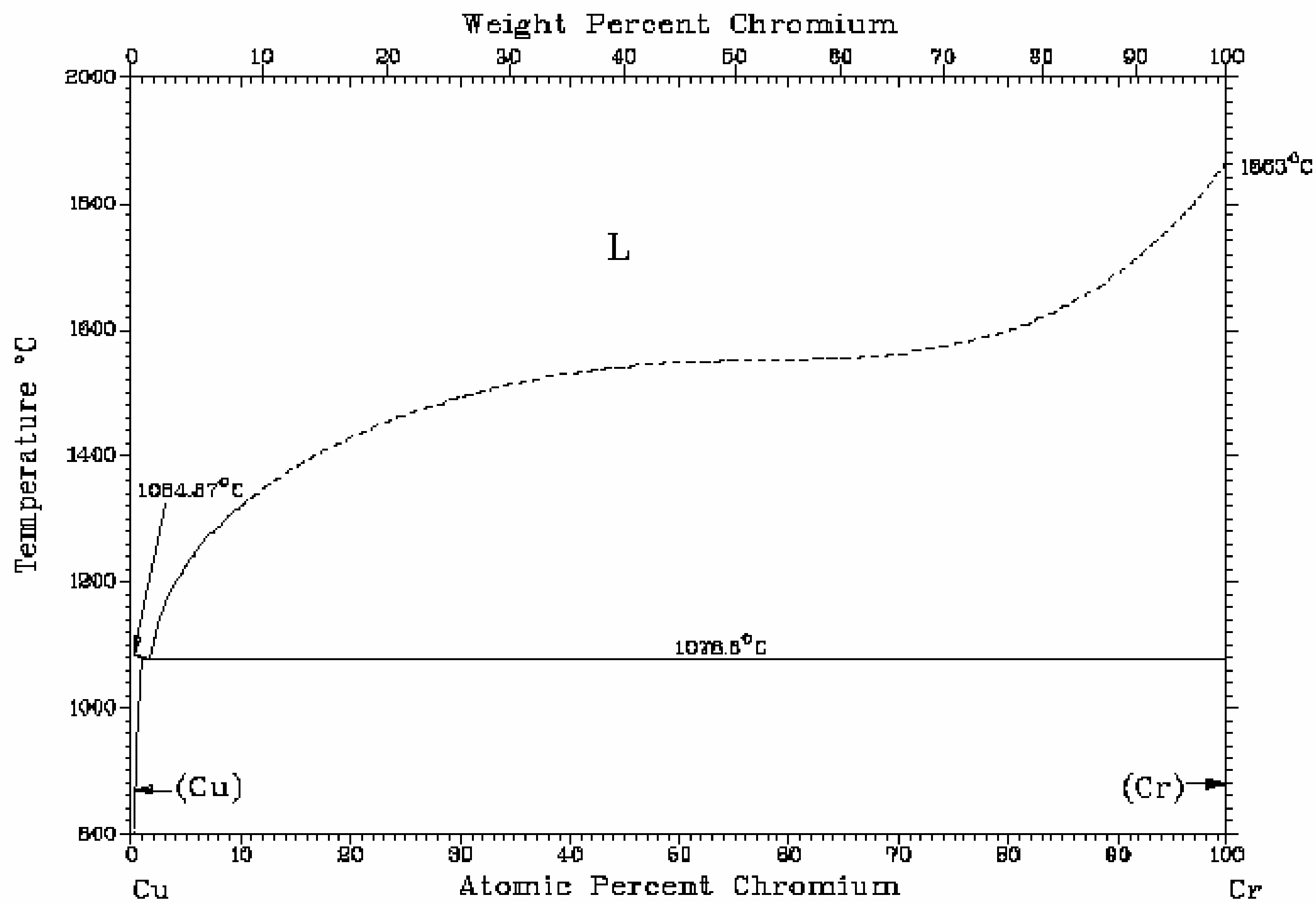


Figure 71–Cu-Cr binary phase diagram.[182]

### 5.7.4 *Dissolution*

The dissolution stage was not studied in detail, however, experiments to determine the liquidus ($C_{Liq}$) and solidus ($C_{Sol}$) compositions in 48–2–2 and GMPX bonds were conducted as a matter of comparison. Knowledge of these values is beneficial as they determine the amount of base material the solute must dissolve ($C_{Liq}$) and the amount of solute the base material must accept ($C_{Sol}$) in order to achieve local equilibrium between the solid and liquid phases. These values are also needed for modeling work discussed in section 5.8. The dissolution process is discussed in detail in section 2.7.5.1.

These experiments were conducted in a fashion similar to those done by Zhou[29] in his 48–2–2 studies. A GMPX bond employing a 6:1 Gamma Met plus copper interlayer ratio was thermally cycled for 0 min at $T_B$ (i.e. ramped to the bonding temperature and then immediately cooled). EDS analysis of the resolidified liquid and the edge of the solid phases were determined to have an average copper concentration of 29 at.% ($C_{Liq}$) and 3 at.% ($C_{Sol}$) respectively. Experiments were repeated for 48–2–2 bonds employing a 6:1 48–2–2 plus copper interlayer. The results for 48–2–2 bonds were identical to those determined by Zhou, which were 22 at.% copper for $C_{Liq}$ and 3 at.% copper for $C_{Sol}$.

These results reveal yet another difference in the GMPX and 48–2–2 systems. The lower $C_{Liq}$ determined for 48–2–2 bonds suggests that the liquid copper is able to dissolve more of the TiAl powders in the bond-line of 48–2–2 joints than the TiAl powders in the bond-line of GMPX joints. Since the bond-line powders have a much higher surface area than the substrates, it is assumed that only the bond-line TiAl

powders are dissolved. This result could explain some of the observed differences in GMPX and 48−2−2 bonds. The ability to dissolve more of the solid phase would produce a greater amount of liquid. This greater amount of liquid could result in more liquid extruded from the joint cavity, and hence the production of larger fillets, as was observed in 48−2−2 bonds.

### *5.7.5 Contribution of Other Observations*

The origin of some observations, such as preferred dissolution of some 48–2–2 grain boundaries and greater epitaxial growth of GMPX substrates, is not well understood, but could help explain some of the observed differences in GMPX and 48–2–2 wide-gap TLP bonds. As previously mentioned, dissolution of some grain boundaries by liquid copper was observed in 48–2–2 bonds, but not in GMPX bonds. This grain boundary penetration significantly increases the surface area over which diffusion of copper into the substrates can occur, and hence expedites removal of copper from the bond-line. Thermodynamically, the penetration of liquid into the grain boundary is favored only when the following equation results in a negative Δγ.

$$\Delta \boldsymbol{g} = 2\boldsymbol{g}_{ls} - \boldsymbol{g}_{gb} \qquad [7]$$

Here, $\boldsymbol{g}_{gb}$ is the TiAl grain boundary interfacial energy and $\boldsymbol{g}_{ls}$ is the $Solid_{TiAl} - Liquid_{Cu}$ interfacial energy. Since grain boundary penetration was not observed in GMPX bonds, there could be a difference in $\boldsymbol{g}_{ls}$ for copper on GMPX and 48–2–2 substrates. However, this difference cannot be determined without a carefully study of $\boldsymbol{g}_{ls}$ for GMPX and 48–2–2 substrates. There could also be a difference in $\boldsymbol{g}_{gb}$ for GMPX and 48–2–2, which could be attributed to the different processing routes for the two alloys. High angle grain boundaries (high interfacial energy) are dissolved more readily than low angle grain boundaries (low interfacial energy) during TLP bonding.[184] In the as-cast 48–2–2 alloy, the nucleation and growth of grains with random orientation could result in the infrequent occurrence of low angle grain boundaries. Conversely, texturing (i.e. non-random grain boundary orientation) due to the extrusion process in the GMPX alloy

could lead to the frequent occurrence of low angle grain boundaries. Although the latter does offer a possible explanation of the observed difference in dissolution behavior for the two alloys, determining the exact cause could prove to be problematic.

Fractographic investigations by Zhou[29] and the present author, of 48–2–2 and GMPX wide-gap TLP bonds respectively, determined that failure typically occurred in the vicinity of epitaxial substrate growth into the bond-line. Thus, it is reasonable to assume that the size of these grains could contribute to the observed mechanical property differences in 48–2–2 and GMPX bonds. The degree of epitaxial grain growth could be directly related to the time required for isothermal solidification. For example, a rapid isothermal solidification time would result in minimal epitaxial grain growth, whereas a protracted isothermal solidification time would allow for significant epitaxial grain growth. However, HSLM investigations suggested that the time require for isothermal solidification of copper droplets on 48–2–2 substrates was significantly longer than the time required for isothermal solidification of copper droplets on GMPX substrates.

### *5.7.6 Summary of Mechanistic Studies*

As mentioned above, the purpose of conducting these mechanistic studies was to aid in understanding the origins of the observed differences between GMPX and 48–2–2 wide gap TLP bonds. The studies conducted were not inclusive of all the mechanisms associated with TLP bonding and not all the observed differences could be explained. Additional studies that could be conducted to gain a better understanding of the observed differences between GMPX and 48–2–2 wide gap TLP bonds are discussed in section 7. In an effort to summarize the results of the mechanistic studies presented in this work, and how these mechanisms might contribute to the observed microstructural and

mechanical property differences, refer to the flow chart in Figure 72. As can be seen from the flow chart, more than one mechanism may contribute to the observed differences.

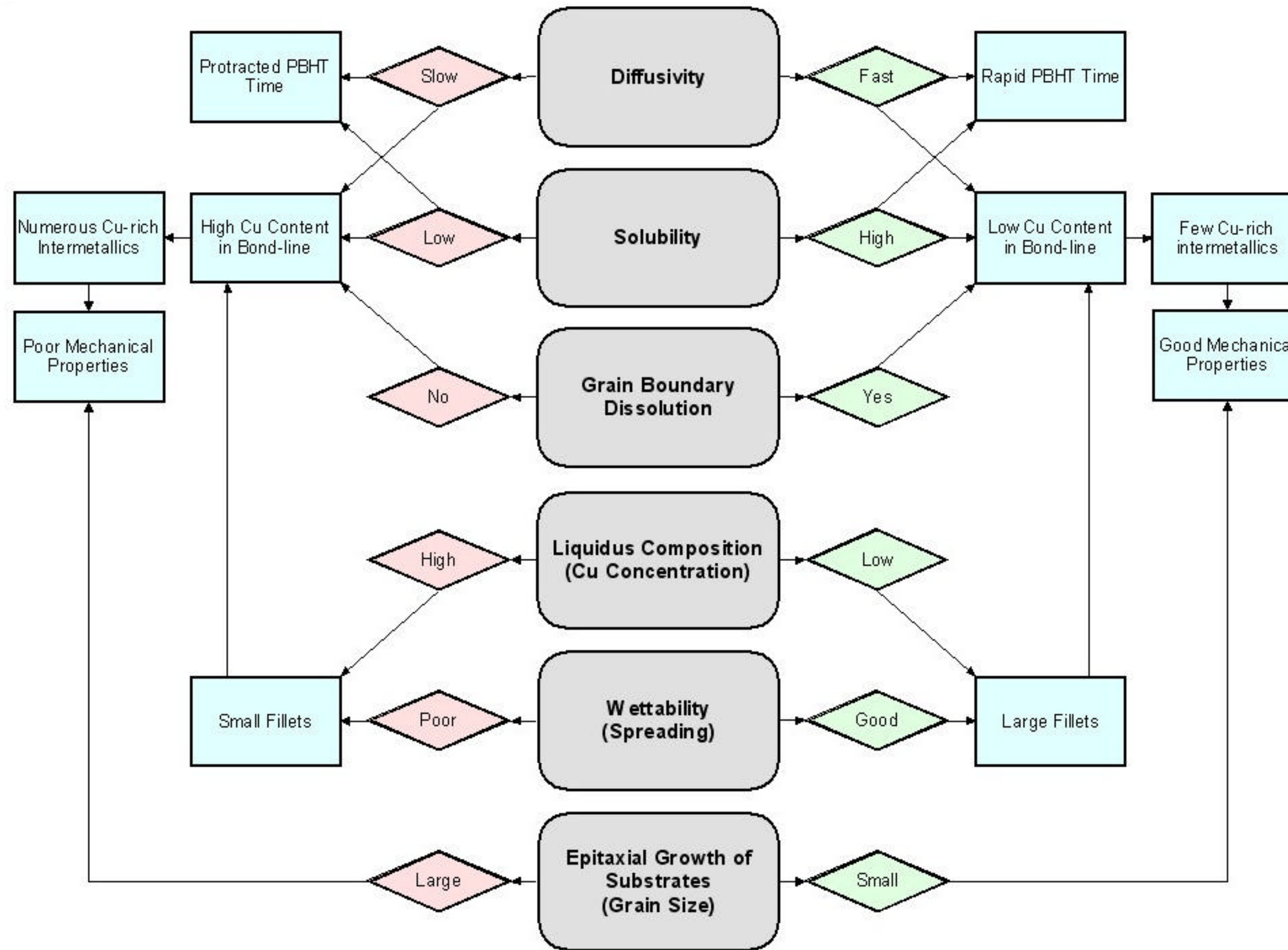


Figure 72–Flow chart summarizing the results of the mechanistic studies and how these mechanisms might contribute to the observed microstructural and mechanical property differences observed in 48–2–2 and GMPX bonds.

## 5.8 Modeling of Wide-gap TLP Bonding for 48-2-2 and GMPX Alloys

Zhou[29,180] identified the need for and produced a model for wide-gap TLP bonding using a composite interlayer. This model focused on wide gap TLP bonding of 48–2–2 using a 48–2–2 plus copper composite interlayer. In particular, the role of 48–2–2 powder particles in the composite interlayer during the isothermal solidification process was studied. During the isothermal solidification stage, there were two issues regarding the 48–2–2 powder particles at the bond-line. Firstly, the semi-infinite 48–2–2 particles could become saturated with copper after some time at the bonding temperature and then play no further part in the bonding process. Thus, Zhou attempted to estimate the time at which the 48–2–2 particles would become saturated with copper. Secondly, any copper absorbed by the 48–2–2 powder particles during the bonding process would result in less copper for the substrates to absorb during the homogenization stage. Thus, Zhou also attempted to estimate how much copper would be absorbed by the 48–2–2 particles during the bonding process. The importance of the latter issue was to determine whether the role of the 48–2–2 particles was a diffusion sink for copper or simply to reduce the amount of copper needed to fill the joint gap. Although Zhou estimated the amount of copper that must be absorbed by the substrates during the homogenization stage, the time required to complete this process was not estimated.

Due to unknown parameters at the time, Zhou was forced to make numerous assumptions. Although most of the assumptions made by Zhou were required to maintain a simplistic model, a few of the assumptions, such as those listed below, could significantly affect the accuracy of the model.

- The diffusion coefficient of copper, $D_{Cu}$, in 48–2–2 powder particles is equal to $D_{Cu}$ in 48–2–2 substrates.
- Copper solubility in 48–2–2 powder particles is equal to the copper solubility in 48–2–2 substrates.
- Thickness of as-deposited composite interlayer is 100 μm.
- There is no extrusion of liquid from the joint cavity.

The present author has addressed some of the above assumptions and incorporated more accurate data into Zhou's model for wide-gap TLP bonding of 48–2–2. In addition, modeling work which estimates the time required for completion of the homogenization stage has been conducted. The results of this model are discussed below. This model has also been extended to wide-gap TLP bonding of GMPX. The results of this model and a comparison to the results of the 48–2–2 modeling work are also discussed below.

### *5.8.1 Modeling on Wide-Gap TLP Bonding of 48-2-2*

Similar to other modeling work on TLP bonding, the process is divided into sequential stages of dissolution, isothermal solidification and homogenization.

#### *5.8.1.1 The Dissolution Stage*

As mentioned in section 5.7.4, experiments to determine the liquidus ($C_{Liq}$) and solidus ($C_{Sol}$) composition were conducted. The assumptions of this modeling stage are as follows:

- Considering the 48–2–2 powder particles in the bond-line have a much higher surface area than that of the substrates, it is assumed that only the powders are dissolved by liquid copper.

- The thickness of the as-deposited interlayer equal 250 μm. This value is more accurate than the 100 μm thickness assumed by Zhou.[13]

- The weight ratio of 48–2–2 to copper powders is 6:1 and the corresponding volume ratio is 7:1. Thus the total weight of copper per unit area is 161 g $m^{-2}$ and the weight of 48–2–2 is 965 g $m^{-2}$.

- $C_{Liq}$ is 22 at.% copper (~32 wt.% copper) and $C_{Sol}$ is 3 at.% copper (~4 wt.% copper).

Since $C_{Liq}$ and the weight of copper per unit area are known, the total amount of 48–2–2 powder particles dissolved by liquid copper was determined to be 349 g $m^{-2}$. Thus, the liquid copper will dissolve approximately 36% of the 48–2–2 powders originally placed in the joint and about 616 g $m^{-2}$ remain.

During the dissolution process, any copper-rich liquid extruded from the joint cavity would result in less copper that must diffuse into the substrates during the homogenization. As a result, the time required for completion of the homogenization process could be reduced. See section 5.8.1.3 for further discussion of fillets produced in 48–2–2 bonds.

---

[13] The thickness of the as-deposited interlayer ranged from 250-500 μm in both Zhou's[29,180] work and the work presented here. For unknown reasons, Zhou employed a value of 100 μm for the thickness of the as-deposited interlayer in his modeling work.

#### *5.8.1.2 The Isothermal Solidification Stage*

As mentioned above, Zhou attempted to estimate the time at which the 48−2−2 particles would become saturated with copper. Since no data for the diffusion coefficient of copper in γ-TiAl alloys could be found, Zhou began by using an experimental method to determine the apparent diffusion coefficient of copper in 48−2−2. Zhou also modeled the diffusion of copper in 48−2−2 substrates using data from similar systems.[29,180] This was done by using a standard model for grain boundary and bulk diffusion modified for the diffusion of copper in 48−2−2 alloys with a lamellar $\gamma + \alpha_2$ microstructure. The results obtained from the model were quite similar to the experimentally determined $D_{Cu}$ in the 48−2−2 substrate material. It should be reiterated that Zhou assumed $D_{Cu}$ in the 48−2−2 powders to be the same as the experimentally determined $D_{Cu}$ value in the 48−2−2 substrate material. However, these values are not necessarily equal (due to differences in microstructure, grain size, and phases present) and could lead to inaccurate results when estimating the time required for the 48−2−2 powders to become saturated with copper.

Once $D_{Cu}$ in the 48−2−2 substrates was determined, an investigation into the time necessary for saturation of the 48−2−2 particles with copper was conducted. Considering the high interfacial area of 48−2−2 powders compared to the substrates, Zhou assumed diffusion of copper only occurs in the powder particles. Also, unlike the substrates, the powder particles are not semi-infinite and will become saturated with copper after some finite time. To determine the saturation time for the 48−2−2 particles, Zhou used a

model, described by Crank,[185] for concentration distribution in a sphere. The details of this model will now be discussed.

For the cases in which the diffusion is radial, the equation for a constant diffusion coefficient can be expressed as:

$$\frac{\partial C}{\partial t} = D\left(\frac{\partial^2 C}{\partial r^2} + \frac{2}{r}\frac{\partial C}{\partial r}\right) \qquad [8]$$

where $C$ is the concentration of the diffusing substance, $D$ the diffusion coefficient, $r$ is the diffusing distance (radius of sphere), and $t$ is the diffusion time. By assuming $u = C * r$, Equation 8 becomes:

$$\frac{\partial u}{\partial t} = D\frac{\partial^2 u}{\partial r^2} \qquad [9]$$

Since this is the equation is similar to Fick's second law for non-steady state diffusion in one dimension, the solution for the radial diffusion in a sphere can be reduced to a simple linear problem.

For the diffusion of copper, in the liquid phase, into the 48–2–2 sphere particles, it is assumed that the concentration $C_S$ at the surface of the sphere is constant (Figure 73). The boundary conditions for Equation 9 are as follows:

$$\begin{aligned} &u = 0, \qquad r = 0, \qquad t > 0 \\ &u = aC_S, \qquad r = a, \qquad t > 0 \\ &u = 0, \qquad t = 0, \qquad 0 < r < a \end{aligned}$$

Here, $a$ is the radius of the 48−2−2 particles. If the 48−2−2 particles initially have a zero concentration of copper, $C_0$, and the surface concentration is maintained constant at $C_S$, the solution for Equation 9 becomes:

$$\frac{C - C_0}{C_S - C_0} = \frac{a}{r}\sum_{n=0}^{\infty}\{erfc\frac{a(2n+1)-r}{2\sqrt{Dt}} - erfc\frac{a(2n+1)+r}{2\sqrt{Dt}}\} \qquad [10]$$

This solution can be written in terms of the two dimensionless parameters $Dt/a^2$ and $r/a$. The curves in Figure 74 show concentration distributions at various times in a sphere with initial concentration $C_0$ and surface concentration $C_S$. Numbers on curves are of $Dt/a^2$.[29,180] Figure 74 shows that the concentration of the diffusing constituent, in this case copper, into the sphere, in this case 48−2−2, is quite homogeneous (i.e. saturated) once the $Dt/a^2$ is ≥0.4. If a graph for $t$ versus $a$ is constructed, the saturation time for particles of varying radii can be determined.

According to Figure 59, the radius of as-received −270 mesh 48−2−2 particles are in the range of 3 − 30 μm. Thus, the relation between $t$ and $a$ for particles with a radius of 3 to 30 μm was determined for varying diffusion coefficients and is shown in Figure 75. As mentioned above, Zhou assumed $D_{Cu}$ in the 48−2−2 powders to be the same as the experimentally determined $D_{Cu}$ in the 48−2−2 substrates, which was approximately $10^{-13}$ $m^2$ $s^{-1}$. However, as discussed in section 5.7.1, $D_{Cu}$ in the powders could be as rapid as $10^{-12}$ $m^2$ $s^{-1}$.

From Figure 75, it can be determined that a 48−2−2 particle with a 10 μm radius will take approximately 10 min to become saturated with copper if a diffusivity value of

$10^{-13}$ m$^2$ s$^{-1}$ is employed. If a diffusivity value of $10^{-12}$ m$^2$ s$^{-1}$ is used, a particle with a radius of 10 μm will take approximately 1 min to become saturated with copper. Since a significant percentage of the 48–2–2 particles have a radius ≥10 μm, after dissolution, it seems that a bonding time of less than 10 min would be sufficient to allow for complete saturation of the 48–2–2 powders by copper, and there would be no benefit in bonding for longer than a few minutes. In fact, microstructures of 48–2–2 joints, employing a 6:1 interlayer ratio, after bonding for <10 min compared well with the microstructures of 48–2–2 joints after bonding for ≥10 min.

Although some of Zhou's assumptions were addresses, those that remain for the present isothermal solidification model are as follows:

- Considering higher interfacial area of 48–2–2 powders compared to substrates, diffusion of copper only occurs in 48–2–2 powder particles.
- $D_{Cu}$ at the bonding temperature is constant throughout the bonding process (i.e. $D_{Cu}$ is independent of copper concentration and remains constant in spite of any phase transformations of the 48–2–2 powder particles).
- The surface of the solid keeps a constant copper concentration.
- The 48–2–2 particles have a spherical shape.
- Copper solubility changes as a function of temperature can be neglected.

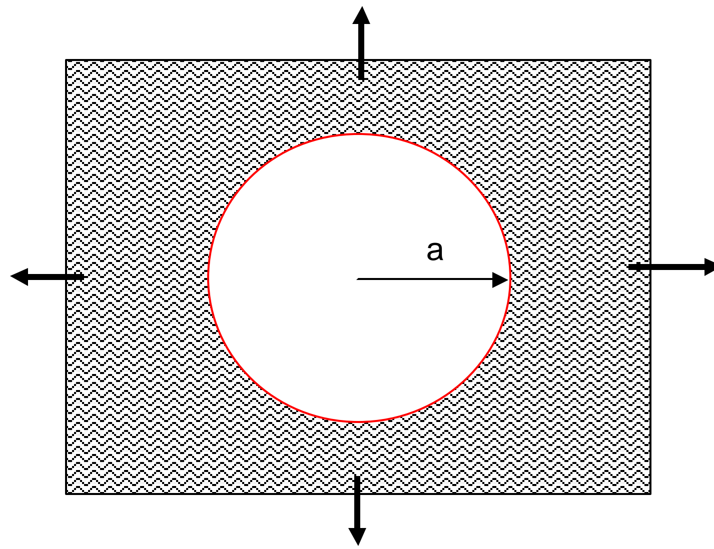

48-2-2 powder particle (finite radius a)

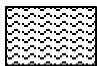

Cu-rich liquid phase (assumed to be semi-infinite)

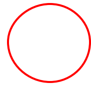

Constant $C_S$ (solidus composition) at the surface of the sphere

Figure 73–Schematic for the diffusion in sphere.[29,180]

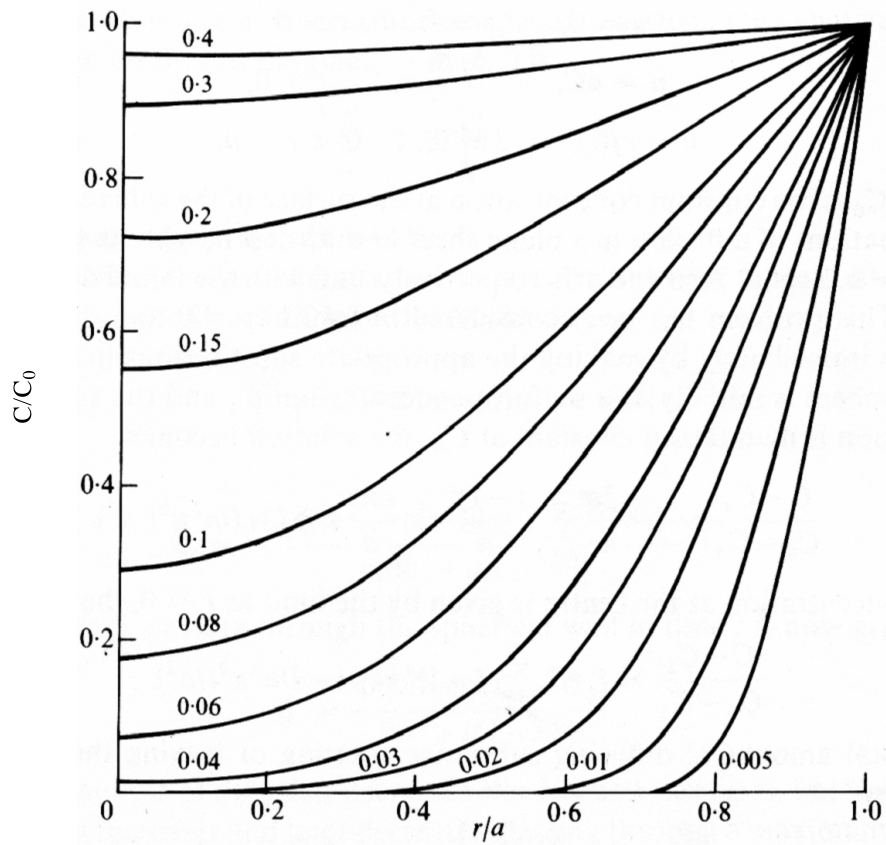


Figure 74–Concentration distributions at various times in a sphere with surface concentration $C_0$. Numbers on curves are values of $Dt/a^2$.[185]

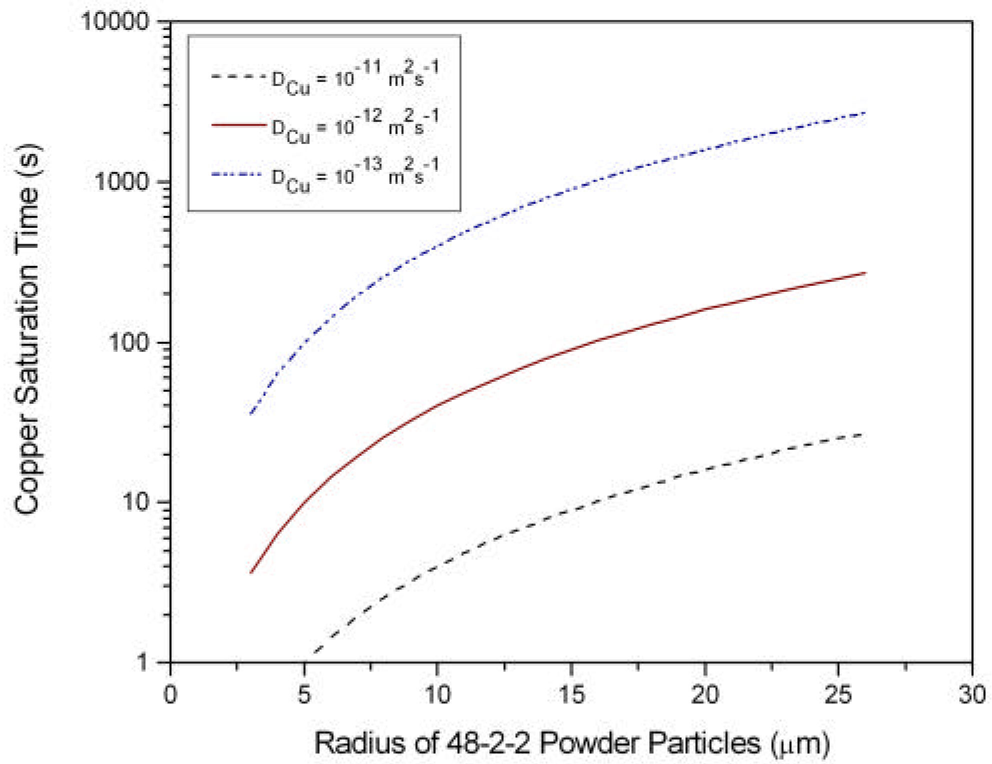


Figure 75−The relation between the size of 48−2−2 particles and the saturation time for Cu during the isothermal solidification process.

#### 5.8.1.3 *The Homogenization Stage*

Depending upon the intended application, a PBHT may be required after completion of the bonding process. A suitable PBHT would remove any copper containing phases in the bond region and transform the bond-line to a desired microstructure. Since the diffusion coefficients of copper in the temperature regime of 850 − 1450°C can be calculated from the Arrhenius plot in Figure 64, it would be of interest to estimate the time necessary for completion of the homogenization process. Before this can be done, the amount of copper remaining in the bond-line after the isothermal solidification process should be estimated.

##### 5.8.1.3.1 *Amount of Copper Remaining in Bond-line Prior to Homogenization*

Based on those conditions in section 5.8.1.1, the percentage (by weight) of the copper originally placed in the joint that can be absorbed by the 48−2−2 particles remaining after dissolution, without exceeding their copper solubility, is approximately 19% (31 g $m^{-2}$). Zhou[29,180] determined this value to be only 6%, primarily due to the fact that he assumed the solubility in the 48−2−2 powders to be the same as that of the 48−2−2 substrates (2 at.% copper). The present author observed that the copper solubility in the 48−2−2 powder particles to could be as much as 3 at.% (see section 5.7.2).

However, as discussed in section 5.6.3, large fillets, relative to the small area of the bonding surface, were observed in 48−2−2 bonds. Any copper lost to the fillets would result in less copper that must be absorbed by the substrates during the homogenization process. Thus, the total fillet volume was estimated by determining the average fillet cross-sectional area and multiplying by the length of the fillet (i.e. the

perimeter of the substrate). By knowing the total fillet volume and the weight percent of the constituents in the fillets, determined by EDS analysis, the amount of copper lost to the fillets was estimated. This value was expressed as mass of copper per unit area of the bonding surface and was determined to be 62 g $m^{-2}$. This value equates to approximately 38% (by weight) of the copper originally placed in the joint. The resulting amount of copper that must be absorbed by the substrates during the homogenization process is 68 g $m^{-2}$ or 42% of the copper originally placed in the joint. This amount of copper is the equivalent of an 8 μm thick pure copper foil. It is assumed that extrusion of copper-rich liquid from the joint cavity occurs after the dissolution process. This former value seems large at first, but is reasonable considering the size of the fillets relative to the small area of the bonding surface, which was approximately $10^{-4}$ $m^2$. However, provided the fillet cross-sectional area does increase significantly with increasing area of the bonding surface, the percentage (by weight) of the copper lost to the fillets becomes insignificant with large bonding areas (Figure 76). For example, assuming no change in fillet cross-sectional area, copper lost to the fillets of substrates with a contact surface area of $10^{-2}$ $m^2$ would only account for 4% (by weight) of the copper originally placed in the joint. Cross-sectional joining of a turbine blade is an example of an application with a single relatively large bonding surface. A corrugated or honeycomb structure joined to flat sheet panels is an example of an application with numerous bonds with small contact areas.

A table summarizing the amount of copper absorbed by the substrates during the homogenization process (including and excluding copper lost to fillets) and the equivalent amount of copper for a thin pure copper foil is provided in Table 5.

#### *5.8.1.3.2 Time Required for Completion of Homogenization*

As alluded to in section 2.7.5.4, most models developed to predict the time required for completion of the post-solidification homogenization stage of TLP bonding are based on solutions to Fick's second law, where the concentration gradient changes with time and position (i.e. non-steady state diffusion). In order to maintain simplicity, most analytical models assume the interlayer constituents are soluble in the bulk substrates (i.e. no phase boundary is present). However, as discussed in section 5.7.2, not only does copper have a low solubility in TiAl, but has different solubility limits in 48−2−2 and GMPX substrates. Thus, the homogenization model presented here employs a moving interface solution, where the solubility of the interlayer in the bulk substrates in taken into account. This model employs the following assumptions:

- Only a single two-phase moving planar interface is present.
- The substrates are semi-infinite.
- The copper diffused into the substrates during the PBHT is assumed to be in the form of a pure copper foil with a calculated equivalent thickness.
- The hypothetical pure copper foil remains solid and thus homogeneous during the homogenization stage.
- $D_{Cu}$ during PBHT is constant throughout the bonding process (i.e. $D_{Cu}$ is independent of copper concentration and remains constant in spite of any phase transformations of the 48−2−2 substrates).
- The diffusion along phase and twin boundaries can be neglected and only bulk diffusion considered.

- ♦ Copper solubility changes as a function of temperature and/or microstructure can be neglected.

From the last section, it was estimated how much copper remained in the joint following the bonding cycle, and the thickness of a pure copper interlayer that requires the diffusion of an equivalent amount of copper was calculated. A schematic of the concentration profile across the bond-line prior to the homogenization process is shown in Figure 77. If this concentration profile is rotated by 90°, and only one half is considered, the profile takes the form of that shown in Figure 78. Note the x-axis is the distance across the bond-line, where the joint center-line is taken as x = 0, and the y-axis is the concentration of copper. The concentration of copper in the foil ($C_F$) is 100 at.% and the solubility of copper in the 48–2–2 substrate material ($C_{TiAl}$) is 2 at.% or ~4 wt.% copper. The initial concentration of copper in the base material ($C_0$) is assumed to be 0 at.% copper. The net flux of copper atoms that must be moved to advance the interface a distance $dx$ during a given time $dt$ is given as $J_{Cu}$ and can be expressed in the following equation:

$$J_{Cu} = (C_F - C_{TiAl})\frac{dx}{dt} \qquad [11]$$

Now let $x$ equal the distance from the origin of growth to the current location of the interface. Also, let $d$ equal the distance from the origin of growth to the point where the copper concentration equals zero. According to the law of conservation of solute (Figure 79), the following expression can be made:

$$d - x = \frac{2x(C_F - C_{TiAl})}{(C_{TiAl} - C_0)} \qquad [12]$$

According to Fick's first law, the flux of diffusing copper atoms ($J_{Cu}$) is proportional to the product of $D_{Cu}$ and the concentration gradient $\left(\frac{\partial C}{\partial x}\right)$, and can be written as:

$$J_{Cu} = -D_{Cu}\frac{\partial C}{\partial x} \qquad [13]$$

If the solute distribution is approximated to Fick's first law, the following expression can be obtained:

$$J_{Cu} = \frac{D_{Cu}\left(C_F - C_{TiAl}\right)}{d - x} = \left(C_F - C_{TiAl}\right)\frac{dx}{dt} \qquad [14]$$

After making a substitution from Equation 12, followed by a simple integration, the following relationship between distance ($x$)[14], time ($t$) and the copper diffusivity in 48–2–2 ($D_{Cu}$) can be obtained:

$$t = \frac{x^2\left(C_F - C_{TiAl}\right)^2}{D_{Cu}\left(C_{TiAl} - C_0\right)^2} \qquad [15]$$

A plot of predicted PBHT (i.e. homogenization) times as a function of interlayer thickness and PBHT temperatures, is shown in Figure 80, assuming that the concentration of the copper interlayer must fall to 0 at.% from an initial concentration of 100 at.% without exceeding the solubility of 2 at.%. As estimated above, a 48–2–2 joint employing a 6:1 interlayer ratio will have the equivalent of a 8 µm thick copper foil interlayer remaining in the bond-line after bonding. This amount of copper will require a homogenization time of approximately 1 hr at 1350°C. This estimated value is actually very similar to that determined experimentally by Zhou.[29]

[14] Note: $x$ is assumed to be half the interlayer thickness.

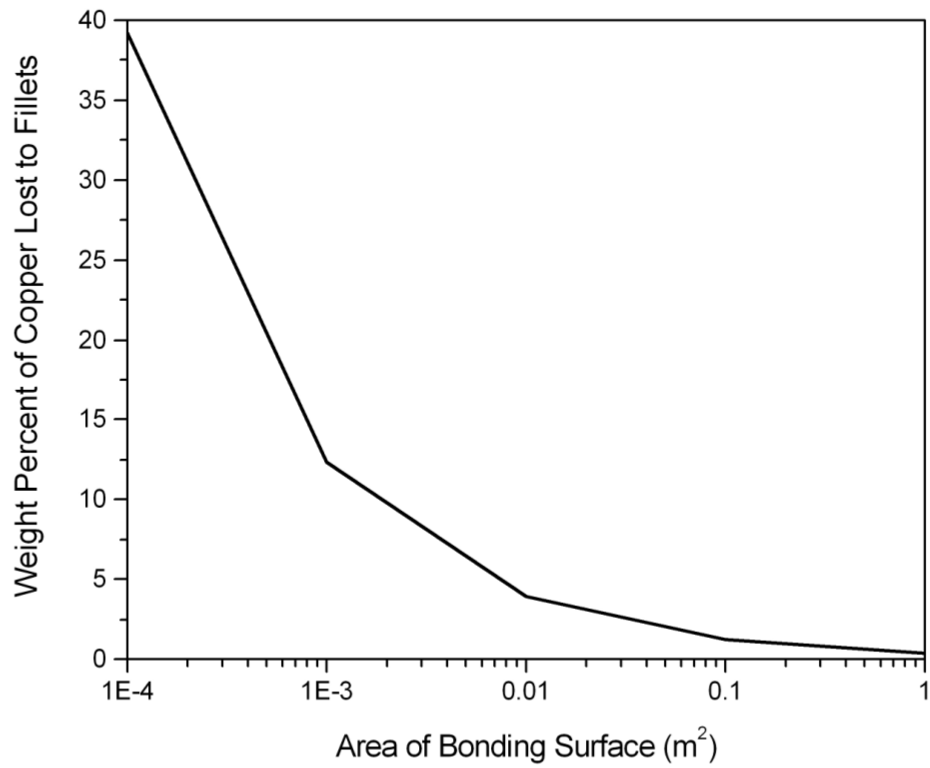


Figure 76–Percentage (by weight) of copper lost to fillets as a function of bond surface area, assuming no change in cross-sectional area of fillets.

| | As-deposited interlayer (250 µm) – Including copper lost to fillets | As-deposited interlayer (250 µm) – Excluding copper lost to fillets | As-deposited interlayer (100 µm) – From Zhou's model [29,180] |
|---|---|---|---|
| As-deposited weight ratio of 48–2–2 to copper | 6:1 | 6:1 | 6:1 |
| The amount of copper per unit area of as-deposited interlayer (based on specified thickness) | 161 g $m^{-2}$ | 161 g $m^{-2}$ | 63 g $m^{-2}$ |
| The amount of copper per unit area of interlayer that can be absorbed by the 48–2–2 particles, remaining after dissolution, without exceeding their copper solubility | 31 g $m^{-2}$ | 31 g $m^{-2}$ | 4 g $m^{-2}$ |
| The amount of copper per unit area of interlayer lost to fillets | 62 g $m^{-2}$ | 0 g $m^{-2}$ | N/A |
| The amount of copper per unit area of interlayer that must eventually diffuse into the substrates during homogenization | 68 g $m^{-2}$ 42% of total weight of as-deposited copper | 130 g $m^{-2}$ 81% of total weight of as-deposited copper | 59 g $m^{-2}$ 94% of total weight of as-deposited copper |
| Thickness of a pure copper interlayer that requires the diffusion of an equivalent amount of copper | 8 µm | 14.5 µm | 6.5 µm |

Table 5−The distribution of copper in 48−2−2 bonds during various stages of the TLP bonding process.

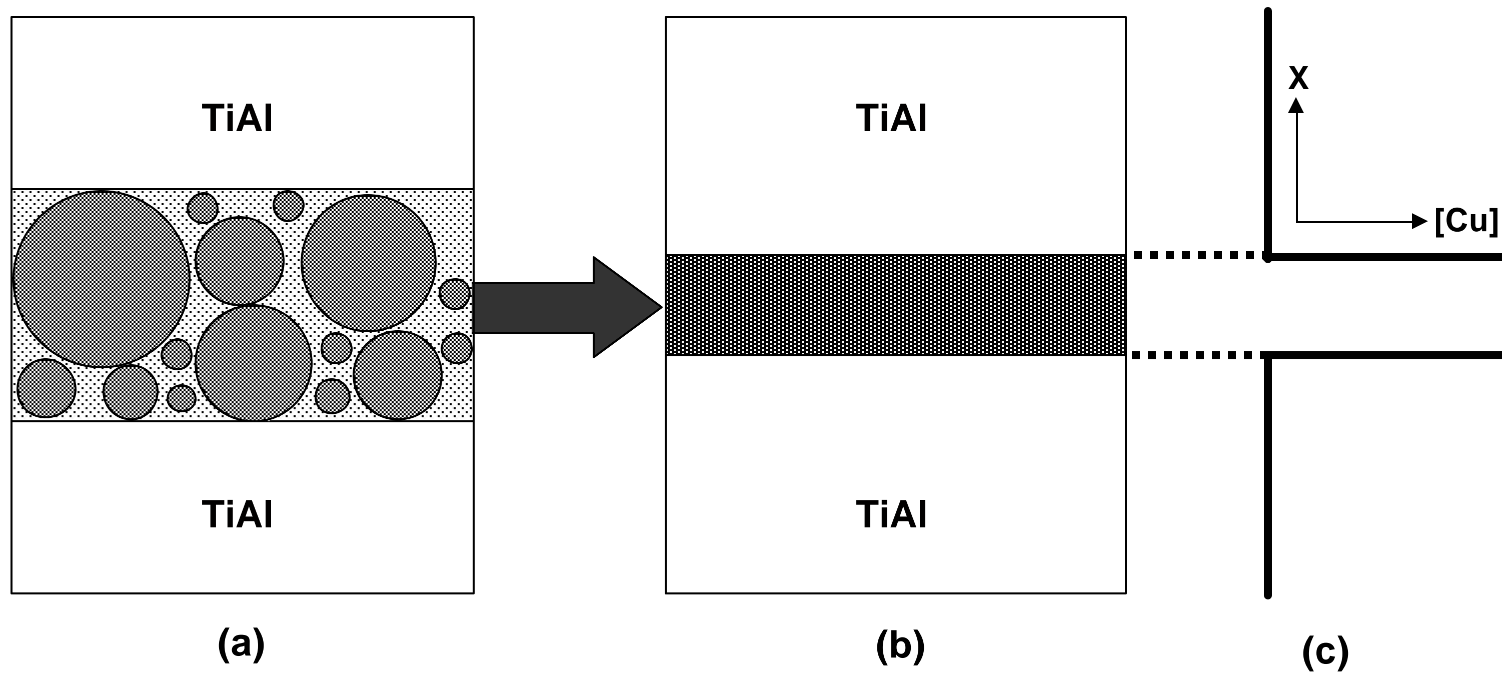


Figure 77–Schematic of (a) post-bond condition when employing a composite interlayer; (b) pre-PBHT condition employing an equivalent copper foil interlayer; and (c) concentration profile across bond-line at t = 0 (i.e. prior to homogenization process).

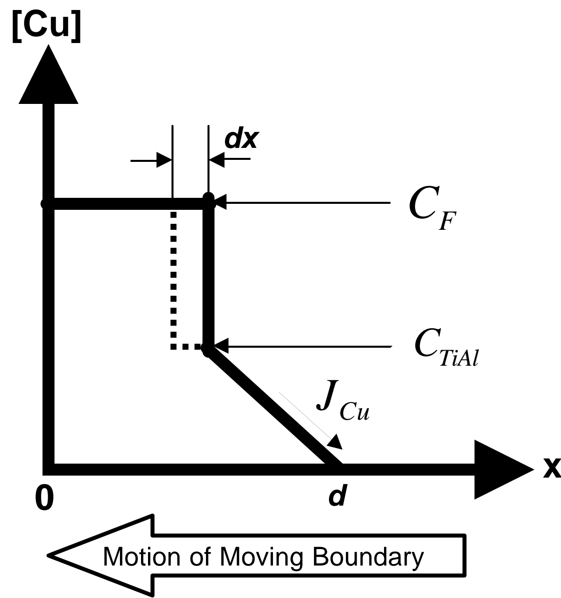


Figure 78–Schematic of copper concentration profile across one half of bond-line during the homogenization stage. The concentration of copper in the foil interlayer is given as $C_F$ and the solubility of copper in the TiAl substrate material is given as $C_{TiAl}$. The net flux of copper atoms that must be moved to advance the interface a distance $dx$ during a given time is given as $J_{Cu}$. The homogenization stage is complete when the interlayer-substrate interface reaches the joint centerline (i.e. x = 0).

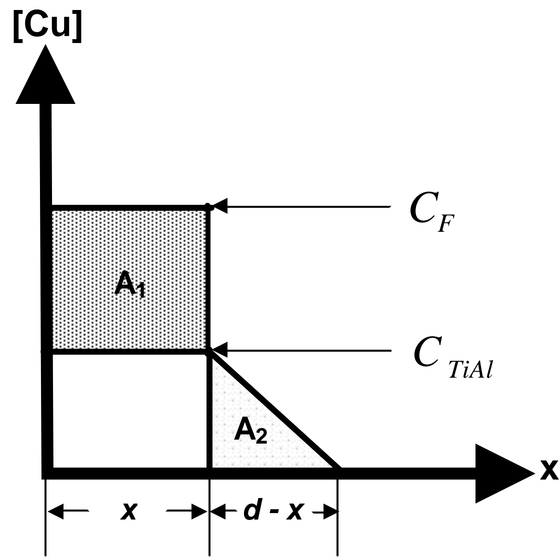


Figure 79– Schematic of copper concentration profile across one half of bond-line during the homogenization stage. According to the law of conservation of solute: $A_1 = A_2$.

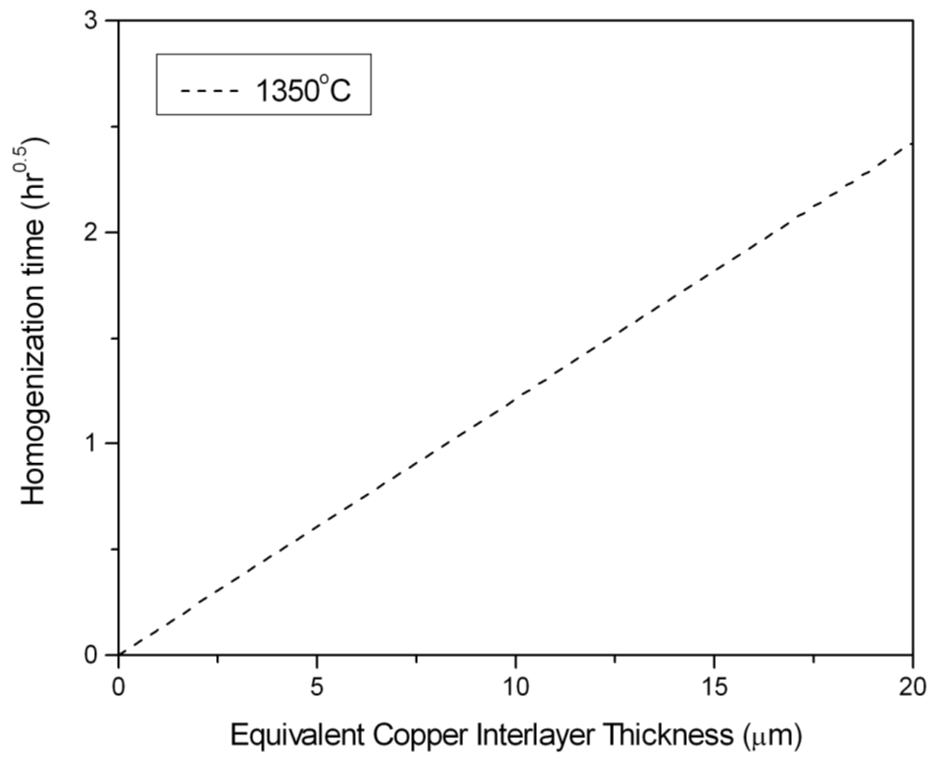


Figure 80–Prediction of PBHT (homogenization) times for 48–2–2 bonds as a function of equivalent copper interlayer thickness and PBHT temperature.

### 5.8.2 Modeling on Wide-Gap TLP Bonding of GMPX

The above model will now be applied to wide-gap TLP bonding of GMPX. Unless noted otherwise, the calculations and assumptions are the same as those discussed above.

#### 5.8.2.1 The Dissolution Stage

Most of the assumptions employed in this modeling stage are similar to those used in modeling of the dissolution stage in 48–2–2 bonds. The only exception is different values for the liquidus and solidus.

- Considering the Gamma Met powder particles in the bond-line have a much higher surface area than that of the substrates, it is assumed that only the powders are dissolved by liquid copper.
- The thickness of the as-deposited interlayer equal 250 µm.
- The weight ratio of Gamma Met to copper powders is 6:1 and the corresponding volume ratio is 7:1. Thus, the total weight of copper per unit area is 161 g $m^{-2}$ and the weight of Gamma Met is 965 g $m^{-2}$.
- $C_{Liq}$ is 29 at.% copper (~37 wt.% copper) and $C_{Sol}$ is 3 at.% copper (~4 wt.% copper).

The total amount of Gamma Met powder particles dissolved by liquid copper was determined to be 232 g $m^{-2}$. Thus, the liquid copper will dissolve approximately 24% of the Gamma Met powders originally placed in the joint and about 733 g $m^{-2}$ remain.

Recall, in the dissolution stage of 48–2–2 bonds, the 48–2–2 powders were able to dissolve approximately 36% of the 48–2–2 powders originally placed in the joint.

This calculated dissimilarity in dissolution of bond-line TiAl powders is a result of different liquidus values. The liquidus value for GMPX bonds was determined to be 29 at.% copper, while the liquidus value for 48–2–2 bonds was determined to be 22 at.% copper. Thus, it is comprehensible that the liquid copper is able to dissolve more 48–2–2 powders than Gamma Met powders.

When employing an interlayer ratio containing less copper, the amount of Gamma Met powders that are dissolved by liquid copper is reduced. A weight ratio of Gamma Met to copper powders of 50:1 has a corresponding volume ratio of approximately 99:1. Thus, the total weight of copper per unit area is 21 g $m^{-2}$ and the weight of Gamma Met is 1030 g $m^{-2}$. The total amount of Gamma Met powder particles dissolved by liquid copper, when employing a 50:1 Gamma Met to copper interlayer ratio, was determined to be 67 g $m^{-2}$. Thus, the liquid copper will dissolve approximately 24% of the Gamma Met powders originally placed in the joint and about 963 g $m^{-2}$ remain.

#### *5.8.2.2 The Isothermal Solidification Stage*

Considering the high interfacial area of the Gamma Met bond-line powders relative to the GMPX substrates, this model assumes copper only diffuses into the powders. Considering the as-received Gamma Met and 48–2–2 powder particles were determined to have similar copper diffusivities and copper solubilities (at the bonding temperature), the model constructed for the isothermal solidification stage of 48–2–2 bonds can be applied to GMPX bonds without modifications.

However, copper was detected in the TiAl powders and the substrates in both systems. Although the copper solubility in the Gamma Met and 48–2–2 bond-line powders was determined to be similar, the copper solubility in the 48–2–2 substrates was

determined to be greater than the copper solubility in GMPX substrates. A difference in solute solubility in the substrates could have a profound impact on time required for completion of the isothermal solidification and homogenization processes. A higher solubility of the solute in the base material decreases the time required for isothermal solidification and also the time required for homogenization. Due to the assumption that copper only diffuses in the bond-line powders, the substrates and hence copper solubility in the substrates were ignored in modeling of the isothermal solidification stage. However, the difference in copper solubility in the 48–2–2 and GMPX substrates was taken into account in modeling of the homogenization stage.

#### *5.8.2.3 The Homogenization Stage*

Similar to the homogenization model for 48–2–2 bonds, the amount of copper remaining in the bond-line after the bonding process should be estimated. This will first be calculated for a bond employing a 6:1 Gamma Met to copper interlayer ratio and then for a bond employing a 50:1 interlayer ratio.

##### *5.8.2.3.1 Amount of Copper Remaining in Bond-line Prior to Homogenization*

Based on those conditions in section 5.8.2.1, the percentage (by weight) of the copper originally placed in the joint that can be absorbed by the Gamma Met particles remaining after dissolution, without exceeding their copper solubility, is approximately 24% (39 g $m^{-2}$). This value is higher than that determined for 48–2–2 bonds due to the greater mass per unit area of TiAl powders remaining after dissolution.

Like 48–2–2 bonds, large fillets, relative to the small area of the bonding surface, were observed in GMPX bonds. However, the fillets of GMPX bonds appeared to be significantly smaller than those of 48–2–2 bonds. Initially, it was thought that the

smaller fillets would result in less copper-rich liquid extruded from the joint cavity, and hence more copper required to diffuse into the substrates during homogenization. Although the average cross-sectional area of the GMPX fillets was determined to be ~10% smaller than 48–2–2 fillets, the higher copper concentration of the GMPX fillets compensated for the smaller fillet size. The mass of copper per unit area of copper lost to the fillets was determined to be 64 g $m^{-2}$ (compared to 62 g $m^{-2}$ for 48–2–2 bonds). This value equates to approximately 40% (by weight) of the copper originally placed in the joint. The resulting amount of copper that must be absorbed by the substrates during the homogenization process is 58 g $m^{-2}$ or 36% of the copper originally placed in the joint. This amount of copper is the equivalent of a 6 μm thick pure copper foil. According to the model, the higher concentration of copper in the GMPX fillets resulted in slightly less copper remaining in the joint cavity of GMPX bonds, after the bonding process, than 48–2–2 bonds.

The amount of copper remaining in the bond-line of GMPX joints when employing a 50:1 Gamma Met to copper interlayer ratio will now be discussed. Based on those conditions in section 5.8.2.1, the percentage (by weight) of the copper originally placed in the joint that can be absorbed by the Gamma Met particles remaining after dissolution, without exceeding their copper solubility, is approximately 81% (17 g $m^{-2}$). Since no fillets were observed in bonds employing a 50:1 interlayer ratio, it is assumed that no copper was lost to the fillets. The resulting amount of copper that must be absorbed by the substrates during the homogenization process is 4 g $m^{-2}$ or 19% of the copper originally placed in the joint. This amount of copper is equivalent to a 0.40 μm

thick pure copper foil. The equivalent pure copper foil thickness as a function of the Gamma Met to copper interlayer weight ratio is shown in Figure 81.

A table summarizing the amount of copper absorbed by the substrates during the homogenization process and the equivalent amount of copper for a thin pure copper foil is provided in Table 6.

***5.8.2.3.2 Time Required for Completion of Homogenization***

From Equation 15, the time required for completion of the homogenization process can be estimated. Like the 48−2−2 model, the concentration of copper in the foil ($C_F$) is 100 at.%, however, the solubility of copper in the GMPX substrate material ($C_{TiAl}$) is 1 at.% or ~2 wt.% copper.

A plot of predicted PBHT times as a function of interlayer thickness and PBHT temperatures, is shown in Figure 82, assuming that the concentration of the copper interlayer must fall to 0 at.% from an initial concentration of 100 at.% ($C_F$) without exceeding the solubility of 1 at.% ($C_{TiAl}$). As estimated above, a GMPX joint employing a 50:1 interlayer ratio will have the equivalent of a 0.4 µm thick copper foil interlayer remaining in the bond-line after bonding. According to the model, this amount of copper would require a homogenization time of approximately 1 min at 1290°C. This time differs to that determined experimentally, which was 24X hr at 1290°C, by at least two orders of magnitude. One assumption that could partly account for this large discrepancy is the uniform distribution of the interlayer. As discussed in section 5.1, the bond-line of joints employing a 50:1 interlayer ratio often contained regions of completely dissolved powders and regions of only sintered Gamma Met powders. Thus, those regions

containing a small amount of copper could homogenize very rapidly, while those regions containing a high amount of copper would require a protracted homogenization time. Also, as discussed in section 5.7.1, experimental procedure used to estimate the copper diffusivity in the TiAl substrates has significant limitations that can lead to uncertainties in the accuracy of the data. These possible inaccuracies can ultimately lead to uncertainties in the homogenization model. In the homogenization model discussed here, the time required for homogenization is inversely proportional to the diffusivity of copper in the substrates. Thus, an order of magnitude error in the diffusion coefficient will result in an order of magnitude error in the estimated time required for homogenization.

In an effort to compare the results of the model for the 48–2–2 and GMPX systems, consider the equivalent of an 8 μm thick copper interlayer remaining the in the bond-line post-bonding. This amount of copper will require a homogenization time of approximately 6 hr at 1350°C in the GMPX system, compared to ~1 hr for 48–2–2 system. Since the estimated $D_{Cu}$ was found to be similar for the two substrate materials and the amount of copper in the bond-line is equal for both bonds; this significant difference in homogenization time is attributed solely to the difference in copper solubilities for the two alloys.

The former calculation suggests that this model may not be suitable for accurately predicting the time required for completion of the homogenization process, especially when an interlayer with a very small amount of solute material. However, the latter comparison demonstrates (theoretically) that a minute change in solute solubility can significantly affect the time required for completion of the homogenization process.

| | As-deposited interlayer (250 µm) – Including copper lost to fillets | As-deposited interlayer (250 µm) – Excluding copper lost to fillets | As-deposited interlayer (250 µm) |
|---|---|---|---|
| As-deposited weight ratio of Gamma Met to copper | 6:1 | 6:1 | 50:1 |
| The amount of copper per unit area of as-deposited interlayer (based on specified thickness) | 161 g $m^{-2}$ | 161 g $m^{-2}$ | 21 g $m^{-2}$ |
| The amount of copper per unit area of interlayer that can be absorbed by the Gamma Met particles, remaining after dissolution, without exceeding their copper solubility | 39 g $m^{-2}$ | 39 g $m^{-2}$ | 17 g $m^{-2}$ |
| The amount of copper per unit area of interlayer lost to fillets | 64 g $m^{-2}$ | 0 g $m^{-2}$ | N/A |
| The amount of copper per unit area of interlayer that must eventually diffuse into the substrates during homogenization | 58 g $m^{-2}$ 36% of total weight of as-deposited copper | 122 g $m^{-2}$ 76% of total weight of as-deposited copper | 4 g $m^{-2}$ 19% of total weight of as-deposited copper |
| Thickness of a pure copper interlayer that requires the diffusion of an equivalent amount of copper | 6 µm | 13.6 µm | 0.4 µm |

Table 6–The distribution of copper in GMPX bonds during various stages of the TLP bonding process.

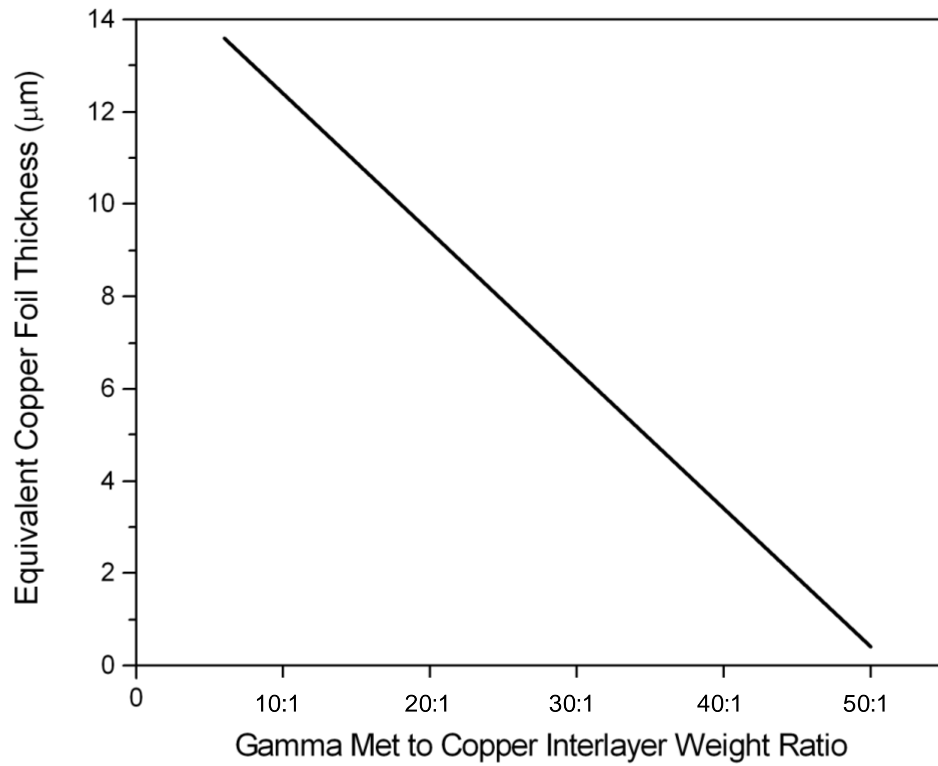


Figure 81−Plot of equivalent copper foil thickness as a function of Gamma Met to copper interlayer weight ratios.

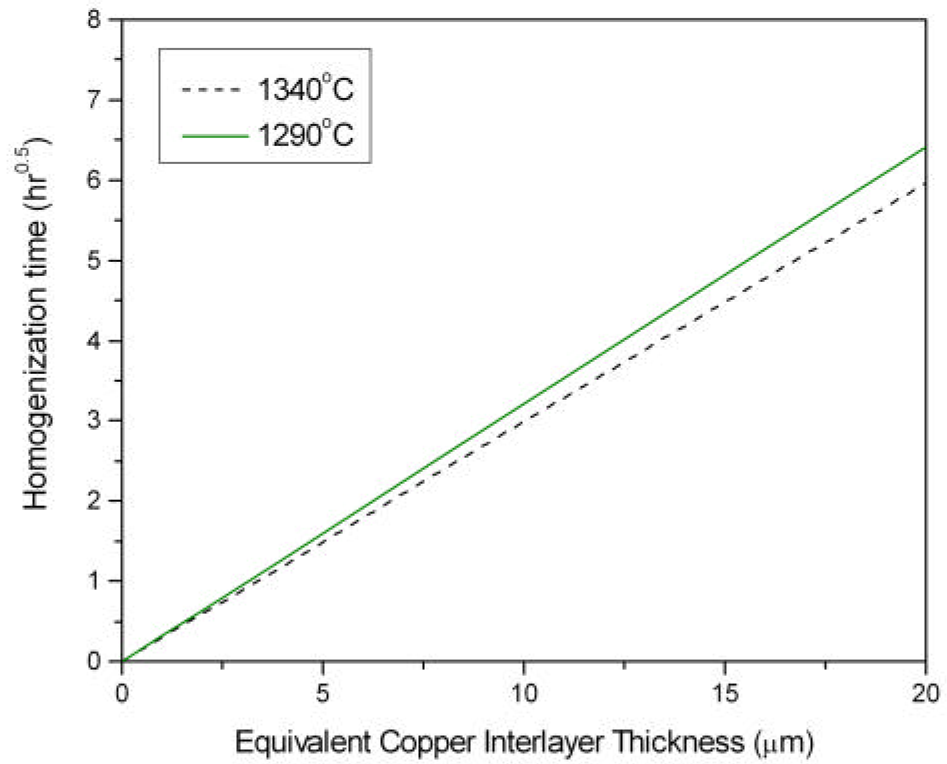


Figure 82−Prediction of PBHT (homogenization) times for GMPX bonds as a function of equivalent copper interlayer thickness and PBHT temperatures.

# 6. CONCLUSIONS

- Gamma Met PX (GMPX) wide-gap transient liquid phase (TLP) bonds employing a 50:1 (by weight) Gamma Met to copper interlayer ratio produced bonds with a microstructure and room temperature mechanical properties (microhardness, four-point bend and tensile) somewhat comparable to the bulk material after bonding for a suitable time at a temperature slightly above the melting temperature of copper.

- A post-bond heat treatment (PBHT) for a suitable time below the alpha transus temperature of GMPX produced a duplex microstructure in the bulk material and at the original bond-line. Although a coarser microstructure in the bond-line caused the joint to remain somewhat discernable following the post-bond heat treatment, the composition and microhardness of the bond region was found to be similar to that of the bulk material subjected to the same thermal cycle.

- A PBHT for a suitable time below the alpha transus temperature of GMPX plus a suitable exposure to a temperature above the alpha transus temperature produced a relatively fine grained fully lamellar microstructure in the bulk material and at the original bond-line. The composition, microhardness and room temperature mechanical properties (four-point bend

and tensile) of the bond-line was found to be similar to that of the bulk material, subjected to the same thermal cycle.

- The copper solubility, at the bonding temperature, in the Ti – 48 at.% Al – 2 at.% Cr – 2 at.% Nb (48–2–2) and GMPX alloys was determined to be ~2 at.% and ~1 at.% respectively. This dissimilarity is likely due to an apparent difference in the volume fraction of the $\alpha_2(Ti_3Al)$ phase in the 48–2–2 and GMPX alloys. This difference in solubility was attributed to (at least in part) to the observed differences in as-bonded GMPX and 48–2–2 joints. To compensate for the lower copper solubility in GMPX, the copper content of the composite interlayer employed in GMPX bonds was reduced from an initial ratio of 6:1 to 50:1.

- The liquidus composition, at the bonding temperature, in 48–2–2 and GMPX bonds was determined to be 22 and 29 at.% copper respectively. This dissimilarity is likely due to a difference in alloy composition. The lower liquidus composition determined for 48–2–2 bonds suggests that the liquid copper is able to dissolve more of the TiAl powders in the bond-line of 48–2–2 joints than the TiAl powders in the bond-line of GMPX joints. Thus, more liquid was produced in 48–2–2 bonds. The latter is attributed to (at least in part) the larger fillets observed in 48–2–2 bonds. Despite the larger fillets produced in 48–2–2 bonds, a lower concentration of copper in the 48–2–2 fillets, compared to the GMPX fillets, resulted in an equal

amount of copper extruded from the joint cavity in both 48–2–2 and GMPX bonds.

- Differences in composition and/or microstructure did not have a discernable difference on the activation energy of copper diffusion in 48–2–2 and GMPX alloys in the temperature regime of 850 to 1450°C. Thus, the differences observed in as-bonded 48–2–2 and GMPX joints employing a 6:1 interlayer ratio cannot be attributed to differences in copper diffusion.
- 48–2–2 bonds employing a 48–2–2 plus copper powder interlayer can tolerate a higher concentration of copper (e.g. 6:1 weight ratio of 48–2–2 to copper) than GMPX bonds, primarily due to the higher solubility of copper in the 48–2–2 substrates. As a result, the bond-line of 48–2–2 joints had a lower concentration of copper, and the time required for completion of homogenization was less protracted than GMPX bonds.
- Although TiAl powders of differing composition were employed in the composite interlayer of 48–2–2 and GMPX bonds, unlike the substrates, no difference in copper solubility or copper diffusivity at the bonding temperature was observed (at least prior to any phase transformations from the as-received condition). This is attributed to the similar processing route of the TiAl powders. The rapidly solidified gas-atomized powders were predominately the $\alpha$(Ti)-Al solid solution, while the substrates were predominately the $\gamma$(TiAl) phase with varying volume fractions of the $\alpha_2$($Ti_3Al$) phase.

# 7. FUTURE WORK

- *High temperature mechanical testing:* Considering GMPX is intended to be employed in high temperature environments, it is imperative that high temperature mechanical testing of as-bonded and as-PBHT specimens be conducted.

- *Bonding with higher compressive force:* In an effort to avoid a large test matrix, the compressive force used in bonding of GMPX was the same as that employed by Zhou. Considering a higher compressive force could result in a greater amount of copper-rich liquid extruded from the joint cavity, a series of experiments employing different compression forces warrants an investigation.

- *Bonding in longitudinal direction:* Due to a limited amount of available GMPX material, a large test matrix was avoided by only bonding transverse surface of the extruded bar to another transverse surface (i.e. in direction of extrusion). Bonding in the longitudinal direction (i.e. extruded surface to extruded surface) would be of interest to determine if orientation or elongated grains have any profound effects on bonding.

- *Mechanical testing of bulk alloy with copper additions:* Since the presence of copper in as-bonded joints could result in degradation of mechanical properties of GMPX, mechanical testing of the bulk alloy with small copper additions is suggested. This should be conducted at both room and elevated temperatures.

- *The effect of copper on phase transformation:* Even after protracted post-bond heat treatments to produce a duplex microstructure, a coarser microstructure at the original the bond-line caused the joint to remain slightly discernable. This could be attributed to the phase transformation mechanisms of Gamma Met and/or GMPX alloys being affected by the presence of residual copper. Thus, a careful study on the phase transformation mechanisms of Gamma Met and GMPX alloys containing small additions of copper is suggested.

- *Comparison of GMPX and Gamma Met phase transformations:* The discernable bond-lines referenced above could also be attributed to different phase transformation mechanisms in GMPX and Gamma Met alloys. Considering the difference in composition of these two alloys, a difference in phase transformation mechanism is possible. Thus, a study to compare the phase transformation mechanisms in GMPX and Gamma Met alloys should be conducted.

- *Copper diffusivity in Gamma Met alloy:* The work discussed here suggested that the diffusion coefficient of copper could be more rapid in the as-received Gamma Met powders than the as-received GMPX substrates. This

possible difference in copper diffusion coefficient was attributed to a faster copper diffusivity in the $\alpha$(Ti)-Al solid solution phase than the $\gamma$(TiAl) + $\alpha_2$($Ti_3Al$) phase. Although detailed studies to determine the diffusion coefficient of copper in the Gamma Met powders were not conducted in the present work, these data should be experimentally determined to validate the latter theory.

- *Copper solubility changes as a function of temperature:* One of the assumptions in the homogenization model was that copper solubility changes as a function of temperature were neglected. The copper solubility value determined for the bonding temperature was employed for all temperatures. By determining and incorporating copper solubility values for other temperatures of interest (e.g. post-bond heat treatment temperatures) the homogenization model could be made more accurate.

- *Terminal spreading distance studies of copper on Gamma Met:* Terminal spreading diameter of copper droplets were only conducted on GMPX and 48–2–2 substrates. Considering the compositional dissimilarities in the three alloys, the terminal spreading diameter of liquid copper on Gamma Met would be interesting to compare with the existing data.

- *Wetting experiments of 48-2-2, GMPX and Gamma Met substrates:* Wetting (i.e. thermodynamic equilibrium between the liquid and solid) experiments were not conducted. Wetting will effect how well a liquid "wets" a solid, and hence will impact spreading. This study can be

conducted by measuring the contact angle of liquid copper on 48−2−2, GMPX and Gamma Met substrates. This study would provide a beneficial supplement to the terminal spreading diameter studies.

## 8. BIBLIOGRAPHY


1. T. A. Wallace, and R. K. Bird: "Development of Oxidation Protection Coatings for Gamma Titanium Aluminide Alloys," Proceedings of *Annual Joint Army-Navy-NASA-Air Force Meeting*, Colorado Springs, CO, 2003.

2. S. Draper, G. Das, I. E. Locci, J. D. Whittenberger, B. A. Lerch, and H. Kestler: "Microstructure and Mechanical Properties of Extruded Gamma Met PX," in *Gamma Titanium Aluminides 2003*, edited by Y.-W. Kim, H. Clemens, and A. H. Rosenberger, TMS, Warrendale, PA, 2003, pp. 207-212.

3. M. Shazly, V. Prakash, and S. Draper: *Int. J. Solids Struct.*, 2004, 41, pp. 6485-6503.

4. R. LeHolm, B. Norris, and A. Gurney: *Adv. Mater. Process.*, 2001, 159(5), pp. 27-31.

5. J. M. Larson, K. A. Williams, S. J. Balsone, and M. A. Stucke: "Titanium Aluminides for Aerospace Applications," in *High Temperature Aluminides and Intermetallics*, edited by S. H. Whang, C. T. Liu, D. P. Pope, and J. O. Stiegler, TMS, Warrendale, PA, 1990, pp. 521-556.

6. G. Das: "The Development of Sheet Gamma TiAl Technology under the Enabling Propulsion Materials/High Speed Civil Transport (EPM/HSCT) Program," in *Gamma Titanium Aluminides 2003*, edited by Y.-W. Kim, H. Clemens, and A. H. Rosenberger, TMS, Warrendale, PA, 2003, pp. 33-45.

7. B. Tabernig, and H. Kestler: "Joining of Sheet Based Titanium Aluminide Products," in *Gamma Titanium Aluminides 2003*, edited by Y.-W. Kim, H. Clemens, and A. H. Rosenberger, TMS, Warrendale, PA, 2003, pp. 619-625.

8. I. C. Wallis, H. S. Ubhi, M.-P. Bacos, P. Josso, J. Lindqvist, and D. Lundstrom: *Intermetal.*, 2004, 12, pp. 303-316.

9. S. J. Lee, and S. K. Wu: *Intermetal.*, 1999, 7, pp. 11-21.

10. S. J. Lee, S. K. Wu, and R. Y. Lin: *Acta Mater.*, 1998, 46(4), pp. 1283-1295.

11. S. J. Lee, S. K. Wu, and R. Y. Lin: *Acta Mater.*, 1998, 46(4), pp. 1297-1305.

12. R. K. Shiue, S. K. Wu, and S. Y. Chen: *Acta Mater.*, 2003, 51, pp. 1991-2001.

13. V. L. Acoff, S. Wilkerson, and M. Arenas: *Mater. Sci. Eng. A*, 2002, 329-331, pp. 763-767.

14. M. Arenas, and V. L. Acoff: "Analysis of Gamma Titanium Aluminide Welds Produced by Gas Tungsten Arc Welding," in *Joining of Advanced and Specialty Materials V*, edited by J. E. Indacochea, J. N. DuPont, T. J. Lienert, W. Tillmann, N. Sobczak, W. F. Gale, and M. Singh, ASM International, Materials Park, OH, 2003, pp. 83-88.

15. S. Wilkerson, and V. L. Acoff: "An Investigation of Texture and its Effect on Welding Gamma-TiAl Sheet Materials," in *Trends in Welding Research*, edited by S. A. David, T. DebRoy, J. C. Lippold, H. B. Smartt, and J. M. Vitek, ASM International, Materials Park, OH, 2002, pp. 660-665.

16. R. A. Patterson, P. L. Martin, B. K. Damkroger, and L. Christodoulou: *Weld. J. Suppl.*, 1990, 69, pp. 39s-44s.

17. C. Buque, and F. Appel: "Microstructural Aspects of Diffusion Bonding of High Niobium Containing Gamma TiAl-Based Alloys," in *Gamma Titanium Aluminides 2003*, edited by Y.-W. Kim, H. Clemens, and A. H. Rosenberger, TMS, Warrendale, PA, 2003, pp. 591-599.

18. G. Cam, H. Clemens, R. Gerling, and M. Kocak: *Intermetal.*, 1999, 7, pp. 1025-1031.

19. P. Yan, and E. R. Wallach: *Intermetal.*, 1993, 1(2), pp. 83-97.

20. W. Glatz, and H. Clemens: *Intermetal.*, 1997, 5, pp. 415-423.

21. J. W. Fergus, T. Zhou, B. Dang, and W. F. Gale: "Oxidation Resistance of Transient Liquid Phase (TLP) Bonded Gamma Titanium Aluminide," in *Trends in Welding Research*, edited by S. A. David, T. DebRoy, J. C. Lippold, H. B. Smartt, and J. M. Vitek, ASM International, Materials Park, OH, 2002, pp. 799-803.

22. D. S. Duvall, W. A. Owczarski, and D. F. Paulonis: *Weld. J.*, 1974, 53, pp. 203-214.

23. W. D. MacDonald, and T. W. Eagar: *Annu. Rev. Mater. Sci.*, 1992, 22, pp. 23-46.

24. X. Wu, R. S. Chandel, and H. Li: *J. Mater. Sci.*, 2001, 36, pp. 1539-1546.

25. W. F. Gale, Y. Xu, X. Wen, and Z. A. M. Abdo: *Metall. Mater. Trans. A*, 1999, 30A, pp. 2723-2726.

26. W. F. Gale, X. Wen, T. Zhou, and Y. Shen: *Mater. Sci. Tech.*, 2001, 17, pp. 1423-1433.

27. W. F. Gale, D. A. Butts, M. D. Ruscio, and T. Zhou: *Metall. Mater. Trans. A*, 2002, 33A, pp. 3205-3214.

28. T. Zhou, W. F. Gale, D. A. Butts, and M. D. Ruscio: "Wide-Gap Transient Liquid Phase Bonding of TiAl Alloys," in *Joining of Advanced and Specialty Materials IV*, edited by J. E. Indacochea, T. J. Lienert, W. Tillmann, and M. Singh, ASM International, Materials Park, OH, 2002, pp. 51-55.

29. T. Zhou: Ph.D. thesis, Auburn University, Auburn, AL, 2002.

30. J. B. McAndrew, and J. B. Kessler: *Trans. AIME*, 1956, 206, pp. 1348.

31. F. H. Foes, and C. Suryanarayana: "Titanium Aluminides," in *Physical and Metallurgy and Processing of Intermetallic Compounds*, edited by N. S. Stoloff and V. K. Sikka, Chapman & Hall, New York, NY, 1994, pp. 297-350.

32. M. Yamaguchi, and H. Inui: "$Al_3Ti$ and its L12 Variations," in *Intermetallic Compound: Principles and Practice*, edited by J. H. Westbook and R. L. Fleischer, John Wiley & Sons Ltd., New York, NY, 1994, pp. 147-173.

33. S. S. Nayak, and B. S. Murty: *Mater. Sci. Eng. A*, 2004, 367, pp. 218-224.

34. Y. V. Milman, D. B. Miracle, S. I. Chugunova, I. V. Voskoboinik, N. P. Korzhova, T. N. Legkaya, and Y. N. Podrezov: *Intermetal.*, 2001, 9, pp. 839-845.

35. Y.-W. Kim: *Acta Mater.*, 1992, 40(6), pp. 1121-1134.

36. Y.-W. Kim, and F. H. Froes: "Physical Metallurgy of Titanium Aluminides," in *High Temperature Aluminides and Intermetallics*, edited by S. H. Whang, C. T. Liu, D. P. Pope, and J. O. Stiegler, TMS, Warrendale, PA, 1990, pp. 465-492.

37. Y.-W. Kim: in *High Temperature Ordered Intermetallic Alloys IV*, edited by L. A. Johnson, D. P. Pope, and J. O. Stiegler, M.R.S, Pittsburgh, PA, 1991, pp. 777-794.

38. F. Appel, and M. Oehring: "Gamma-Titanium Aluminide Alloys: Alloy Design and Properties," in *Titanium and Titanium Alloys*, edited by M. Peters, Wiley-VCH, Germany, 2003, pp. 89-152.

39. H. Kestler, and H. Clemens: "Production, Processing and Application of Gamma(TiAl)-Based Alloys," in *Titanium and Titanium Alloys*, edited by C. Leyens and M. Peters, Wiley-VCH, Germany, 2003, pp. 351-392.

40. Y.-W. Kim, and D. M. Dimiduk: *JOM*, 1991, 43(8), pp. 40-47.

41. Y.-W. Kim: *JOM*, 1994, 46(7), pp. 30-39.

42. G. Lutjering, and J. C. Williams: *Titanium*, Springer, Verlag, Germany, 2003.

43. M. Beschliesser, G. Dehm, H. Kestler, and H. Clemens: "Effect of microstructure on thermal stability and mechanical properties of an engineering γ-TiAl based alloy during long-term exposure at 700C and 800C in air," in *Gamma Titanium Aluminides 2003*, edited by Y.-W. Kim, H. Clemens, and A. H. Rosenberger, TMS, Warrendale, PA, 2003, pp. 459-465.

44. R. R. Botten, A. B. Godfrey, and M. H. Loretto: "The effect of compostion on the stability at 700C and on the mechanical properties of gamma titanium aluminides," in *Gamma Titanium Aluminides 1999*, edited by Y.-W. Kim, D. M. Dimiduk, and M. H. Loretto, TMS, Warrendale, PA, 1999, pp. 455-459.

45. B. G. Kim, G. M. Kim, and C. J. Kim: *Scripta Metall. Mater.*, 1995, 33(7), pp. 1117-1125.

46. C. Leyens: "Oxidation and Protection of Titanium Alloys and Titanium Aluminides," in *Titanium and Titanium Alloys*, edited by C. Leyens and M. Peters, Wiley-VCH, Germany, 2003, pp. 187-230.

47. S. C. Huang, and D. S. Shih: "Microstructure-Property Correlation in TiAl-Base Alloys," in *Microstructure/Property Relationships in Titanium Alumindes and Alloys*, edited by Y.-W. Kim and R. R. Boyer, TMS, Warrendale, PA, 1990, pp. 105-122.

48. D. S. Shih: in *Microstructure/Property Relationships in Titanium Aluminides and Alloys*, edited by R. R. Boyer, TMS, Warrendale, PA, 1990, pp. 135-148.

49. C. T. Liu, P. J. Maziasz, and J. L. Wright: "Key Microstructures Controlling the Mechanical Properties of Two-Phase TiAl Alloys with Lamellar Structures," in *High-Temperature Ordered Intermetallic Alloys VII*, edited by C. C. Koch, C. T. Liu, N. S. Stoloff, and A. Wanner, Materials Research Society, Pittsburgh, PA, 1996, pp. 83-90.

50. K. S. Chan, and Y.-W. Kim: in *Microstructure/Property Relationships in Titanium Aluminides and Alloys*, edited by R. R. Boyer, TMS, Warrendale, PA, 1990, pp. 179-196.

51. D. S. Schwartz, and W. O. Soboyejo: in *Microstructure/Property Relationships in Titanium Aluminides and Alloys*, edited by Y.-W. Kim and R. R. Boyer, TMS, Warrendale, PA, 1990, pp. 65-74.

52. J. Yang, J. N. Wang, Y. Wang, and Q. Xia: *Intermetal.*, 2003, 11, pp. 971-974.

53. K. S. Chan: *Metall. Mater. Trans. A*, 1993, 24A, pp. 569-583.

54. K. S. Chan, and Y.-W. Kim: *Metall. Mater. Trans. A*, 1992, 23A, pp. 1663-1677.

55. S. Mitao, S. Tsuyama, and K. Minakawa: "Effect of Aluminum Content on Creep Deformation," in *Microstructure/Property Relationships in Titanium Aluminides and Alloys*, edited by Y.-W. Kim and R. R. Boyer, TMS, Warrendale, PA, 1990, pp. 297-311.

56. J. S. Huang, and Y.-W. Kim: *Scripta Metall. Mater.*, 1991, 25(8), pp. 1901-1906.

57. Y.-W. Kim: *JOM*, 1989, 41(7), pp. 24-29.

58. S. C. Huang: "Alloying Considerations in Gamma-Based Alloys," in *Structural Intermetallics*, edited by R. Darolia, J. J. Lewandowski, C. T. Liu, P. L. Martin, D. B. Miracle, and M. V. Nathal, TMS, Warrendale, PA, 1993, pp. 299-307.

59. P. J. Maziasz, R. V. Ramanujan, C. T. Liu, and J. L. Wright: *Intermetal.*, 1997, 5(2), pp. 83-95.

60. T. T. Cheng, and M. R. Willis: *Scripta Mater.*, 1998, 39(9), pp. 1255-1265.

61. D. J. Larson, C. T. Liu, and M. K. Miller: *Intermetal.*, 1997, 5, pp. 411-414.

62. M. E. Hyman, C. McCullough, C. G. Levi, and R. Mehrabian: *Metall. Mater. Trans. A*, 1991, 22A, pp. 1647-1662.

63. T. T. Cheng: "On the Mechanism of Boron-Induced Grain Refinement in TiAl-Based Alloys," in *Gamma Titanium Aluminides 1999*, edited by Y.-W. Kim, D. M. Dimiduk, and M. H. Loretto, TMS, Warrendale, PA, 1999, pp. 389-396.

64. T. Noda, M. Okabe, S. Isobe, and M. Sayashi: *Mater. Sci. Eng. A*, 1995, 192/193, pp. 774-779.

65. F. Appel, M. Oehring, and P. J. Ennis: "Micromechanisms of Creep in Gamma-Base Titanium Aluminides," in *Gamma Titanium Aluminides 1999*, edited by Y.-W. Kim, D. M. Dimiduk, and M. H. Loretto, TMS, Warrendale, PA, 1999, pp. 603-618.

66. G. L. Chen, W. J. Zhang, Y. Wang, Z. Q. Sun, Y. Wu, and L. Zhou: "Ti-Al-Nb Intermetallic Alloys Based on the Ternary Intermetallic Compound," in *Structural Intermetallics*, edited by R. Darolia, J. J. Lewandowski, C. T. Liu, P. L. Martin, D. Miracle, and M. V. Nathal, TMS, Warrendale, PA, 1993, pp. 319-324.

67. G. L. Chen, W. J. Zhang, Z. C. Liu, and S. J. Li: "Microstructure and Properties of High-Nb Containing TiAl-Base Alloys," in *Gamma Titanium Aluminides 1999*, edited by Y.-W. Kim, D. M. Dimiduk, and M. H. Loretto, TMS, Warrendale, PA, 1999, pp. 371-380.

68. F. Appel, M. Oehring, J. D. H. Paul, and U. Lorenz: "Design, Properties and Processing of Novel TiAl Alloys," in *Structural Intermetallics*, edited by K. J. Hemker, D. M. Dimiduk, H. Clemens, R. Darolia, H. Inui, J. M. Larson, V. K. Sikka, M. Thomas, and J. D. Whittenberger, TMS, Warrendale, PA, 2001, pp. 63-72.

69. F. Appel, U. Lorenz, J. D. H. Paul, and M. Oehring: "The Mechanical Properties of Niobium Alloyed Gamma Titanium Aluminides," in *Gamma Titanium Aluminides 1999*, edited by Y.-W. Kim, D. M. Dimiduk, and M. H. Loretto, TMS, Warrendale, PA, 1999, pp. 381-388.

70. Z. C. Liu, J. P. Lin, S. J. Li, and G. L. Chen: *Intermetal.*, 2002, 20, pp. 653-659.

71. J. D. H. Paul, F. Appel, and R. Wagner: *Acta Mater.*, 1998, 46, pp. 1075-1085.

72. R. Pather, A. Wisbey, A. Partridge, T. Halford, D. N. Horspool, P. Bowen, and H. Kestler: "Thermo-mechanical Processing of High Niobium Gamma-TiAl Alloys: Microstructure and Mechanical Properties," in *Structural Intermetallics*, edited by K. J. Hemker, D. M. Dimiduk, H. Clemens, R. Darolia, H. Inui, J. M. Larson, V. K. Sikka, M. Thomas, and J. D. Whittenberger, TMS, Warrendale, PA, 2001, pp. 207-215.

73. G. Chen, Z. Sun, and X. Zhou: *Mater. Sci. Eng. A*, 1992, 153(1-2), pp. 597-601.

74. G. L. Chen, K. Q. Ni, X. T. Wang, S. M. Hao, J. X. Cao, J. J. Ding, and X. Zhang: *Intermetal.*, 1996, 4(1), pp. 13-22.

75. G. L. Chen, Z. C. Liu, J. P. Lin, and W. J. Zhang: "Strengthening Mechanism in High Nb Containing TiAl Base Alloys," in *Structural Intermetallics*, edited by K. J. Hemker, D. M. Dimiduk, H. Clemens, R. Darolia, H. Inui, J. M. Larson, V. K. Sikka, M. Thomas, and J. D. Whittenberger, TMS, Warrendale, PA, 2001, pp. 475-481.

76. C. Woodward, S. A. Kajihara, S. I. Rao, and D. M. Dimiduk: "The Influence of Solid Solutions on Flow Behavior," in *Gamma Titanium Aluminides 1999*, edited by Y.-W. Kim, D. M. Dimiduk, and M. H. Loretto, TMS, Warrendale, PA, 1999, pp. 49-58.

77. F. Appel, M. Oehring, and P. J. Ennis: *Intermetal.*, 2000, 8, pp. 1283-1312.

78. W. Zhang, G. Chen, and Z. Sun: *Scripta Metall. Mater.*, 1993, 28(5), pp. 563-567.

79. Y.-C. Zhu, Y. Zhang, X. Y. Li, K. Fujita, and N. Iwamoto: *Oxid. Met.*, 2001, 55(1/2), pp. 119-135.

80. M. Schmitz-Niederau, and M. Schütze: *Oxid. Met.*, 1999, 52(3/4), pp. 225-240.

81. S. Becker, A. Rahmel, M. Schorr, and M. Schütze: *Oxid. Met.*, 1992, 38(5/6), pp. 425-464.

82. K. Maki, M. Shioda, M. Sayashi, T. Shimizu, and S. Isobe: *Mater. Sci. Eng. A*, 1992, 153, pp. 591-596.

83. S. K. Varma, A. Chan, and R. N. Mahapatra: *Oxid. Met.*, 2001, 55(5/6), pp. 423-435.

84. U. Figge, A. Elschner, N. Zheng, H. Schuster, and W. J. Quadakkers: *Fresen. J. Anal. Chem.*, 1993, 346, pp. 75-78.

85. S. Becker, M. Schütze, and A. Rahmel: *Oxid. Met.*, 1993, 39(1/2), pp. 93-106.

86. V. Güther, A. Otto, H. Kestler, and H. Clemens: "Processing of Gamma TiAl Based Ingots and Their Characterization," in *Gamma Titanium Aluminides 1999*, edited by Y.-W. Kim, D. M. Dimiduk, and M. H. Loretto, TMS, Warrendale, PA, 1999, pp. 225-230.

87. C. M. Austin, and T. J. Kelly: "Development and Implementation Status of Cast Gamma Titanium Aluminide," in *Structural Intermetallics*, edited by R. Darolia, J. J. Lewandowski, C. T. Liu, P. L. Martin, D. B. Miracle, and M. V. Nathal, TMS, Warrendale, PA, 1993, pp. 143-150.

88. T. Tetsui, and S. Ono: *Intermetal.*, 1999, 7, pp. 689-697.

89. M. Peters, and C. Leyens: "Fabrication of Titanium Alloys," in *Titanium and Titanium Alloys*, edited by C. Leyens and M. Peters, Wiley-VCH, Germany, 2003, pp. 245-261.

90. C. F. Yolton, Y.-W. Kim, and U. Habel: "Powder metallurgy processing of Gamma Titanium Aluminide," in *Gamma Titanium Aluminides 2003*, edited by Y.-W. Kim, H. Clemens, and A. H. Rosenberger, TMS, Warrendale, PA, 2003, pp. 233-240.

91. R. LeHolm, H. Clemens, and H. Kestler: "Powder Metallurgy (PM) Gamma-Based Titanium Aluminide Structures for use in Various High Temperature Aerospace Applications," in *Gamma Titanium Aluminides 1999*, edited by Y.-W. Kim, D. M. Dimiduk, and M. H. Loretto, TMS, Warrendale, PA, 1999, pp. 25-33.

92. R. Gerling, H. Clemens, F. P. Schimansky, and G. Wegmann: "PM-Processing of an Advanced Gamma-TiAl Alloy: Technologies, Microstructures and Mechanical Properties," in *Structural Intermetallics 2001*, edited by K. J. Hemker, D. M. Dimiduk, H. Clemens, R. Darolia, H. Inui, D. J. Larson, V. K. Sikka, M. Thomas, and J. D. Whittenberger, TMS, Warrendale, PA, 2001, pp. 139-148.

93. U. Habel, C. F. Yolton, and J. H. Moll: "Gas Atomized Gamma-Titanium Aluminide Based Alloys - Processing, Microstructure and Mechanical Properties," in *Gamma Titanium Aluminides 1999*, edited by Y.-W. Kim, D. M. Dimiduk, and M. H. Loretto, TMS, Warrendale, PA, 1999, pp. 301-308.

94. R. Gerling, A. Bartels, H. Clemens, H. Kestler, and F. P. Schimansky: *Intermetal.*, 2004, 12, pp. 275-280.

95. H. Kestler, H. Clemens, H. Baur, R. Joos, R. Gerling, G. Cam, A. Bartels, C. Schleinzer, and W. Smarsly: "Characterization of Gamma-TiAl Sheet Material for Aeroengine Application," in *Gamma Titanium Aluminides 1999*, edited by Y.-W. Kim, D. M. Dimiduk, and M. H. Loretto, TMS, Warrendale, PA, 1999, pp. 423-430.

96. H. Clemens, H. Kestler, N. Eberhardt, and W. Knabl: "Processing of $\gamma$-TiAl Based Alloys an an Industrial Scale," in *Gamma Titanium Aluminides 1999*, edited by Y.-W. Kim, D. M. Dimiduk, and M. H. Loretto, TMS, Warrendale, PA, 1999, pp. 209-223.

97. A. Venskutonis, and K. Riβbacher: *Preparing for the Future*, 2000, 10(2), pp. 2-3.

98. P. A. Bartolotta, and D. L. Krause: "Titanium Aluminide Applications in the High Speed Civil Transport," in *Gamma Titanium Aluminides 1999*, edited by Y.-W. Kim, D. M. Dimiduk, and M. H. Loretto, TMS, Warrendale, PA, 1999, pp. 3-10.

99. W. Smarsly, H. Baur, G. Glitz, H. Clemens, T. Khan, and M. Thomas: "Titanium Aluminides for Automotive and Gas Turbine Applications," in *Structural Intermetallics*, edited by K. J. Hemker, D. M. Dimiduk, H. Clemens, R. Darolia, H. Inui, J. M. Larson, V. K. Sikka, M. Thomas, and J. D. Whittenberger, TMS, Warrendale, PA, 2001, pp. 25-34.

100. T. Tetsui: *Solid State Mater. Sci.*, 1999, 4, pp. 243-248.

101. M. Blum, P. Busse, G. Jarczyk, H. Franz, H. J. Laudenberg, K. Segtrop, and P. Seserko: "First Production Results from a Prototype Plant for Mass Production of Gamma-TiAl Valves," in *Gamma Titanium Aluminides 2003*, edited by Y.-W. Kim, H. Clemens, and A. H. Rosenberger, TMS, Warrendale, PA, 2003, pp. 9-14.

102. H. Baur, D. B. Wortberg, and H. Clemens: "Titanium Aluminides for Automotive Applications," in *Gamma Titanium Aluminides 2003*, edited by Y.-W. Kim, H. Clemens, and A. H. Rosenberger, TMS, Warrendale, PA, 2003, pp. 23-31.

103. A. W. Sommer, and G. C. Keijzers: "Gamma TiAl and the Engine Exhaust Valve," in *Gamma Titanium Aluminides 2003*, edited by Y.-W. Kim, H. Clemens, and A. H. Rosenberger, TMS, Warrendale, PA, 2003, pp. 3-7.

104. T. Tetsui: *Mater. Sci. Eng. A*, 2002, 329-331, pp. 582-588.

105. T. Noda: *Intermetal.*, 1998, 6, pp. 709-713.

106. M. L. Escudero, M. A. Muñoz-Morris, M. C. García-Alonso, and E. Fernández-Escalante: *Intermetal.*, 2004, 12, pp. 253-260.

107. M. Ruales, D. Martell, F. Vazquez, F. A. Just, and P. A. Sundaram: *J. Alloy Compd.*, 2002, 339, pp. 156-161.

108. D. M. Dimiduk, D. Miracle, and C. H. Ward: *Mater. Sci. Tech.*, 1992, 8, pp. 367-375.

109. W. F. Gale: *JOM*, 1999, 51(2), pp. 49-52.

110. M. F. Arenas, and V. L. Acoff: *Scripta Mater.*, 2002, 46(3), pp. 241-246.

111. M. G. Nicholas: *Joining Processes: Introduction to Brazing and Diffusion Bonding*, Kluwer Academic Publishers, Boston, MA, 1998.

112. D. S. Duvall, W. A. Owczarski, D. F. Paulonis, and W. H. King: *Weld. J. Suppl.*, 1972, 53, pp. 41s-49s.

113. A. Rabinkin: *Weld. J.*, 1989, 68(10), pp. 39-45.

114. T. J. Moore, and T. K. Glasgow: *Weld. J. Suppl.*, 1985, 64(8), pp. 219s-226s.

115. W. Li, T. Jin, X. F. Sun, Y. Guo, H. R. Guan, and Z. Q. Hu: *Scripta Mater.*, 2003, 48, pp. 1283-1288.

116. D. S. Duvall, W. A. Owczarski, D. F. Paulonis, and R. P. Schaefer: U.S. Patent No. 4,008,844, 1977.

117. M. A. Burke, G. W. Swartzbeck, and P. D. Freyer: U.S. Patent No. 6,508,000, 2003.

118. V. M. Philip: U.S. Patent No. 6,726,086, 2004.

119. C. J. Thwaites: *Capillary Joining - Brazing and Soft Soldering*, Research Studies Press, Hertfordshire, UK, 1982.

120. T. J. Kelly: *Weld. J. Suppl.*, 1982, 61(10), pp. 317s-319s.

121. T. I. Khan, and E. R. Wallach: *J. Mater. Sci.*, 1996, 31, pp. 2937-2943.

122. A. Ekrami, and T. I. Khan: *Mater. Sci. Tech.*, 1999, 15, pp. 946-950.

123. Y. Zhai, and T. H. North: *J. Mater. Sci.*, 1997, 32, pp. 5571-5575.

124. C. A. Blue, V. K. Sikka, R. A. Blue, and R. Y. Lin: *Metall. Mater. Trans. A*, 1996, 27A, pp. 4011-4017.

125. Z. Li, Y. Zhou, and T. H. North: *J. Mater. Sci.*, 1995, 30, pp. 1075-1082.

126. S. V. Orel, L. C. Parous, and W. F. Gale: *Weld. J. Suppl.*, 1995, 74, pp. 319s-324s.

127. W. F. Gale, and S. V. Orel: *J. Mater. Sci.*, 1996, 31, pp. 345-349.

128. Y. Guan, and W. F. Gale: *Mater. Sci. Tech.*, 1999, 15, pp. 207-212.

129. W. F. Gale, and Y. Guan: *Metall. Mater. Trans. A*, 1996, 27A, pp. 3621-3629.

130. Y. Zhai, T. H. North, and J. Ren: *J. Mater. Sci.*, 1997, 32, pp. 1399-1404.

131. Y. Zhai, T. H. North, and J. Serrato-Rodregues: *J. Mater. Sci.*, 1997, 32, pp. 1393-1397.

132. G. E. Sheward: *High Temperature Brazing in Controlled Atmospheres*, Pergammon, Oxford, UK, 1985.

133. L. A. Greer: *Curr. Opin. Solid St. M.*, 1997, 2(4), pp. 412-416.

134. H. H. Liebermann: *J. Mater. Sci.*, 1984, 19(5), pp. 1391-1396.

135. W. Ozgowicz, J. Tyrlik-Held, G. Thomas, A. Zahara, and J. L. Coze: *Scripta Metall. Mater.*, 1983, 17(3), pp. 295-298.

136. Y. Taniguchi, and K. Kato: *JSAE Rev.*, 1997, 18, pp. 143-173.

137. A. Rabinkin, E. Wenski, and A. Ribaudo: *Weld. J. Suppl.*, 1998, pp. 66s-75s.

138. W. D. Zhuang, and T. W. Eagar: *Weld. J. Suppl.*, 1997, pp. 157s-162s.

139. C. Wan, H. Xiong, and Z. Zhou: *J. Mater. Sci.*, 1999, 34, pp. 3013-3019.

140. E. Lugscheider, K. Bobzin, and M. K. Lake: *Surf. Coat. Tech.*, 2001, 142-144, pp. 813-816.

141. I. Tuah-Poku, M. Dollar, and T. B. Massalski: *Metall. Mater. Trans. A*, 1988, 19A, pp. 675-686.

142. W. F. Gale, and D. A. Butts: *Sci. Technol. Weld. Join.*, 2004, 9(4), pp. 283-300.

143. R. Thamburaj, W. Wallace, and J. A. Goldak: *Int. Mater. Rev.*, 1983, 28(1), pp. 1-22.

144. E. Lugscheider, T. Schittny, and E. Halmoy: *Weld. J.*, 1989, 68(1), pp. 9s-13s.

145. Y. S. Kwon, J. S. Kim, J. S. Moon, and M. J. Suk: *J. Mater. Sci.*, 2000, 35, pp. 1917-1924.

146. M. K. Kitchings, Y. Guan, and W. F. Gale: "Microstructural Development during Transient Liquid Phase Bonding of Structural Intermetallic Compounds," in *Analysis of in-Service Failures and Advances in Microstructrual Characterization*, edited by E. Abramovici, D. O. Northwood, M. T. Shehata, and J. Wylie, ASM International, Materials Park, OH, 1999, pp. 425-430.

147. T. Tetsui: *Intermetal.*, 2001, 9, pp. 253-260.

148. A. Shapiro, and A. Rabinkin: *Weld. J.*, 2003, 82(10), pp. 36-43.

149. B. Dang: M.S. thesis, Auburn University, Auburn, AL, 2000.

150. G. Petzow, and G. Effenberg (Eds.): *Ternary Alloys: A Comprehensive Compendium of Evaluated Constitutional Data and Phase Diagrams: Al-Cu-S to Al-Gd-Sn*, VCH Publishers, New York, 1992.

151. W. F. Gale, Y. Shen, J. W. Fergus, and X. Wen: *J. Mater. Res.*, 1999, 14(10), pp. 3889-3894.

152. D. A. Butts, T. Zhou, and W. F. Gale: "Transient Liquid Phase Bonding of TiAl-Alloys: Wettability, Microstructure, Mechanical Properties and Potential for Automation," in *Trends in Welding Research*, edited by S. A. David, T. DebRoy, J. C. Lippold, H. B. Smartt, and J. M. Vitek, ASM International, Materials Park, OH, 2003, pp. 495-499.

153. Y. Shen, W. F. Gale, J. W. Fergus, and X. Wen: *Mater. Sci. Tech.*, 2001, 17, pp. 1293-1298.

154. W. D. MacDonald, and T. W. Eagar: *Metall. Mater. Trans. A*, 1998, 29A, pp. 315-325.

155. K. Ohsasa, T. Shinmura, and T. Narita: *J. Phase Equilib.*, 1999, 20(3), pp. 199-206.

156. S. R. Cain, J. R. Wilcox, and R. Venkatraman: *Acta Mater.*, 1997, 45(2), pp. 701-707.

157. C. W. Sinclair: *J. Phase Equilib.*, 1999, 20(4), pp. 361-369.

158. J. T. Niemann, and R. A. Garret: *Weld. J.*, 1974, 52, pp. 175-184.

159. Y. Nakao, K. Nishimoto, K. Shinozaki, and C. Kang: "Theoretical Research on Transient Liquid Insert Metal," in *Superalloys 1988*, edited by S. Reichman, D. N. Duhl, G. Maurer, S. Antolovich, and C. Lund, Metallurgical Society of AIME, Warrendale, PA, 1989, pp. 775-783.

160. H. Nakagawa, C. H. Lee, and T. H. North: *Metall. Mater. Trans. A*, 1991, 22A, pp. 543-555.

161. Y. Zhou: *J. Mater. Sci.*, 2001, 20, pp. 841-844.

162. Y. Zhou, M. L. Kuntz, and S. F. Corbin: "Prediction of the Completion Time for Isothermal Solidification in TLP Bonding," in *Joining of Advanced and Specialty Materials V*, edited by J. E. Indacochea, J. N. DuPont, T. J. Lienert, W. Tillmann, N. Sobczak, W. F. Gale, and M. Singh, ASM International, Materials Park, OH, 2003, pp. 75-82.

163. G. W. Qin: *Intermetal.*, 2003, 11, pp. 907-910.

164. B. D. Cullity, and S. R. Stock: *Elements of X-Ray Diffraction*, 3rd Prentice Hall, Upper Saddle River, NJ, 2001.

165. A. Shapiro, and A. Rabinkin: "State-of-the-Art and New Potential Aerospace Applications of Titanium-Based Brazing Filler Metals: Overview," Proceedings of *International Brazing and Soldering Conference*, San Diego, CA, 2003.

166. Q. Xu, M. C. Chaturvedi, N. L. Richards, and N. Goel: "Diffusion Brazing of a TiAl Alloy," Proceedings of *International Brazing and Soldering Conference*, 2000.

167. R. W. Hertzberg: *Deformation and Fracture Mechanics of Engineering Materials*, 4th John Wiley and Sons, Inc., New York, 1996.

168. H. Clemens, W. Glatz, N. Eberhardt, H.-P. Martinz, and W. Knabl: "Processing Properties and Applications of Gamma Titanium Aluminide Sheet and Foil Materials," in *High-Temperature Ordered Intermetallic Alloys VII*, edited by C. C. Koch, C. T. Liu, N. S. Stoloff, and A. Wanner, Materials Research Society, Pittsburgh, PA, 1996, pp. 29-44.

169. G. Das: Pratt & Whitney, East Hartford, CT, Personal Communication, 2002.

170. J. Rüsing, and C. Herzig: *Scripta Mater.*, 1995, 33(4), pp. 561-566.

171. W. Sprengel, N. Oikawa, and H. Nakajima: *Intermetal.*, 1996, 4, pp. 185-189.

172. J. Rüsing, and C. Herzig: *Intermetal.*, 1996, 4, pp. 647-657.

173. H. Nakajima, W. Sprengel, and K. Nonaka: *Intermetal.*, 1996, 4, pp. 17-28.

174. H. Nakajima, K. Nonaka, W. Sprengel, and M. Koiwa: *Mater. Sci. Eng. A*, 1997, 239-240(1-2), pp. 819-827.

175. C. Herzig, T. Wilger, T. Przeorski, F. Hisker, and S. Divinski: *Intermetal.*, 2001, 9, pp. 431-442.

176. J. Breuer, T. Wilger, M. Friesel, and C. Herzig: *Intermetal.*, 1999, 7, pp. 381-388.

177. R. Kainuma, and G. Inden: *Z. Metallkd.*, 1997, 88, pp. 429-432.

178. Y. Mishin, and C. Herzig: *Acta Mater.*, 2000, 48, pp. 589-623.

179. W. F. Gale, and T. C. Totemeier (Eds.): *Smithells Metals Reference Book*, 8th Edition, Butterworth-Heinemann, Oxford, 2004.

180. T. Zhou, and W. F. Gale: *Mater. Sci. Tech.*, 2003, 19, pp. 1084-1090.

181. R. J. Klein-Wassink: *J. I. Met.*, 1967, 95, pp. 38-43.

182. Binary Alloy Phase Diagrams, 2nd Edition, Version 1.0, ASM International Software, Materials Park, OH, 1996.

183. J. C. Ambrose, M. G. Nicholas, N. Young, and S. L. Jenkins: *Mater. Sci. Tech.*, 1990, 6, pp. 1021-1031.

184. K. Saida, Y. Zhou, and T. H. North: *J. Mater. Sci.*, 1993, 28, pp. 6427-6432.

185. J. Crank: *The Mathematics of Diffusion*, 2nd Oxford University Press, Oxford, UK, 1975.